Experimental Investigation of Transient RCCI Combustion in a Light Duty Diesel Engine

By

Reed M. Hanson

A dissertation submitted in partial fulfillment of the requirements for the degree of

Doctor of Philosophy

(Special Graduate Committee: Combustion Engineering)

at the

University of Wisconsin-Madison

2014

Date of final oral examination: November 27th, 2013

The dissertation is approved by the following members of the Final Oral Committee:
Rolf D. Reitz, Wisconsin Distinguished Professor, Mechanical Engineering
David A. Rothamer, Assistant Professor, Mechanical Engineering
James J. Schauer, Professor, Civil and Environmental Engineering
Tracey A. Holloway, Associate Professor, Civil and Environmental Engineering
Michael L. Corradini, Wisconsin Distinguished Professor, Engineering Physics

Abstract

Low Temperature Combustion (LTC) is currently being researched as a way to reduce problematic emissions (i.e., NO_x and PM) from compression-ignition engines while maintaining high fuel efficiency. One of the primary types of LTC is Premixed Compression Ignition (PCI), with some examples of PCI being homogeneous charge compression ignition (HCCI), premixed charge compression ignition (PCCI), reactivity controlled compression ignition (RCCI) and partially premixed combustion (PPC). These LTC strategies use early fuel injections to allow sufficient time for air/fuel mixing before combustion. By increasing the amount of air/fuel premixing, NO_x and PM emissions can be lowered due to the reduced local and global equivalence ratios. The lean nature of PCI also maintains high thermal efficiency due to the reduced heat transfer losses from the reduced peak combustion temperatures. However, too much air/fuel premixing can lead to rapid energy release rates, limiting the operation space for PCI. To combat this problem, the combustion strategy of interest for the study, RCCI, uses fuel reactivity gradients to increase combustion duration (i.e., reduce the energy release rate) and phasing control, thereby increasing the engine operating space for PCI operation.

Previous tests [1-7] have shown promising results for petroleum-based fuels with RCCI. Recent work at Oak Ridge National Laboratory (ORNL) has shown how blends of biofuels with petroleum fuels can improve RCCI combustion performance [8,9] The work sets out to examine biofuel performance over a wide engine operating space both at steady-state and transient operating conditions with RCCI

combustion. It is hoped to demonstrate the capability and effects of using bio-derived fuels in place of conventional petroleum-derived fuels for advanced combustion strategies under real-world operating conditions. In RCCI operation, blends of biodiesel and ethanol fuels will be investigated to examine the fuel effects on the combustion event.

Acknowledgements

This is dedicated to the memory of my grandmother, Myrna “Babe” Backberg, who passed away during the writing of this dissertation

Table of Contents

List of Figures

List of Tables

Nomenclature

Acronyms

AFR	Air Fuel Ratio
AHRR	Apparent Heat Release Rate
ATDC	After Top Dead Center
BC	Black Carbon
BMEP	Brake Mean Effective Pressure
BTDC	Before Top Dead Center
BTE	Brake Thermal Efficiency
BSFC	Brake Specific Fuel Consumption
CA	Crank Angle
CA50	Crank Angle of Fifty Percent Mass Fraction Burned
CDC	Conventional Diesel Combustion
CFD	Computational Fluid Dynamics
CI	Compression Ignition
CL	Closed Loop
CN	Cetane Number
COV	Coefficient of Variation
CR	Compression Ratio
DAQ	Data Acquisition System
DOC	Diesel Oxidation Catalyst
DPF	Diesel Particulate Filter
DI	Direct Injection
ECT	Engine Coolant Temperature
ECU	Engine Control Unit
EGR	Exhaust Gas Recirculation
EIA	Energy Information Agency
EPA	Environmental Protection Agency
FID	Flame Ionization Detector
FSN	Filter Smoke Number
FTIR	Fourier Transform Infrared
FTP	Federal Test Procedure
GDI	Gasoline Direct Injection
GHG	Green House Gas
GM	General Motors
GMEP	Gross Mean Effective Pressure
GTE	Gross Thermal Efficiency
HC	Hydrocarbon
HCCI	Homogeneous Charge Compression Ignition
HD	Heavy-Duty
HP	High Pressure

HRR	Heat Release Rate
HTC	High Temperature Combustion
HTHR	High Temperature Heat Release
IC	Internal Combustion
ICE	Internal Combustion Engine
ISFC	Indicated Specific Fuel Consumption
IMEP	Indicated Mean Effective Pressure
IPCC	International Panel on Climate Change
IVC	Intake Valve Closing
LD	Light-duty
LFE	Laminar Flow Element
LNT	Lean NOx Trap
LP	Low Pressure
LTC	Low Temperature Combustion
LTHR	Low Temperature Heat Release
LTO	Low Temperature Oxidation
MAF	Mass Air Flow
MCE	Multi-cylinder
MON	Motor Octane Number
MPRR	Maximum Pressure Rise Rate
NASA	National Aeronautical and Space Administration
NC	Next Cycle
NDIR	Non-Dispersive Infrared
NO	Nitrogen Oxides
NMEP	Net Mean Effective Pressure
NTC	Negative Temperature Coefficient
NTE	Net Thermal Efficiency
NTL	N-heptane Toluene
NVO	Negative Valve Overlap
OECD	Organization for Economic Co-operation and Development
OEM	Original Equipment Manufacturer
OL	Open Loop
ON	Octane Number
ORNL	Oak Ridge National Laboratory
PAH	Polycyclic Aromatic Hydrocarbon
PCCI	Premixed Charge Compression Ignition
PCI	Premixed Compression Ignition
PFI	Port Fuel Injection
PID	Proportional Integral Differential
PM	Particulate Matter
PMEP	Pumping Mean Effective Pressure
PON	Pump Octane Number
PPC	Partially Premixed Combustion
PRF	Primary Reference Fuel

PRR	Pressure Rise Rate
RCCI	Reactivity Controlled Compression Ignition
RF	Radiative Forcing
RON	Research Octane Number
SAE	Society of Automotive Engineers
SCCI	Stratified Charge Compression Ignition
SCE	Single-cylinder Engine
SCOTE	Single Cylinder Oil Test Engine
SCR	Selective Catalyst Reduction
SI	Spark Ignition
SME	Soy Methyl Ester
SOI	Start of Injection
TDC	Top Dead Center
TWC	Three Way Catalyst
ULSD	Ultra Low Sulfur Diesel
VCT	Variable Cam Timing
VGT	Variable Geometry Turbine
VSA	Variable Swirl Actuator

Chapter 1 Introduction

1.1 Background

One of the most significant inventions in recent history has been the internal combustion engine. The internal combustion engine has allowed a fundamental change in mobility that people could travel distances never before imagined. The history of the internal combustion engine begins in the late 1800's when Nicolaus Otto and Rudolf Diesel started out designing engines for stationary power applications and helped develop the two main types of engines we see today, namely the compression-ignition and spark-ignition engines [10]. While they were revolutionary for their time, they were inefficient as compared modern engines. However, advancements from many engineers in materials, operating pressures, air systems, fuel systems, etc., have been able to drastically increase the energy conversion efficiency of the internal combustion engine.

Even with these improvements, there are still problems with their use. Namely, internal combustion engines produce combustion products that are harmful to both human health and the climate. For engines using carbon based fuels, typical regulated combustion products are CO, CO_2, UHC, PM and NO_x. More specifically, engines can produce ultrafine particles which cause health problems [11], while NO_x and CO_2 are known greenhouse gasses which are responsible for climate change [12]. For continued use of engines as the prime mover for personal transportation,

significant work is needed to reduce the amount of these pollutants and their effects on society.

1.2 Research Objective

Currently, the majority of fundamental engine research is conducted at steady-state operating conditions. While this makes testing easier with currently available laboratory equipment, most vehicles operate under constantly changing engine speeds and loads. Thus, most US Federal certification testing involves using the vehicle operating under simulated realistic operating conditions, usually over transient test cycles such as the US Environmental Protection Agency (EPA) FTP75 [12]. Because transient testing utilizes specialty equipment not needed for steady-state testing, it can be convenient to use and/or extrapolate steady-state results to compare with transient results. Unfortunately, the literature has shown that engine performance under steady-state conditions is not a reliable indicator of transient or in-use emissions [14-15]. Significant portions of the total emissions are generated during the short periods when rapid speed or load changes occur [6].

Work by the US EPA [14] compared results of the ISO 8-mode steady-state duty cycle test with several transient test cycles for a number of different engines. They found that NO_x could be predicted within 10% but HC and PM were 60% under-predicted. Significant variation in emissions for each test cycle and each engine used were found. Additional work [15] had better steady-state to transient agreement, but still had upwards of 60% under-prediction of HC and PM emissions. These results show that it is very difficult to predict transient test cycle emissions

based on steady-state results. These findings are important because low temperature combustion (LTC) strategies are being developed with most of the data in the literature being taken at steady-state. In order to assess their performance in vehicle operation, assumptions need to be made on how they will respond to transient operation and/or experiments need to be done to verify transient LTC performance. Such experiments are difficult to do because of the complex nature of LTC, so much less is known about LTC transient operation compared to high temperature combustion transient operation in the literature.

Because of this lack of understanding, the focus of the work is to investigate advanced LTC strategies, RCCI combustion in this work, to reduce the amount health- and climate- impacting emissions from multi-cylinder, compression-ignition engines under steady-state and transient operating conditions.

The experimental setup was chosen to more closely approximate a production engine than typical research engines by using a multi-cylinder engine. Normally, research uses single-cylinder engines to obtain more accurate control of the boundary conditions of the experiment, namely more accurate temperature and pressure control. By using a multi-cylinder engine, a more realistic approximation of how advanced combustion strategies operate under real world boundary conditions can be observed. Finally using a multi-cylinder engine under transient operating conditions in the lab is as close to vehicle operation as possible.

The overall goal was to investigate transient operation of Reactivity Controlled Compression Ignition (RCCI) combustion as compared to transient operation with

conventional diesel combustion (CDC). RCCI is a LTC strategy that uses two fuels with different auto-ignition characteristics such that there are optimized fuel reactivity and equivalence ratio gradients throughout the combustion chamber. Having optimized reactivity stratification allows for low engine-out PM and NO_x emissions because of the low peak combustion temperature, and control of the heat release rate (HRR) event over a wide range of operating conditions. The use of two fuels also allows the global and local reactivity to be optimized on a cycle-by-cycle basis with an appropriate engine controller.

Understanding how advanced combustion modes, such as RCCI, behave under the widest variety of operating conditions will help the community's understanding to grow such that it will accelerate the time of adoption of advanced combustion modes into mass production in order to realize improvments of GHG and smog forming emissions from the transportation sector.

Chapter 2 Literature Review

2.1 Anthropogenic Global Warming

For last 100 years, the temperatures of the ocean and surface air have been increasing at an unprecedented rate. [12]. It is an understatement to say that this is a problem that's much wider in scope than is possible to cover in this work. Figure 2.1 shows trends for global sea level, average temperature and snow cover [12].

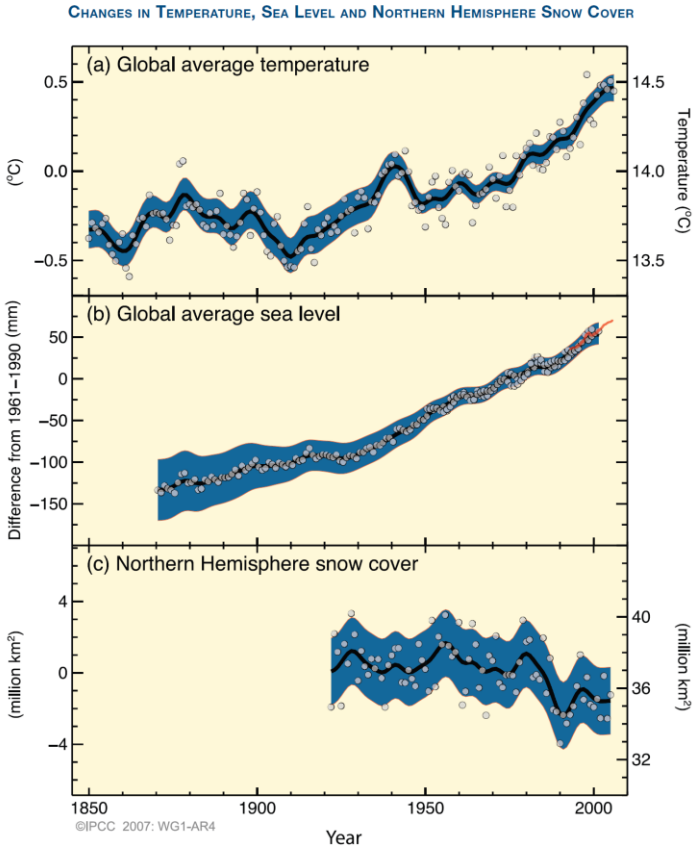

Figure 2.1 Global average temperatures and sea level changes vs. time [12]

This warming trend can be shown to cause numerous problems – from rising sea levels which could cause wide spread property destruction and displacement of

large numbers of people, increases in the ocean acidity, changes to global and local weather patterns and loss of biodiversity. According to the findings by the International Panel on Climate Change (IPCC), climate change is caused by increasing concentrations of positive radiative forcing molecules (CO_2, CH_4 and N_2O) in the atmosphere and their resulting changes to the overall radiation heat transfer balance of the Earth. Changes in the concentration of greenhouse gases (GHG) as a function of time are shown in Figure 2.2.

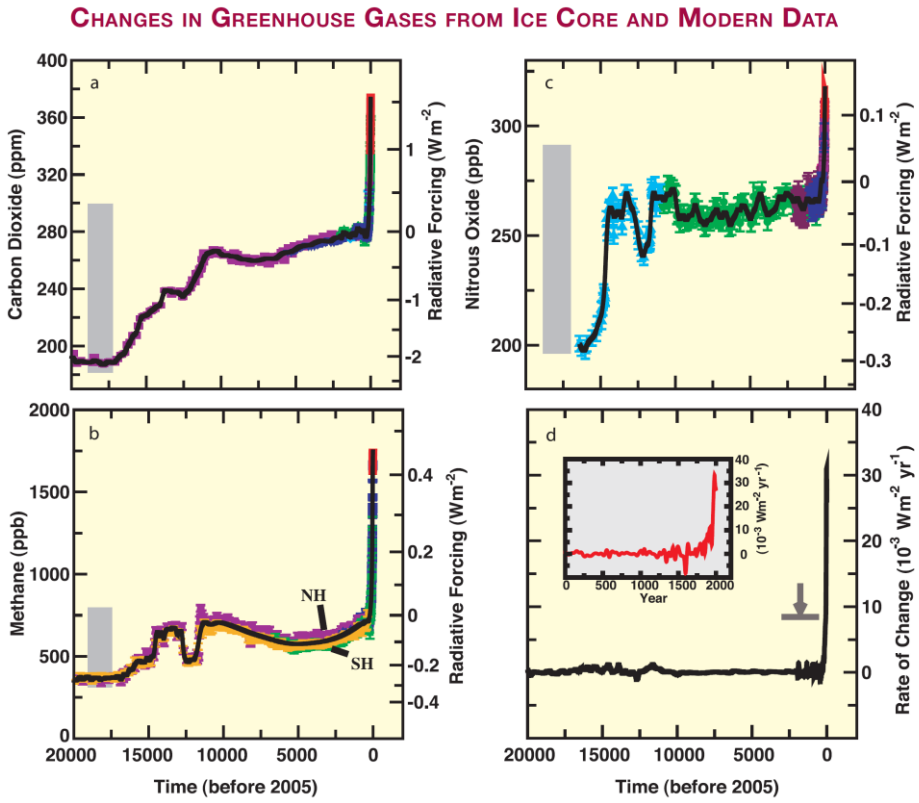

Figure 2.2 GHG concentrations vs. time [12]

Rising concentrations of these GHGs are caused by human activities such as burning of fossil fuels agriculture and land use. The current models show the

increasing temperature trend, and without anthropogenic GHG effects, the models do not match the observations from just natural forcing only, as shown in Figure 2.3.

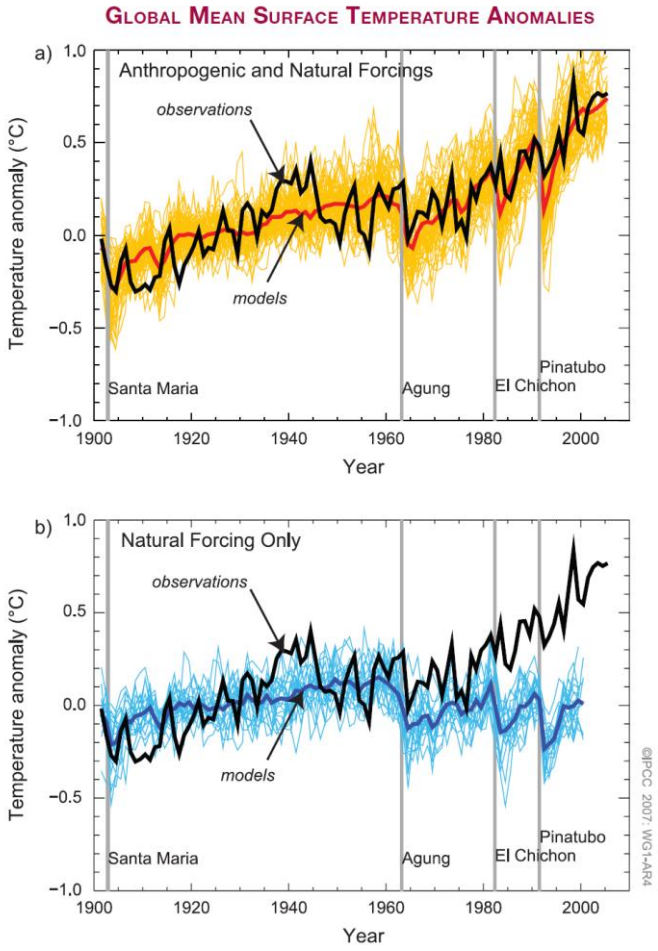

Figure 2.3 Global mean surface temperatures with anthropogenic and natural forcings [12]

With the long life time of GHGs, warming is expected to occur even if their use slows. Current projections for the long term temperature sensitivity of the climate predict an increase of 2-4.5°C.

Also discussed in the IPCC report are some secondary causes of climate change, such as anthropogenic aerosols. One of the most emitted, and relative to

the current work, are aerosols and in particular, black carbon (BC). Black carbon can be described as an agglomeration of carbon molecules (along with adsorbed HC and organic species) into clusters the sizes of 10-200 nm [10]. BC typically occurs is combustion with high temperatures and low oxygen concentrations. Some man made sources of BC are biomass burning, coal and diesel combustion, shown in Figure 2.4. [16,17]

Figure 2.4 Photographs of BC being emitted from combustion sources [17]

Reducing BC is an important part of slowing climate change as described by the EPA and National Aeronautical and Space Administration (NASA). The effect of aerosols on climate change is a complicated issue as the net radiative forcing of BC is under debate. It is emitted with other aerosols that have a negative radiative forcing (RF) but it is currently thought that BC has a net positive RF. Reducing BC emissions will also increase local human health as BC can cause respiratory illness due to small particles depositing in the lungs. Also, BC reduction will have an immediate impact as BC has short lifetime of only weeks in the atmosphere compared with other GHGs which persist for much longer periods. Climate Change benefits of BC reduction are mainly changes to the albedo in areas with dense

snow/ice pack such as the Himalayas and the Arctic. Reducing the rate of snow/ice coverage loss is of importance because it can slow down the time scale of climate change and keep it from getting into positive feedback loops.

Thus, it is important to reduce BC, and in the case of this work, BC from diesel engines. This can be done by using more efficient combustion modes and utilizing advanced exhaust gas aftertreatment, such as diesel particulate filters. Advanced combustion modes such as Low Temperature Combustion (LTC) can accomplish particulate reduction with efficiency benefits making it most ideal solution as it is a win-win for both CO_2 and BC. Figure 2.5 shows that a combination of BC and CO_2 reduction measures can help to keep climate temperature change below 2°C [16].

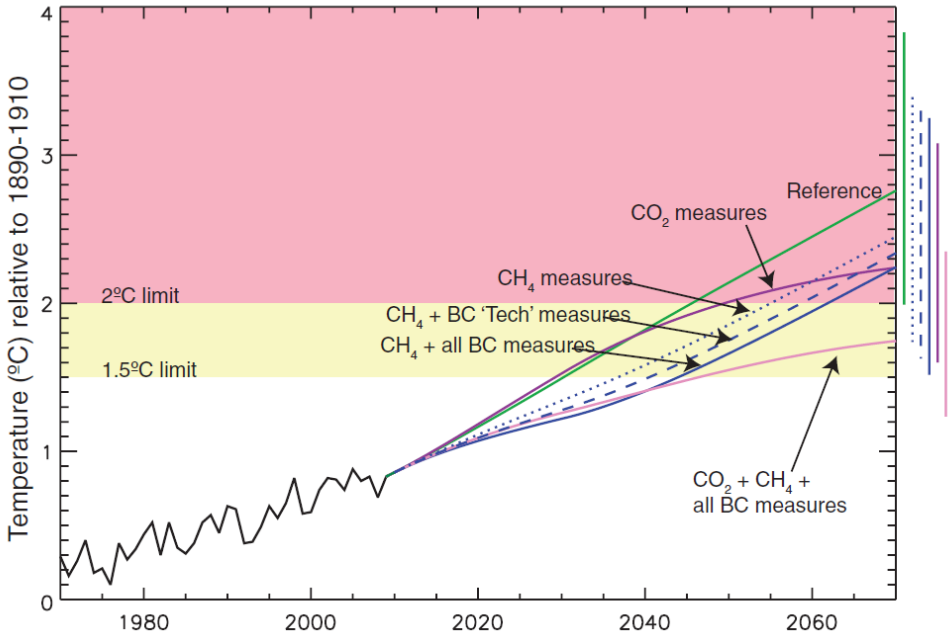

Figure 2.5 BC and CO_2 reduction measures [16]

2.2 Energy Usage

Unfortunately for climate change concerns, according to the US Energy Information Agency (EIA) [18], energy usage is expected to increase usage, with most of the increase from non-Organization for the Economical Co-operation and Development (OECD) countries. However, this gives the opportunities to start fresh with rapid use of new technologies. The global energy use projection is shown in Figure 2.6.

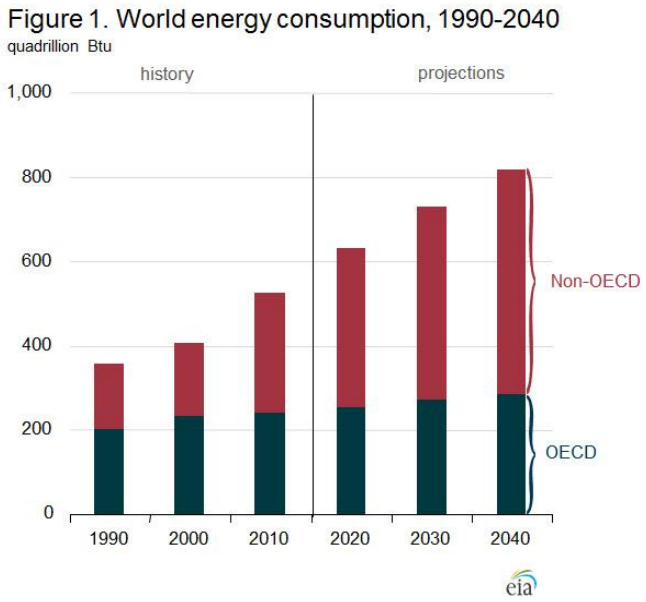

Figure 2.6 World energy consumption as a function of time [18]

Of this projected energy use increase, most is going to come from fossil fuels like coal, oil and natural gas. The rest will be from renewables and nuclear as shown in Figure 2.7.

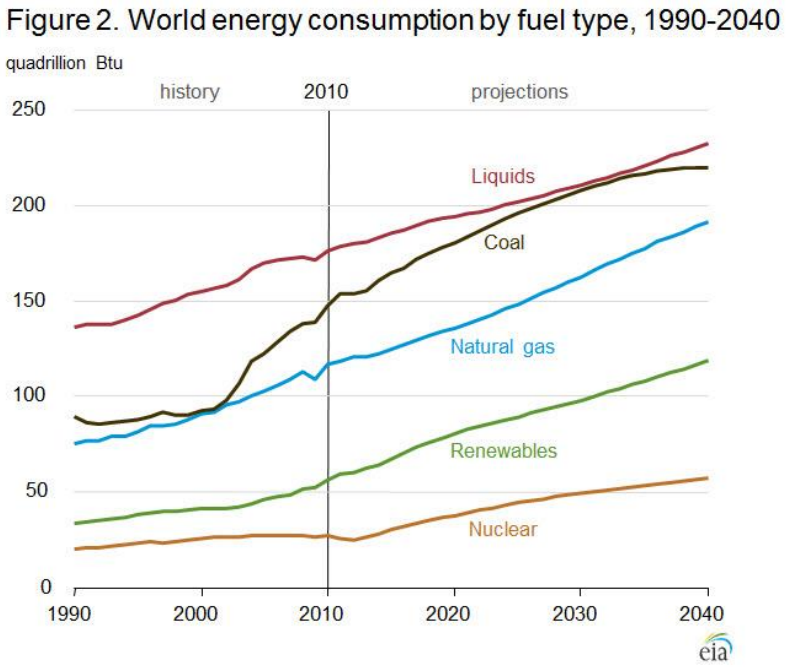

Figure 2.7 World energy consumption by fuel type [18]

Currently, transportation uses 27% of the total energy [18] with 93% of that coming from petroleum. Since transportation is likely to use internal combustion engines for the foreseeable future, it is important to reduce the amount of fuel used by these devices to decrease CO_2, BC and PM. The two ways to do this in this explored work are to use low carbon fuels, such as biofuels which have a higher H_2 content and possibly have a lower lifecycle carbon footprint depending on the production method. Second, is to increase the efficiency of the engine. By doing this we get more work per a given amount of fuel, thus reducing the emitted CO_2 from the engine.

2.3 Internal Combustion Engine Efficiency

Because one of the goals of the research is to increase engine efficiency, it is important to review internal combustion engine fundamentals. An internal combustion engine is an open system where a new set of reactants (i.e., air and fuel) are combined and form products for each cycle. Since it is an open system, there is no requirement to return the working fluid to the original conditions such as in a closed Carnot cycle heat engine. Following a first and second law analysis on an open, reacting system, the maximum work available for an internal combustion engine can be shown to be the Gibbs free energy at the reference temperature and pressure. Depending on the fuel's energy to exergy ratio, the maximum efficiency approaches 100%. To visualize areas where additional work can be extracted, a first and second law analysis of where the energy and exergy are lost can be seen in Figure 2.8 [19]. Here, it can be seen that the areas that are available for extracting additional work are to minimize heat transfer, to recover some of the exhaust energy/exergy and to reduce combustion irreversibilities.

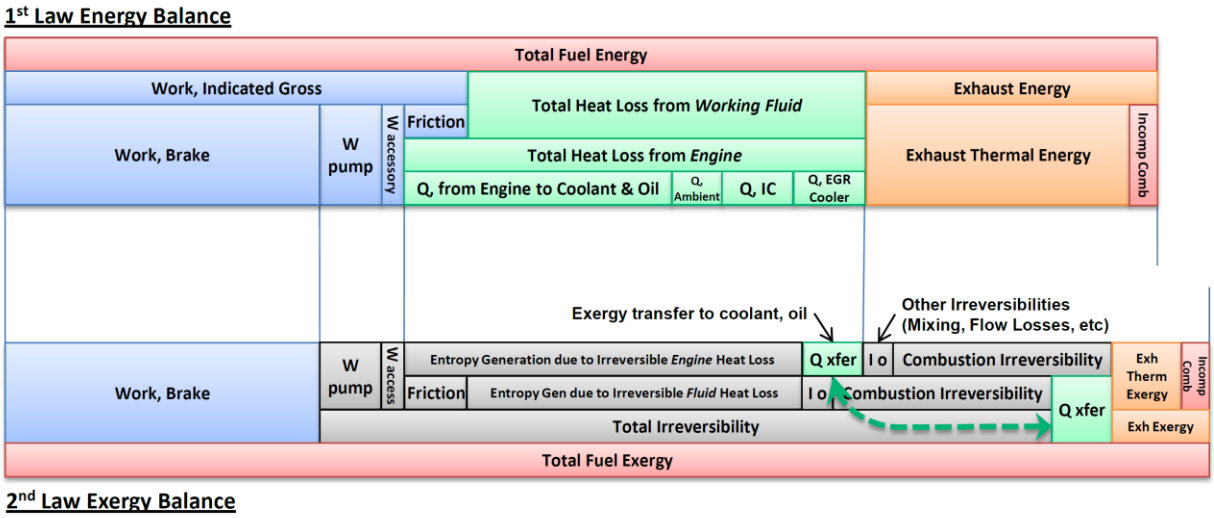

Figure 2.8 1st and 2nd law balances on an internal combustion engine [19]

While it is practically difficult to reduce combustion irreversibilites, it is possible by having higher combustion temperatures and using simpler fuel molecules such as H_2 and CO. The problem with operating at higher temperatures is the limited material strength of the engine hardware. Storage of gaseous fuels such as H_2 and CO onboard a vehicle is also difficult. As shown by Caton, having lower combustion irreversibilities does not always give higher brake thermal efficiency [20].

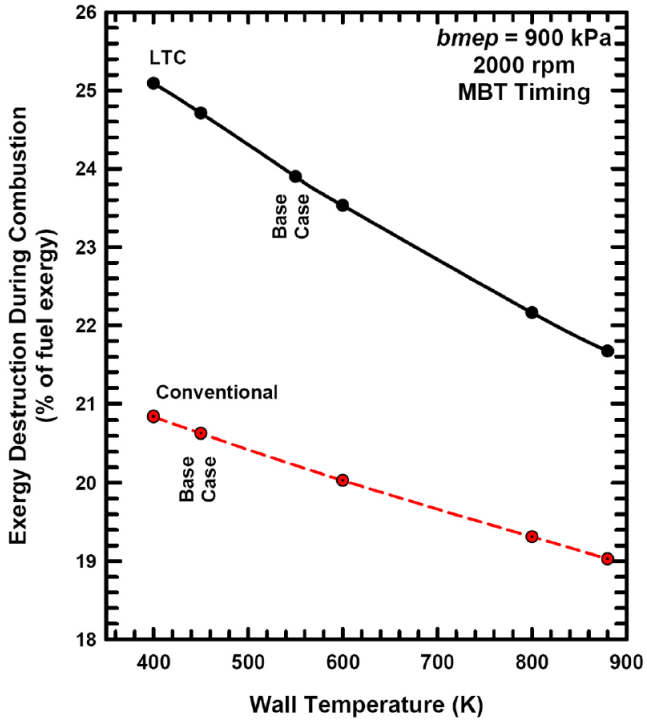

Figure 2.9 Exergy destruction for conventional vs. low temperature combustion [20]

As shown in Figure 2.9, while higher exergy was destroyed during combustion with LTC, the additional exergy in the conventional combustion exhaust does not contribute to additional piston work and would have to have been recovered later by another process. Even with higher combustion availability loss, LTC has a net gain in thermal efficiency from lower availability losses to heat transfer and by having more favorable working fluid properties.

As seen in [19], additional work can be gained by extracting work from the exhaust flow with a waste heat recovery system. Current systems being investigated are thermo-electrics, turbo-compounding and organic Rankine cycles. By converting this exergy in the exhaust stream into shaft or electrical work, an additional 3-10% thermal efficiency improvement can be achieved [21, 22].

Another way to increase engine thermal efficiency is to reduce the availability lost as heat transfer. One of the most practical ways to accomplish this is to lower the peak combustion temperature. LTC has two main benefits as it reduces heat transfer to the engine coolant system where its availability is low (due to the small temperature difference between it and the environment) and that it can improve the working fluid properties [20, 23].

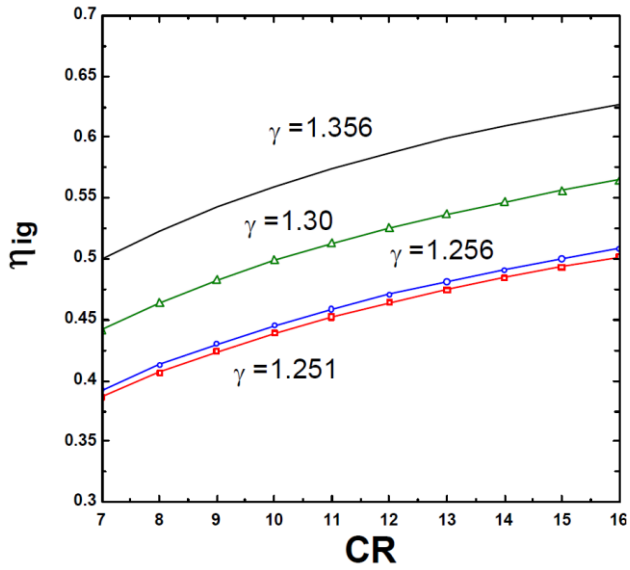

Figure 2.10 Indicated gross thermal efficiency as a function of compression ratio for different values of gamma [23]

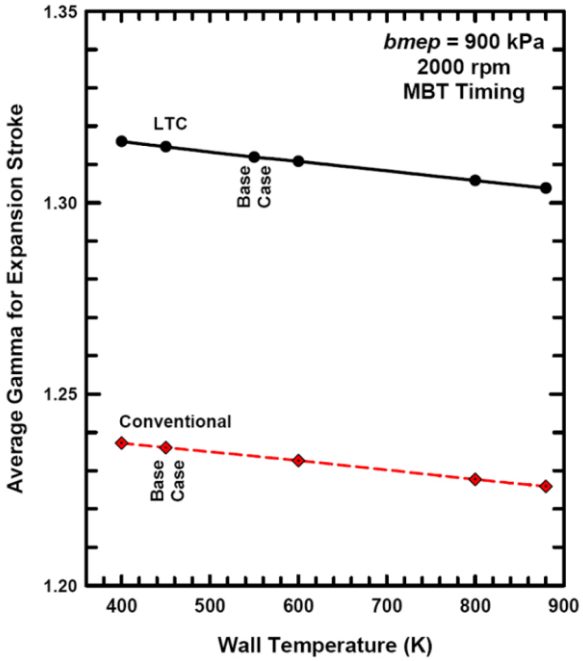

Figure 2.11 Expansion stroke gamma of low temperature combustion vs. conventional combustion for various wall temperatures [20]

As seen in Figure 2.10 and Figure 2.11, gamma (i.e., the ratio of specific heats) of the working fluid (air in this case) is a function of temperature. If the gas temperature is lowered, there can be more work extracted per unit volume and thus the engine efficiency will increase. The net gain in gamma and lower heat transfer more than offsets losses and combustion exergy increases from LTC.

When taken to extreme values, having a working fluid made of monatomic molecules, such as Argon, would be desirable, as its gamma would be higher than air (1.67 vs. 1.4 at standard temperature). Having a higher gamma means there are less available energy storage modes to adsorb the energy that could be used to

increase the pressure of the fluid and be extracted as shaft work during the expansion process.

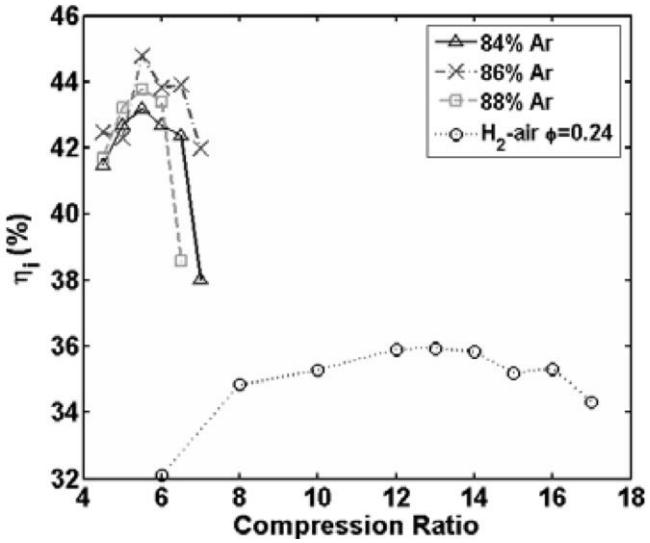

Figure 2.12 Indicated gross thermal efficiency when operating with H_2-air mixtures compared with Ar-O_2 mixtures [24]

As shown in Figure 2.12, Dibble, et al. found that at 86% Ar/14% O_2 mixtures, the peak thermal efficiency could be increased by ~8%. While impractical for real engines, these experiments show how changes to the working fluid of the engine can result in dramatic improvements to thermal efficiency [24].

2.4 Conventional Diesel Combustion

The diesel-fueled compression-ignition engine is the most efficient type of engine currently sold. While having the advantage in fuel efficiency over spark-ignition (SI) engines, diesel engines also have emissions both benefits and problems. Diesel engines offer decreased emissions of partial combustion products

such as CO and HC. In contrast, diesel engines also feature increased NO_x and PM emissions compared to spark-ignition engines.

Since widely used and compared to in the present work, it is important to understand the conventional diesel combustion (CDC) process. In work by Dec in his conceptual model, the mixing-controlled combustion process was explained through the use of optical diagnostic techniques [25]. Diesel combustion is different from SI combustion in that it does not use a spark plug to initiate combustion; rather it uses higher charge gas temperatures to auto-ignite a high reactivity fuel. Load is controlled by the injected quantity of fuel and the airflow is unthrottled, usually at high excess air ratios. During conventional diesel combustion, fuel is injected near top dead center (+/- 20°) at high pressures (1,000-3,000 bar). High fuel pressures are needed to atomize the fuel and mix the air with the fuel before ignition. After injection, the fuel penetrates into the cylinder as a liquid for a distance commonly referred to as the liquid length (as seen in Figure 2.13). This distance is a function of injector hole size, TDC temperature and density [3]. As hole size increases, the liquid length increases due to the additional time needed for vaporization. As the combustion temperature and density decreases, liquid length increases again due to slower vaporization. After the liquid has vaporized (~25mm), the fuel rich (equivalence ratio > 2) vapor autoignites and sets up a stoichiometric diffusion flame. This ignition phase is also known as the premixed burn phase, but it only accounts for a small portion of the total combustion. The premixed combustion is also responsible for the loud combustion noise “knocking” associated with diesel

engines due to the fast pressure rise rates. After the premixed combustion sets up the flame, the rest of the fuel is consumed in the diffusion burn part of the combustion event. Here, rich combustion products such as polycyclic aromatic hydrocarbons (PAH) and acetylene continue to form and penetrate further into the cylinder in the center of the reacting fuel jets. With the combustion only occurring at the flame outer surface, the rich, partially broken down fuel fragments wait to be combusted. The rate of combustion is limited by how fast the air and fuel can physically mix (i.e., mass transfer rates) at the flame, which is why diesel combustion is also called diffusion or mixing-controlled combustion.

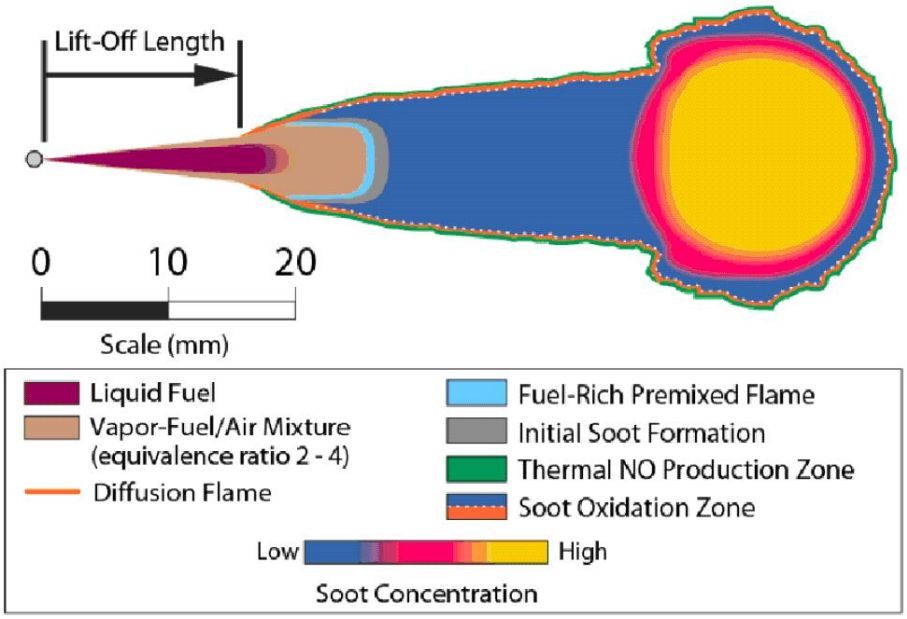

Figure 2.13 Combustion regions and soot formation in diffusion flame [25].

This type of non-premixed combustion produces well known emissions trends [26] and the resulting high emission levels are the reason for new emission standards and continued combustion research. NO_x emissions are high with this

type of combustion due to the high temperatures seen in the near stoichiometric flame. Temperatures here are approximately on the order of the adiabatic flame temperature (2,000+ K), which is well above the temperature (1,900 K) needed for thermal NO_x production [26]. PM emissions are also a problem since this is a non-premixed system. Because of the large air/fuel gradients, with extremely rich areas greater than equivalence ratio = 2, there is a possibility for some of the fuel particles in the middle of the spray plume to not be combusted before the flame is extinguished. The oxidation rate of these uncombusted, rich fuel particles is slowed because of the low in-cylinder temperatures late in the cycle. Thus, PM is frozen as the black soot particle seen coming out of some commercially available diesel engines. HC and CO are, fortunately, not usually a problem for this type of combustion as there is no ring-pack flow for HC to become trapped early in the cycle [10]. There is excess air and high in-cylinder temperatures (1,300+ K [25]), which combine to oxidize both HC and CO to complete combustion products, H_2O and CO_2. Any additional HC and CO that are left can be oxidized in a Diesel Oxidation Catalyst (DOC). However, NO_x and PM emissions are difficult to remove via changes to the in-cylinder combustion event, and therefore devices are required to treat the exhaust before it is released into the atmosphere in order to pass regulated emissions mandates. While these devices (DOC, Diesel Particulate Filter, Lean NOx Trap and/or Selective Catalyst Reductant) are successful in treating exhaust pollutants, they also can decrease the fuel efficiency [27, 28].

2.5 Low Temperature Combustion

Due to the fuel efficiency penalty of current exhaust aftertreatment devices to remove exhaust pollutants formed in the CDC combustion process, current engine research is focusing on utilizing advanced combustion techniques to lower problematic emissions in-cylinder. By eliminating NO_x and PM emissions in the combustion chamber, fuel efficiency is not compromised by conventional exhaust aftertreatment systems. A common classification of these advanced combustion strategies is called low temperature combustion (LTC). There are several different LTC strategies, but most fall under the category of premixed compression ignition (PCI). Specific examples include homogeneous charge compression ignition (HCCI), premixed charge compression ignition (PCCI), reactivity controlled compression ignition (RCCI) and partially premixed combustion (PPC). All of these combustion strategies focus on lowering the peak combustion temperature and creating a more homogeneous charge (as compared to conventional diesel combustion (CDC)) so as to produce low levels of NO_x and PM emissions.

Similar to the Dec model, a conceptual model for LTC has been proposed by researchers at Sandia National Laboratory [29]. In the work, LTC combustion with diesel fuel and high exhaust gas recirculation (EGR) rates were examined to show the differences between high temperature combustion (HTC) and LTC over early and late combustion phasings. It is useful to examine how the LTC combustion process progresses compared to HTC. Figure 2.14 shows the progression of the

fuel spray and combustion for an early and late injection diesel partially premixed combustion strategy.

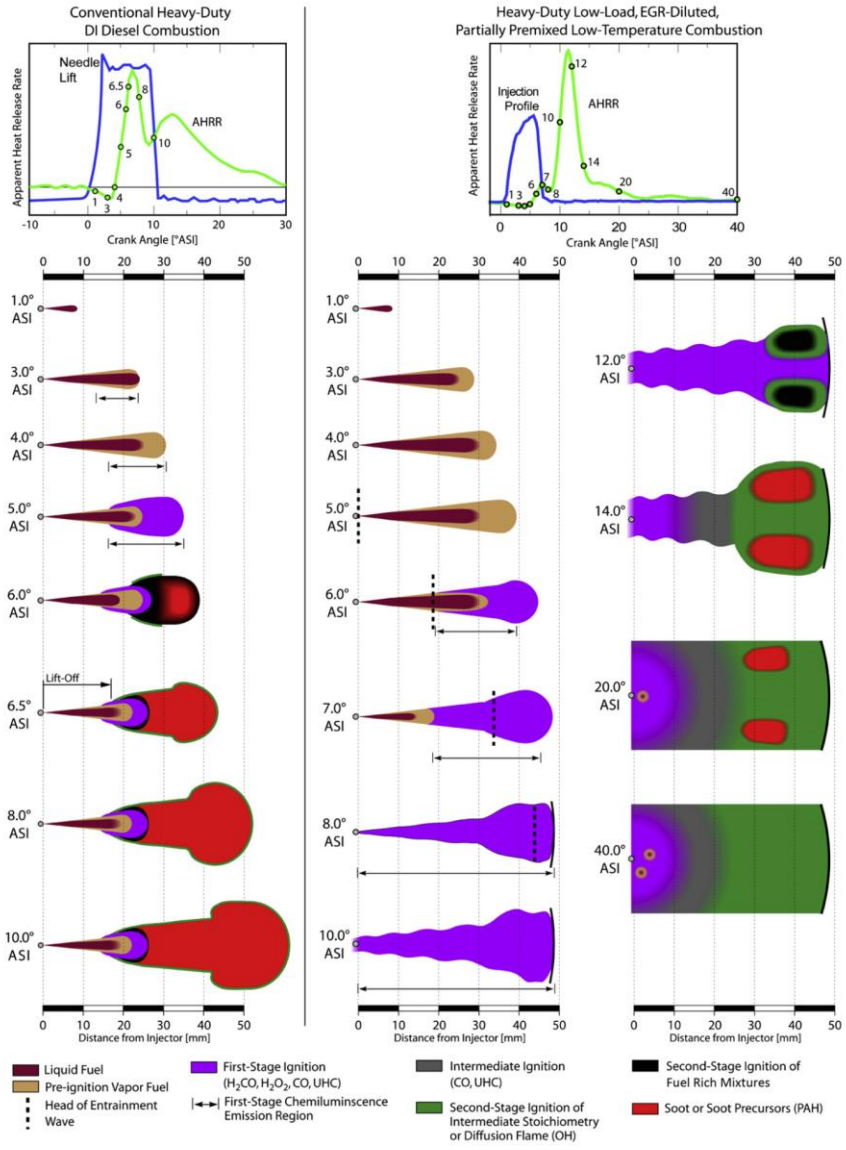

Figure 2.14 A conceptual model for low temperature diesel combustion [29]

As the results show, the combustion progression for the LTC strategy is much different than for CDC. The main difference is the obvious reduction in the peak combustion temperatures due to dilution from EGR or excess O_2. For the LTC

strategy, the fuel is injected earlier or later in the engine cycle where the ambient gas temperature and density is lower than for CDC. With the lower ambient conditions the jet can penetrate farther into the chamber, thereby decreasing the local equivalence ratio throughout the jet. Also, because the injection duration is short, all of the fuel is injected before combustion starts, again increasing the premixedness of the charge. With the short injection there is no liftoff, premixed zone and/or quasi steady mixing controlled combustion. Therefore, as shown in Figure 2.14, the combustion is more controlled by chemical kinetics than mixing. The figure shows that after injection, 1^{st} stage ignition (chemiluminescence) occurs through a large portion of the jet until the second stage (hot combustion) occurs with most regions nearer to stoichiometric, thereby producing less soot than CDC. Similarly less NO_x is produced though the same mechanisms (lower temperature and leaner mixtures at the start of combustion). These fundamental differences in the combustion process that utilize lower temperatures and increased mixing prior to combustion is exploited in the following reviewed literature and throughout this work.

2.6 Premixed Compression Ignition Combustion

The most common forms of PCI combustion are similar in that they inject fuel early in the cycle as a means to promote a well-mixed charge throughout the cylinder. Specific differences in the combustion strategy come about from differences in what fuel(s) are used and when they are injected. PCI research is still a relevant research topic and has been investigated by many researchers [e.g., 30,

31, 32]. PCI research started with basic HCCI experiments to probe the autoignition characteristics of gasoline and diesel fuels. Then research shifted to use of high EGR and early injection diesel PCCI tests. Finally, dual-fuel RCCI experiments are becoming current favored research topics. As time has passed, PCI combustion strategies have considered the use of gradients in equivalence ratio, temperature and fuel reactivity to decrease combustion noise and increase control over combustion phasing [1-8, 33-35]. Better control over the combustion event allows for an increased engine operating space where PCI can be utilized. While significant progress has been made in the understanding of PCI combustion, there is still much more work to be completed before PCI engines can become commercially available and their benefits made available for consumers.

2.7 Homogeneous Charge Compression Ignition

HCCI is a type of PCI combustion currently being researched as a way to lower problematic emissions from diesel engines (namely PM and NO_x) while maintaining high thermal efficiency. HCCI research has been conducted in both 2 and 4 stroke engines by many researchers [30-32]. HCCI combustion is generally characterized by injecting a lean quantity of fuel and air (equivalence ratio ~ 0.2-0.4 [36]) early in the cycle (typically -320 °ATDC to -180 °ATDC), thereby allowing sufficient time for complete air/fuel mixing before combustion. After the homogenous mixture has been subjected to the appropriate initial thermodynamic conditions (as a function of engine speed, equivalence ratio, IVC temperature and pressure), the well-mixed charge autoignites across the entire cylinder nearly

simultaneously [36]. Due to this fast combustion, the cylinder pressure also increases rapidly and if the pressure rise rate is high enough, can cause engine damage. Therefore, HCCI combustion is generally limited to low loads in order to keep the peak cylinder pressure and peak pressure rise rate below the mechanical limits of the engine. Current research has sought out techniques to slow the HRR and phase combustion so that HCCI can be utilized over a wider range of engine speeds and loads. However, HCCI is not initiated by either a spark or a fuel injection event; it is difficult to control the start of combustion timing.

Efforts to control the heat release rate of HCCI have been investigated by Dec et al. [36, 37]. Using high speed chemiluminescence, the research showed natural stratification of both temperature and composition. Combustion was shown to progress from hotter to colder regions. A single zone Chemkin model was used, which over predicts the start of combustion timing and PRR because it assumes a truly homogenous mixture. But, the benefit of stratification is that a higher fueling rate is able to be used than is predicted with simple models.

2.8 Partially Premixed Combustion

With the lack of a direct method to control the start of combustion in HCCI, the use of late injections of a single, low reactivity fuel for premixed combustion in a heavy-duty compression ignition engine have been investigated by numerous researchers [38, 39, 40] but most notably by Kalghatgi et al. (2007). In that work, a gasoline with a research octane number (RON) of 95 and a commercially available Swedish diesel were compared in a single cylinder heavy-duty research engine [41].

The gasoline and diesel fuels were compared for a number of different start of injection (SOI) timings, EGR rates and loads. Generally, the gasoline had lower PM than diesel fuel for all the operating conditions. The low PM for gasoline was attributed to its high resistance to autoignition, thereby increasing the ignition delay, which increases air/fuel mixing before combustion. Figure 2.15 and Figure 2.16 demonstrate this by showing that smoke increases with advanced SOI timings for diesel fuel, while gasoline has low smoke at all SOI timings.

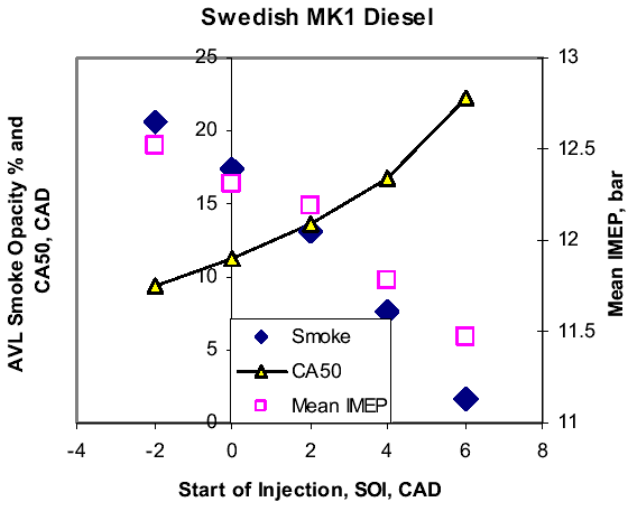

Figure 2.15 Effect of SOI timing on smoke, IMEP and CA50 for diesel fuel [41].

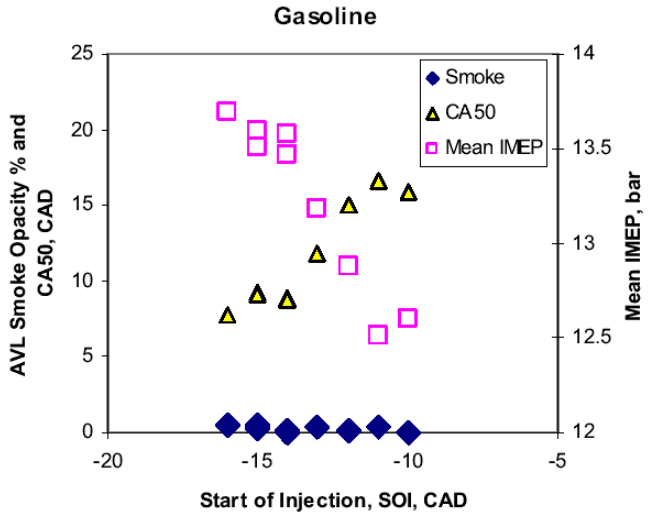

Figure 2.16 Effect of SOI timing on smoke, IMEP and CA50 for gasoline fuel [41].

Several features of this combustion mode are similar to those of MK combustion where late injections that lead to combustion phasings after top dead center. If all the fuel is injected before combustion starts, low PM emissions can result. In order to avoid injection/HRR overlap, dual injections were used by Kalghatgi et al. [41] to achieve combustion at high loads (15-17 bar IMEP). As seen in Figure 2.17 and Figure 2.18, the early pilot injection of diesel fuel starts with low temperature heat release (LTHR) before TDC, and then the main injection event initiates combustion there is much overlap with the injection event. This overlap, does not allow for complete air/fuel mixing before combustion, as seen with gasoline combustion in Figure 2.18, and accounts for the high AVL smoke opacity of 8.7% vs. 0.9% for gasoline.

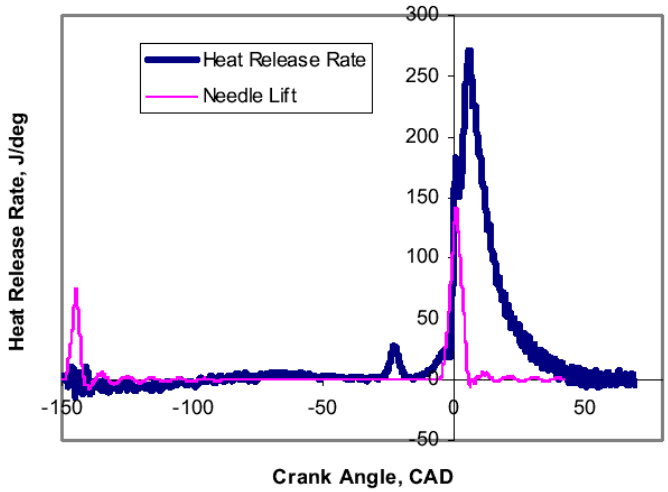

Figure 2.17 HRR and needle lift for dual-injection of diesel fuel [41].

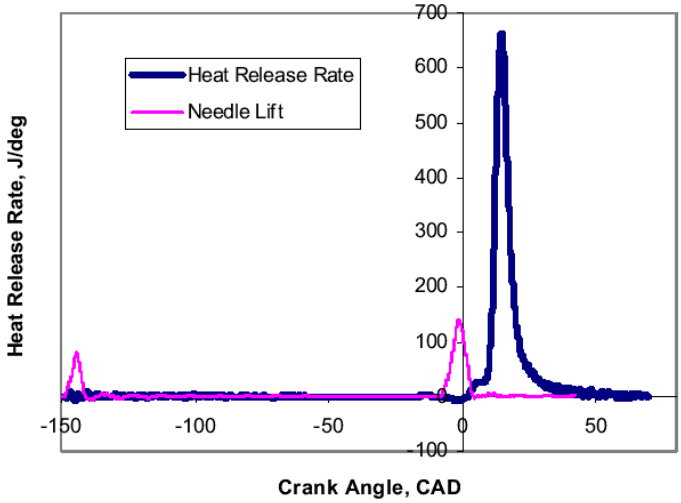

Figure 2.18 HRR and needle lift for dual- injection of gasoline [41].

With dual injections, gasoline was able to be used for loads up to 17 bar IMEP while maintaining NOx emissions of 0.58 (g/kWh) and PM of 0.7 filter smoke number (FSN). Other promising results for this combustion strategy are that it can be directly controlled with the SOI timing, something that is not possible with most other premixed combustion concepts. However, with gasoline's high resistance to

autoignition, there is difficulty in operating the engine from idle up to about 25% load.

2.9 Reactivity Controlled Compression Ignition

A concept for controlling PCCI combustion by means of varying fuel reactivity was proposed by Inagaki et al. [42]. The fuel reactivity was controlled by using two different fuel systems to direct-inject and port-inject fuel in the same cycle. Iso-octane was injected in the intake port to generate a homogenous air/fuel mixture. Then, diesel fuel was injected by a common-rail injector around ~40 °BTDC to provide the ignition source. By injecting two fuels, both equivalence ratio and fuel reactivity stratification can be controlled. The diesel fuel was found to react with typical low temperature reactions, which then released enough energy to ignite the gasoline. This two-stage ignition helped to increase the combustion duration and lower the peak heat release rate compared to HCCI combustion, as shown in Figure 2.19.

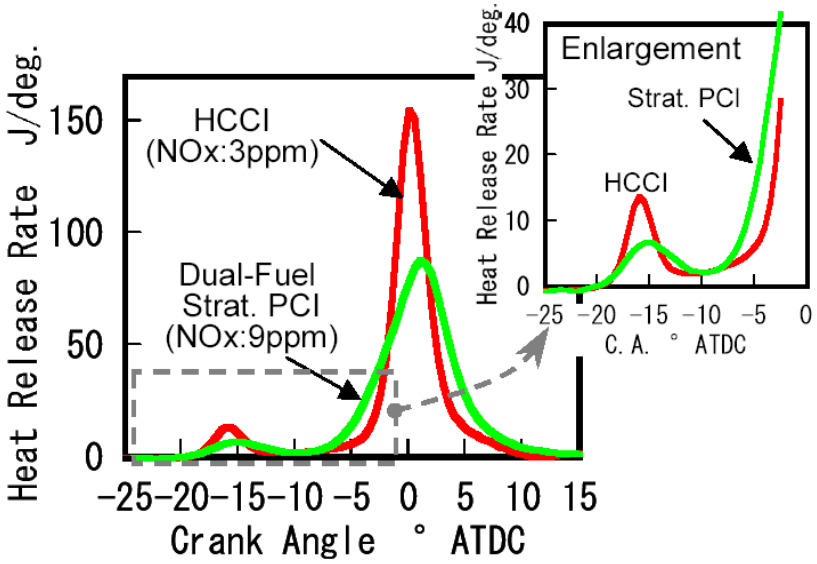

Figure 2.19 Heat release of dual-fuel PCCI vs. single fuel HCCI [42].

The combustion phasing was found to be controlled by the ratio of the two fuels, with a higher iso-octane concentration igniting later and a higher diesel fuel concentration igniting earlier. The phasing of the high temperature heat release (HTHR) was also found be a function of the local equivalence ratio. The local equivalence ratio was found to vary greatly with the timing of the diesel fuel injection. The HTHR was advanced for late diesel fuel injections because of rich regions formed by more fuel being trapped in the squish region. As the diesel fuel injection was advanced, the fuel was able to better mix with the air, lowering the equivalence ratio and thus delaying the HTHR. With the proper injection timings, the dual-fuel concept was able to operate without EGR up to 12 bar IMEP. Operation without EGR and slower HRR allowed for very high thermal efficiencies of 50+% by lowering heat transfer and increasing the ratio of specific heats. The emissions were also very low with dual-fuel combustion, and were ~10 ppm NO_x and < 0.1 FSN for

smoke all the way up to 12 bar IMEP. Further load increase beyond 12 bar was limited by high combustion noise.

Further investigations into RCCI combustion have been a recent research topic of interest at many universities and government laboratories. A majority of engine testing was conducted in single-cylinder engines (SCE) to learn the basic combustion fundamentals for RCCI. Then those results were used in multi-cylinder engines (MCE) with steady state tests and finally in MCE over transient operating conditions. The base operating conditions studied in the present work came from the SCE experiments that developed the underlying operating strategies for RCCI. At the core of the strategy, dual fuel, low and high reactivity fuels, gasoline/diesel, used double injection strategies with injections around -57/-35 deg. aTDC, with 60% of the DI fuel in the first direct-injection and 80-95% of the total fuel injected as gasoline. Results with a sweep of the gasoline fraction are shown in Figure 2.20 [1].

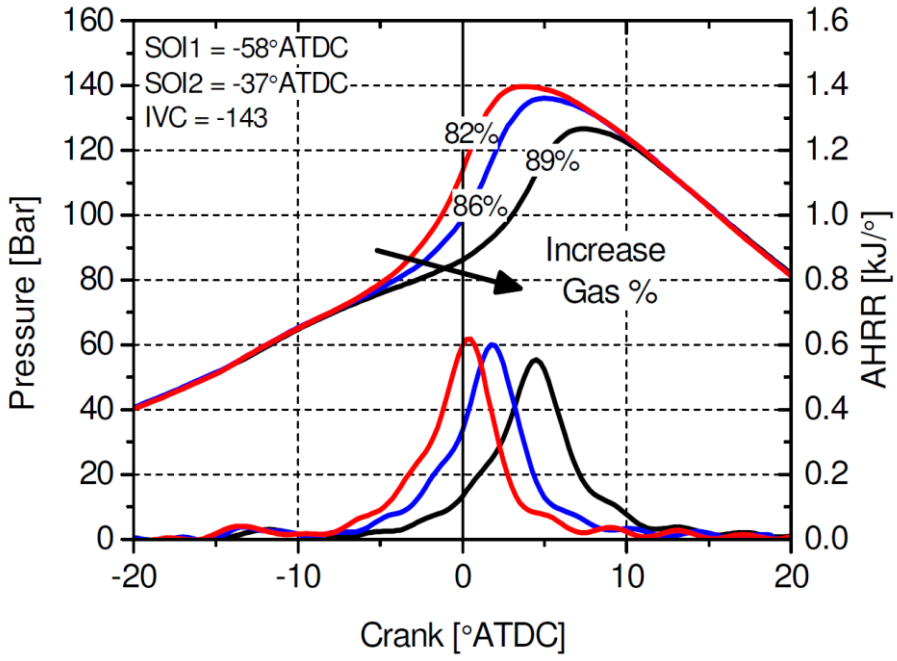

Figure 2.20 RCCI combustion for different gasoline-to-diesel ratios [1]

Moderate to high EGR rates (30-50%) were used along with intake pressures up to two bar. Intake temperatures were found to be optimal at around 32°C but operation up to 60°C was found to be possible. Using this base injection strategy RCCI operation was tested at multiple speeds and loads. Next, alternative fuels were investigated, especially those with lower reactivities like ethanol. Another operating strategy taken on was the possibility of using one base fuel but adding a small amount of a reactivity enhancer. It was thought that not having two fuel tanks may be advantageous for some markets, such as in light-duty vehicles. Typical cetane improvers used in diesel fuels were found to work well with gasoline at 1.5 to 3% by volume [2, 4]. Figure 2.21 shows combustion results with gasoline/ (di-tertiary butyl ether/gasoline) mixtures compared to gasoline/diesel RCCI operation.

As can be seen, combustion performance was nearly equal and under some conditions offered improved thermal efficiency via improvements to the combustion efficiency.

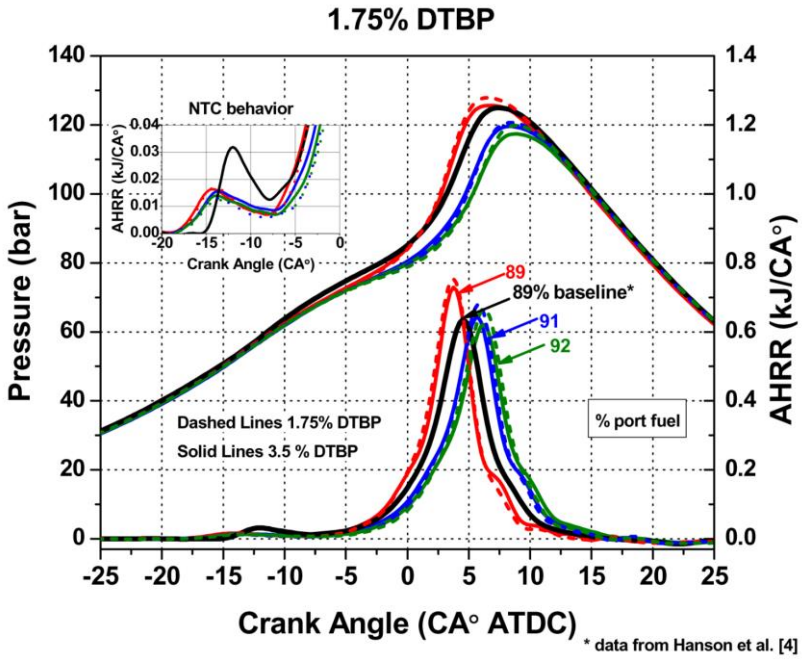

Figure 2.21 RCCI combustion comparing operation with CN improved gasoline and diesel fuel [2]

Finally, use of the KIVA 3D computational fluid dynamics (CFD) tools allowed insight to the combustion process and the combustion formation of intermediate species, as well as sources of efficiency benefits and losses. In Figure 2.22, the peak combustion temperature for RCCI and CDC are compared. As can be expected, RCCI combustion temperatures are much lower and the peak temperature locations are farther away from the piston and cylinder walls. This

reduces the heat lost to the cooling system, which is one of the reasons for the increased thermal efficiency of RCCI [43].

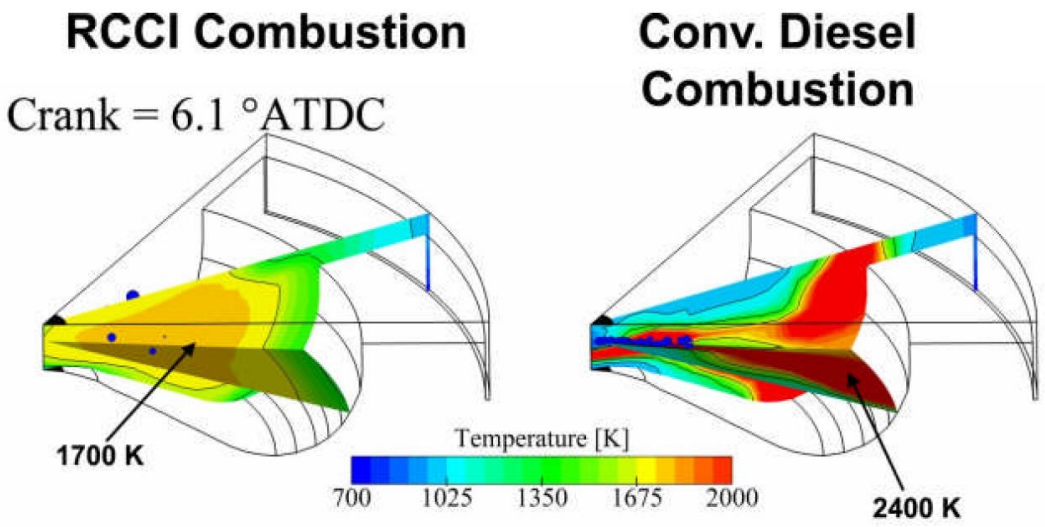

Figure 2.22 Simulated RCCI vs. CDC peak combustion temperatures [43]

Detailed PM and HC speciation was investigated at ORNL. In work by Prikhodko et al., they investigated detailed HC speciation and PM mass using Teflon filters and gas chromatograph mass spectrometry. Results from the HC speciation can be seen in Figure 2.23. As can be seen, there was an increase in aldehydes, ketones and gasoline specific species like benzene toluene compared to CDC and diesel PCCI [44].

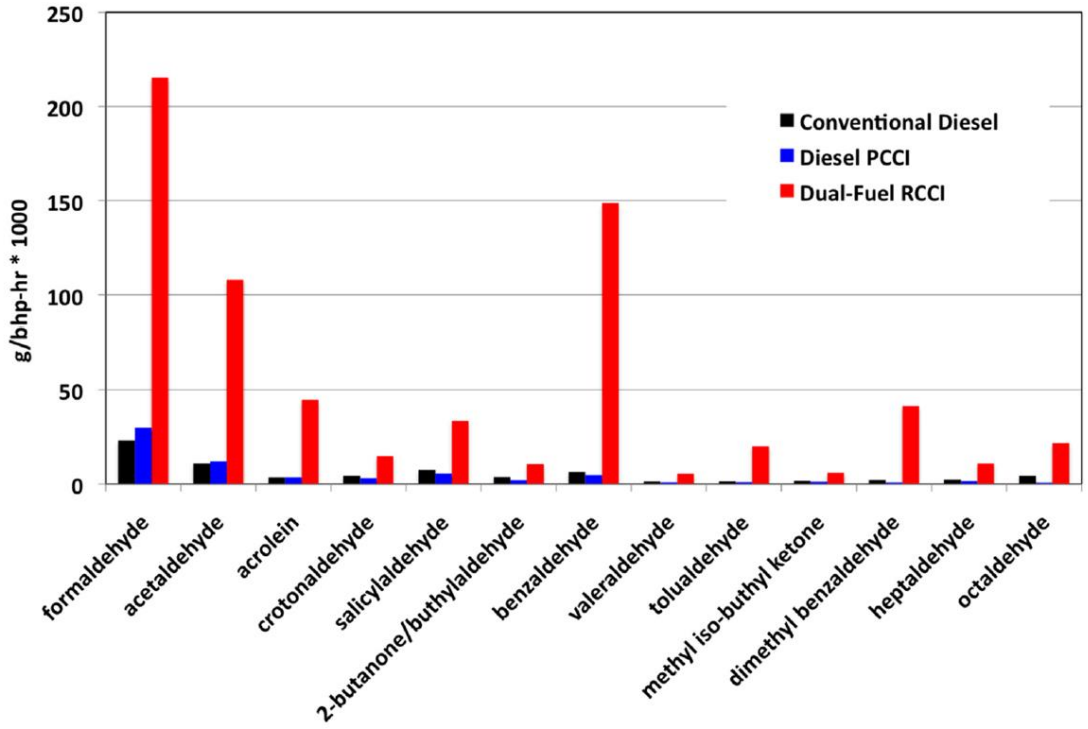

Figure 2.23 Combustion intermediate species [44]

While RCCI showed to have lower particle numbers, it showed to have higher PM mass due to volatile HC accumulating on the filter, as shown in Figure 2.24. Pictures of the RCCI, CDC and PCCI filters are shown in Figure 2.25.

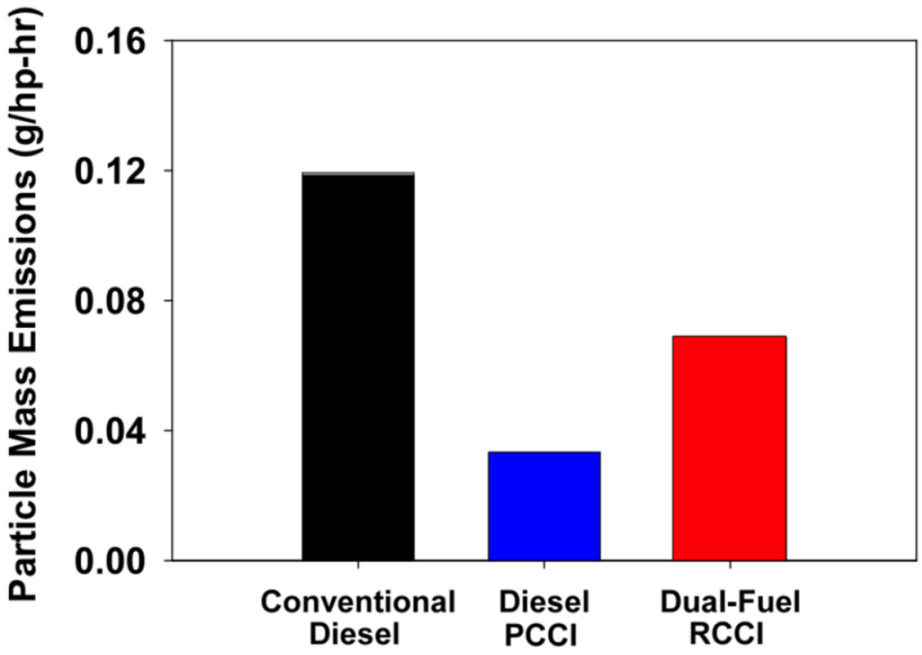

Figure 2.24 Particulate mass emissions for PCCI, RCCI and CDC [44]

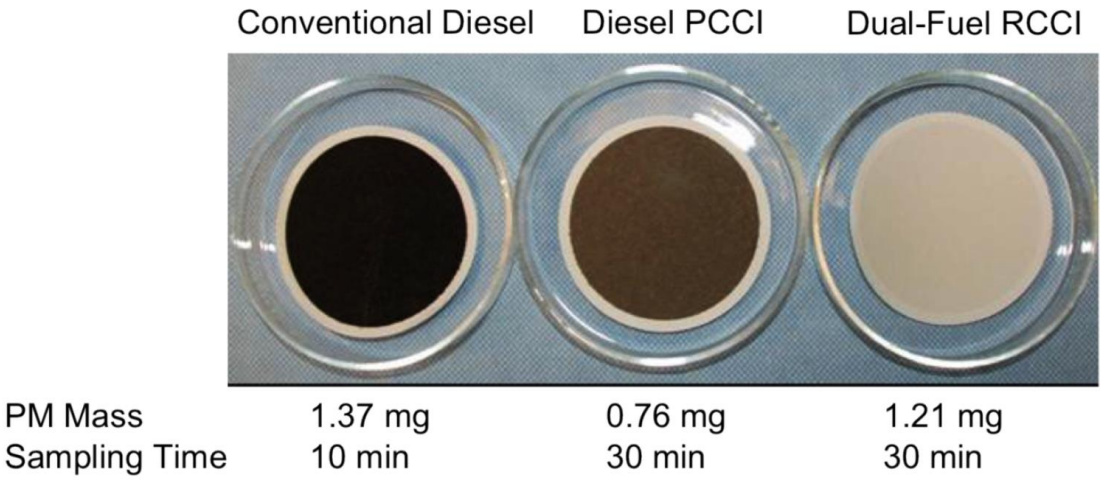

Figure 2.25 Pictures of RCCI, PCCI and CDC filters loaded with PM [44]

Here it is interesting to see the different colors of the PM, which were shown to be correlated to the BC content of the PM, so the CDC had the highest BC fraction and RCCI had the least (~1%). Finally, they investigated the DOC

performance for the 3 combustion modes. As shown in Figure 2.26, the DOC was effective at removing approximately 90+% of the HC, ~100% of the CO and over 90% of the engine-out aldehydes.

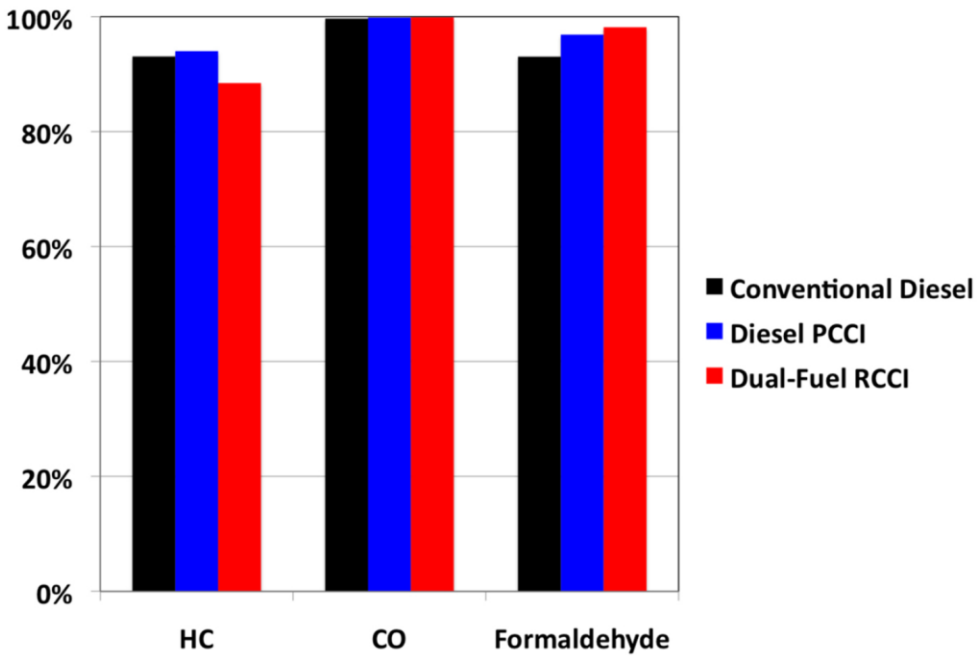

Figure 2.26 DOC efficiencies for RCCI, PCCI and CDC [44]

Additional RCCI PM studies were characterized by Prikhodko et al. [45]. In this work they investigated the effectiveness of the DOC at reducing PM. Since most of the RCCI PM was shown to be very small <10 nm volatile organic compounds, the DOC was effective at reducing PM in the 10 nm range with little oxidation of PM particles larger than 23 nm. This is seen in Figure 2.27 and Figure 2.28.

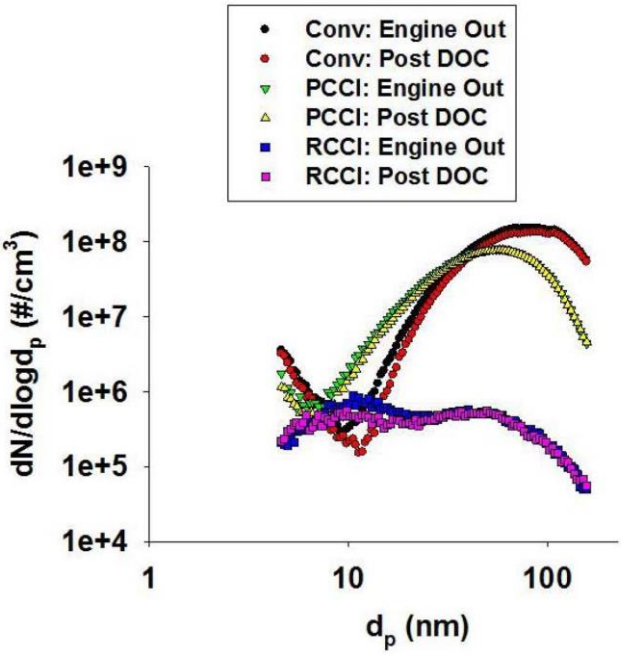

Figure 2.27 Particle size distribution for RCCI, PCCI and CDC [45]

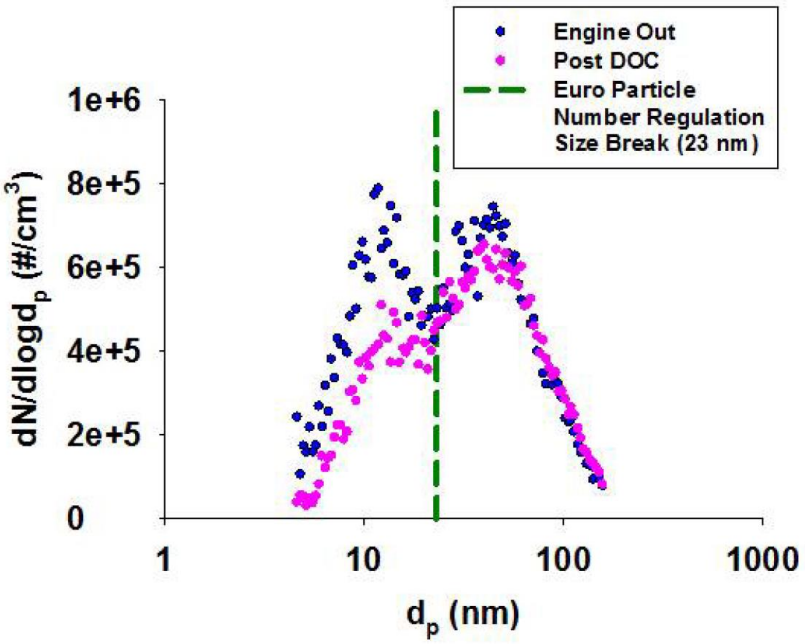

Figure 2.28 Particle size distribution for pre and post DOC for RCCI [45]

Finally, they measured the PM mass using similar Teflon filters as used in the previous paper. Here they found the DOC was able to reduce PM mass by nearly 50% for RCCI while CDC and PCCI only had a 30 and 6% reduction, respectively. This was again thought to be caused by the DOC oxidizing volatile organic compounds.

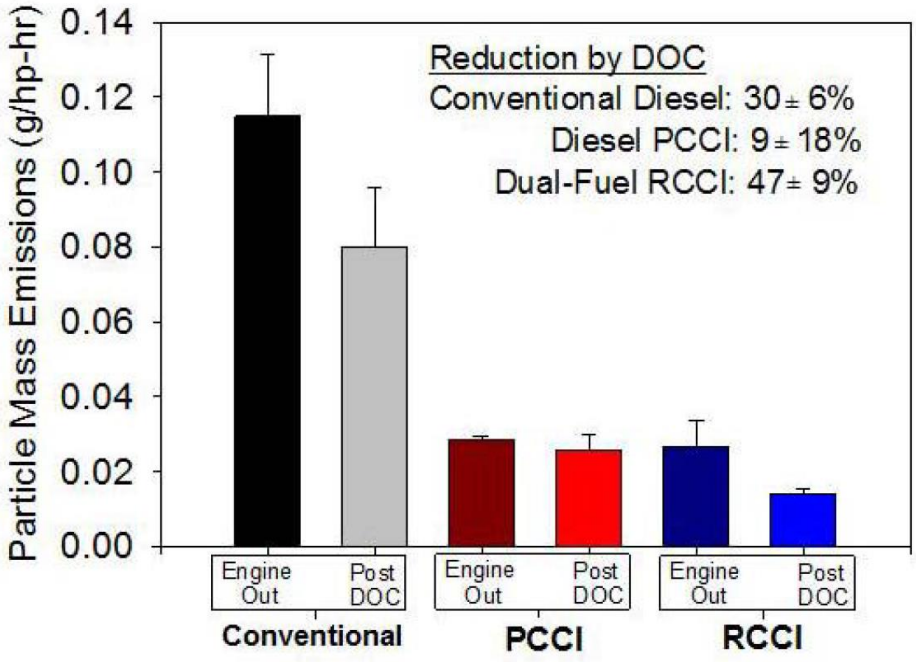

Figure 2.29 PM mass reduction by use of a DOC for RCCI, PCCI and CDC [45]

2.10 PCI Kinetics

Ando et al. (2009) proposed universal rules for HC oxidation [45]. Most normal chain HC fuels, such as n-heptane or diesel fuel, exhibit what is called a cool flame around 10-20° before the main heat release. The cool flame tends to only release a small amount of heat compared to the subsequent high temperature

heat release. This early reaction is due to normal chain hydrocarbons having a different reaction mechanism than cyclic and isomeric chains, such as iso-octane and aromatics. Normal chain fuels exhibit low temperature oxidation (LTO) where it is possible to have chain branching reactions at temperatures between 750 and 800 K. After 800K the chain branching reactions stop and recombination reactions forming HO_2 begin. This change in reaction mechanism is called the negative temperature coefficient (NTC) region as the temperature increases, yet the reaction rate does not. Between 800 and 900K, is called the thermal preparation stage. Here, the H_2O_2 system is dominant and accumulates CH_2O and H_2O_2 until enough H_2O_2 is formed and releases enough heat to switch into the final thermal ignition stage. After 900K, the H_2O_2 breaks down into OH and then follows the chain branching steps of the H_2-O_2 system to completion, as depicted in Figure 2.30.

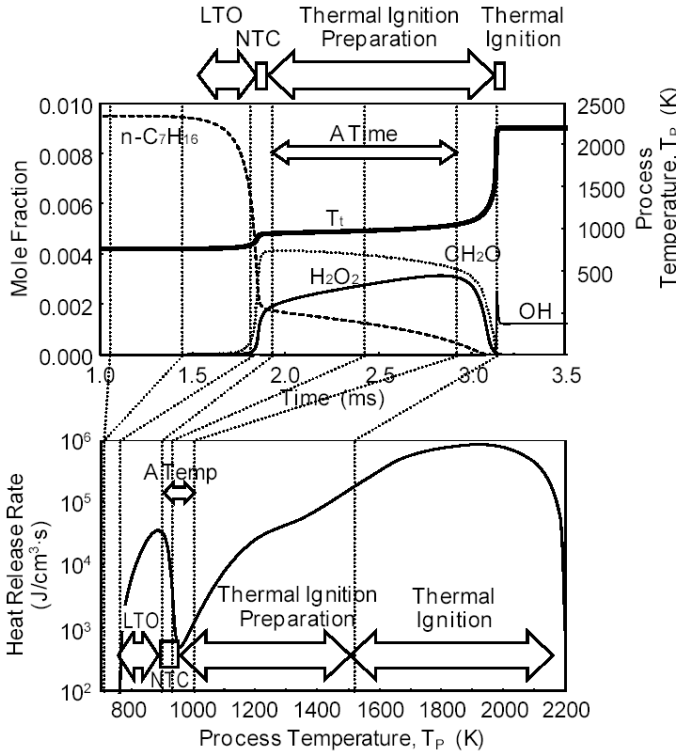

Figure 2.30 Three steps for HC oxidation [45].

Gasoline or non-normal chain fuels tend to follow the same reaction path, but usually skip the NTC and LTO phases and go directly to the thermal preparation stage, as shown in Figure 2.31.

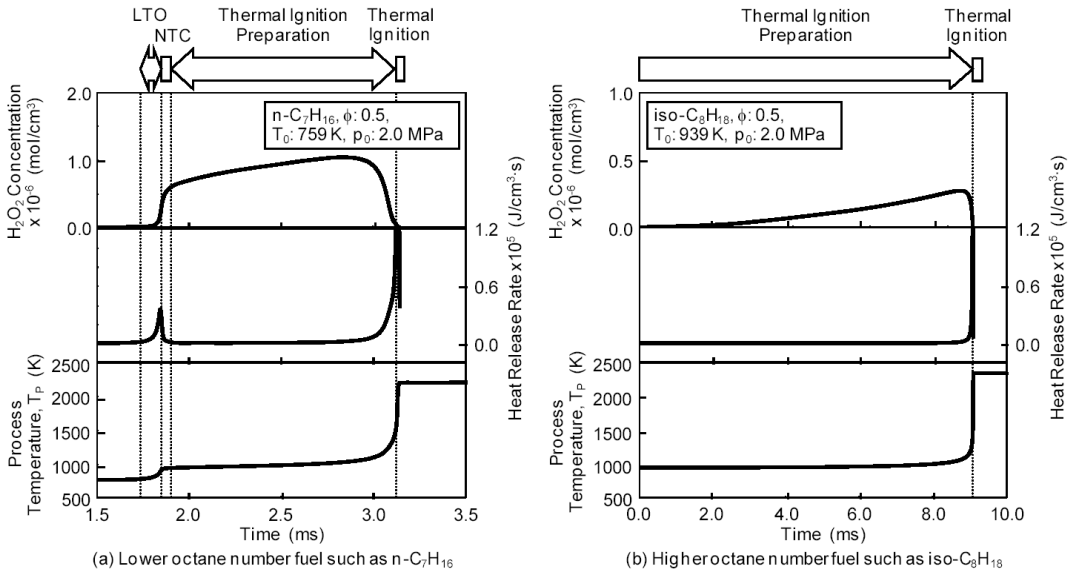

Figure 2.31 Ignition processes for n-heptane and iso-octane [45].

Another unique finding by Ando et al. [45] for normal chain fuels is that depending on the initial temperature of the reactants, they can also skip the LTO and NTC regimes and go straight to the thermal preparation stage, as seen in Figure 2.32. Indeed, when the initial temperature is above the NTC temperature of ~800K, the combustion of the normal chain fuel looks very similar to that of iso-octane.

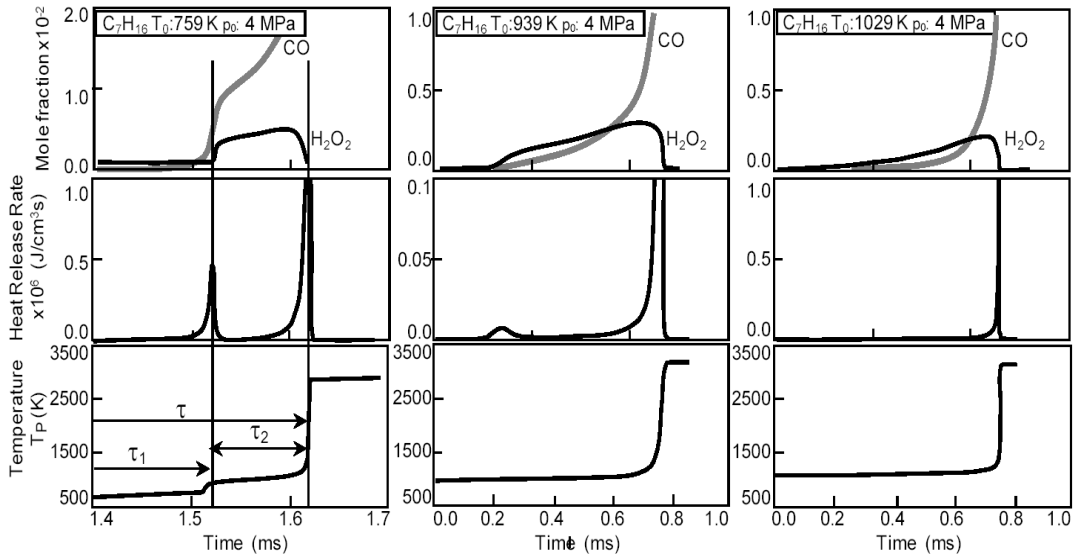

Figure 2.32 Ignition processes for n-heptane at different initial temperatures [45].

2.11 PCI Combustion Control

While PCI combustion strategies offer decreased emissions of NO_x and PM, they come as at the expense of increased combustion noise and lack of control of combustion phasing. Since PCI combustion strategies rely on autoignition of the fuel, they are driven by the engine thermodynamic boundary conditions rather than by fuel injection timing (as in compression-ignition engine) or by spark timing (as in spark-ignition engines). The autoignition process typically results in rapid energy release throughout the combustion chamber and can even cause engine damage if the energy release is rapid enough. Thus, current PCI research has sought techniques to slow the combustion rate while offering increased control over the phasing of combustion by modifying the fuel properties or injection timings. By

offering increased control of the combustion event, PCI strategies can be utilized over a wider range of engine speeds and loads.

2.12 PCI Emissions

One of the main benefits of PCI combustion is the reduction of problematic emissions like PM and NO_x while maintaining high thermal efficiency. NO_x is reduced due to the overall lean air/fuel ratio that is ignited volumetrically with no flame front [50]. However, it is possible to achieve high levels of NO_x with PCI. When operating at high loads, where the equivalence ratio is high, combustion temperatures can exceed 1,900K and form NO_x [26]. Additionally, if there is sufficient mixture inhomogeneity, these rich regions can also cause high NO_x values from the higher local combustion temperatures. High combustion temperatures can be lowered with the use of a diluent such as EGR, which acts to lower the inlet oxygen concentration by displacing the fresh air charge with combustion products and nitrogen. This lowers the peak combustion temperature and thus NO_x levels [26]. PM emissions from PCI combustion are also usually low compared to conventional diesel combustion. The lean, well mixed charge and lack of flame propagation combine to limit PM formation by avoiding the soot formation island in both temperature and equivalence ratio, as can be seen in Figure 2.33 [46,48].

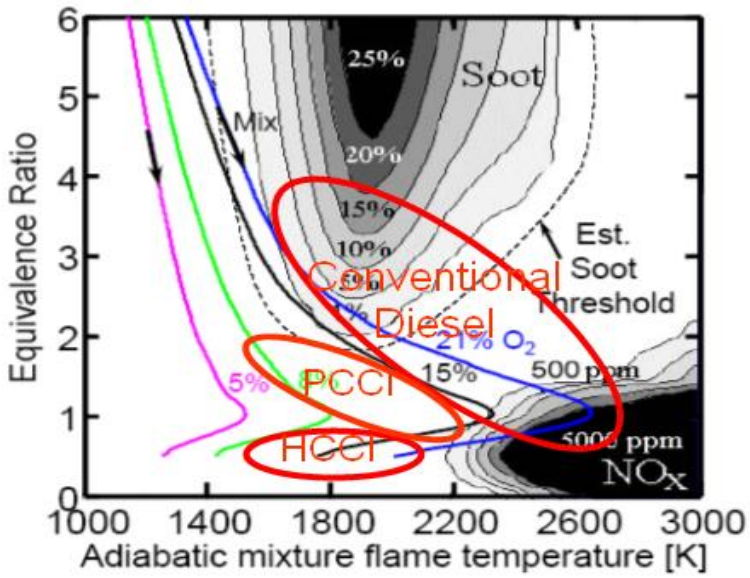

Figure 2.33 Phi-T plot for different combustion regimes [47], adapted from [48].

While PCI combustion has inherently low NO_x and PM emissions, HC and CO emissions are higher than conventional diesel combustion, and can be significantly higher than required by emissions regulations. A main cause for both the increase in HC and CO is the reduced combustion temperatures that slow oxidation rates, as seen in Figure 2.33 [46, 48]. HC emissions for PCI combustion are also seen to be caused by unburned fuel becoming trapped in the engine crevices, such as the top ring land. Since, for PCI, the air/fuel is well mixed before combustion, similar to SI engines, some of the fuel is driven into the ring pack where it encounters cool cylinder walls and combustion is quenched [26]. It is likely that the PCI engine will need an aftertreatment device to meet HC and CO emissions standards. Three way catalysts (TWC) currently used are ~90% effective at oxidizing HC and CO with the exhaust gas temperatures seen in conventional engines. Unfortunately, they currently do not have high conversion efficiency at the low exhaust temperatures

seen in HCCI [49]. Future work will be needed to increase CO and HC oxidation efficiency at these low temperatures to meet future emissions standards.

2.13 PCI Fuels

Because PCI combustion relies on an autoignition process, fuel chemistry is a powerful control parameter over the combustion event. One benefit of PCI as compared to conventional combustion strategies is that with sufficient charge preparation, most any liquid and gaseous fuel (with appropriate ignition and chemical properties) can be used [50]. While there many fuels available, most PCI research involves gasoline-like and diesel-like fuels due to their commercial availability and applicability for current fuel infrastructures. Gasoline-like fuels are volatile and resistant to autoignition while diesel-like fuels are less volatile and are prone to autoignition. Both fuels have their advantages and disadvantages for PCI, which need to be taken into account to optimize their use. Gasoline-like fuels typically have a lower boiling point and vaporize much easier than diesel-like fuels, which allow them to be injected earlier in the cycle (most commonly in the intake port) without impinging on the cylinder walls. Diesel-like fuels are most often direct-injected, but can be injected in the intake port with high intake temperatures to help vaporize the fuel. Since diesel fuel autoignites readily, ignition can occur well before TDC, resulting in excessive amounts of negative work, heat transfer and combustion noise [50]. Conversely, gasoline autoignites less readily. Due to its lower propensity to autoignite, gasoline requires high in-cylinder temperatures and

can ignite late enough in the cycle as to form high levels of partially burned combustion products.

2.14 Biofuels

The majority of engines have been operated with petroleum fuels almost exclusively for most of the history of the internal combustion engine. With new concerns of the effect that burning fossil fuels has on climate change, there is a renewed effort to use biofuels which can have a reduced carbon footprint and can supply the energy needed for sustainable transportation.

Ethanol has been used as alternative fuel for SI engines for nearly the entire life of the automobile. Ethanol is ethyl alcohol, usually made from fermentation of an agricultural feed stock and then distilling it to remove the ethanol. Ethanol is able to be blended with gasoline in common ratios from 10 to 85% by volume. One of the first commercial vehicles to use both ethanol and gasoline was the Ford Model T [51]. Ethanol fuel was used as a way to make vehicle owners, mostly rural farmers at that time, more self-sufficient and able to power their vehicles when gasoline prices were high. Low gasoline prices, legislation on ethanol taxes and Prohibition were responsible for the lack of adoption of ethanol as an engine fuel [52].

The effects of using ethanol as an engine fuel have been studied for nearly the entire life of the internal combustion engine. Typical results show that operating an SI engine on ethanol increases the resistance to autoignition and reduces emissions levels of regulated pollutants such as CO, HC, NO_x and PM. However, ethanol has been shown to increase levels of unregulated pollutants such as

aldehydes and methane [53]. Other drawbacks include difficulty in starting due to low volatility at low temperatures and reduced volumetric fuel economy due to the reduced lower heating value (LHV) compared to gasoline.

The other most widely used biofuel is biodiesel. Biodiesel is defined as a long-chain mono-alkyl ester. Biodiesel is typically made from reacting lipids with an alcohol to produce a fatty acid ester [54]. These fatty acid esters can then be blended into diesel fuel or used in their neat forms. Use of vegetable oils in compression-ignition engines has been noted as far back as the 1900 Paris Exhibition where Rudolph Diesel supposedly demonstrated operating his new engine on peanut oil [55]. Today, commercial engines can operate (depending on manufacturer) up to blends of 20% biodiesel and 80% diesel fuel (B20), and even B100 with modifications to the engine and fuel system.

As with ethanol, switching from diesel to biodiesel has implications for the resulting emissions levels from the combustion process. As seen in Figure 2.34, biodiesel tends to reduce most major regulated emissions compared with conventional diesel fuel [56]. The increase in NO_x emissions from biodiesel combustion is still of interest to researchers as its cause is not fully understood. Current hypotheses include that the oxygen in the fuel causes the equivalence ratio at the flame front to be closer to stoichiometric locally, increasing NO_x [57].

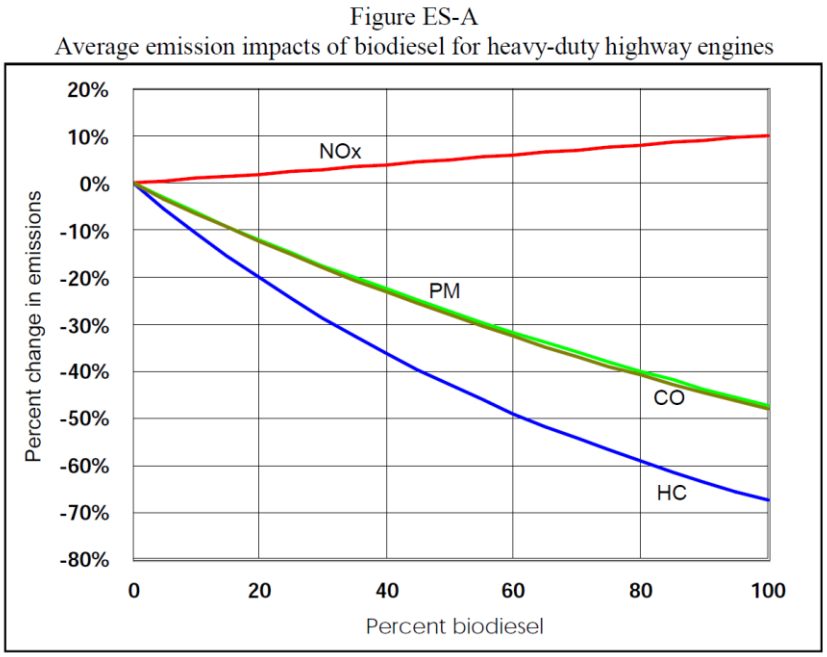

Figure 2.34 Average emissions impacts of increased biodiesel fuel quantity [56]

Unregulated emissions, known as mobile source air toxins (MSATs) from biodiesel combustion were shown, in a preliminary investigation, in Ref. [56]. The bulk average emissions of MSATs were shown to decrease with biodiesel, but the specific levels of emissions from specific MSATs are uncertain.

2.15 LTC Biofuels

With the success of using biofuels to reduce emissions from conventional combustion processes, the next logical step is to extend the use of biofuels to LTC. Since LTC is a fairly new field of research, there is not as much data in the literature to compare to. The use of biodiesel to replace diesel fuel in high EGR diesel LTC has been investigated by [58-61]. The results show that while it is possible to

operate diesel LTC with biodiesel, the results are highly dependent on fuel type, operating strategy and combustion phasing.

The literature also lacks results of using biodiesel as a fuel for a PCI combustion strategy such as HCCI. Similar to the biodiesel LTC tests, the effects of using biodiesel for HCCI lack any consistent trends [62-64]. But, it is possible to operate a biodiesel engine under HCCI conditions.

Using ethanol in LTC is more prevalent in the literature and numerous studies have been conducted (e.g., Refs. [65-67,6,9). Studies have found that ethanol works well as a fuel for HCCI and can have significant impact on the combustion event. Ethanol lowers the intake temperature due to its higher latent heat of vaporization. This lower intake temperature delays the combustion phasing. Ethanol also has a high resistance to autoignition which delays combustion phasing. By delaying the combustion phasing, the peak load limit can be increased. Another benefit of using ethanol in an HCCI engine is that wet ethanol (ethanol with > 5% water) can be used [68]. The water removal process in producing fuel grade ethanol is very energy intensive, so being able to use wet ethanol can have significant energy savings, helping ethanol's overall energy ratio, [68,69].

Moderate blends of biofuels were investigated by Hanson et al. in [70]. In their work, 20% blends of ethanol and biodiesel were used in RCCI combustion in place of petroleum-based gasoline and ULSD, respectively. When E20 was used to replace gasoline, the brake thermal efficiency was able to be increased by

increasing the peak load that could be achieved with MPRR less than 10 bar/deg., as shown in Figure 2.35.

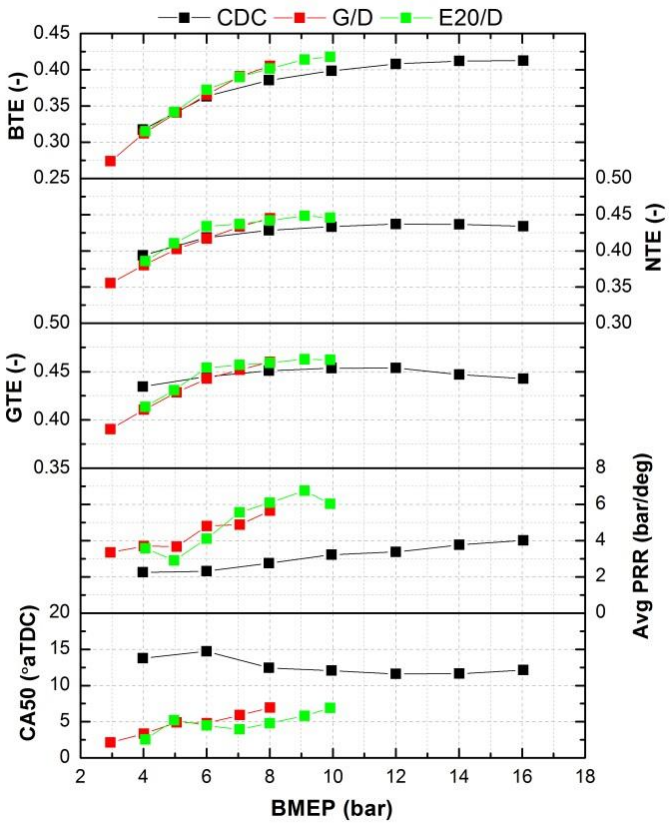

Figure 2.35 Efficiencies of RCCI combustion using gasoline (red) and E20 (green) compared with CDC combustion (black) [70]

The use of B20 in place of ULSD was also investigated. It was found that when using B20, RCCI combustion efficiency was able to be increased as the fraction of high reactivity fuel was able to be increased for the same NO_x value. This increase combustion efficiency showed to have an increase in the brake thermal efficiency, as shown in Figure 2.36.

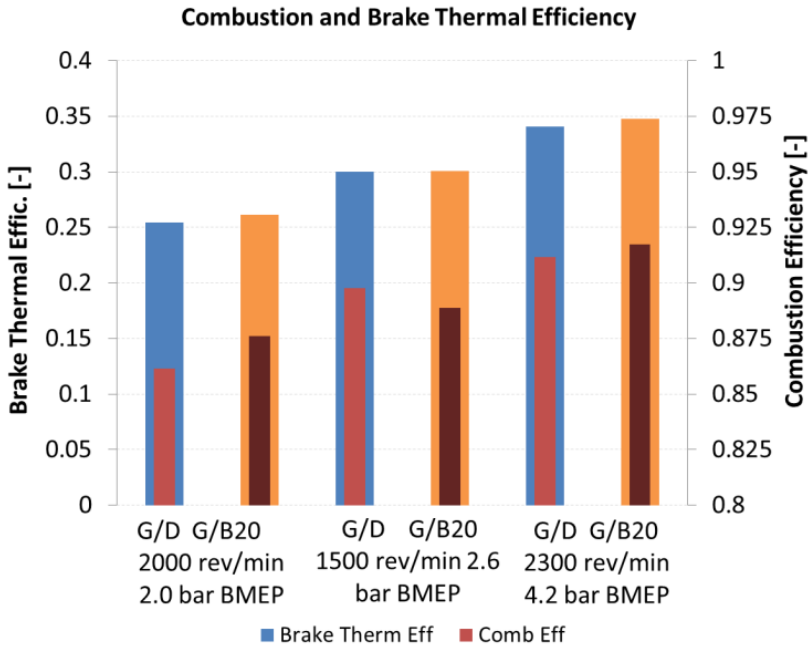

Figure 2.36 BTE and combustion efficiency for RCCI combustion using B20 compared to ULSD [70]

2.16 Multi-Cylinder Effects

Using multi-cylinder engines for combustion research is not common practice. Multi-cylinder engines are not typically used because it is harder to control thermal and pressure boundary conditions as with a single-cylinder engine. Additional cylinder-to-cylinder effects due to varying liner temperatures, gas exchange, internal residual, volumetric efficiency, etc. from cylinder-to-cylinder are avoided with single-cylinder engine. These effects are significant with multi-cylinder engines and need to be understood and taken into account for adaption of PCI strategies to production engines.

There has been some work done in the past to look at multi-cylinder engine HCCI by [65,71-74]. These studies have shown it is possible to operate advanced PCI combustion strategies on multi-cylinder engine using commercially available parts such as turbochargers, fuel injectors and engine blocks.

As can be expected, operating a multi-cylinder engine with HCCI was possible but showed some of the significant problems described above. In 2010, Chalmers University, investigated HCCI and stratified charge compression ignition (SCCI) combustion in a six-cylinder Volvo spark ignition engine modified to operate in HCCI mode by using variable cam timing (VCT) and cam position switching [73]. They looked at HCCI operation with gasoline and E85 fuels and found HCCI to be successful over a fairly wide operating range over their self-imposed noise and emissions limits, as shown in Figure 2.37. They also found E85 to offer an increase in peak load as compared to gasoline at engine speeds above 2,000 rev/min.

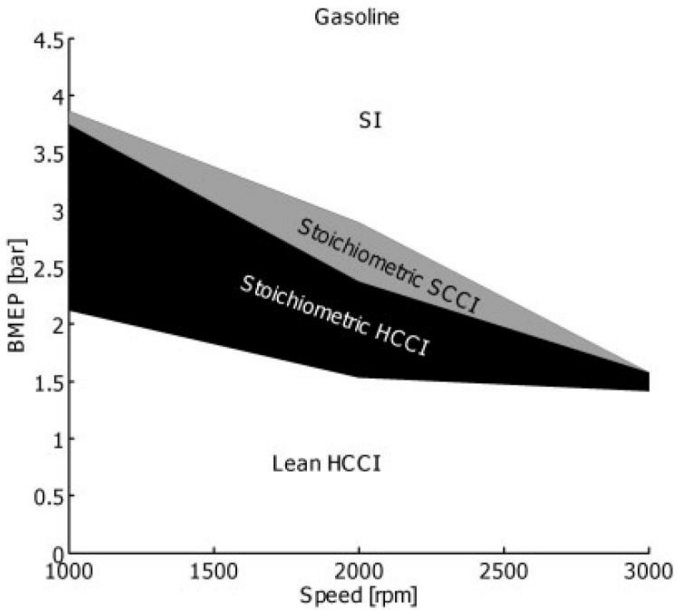

Figure 2.37 Multi-cylinder engine HCCI with gasoline [73]

Lund University in Sweden has also conducted significant amount of single-cylinder and multi-cylinder engine HCCI research. In their 2001 paper, Olsson et al. investigated full load performance of dual-fuel HCCI on a heavy-duty Scania engine [65]. This engine was modified with a smaller turbocharger to improve air handling requirements from the lower exhaust temperatures expected with HCCI. They operated the engine on blends of ethanol and n-heptane to gain additional control over the combustion process while using their in-house engine controller. They found that it was possible to achieve 16 bar BMEP without the use of EGR. Since they were using a well-mixed charge, NO_x and PM emissions were low. However, since they did not use EGR, the fast energy release resulted in high peak cylinder pressures, high pressure rise rates and high pumping losses. These high losses

were found to increase pumping work and frictional losses at high loads which limited peak brake thermal efficiency to 41%.

Caterpillar has also been a leader in HCCI research due to their involvement in the Heavy Truck Clean Diesel Cooperative Research Program with the US Department of Energy [74]. Between 2000 and 2006, Caterpillar and the Department of Energy started a 38 million dollar, 50/50 cost shared program to investigate increasing engine brake thermal efficiency to 50% while meeting 2010 emissions mandates. To meet these targets, Caterpillar chose to investigate HCCI combustion at high loads and production intent hardware. Numerous experiments were conducted over this 5 year project and only some of the results are reported in this literature review. The majority of Caterpillar's research involved developing HCCI combustion systems for both multi-cylinder and single-cylinder engines. Over the 5 year project, significant progress was made to increase the peak load in both the engines, as shown in Figure 2.38 and Figure 2.39.

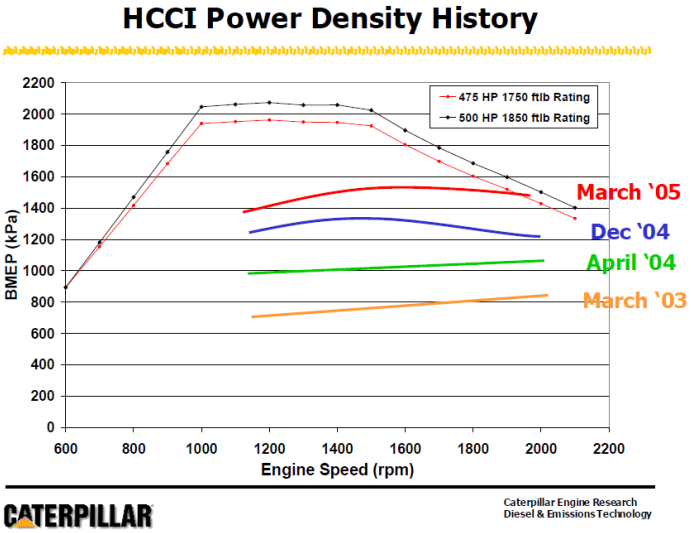

Figure 2.38 Caterpillar HCCI multi-cylinder engine power density [74]

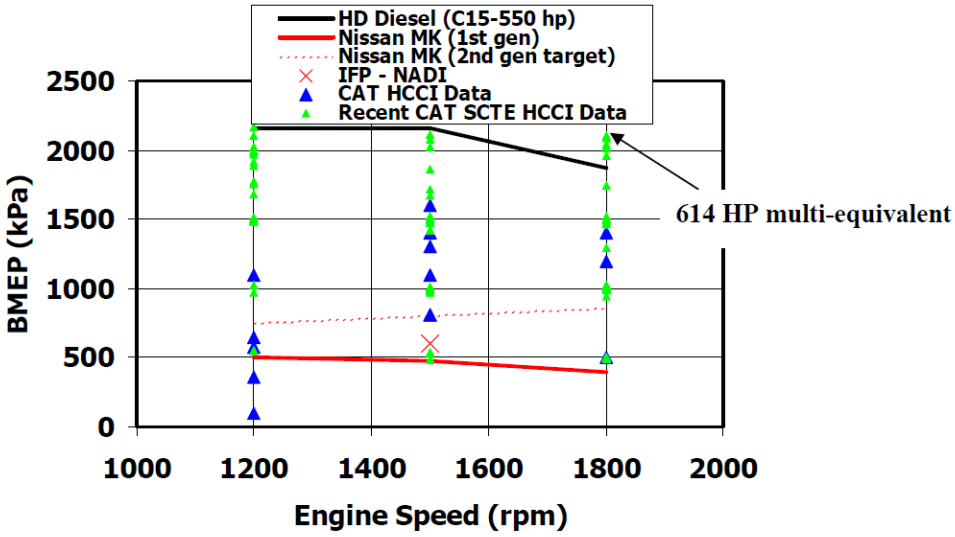

Figure 2.39 Single-cylinder HCCI BMEP vs. engine speed [74]

Most of these results were due to selecting the best air handling systems to minimize the pumping losses, as seen in [74]. Typical of most multi-cylinder engine HCCI tests, low load operation had similar efficiency to CDC, with the high pumping

losses becoming apparent at high loads. For PCI to become more attractive for mass production, significant work needs to be done to design optimal charge air systems to minimize these losses.

2.17 Transient Behavior

Currently, the majority of fundamental engine research is being done at steady-state operating conditions. While this makes testing easier with standard laboratory equipment, most vehicles operate under constantly changing engine speeds and loads. Thus, most US Federal certification testing involves using the vehicle under simulated realistic operating conditions, usually over transient test cycles such as the US EPA FTP75 [75]. Because transient testing utilizes specialty equipment, it is convenient to use and/or extrapolate steady-state results to compare with transient results. Unfortunately, the literature has shown that engine performance under steady-state conditions is not always a reliable indicator of transient or in-use emissions [76-78]. Significant portions of the total emissions are generated during the short periods when rapid speed or load changes occur [78].

Work by the US EPA [14] compared results of the ISO 8-mode steady-state duty cycle test with several transient test cycles for a number of different engines. They found that NO_x could be predicted within 10% but HC and PM were 60% under-predicted. Significant variation in emissions for each test cycle and each engine were found. Additional work [15] had better steady-state to transient agreement, but still had upwards of 60% under-prediction of HC and PM emissions. These results show that it is very difficult to predict transient test cycle emissions

based on steady-state results. These findings are important because low temperature combustion (LTC) strategies are being developed with most of the data in the literature being taken at steady-state. In order to assess their performance in vehicle operation, assumptions need to be made on how they will respond to transient operation and/or experiments need to be done to verify transient LTC performance. Such experiments are difficult to do because of the complex nature of LTC, so much less is known about transient LTC operation compared to high temperature combustion transient operation in the literature.

Glewen explored LTC and CDC transient operation and found that at the tested conditions transient emissions were fundamentally similar to those at steady-state conditions but varied as the boundary conditions changed [79]. He found that the intake O_2 concentration was the main driver of the emissions trends as EGR was used as the NO control mechanism in these two combustion modes. Figure 2.40 shows NO emissions over a transient load experiment for LTC and CDC.

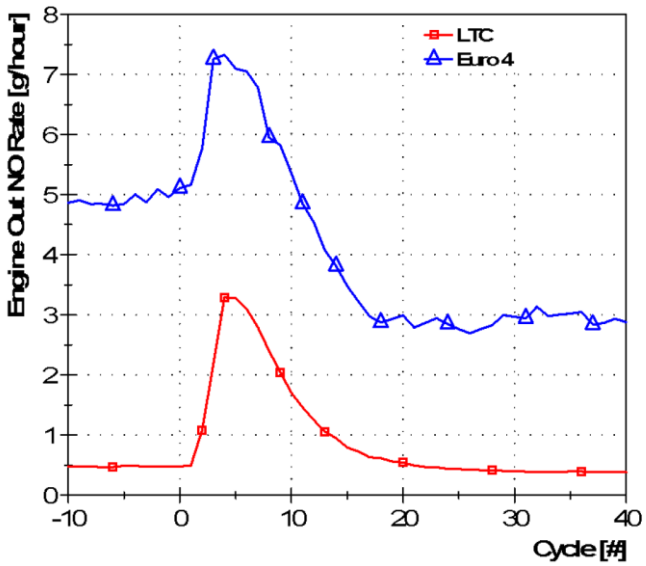

Figure 2.40 NO emissions over a transient load experiment for LTC and CDC [79]

As would be expected, the EGR rate does not change instantaneously during a transient, and depending on the mode and condition can cause NO and PM emissions to deviate from their steady state values. It was also possible to reconstruct these deviations during the transient event by changing the EGR, intake temperature, rail pressure, mass air flow and manifold pressure to those seen during the transient event. Finally, it was found that the thermal inertia of the engine component can affect the transient emissions as operating with different temperatures from the steady state conditions can change the VE, NO and HC emissions.

2.18 Implications for Research

While the reviewed work covers a range of operating conditions for LTC, the main goal was to improve diesel engine efficiency to lower GHG emissions such as CO_2 and BC to reduce the impact they have on human health and the climate.

To improve engine efficiency it is likely that advanced combustion modes will need to be introduced. Thus, being able to apply LTC, including RCCI, to MCEs is of interest as most LTC combustion studies have taken place in SCE. These often have ideal boundary conditions that cannot be replicated in the real engine. A viable LTC strategy needs to be able to account for these non-ideal conditions and still produce high efficiency and low emissions. One of the main limits to high thermal efficiency in MCE in the literature has been the high pumping work needed to give the high excess air ratios needed for most HCCI-like combustion modes. Methods for LTC that use higher equivalence ratios will be of interest to increase brake thermal efficiency (BTE) and allow adoption practical application.

Another main focus for the work is to utilize the unique properties of biofuels to improve combustion performance and GHG emissions from internal combustion engines. By using biofuels, CO_2 emissions can be greatly reduced if the fuel production process is carbon neutral or features low carbon intensity. The high and/or low reactivity of available biofuels is also advantageous as low reactivity fuels can offer higher load operation and thus higher thermal efficiency. So the engine/combustion mode of the future should be fuel flexible, as future fuels will likely higher alcohol/renewable content. Given that the goal is to use these biofuels,

most of the current research has been conducted with HTC modes, so gains in the insight to how biofuels with unique reactivities operate during LTC is of interest.

Finally, since most vehicles will still have normal transmissions and/or hybrid systems, they will operate under transient operating conditions. As has been shown, transient operation can vary greatly from steady state operation and can impart large emissions changes. To meet new emissions regulations understanding how LTC operates in transient conditions will be necessary.

Chapter 3 Lab Setup, Instrumentation and Procedures

3.1 Multi-cylinder Engine Lab Setup

The engine experiments were performed on a modified, General Motors 1.9 liter EURO IV specification diesel engine equipped with standard production hardware, including a variable geometry turbine (VGT), a High Pressure (HP) EGR cooler, and a variable swirl actuation (VSA) intake port geometry. Modifications were made to the engine in order to inject fuel into the intake manifold and for the addition of a Low Pressure (LP) EGR system. The standard intake manifold was machined to accept the additional port-fuel injectors and is shown in Figure 3.1.

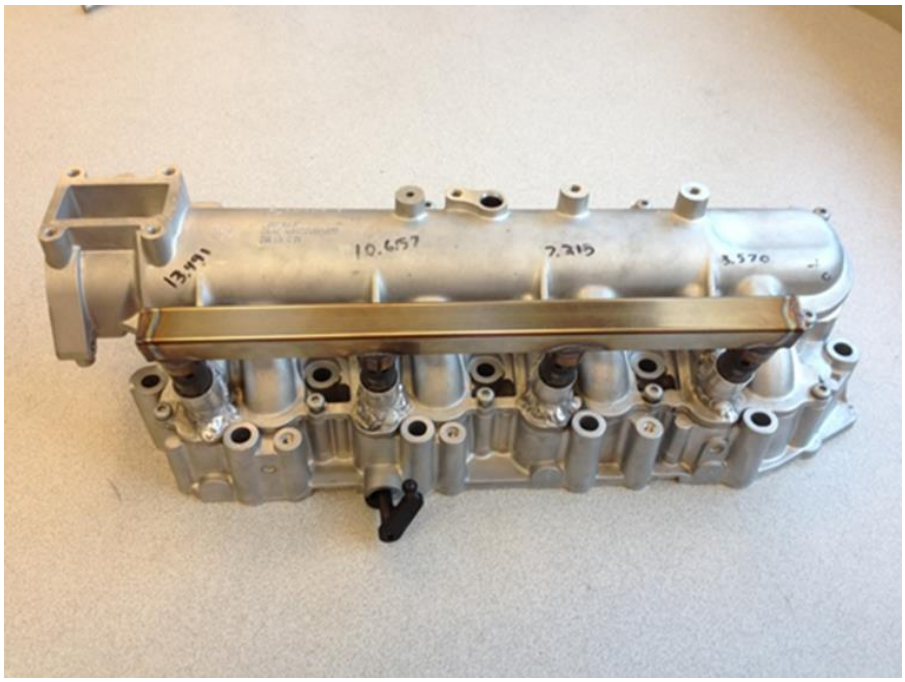

Figure 3.1 Modified GM 1.9L intake manifold

Additionally, the pre-compressor inlet was modified for a (not used in this study) LP EGR system [14]. An air-to-water intercooler was used to replace the

production air-to-air intercooler, but cooling water temperature and flow rates were set to replicate the cooling capacity of the production system. Table 3-1 contains the engine specifications, and an engine system schematic is shown in Figure 3.2. The laboratory setup is well documented in Glewen [79].

Table 3-1 GM 1.9L Engine Configuration

Engine Type	EURO IV Diesel
Bore	82 mm
Stroke	90.4 mm
Displacement	1.9 liters
Cylinder Configuration	Inline 4 4 valves per cylinder
Swirl Ratio	Variable (2.2-5.6)
Compression Ratio	17.5
Piston Bowl Geometry	Re-entrant bowl
EGR System	Hybrid High/Low Pressure, Cooled
ECU (OEM)	Bosch EDC16
ECU (new)	Drivven
Common Rail Injectors	Bosch CRIP2-MI 148° Included Angle 7 holes, 0.141 mm hole dia. 440 flow number.
Port Fuel Injectors	Delphi 2.27 g/s steady flow 340 kPa fuel pressure

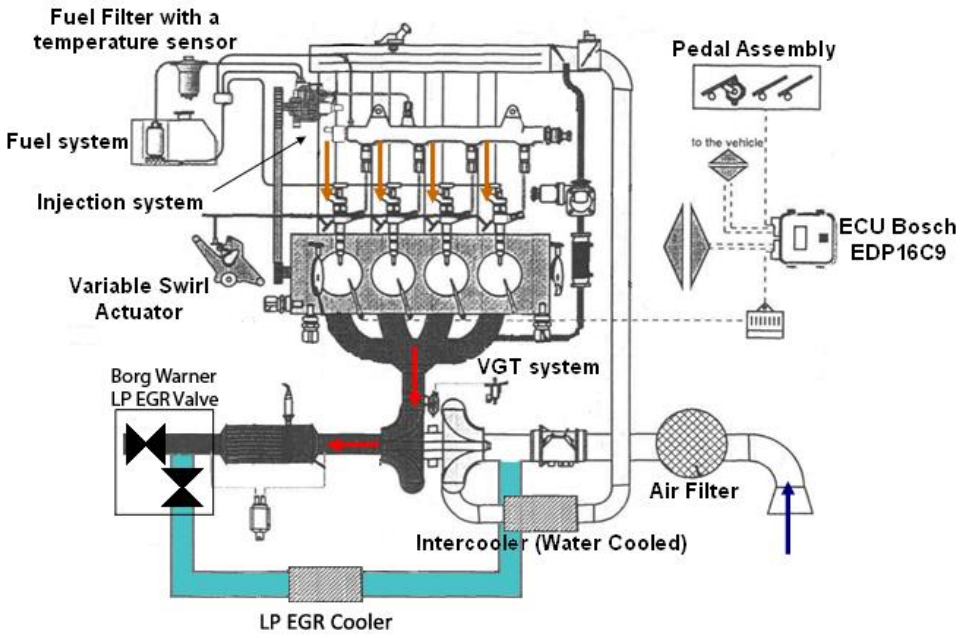

Figure 3.2 Schematic of the test engine lab

3.2 Intake Air Flow Rate

Intake airflow from the building compressed air supply was expanded to ambient pressure and heated to 25°C to minimize day-to-day variation. The flow rate was measured with the original equipment manufacturer (OEM) mass airflow (MAF) sensor and a laminar flow element (LFE). By correlating the LFE to the stock MAF sensor, it was found to adequately measure the airflow and was used to make relative comparisons between the two combustion modes studied in the tests.

3.3 EGR System

High pressure EGR was used for CDC and selected RCCI operation cases. It was supplied to the engine via the OEM high pressure loop. While the low pressure

loop was installed, it was not used as the low load operating points required high temperatures and the low pressure loop provided EGR at too low of a temperature to be optimal for the selected cases.

3.4 Fuel Systems

Since the engine was modified for dual-fuel operation, there are two separate fuel systems. For the direct injection system, the OEM 1,600 bar Bosch common rail system was used and left in its OEM configuration. The laboratory diesel fuel system was left in the configuration as used by Glewen [79]. In order to inject a volatile, low reactivity fuel such as gasoline for RCCI operation, an external additional port fuel injection (PFI) fuel system was added to the stock engine as shown in Section 1.1. To supply the PFI injectors, an additional fuel system was constructed, and a schematic is shown in Figure 3.3.

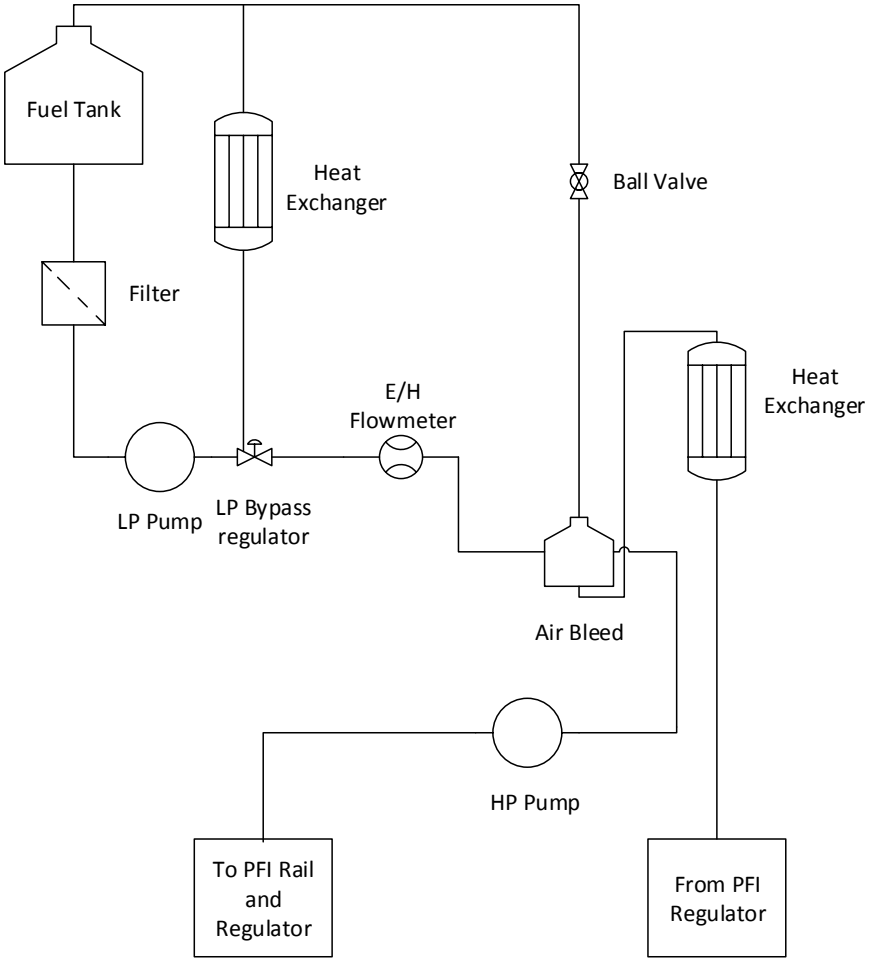

Figure 3.3 PFI fuel cart schematic

3.5 Fuel Flow Rate

For steady-state fuel flow rate measurements, Endress and Hauser coriolis-type meters were used for both DI and PFI systems. However, they were not used for the transient tests as the instrument and system response time is too slow for cycle-resolved measurements. For transient tests, the DI and PFI fuel injection quantities were calculated based on the rail pressure and injection command duration. The transient PFI fuel quantity was calculated based on injection

command duration only as the rail pressure was constant at 340 kPa. The post processing code used these steady-state flow rate values for the transient, fuel related calculations, such as the air fuel ratio (AFR) and equivalence ratio (Phi).

3.6 Fuels

For the RCCI tests, multiple fuels were used, both bio-derived and petroleum-derived. The petroleum fuels were a 96 RON certification gasoline from Haltermann (EEE) and a certification grade Ultra Low Sulfur Diesel (ULSD) also from Haltermann. The same USLD was used in both the RCCI and CDC combustion modes. The fuel properties are shown in Table 3-2 and Table 3-3, respectively.

Table 3-2 EEE Fuel Properties

Lower Heating Value (MJ/kg)	42.866
Ethanol (%)	0
Specific Gravity (@ 15.6 °C)	0.742
H/C (-)	1.86
RON (-)	96.4
MON (-)	88.5
AKI (RON+MON)/2 (-)	92.5

Table 3-3 ULSD Fuel Properties

Lower Heating Value (MJ/kg)	41.2
Specific Gravity (@ 15.6 °C)	0.851
CN [-]	44.4
H/C [-]	1.702

The bio-derived based fuels used for splash blending with the petroleum fuels are shown in Table 3-4 and Table 3-5, respectively. For the biofuel blends,

20% by volume of soy methyl ester (B100) was added to the ULSD and 20% by volume of 98% ethanol/2% denaturant (E98) was added to the EEE. Further details about the fuels used will be discussed in the results section. Detailed fuel property data sheets are shown in Appendix 7.6.

Table 3-4 B100 Fuel Properties

Lower Heating Value (MJ/kg)	37.160
Specific Gravity (@ 15.6 °C)	0.882
CN [-]	56.3
H/C [-]	1.839

Table 3-5 E98 Fuel Properties

Lower Heating Value (MJ/kg)	26.95
Specific Gravity (@ 15.6 °C)	0.785
H/C (-)	2.0
RON (-)	108.6
MON (-)	89.7
AKI (RON+MON)/2 (-)	99.15

3.7 Engine Controller

The OEM engine control unit (ECU) was replaced by a Drivven controller to allow full access to all relevant engine operating parameters and to allow for control over the additional port fuel injectors. The Drivven system allows real-time access and modification to the supplied torque-based engine maps that mimic the OEM EURO IV steady-state calibration. It must be noted that the Drivven controller is supplied as a steady-state controller with no transient tables or controls that would be present in the OEM controller. However, the new controller enabled all relevant parameters such as the direct-injection and PFI timing(s), fuel injection pressure,

EGR quantity, swirl vane position, and other parameters to be adjusted in real time by 2-D torque-based tables. A picture of the Drivven cart is shown in Figure 3.4.

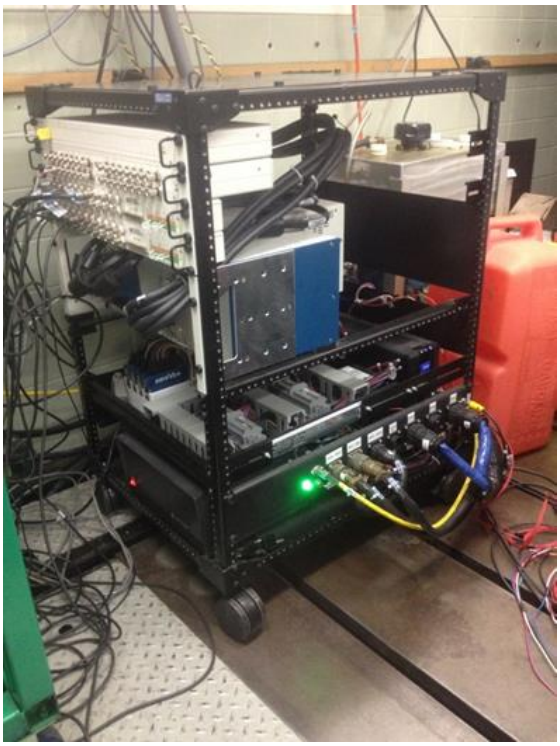

Figure 3.4 Photograph of the Drivven control system

3.8 Hydrostatic Dynamometer

A hydrostatic dynamometer was used the engine tests, with additional detail found in [79,82,83]. The basic principal of the dyno operation is that the traditional electric armature of an AC or DC dyno is replaced by a hydraulic pump/motor assembly with lower rotational inertia which allows for rapid speed and load changes. The main torque absorbing circuit is directly connected to the crankshaft by the main pump/motor and an additional pump/motor is used to supply motoring

torque. To adsorb torque, the main pump/motor is forced to pump hydraulic fluid at high pressures controlled by a high speed servo valve.

3.9 Instrumentation

All data were acquired using the built-in data acquisition (DAQ) software package (DCAT) in the Drivven controller on crank-angle or cycle-basis, depending on the type of measurement. High speed data such as cylinder pressure, manifold pressures and injection commands were sampled on a crank-angle basis at the crankshaft encoder resolution of 2048 pulses per revolution. All other data (i.e., emissions, fueling commands, etc.) were acquired once per engine cycle on the medium speed channel. This system was an upgrade to a previous setup which had multiple data acquisition systems. Acquiring all the data on one system helped to ensure alignment of all the time-based signals. The data were post processed using a custom designed MATLAB code, as shown in Appendix 7.5.

3.10 Gaseous Emissions

High speed measurements of NO and HC were provided by Cambustion CLD 400 and HFR 500 fast response emissions analyzers, respectively. Please note that the Cambustion system does not measure N_2O or NO_2, and only measured NO in the present study. The 10-90% response time of these instruments allows near-crank angle time resolution. For this work, NO or HC concentrations were averaged over all crank angles to give a single value for each cycle. The Cambustion system has two measurement heads for each emissions device, which allowed both NO

and HC to be measured pre- and post-diesel oxidation catalyst (DOC). CO and CO_2 were measured with an MKS Fourier transform infrared spectrometer (FTIR). The FTIR was not used for transient measurements as the exhaust flow and temperature control systems were inadequate to supply the FTIR with a high enough flow rate to achieve cycle-resolved measurements. The FTIR was used to give steady state measurements only. Oxygen concentration was measured in the intake manifold near cylinder 2, in the intercooler, and in the exhaust manifold using commercially available Bosch wideband sensors. Table 3-6 shows the emissions measurement systems.

Table 3-6 UW MCE Emissions Measuement Equipment

Species	Instrument	Measurement Method
NO	Cambustion fNOx400	Heated-Chemiluminescence Detector
CO and Exhaust CO_2	MKS	Fourier Transform Infrared Spectroscopy
Non-methane Unburned Hydrocarbons	Cambustion HFR400	Heated Flame Ionization Detector

3.11 Particulate Matter Measurements

Steady-state filter smoke number (FSN) measurements were made with an AVL 415s Smokemeter. Transient exhaust smoke opacity was measured using an AVL 439 Opacimeter, whose output can be converted to an approximate PM mass value using existing correlations for CDC [80, 81]. Since RCCI has little black carbon content (~1%) and high organic carbon content (~99%), traditional

correlations from FSN or Opacity to g/kWh are likely to be inaccurate [80]. All the data show that the results are below the emissions standards.

3.12 General Temperatures and Pressures

General pressure and temperature measurements were made at multiple locations in the intake and exhaust manifolds, EGR system, and charge air cooler. An HBM T-40 in-line torque transducer was used to measure crankshaft torque. This combination of available instrumentation provided a comprehensive description of the engine system's state during each individual combustion cycle.

3.13 Cylinder Pressure

Cylinder pressure was measured in all 4 cylinders; however, different pressure transducers were used in cylinders 1, 3 and 4 vs. cylinder 2. Cylinders 1, 3 and 4 utilized pressure sensing glow plugs from Borg Warner to give a qualitative indication of combustion phasing to quantify cylinder-to-cylinder timing differences. Cylinder 2 utilized the more accurate Kistler 6058 transducer to calculate metrics such as mean effective pressures, combustion noise, maximum pressure rise rate (MPRR) and CA50. Cylinder 2 was chosen as it was found to best approximate the overall engine operation [84].

3.14 Heat Release Method and Calculation

Calculation of the heat release rate is an important tool for combustion analysis to measure phasing, shape and duration. The method employed in the

present study follows a 1st law analysis with constant gas properties [10]; the resulting equation is

$$\frac{dQ_{chem}}{dt} = \frac{\gamma}{\gamma - 1} P \frac{dV}{dt} + \frac{1}{\gamma - 1} V \frac{dP}{dt} - \frac{dQ_{loss}}{dt} \quad (1)$$

The pressure data were filtered by a zero-phase low pass filter with a cutoff frequency of 2,200 Hz. Because numerical differentiation acts like a poor digital filter and can impart noise to the signal, the pressure derivative was found using the coefficients of a Savitzky-Golay filter. Heat transfer was modeled by correlations for HCCI combustion by Chang [85]. Gamma (i.e., the ratio of specific heats) was calculated from the pressure trace via a linear regression curve fit of the compression and expansion strokes, shown in Figure 3.5.

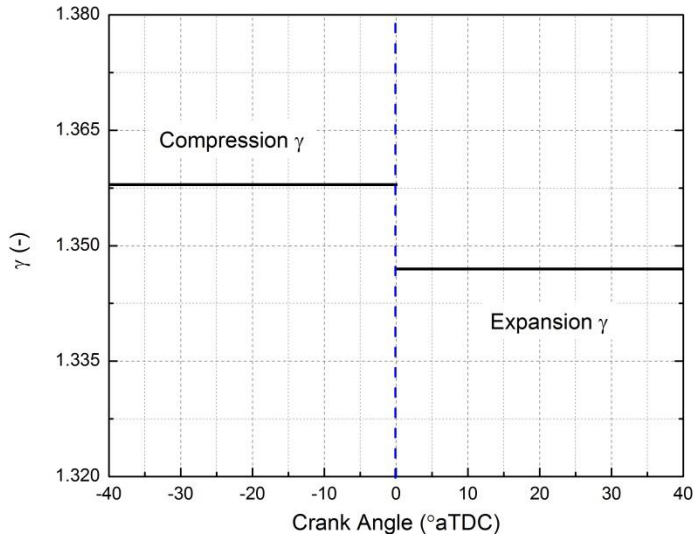

Figure 3.5 Representative two step gamma as a function of crank angle for arbitrary RCCI operating condition

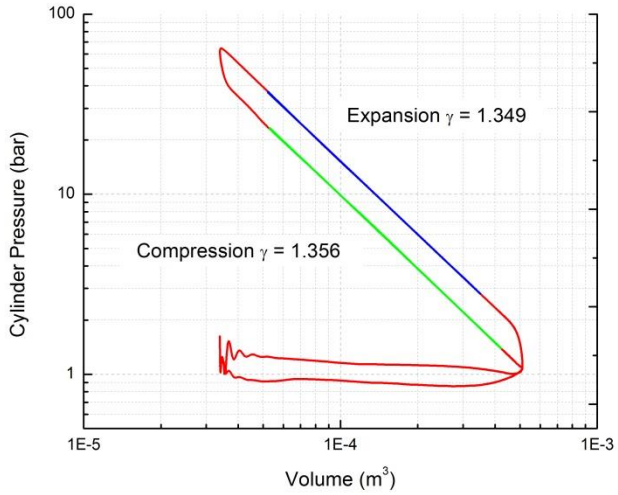

Figure 3.6 Log Pressure vs. Log Volume trace showing nearly constant gammas for compression and expansion strokes

The two step gamma assumption is justified for RCCI because the combustion duration is short enough that the bulk expansion and compression gammas provide an adequate description of gamma during the engine cycle as shown in Figure 3.6. The HCCI gamma correlation provided by Chang [85] was also seen to give similar values as this method.

3.15 Combustion Noise

According to Shahlari [86], engines emit noise due to energy release from the fuel and subsequent cylinder pressure increase. Some of this noise is attenuated by the engine block but the engine still emits sound. Combustion noise can be measured many different ways [86]. One of the most common ways is to use the AVL 450 noise meter. Due to the high cost of the device, cylinder pressure metrics

such as MHRR and MPRR are used by researchers instead of purchasing the device as to compare combustion noise between different lab setups and operating conditions. Shahlari showed that these metrics may not fully correlate the combustion noise for these different conditions [86]. To provide a more accurate combustion noise metric, they proposed a method to mimic the output from the AVL noise meter using only the pressure trace. The noise calculation code from Shahlari is shown in Appendix 7.8.

Combustion noise in the present work was found using the built-in calculation from Drivven. The Drivven method is proprietary, but comparisons of the Drivven noise output to the method proposed by Shahlari have shown that the Drivven method is very similar (or even the same). Combustion noise values are nearly identical for both methods, thus it is assumed that the Drivven noise output is roughly equal to Shahlari's method, which is an excellent approximation of the AVL noise meter.

3.16 Steady State Emissions Calculations

Starting with the "standard" emissions equations used in Stivender et. al. [87], and those of Professor Ghandi [88], additional inputs for oxygenated and dual fuels were added. First, the molecular weights for the PFI and DI fuels were calculated, where y is the H/C ratio and z is the O/C ratio given by the fuel properties.

$$MW_{PFI} = 12.01 + 1.008 \cdot y_{PFI} + z_{PFI} \cdot 16 \quad (2)$$

$$MW_{DI} = 12.01 + 1.008 \cdot y_{DI} + z_{DI} \cdot 16$$

Next, the fuel flow rates were converted to a molar basis, as

$$\dot{N}_{DI} = \frac{\dot{m}_{DI}}{MW_{DI}} \quad (3)$$

$$\dot{N}_{PFI} = \frac{\dot{m}_{PFI}}{MW_{PFI}}$$

Then, the H/C and O/C ratios were found for the combined PFI/DI mixture from

$$y = \frac{\dot{N}_{DI} \cdot y_{DI} + \dot{N}_{PFI} \cdot y_{PFI}}{\dot{N}_{PFI} + \dot{N}_{DI}} \quad (4)$$

$$z = \frac{\dot{N}_{DI} \cdot z_{DI} + \dot{N}_{PFI} \cdot z_{PFI}}{\dot{N}_{PFI} + \dot{N}_{DI}}$$

The molecular weight for the mixture was then found by as.

$$MW_{fuel} = 12.01 + 1.008 \cdot y + z \cdot 16 \quad (5)$$

Next, the molar concentration and mole fractions for each species were found. The number of dry exhaust moles was found from carbon, hydrogen and oxygen balances as:

Carbon

$$1 = n_{CO} + n_{exh,CO2} + n_{HC} \quad (6)$$

Hydrogen

$$y = 2 \cdot n_{H2O} + 2 \cdot n_{H2} + y \cdot n_{HC} \quad (7)$$

Oxygen

$$2 \cdot n_{air} = 2 \cdot n_{exh,CO2} + n_{CO} + n_{H2O} + 2 \cdot n_{O2} + n_{NO} - z \quad (8)$$

Since H_2 was not measured, an empirical H_2 relation was used.

$$n_{H2} = 0.25 \cdot y \cdot n_{CO} \quad (9)$$

Finally, the number of water moles is the number wet minus the number of dry moles:

$$n_{H2O} = n_{exh,wet} - n_{exh,dry} \quad (10)$$

From these equations, the AFR, equivalence ratio (Phi) and emissions index calculations were found according to methods proposed in [10, 39] and are shown in the Appendix 7.5.

3.17 Transient Specific Methodology

When conducting transient experiments with the present lab equipment, some unique methods were used to collect measured values. Since a high speed paramagnetic type O_2 analyzer was not available, O_2 was measured using commercially available wideband sensors in both the intake and exhaust. However, the measurement is pressure sensitive, so the measured value was corrected according to

$$O_{2,corrected} = \frac{O_{2,raw}}{P_{int}} / (P_{ambient} * 6.895)\text{^}0.2598 \qquad (11)$$

This expression was derived by Glewen [79] by measuring known oxygen concentrations and developing a curve fit from the data. Without an intake CO_2 measurement, the EGR rate was calculated by

$$EGR = \frac{O_{2,intake} - O_{2,atmopsheric}}{O_{2,exhaust} - O_{2,atmospheric}} \qquad (12)$$

The transient equivalence ratio and AFR were found using the calculated fuel flow data mentioned in Section 1.5. Similar to methods used by Glewen, instrument response time corrections were not used, as filtering of the data renders them unnecessary [79]. For crank angle resolved measurements, a 1st order transit time correction can be applied to relevant transient measurements, but they were found to be on the order of <0.5 cycles so they were not used in the present study.

3.18 UW Multi-Cylinder Laboratory Measurement Uncertainty

Measurement uncertainty is an important consideration in experimental data to determine actual trends in the data compared to errors in the measurement. The following equations of Dempsey [89] were used to calculate the accuracy and precision of the experimental data. Based on the manufacturer uncertainty, shown in Table 3-7 (additional laboratory measurement uncertainties are shown in Appendix 7.4), a code was developed to calculate the uncertainty for the emissions index, specific emissions, AFR, Phi, BTE and combustion efficiency, as seen Appendix 7.5.

Table 3-7 Emissions and Fuel Flow Measurement Uncertainties

Measurement	Linearity	Noise	Repeatability	Full Scale	Total [%]	Uncertainty
NO	0.01	-	0.01	200 [ppm]	1.41	2.82 [ppm]
HC	0.01	0.01	-	1002 [ppmC3]	1.41	42.5 [ppm]
DI and PFI fuel flow	0.01	-	-	2 [g/s]	0.01	0.02 [g/s]

The HC and NO instrument uncertainty was able to be calculated with an 11 point calibration. To find 95% confidence intervals from the 11 point calibration, internal fitting tools in MATAB were used such as the 2 finds a polynomial curve fit for the residual r_i, viz.,

$$y_i = \sum_{j=1}^{m} \beta_j x_i^{j-1}$$

$$\begin{bmatrix} y_1 \\ y_2 \\ \vdots \\ y_n \end{bmatrix} = \begin{bmatrix} 1 & x_1 & {x_1}^2 & \dots & {x_1}^{m-1} \\ 1 & x_2 & {x_2}^2 & \dots & {x_2}^{m-1} \\ \vdots & \vdots & \vdots & \dots & \vdots \\ 1 & x_n & {x_n}^2 & \dots & {x_n}^{m-1} \end{bmatrix} \begin{bmatrix} \beta_1 \\ \beta_2 \\ \vdots \\ \beta_m \end{bmatrix} \qquad (13)$$

$$\beta_j = (\underline{\underline{X}}^T \underline{\underline{X}})^{-1} \underline{\underline{X}}^T \underline{Y}$$

Calculates the residual r_i and the sum of the residuals

$$r_i = y_i - \sum_{j=1}^{m} \beta_j x_i^{j-1} \qquad (14)$$

$$S = \sum_{i=1}^{N} r_i^2$$

A final set of Equations were used to calculate the variance, confidence interval and standard deviation for a measurement y_d from a measured value x_d.

$$y_d \pm t_{CI;v}\sqrt{Var}$$

$$Var = \underline{X}_d^T \underline{\underline{M}}\, \underline{X}_d$$

$$X_d = \begin{bmatrix} 1 \\ X_d \\ X_d^2 \\ \vdots \\ X_d^{m-1} \end{bmatrix} \qquad (15)$$

$$\underline{\underline{M}} = \sigma^2 \left(\underline{\underline{X}}^T \underline{\underline{X}}\right)^{-1}$$

$$\sigma^2 = \frac{S}{N - m - 1}$$

From these equations the calibration curves and confidence intervals can be found for the HC and NO analyzers. The calibrations are shown in Figure 3.7 and Figure 3.8, respectively.

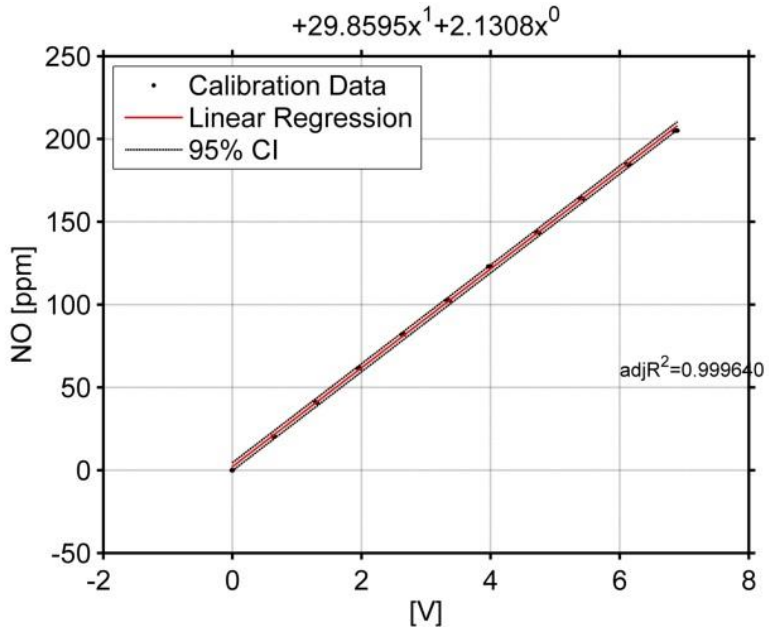

Figure 3.7 Cambustion NO instrument calibration curve with 95% confidence intervals plotted in red

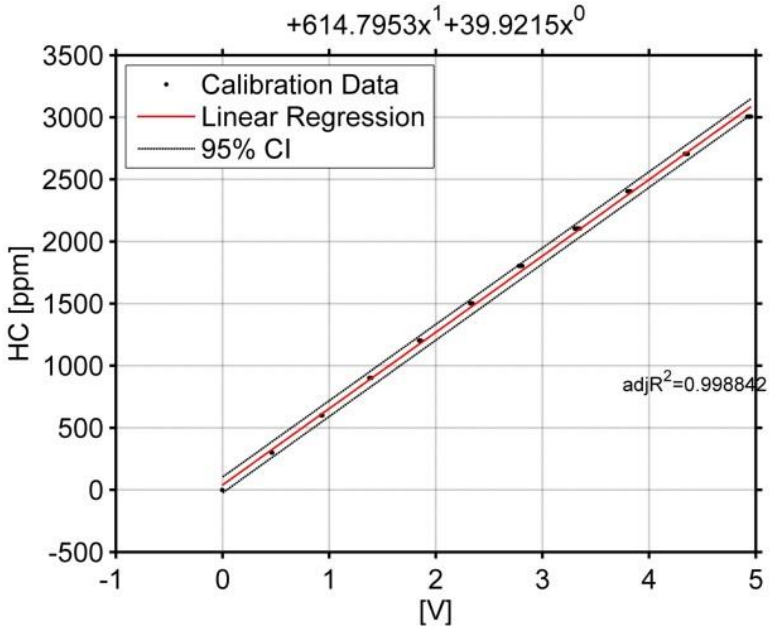

Figure 3.8 Cambustion HC instrument calibration curve with 95% confidence intervals plotted in red

3.19 Cylinder Balancing

As can be expected with a multi-cylinder engine, there are significant variations in the initial conditions, i.e., the cylinder wall temperatures, EGR rate, volumetric efficiency, fuel rail pressures, etc., of each cylinder. With a kinetically controlled combustion strategy like RCCI, these imbalances can lead to decreased performance due to different overly advanced or delayed combustion in each cylinder. Exhaust emissions can also vary significantly for each cylinder with these variations in combustion phasing. To adjust for these variations, the total fueling and ratio of gasoline-to-diesel fuel was varied to match the IMEP and combustion phasing over all 4 cylinders. The balancing was accomplished in the Drivven code by applying a multiplier to the PFI and DI duration command on each cylinder. First, for each cylinder, the DI and PFI adjustment factors were tuned to vary the ratio of gasoline-to-diesel fuel to match CA50 over all 4 cylinders. Next, once the combustion phasing was balanced, the PFI and DI adjustment factors were then raised or lowered in equal amounts to match IMEP over all 4 cylinders. Typically, the PFI and DI adjustment factors needed to be varied by +/- 10% from cylinder-to-cylinder. Results of the cylinder balancing for an arbitrary operating condition are shown in Figure 3.9. Due to the manual cylinder balancing, cylinder-to-cylinder effects from the EGR distribution, engine coolant temperature (ECT), emissions were not studied in the present work.

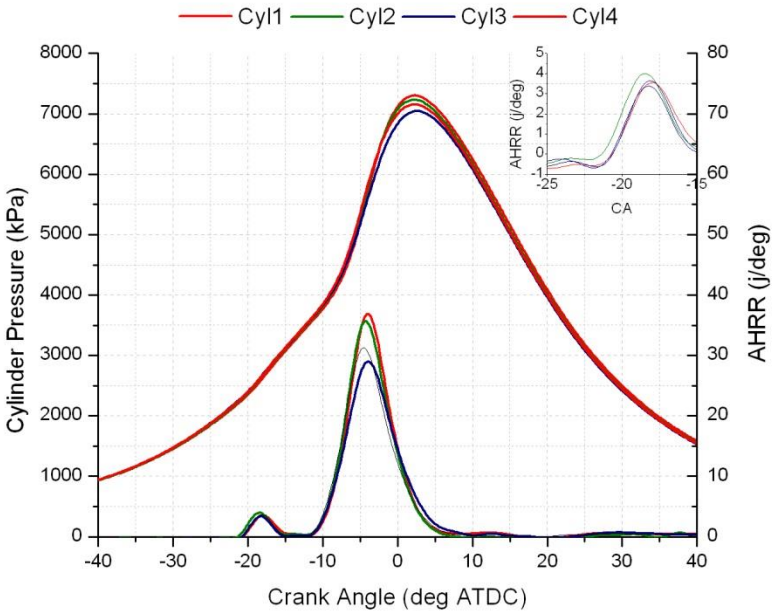

Figure 3.9 Arbitrary engine operating condition showing the balanced combustion phasing and load over all 4 cylinders

3.20 Drivven Controller Strategy

The Drivven controller operates by controlling the intake pressure, EGR, fuel injection parameters and common-rail fuel pressure using 2-D torque-based tables (similar how the OEM controller operates). The tables are sized in 2 mm^3/cycle and 500 rev/min increments and are shown in Appendix 7.9 and 7.10. The controller comes with these tables populated with values for CDC that are a steady-state representation of the OEM 2005 EURO IV calibration. These values were found to give similar steady-state emissions results as those from the OEM Bosch controller. For RCCI operation, additional tables to control the PFI system were added. Next, these tables were re-calibrated at steady-state with RCCI specific values to give the

desired combustion phasing and emissions. To operate the engine, the controller was given a simulated accelerator command. From this pedal position command and the current engine speed, the interpolated table value will be used for the appropriate engine control parameter, such as the PFI duration or target intake manifold pressure.

Once in the main loop, the pedal position is converted to a desired torque response from the 2-D torque table, which is based on the manufacturer settings for noise vibration and harshness, drivability, etc. From the desired torque, a corresponding fueling rate is calculated. From the desired fueling rate, a corresponding fraction is split off in up to 5 main injections and 1 PFI injection. From this split fraction of the total fueling, the injection duration is found using a 2-D table from the rail pressure and torque. These values were also based on manufacturer settings, likely derived from steady-state flow bench testing. From this base value, the fueling command was adjusted by various corrections based on operating temperatures and other conditions.

The first adjustment is the closed-loop adjustment for CA50. The next one is a correction for the PFI ratio, based on the ECT. After that there is an optional correction for intake pressure for the PFI ratio. From the total of all these adjustments, the final duration is found. A flow chart of the adjustments to the fuelling command is shown in Figure 3.10.

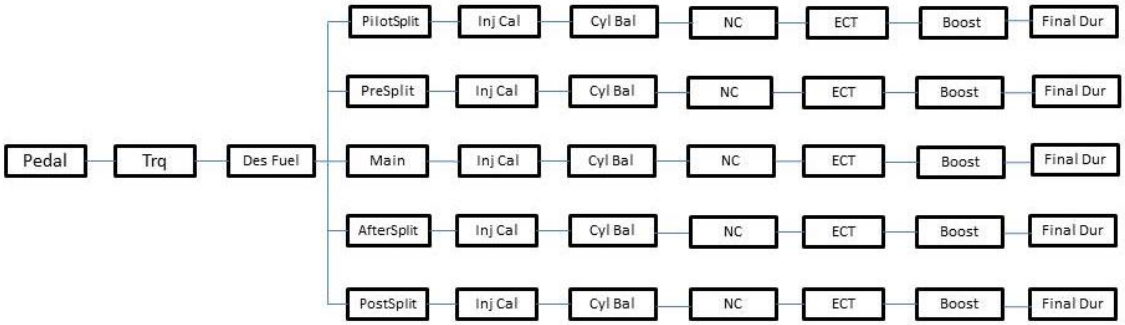

Figure 3.10 Drivven system fueling block diagram

These basic corrections are only a start of what would be required for an OEM application. For perspective, most OEM ECUs contain over 1 million lines of code, with most powertrain engineers spending their time on solving this problem.

Similarly, the SOI timing was calculated via a similar methodology of corrections. The main table value has multiple adjustments which are added or subtracted. The first adjustment is the manual cylinder balance discussed earlier. Then, the closed-loop code controls CA50 via changes to SOI for CDC combustion. The final adjustment is to change SOI timing as a function of ECT. These timing adjustments occur for all 5 diesel injections with no timing adjustments for the PFI injector. A flow chart of this process is shown in Figure 3.11.

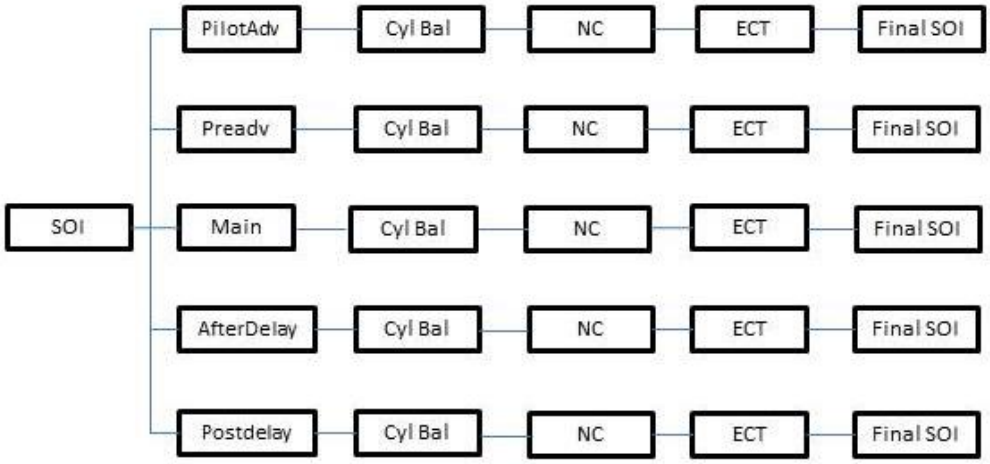

Figure 3.11 Drivven system SOI timing block diagram

3.21 Drivven Closed Loop (Next Cycle) Control

In the present work, two engine combustion phasing control strategies were used for RCCI, namely open-loop and closed-loop, while CDC was operated with open-loop control only. However, CDC has the capability for closed-loop operation. For open-loop control, the Driven controller was used in its original configuration with no feedback control of the combustion phasing. For closed-loop RCCI operation, the same torque-based controller was used with additional code to control the combustion phasing on a cycle-by-cycle basis. For closed-loop operation, an embedded PID controller was used to control the combustion phasing. In the RCCI tests using closed-loop control, CA50 was calculated from the cylinder 2 pressure trace of each cycle and compared to a target value from the 2-D table, shown in Appendix 7.9 and 7.10. Based on the difference of the target vs. the measured value, the PID acts to bring the measured value towards the target value

by manipulating a user defined control metric. Since RCCI combustion phasing has been found to be most sensitive to the PFI ratio [90], it was chosen as the control metric. Thus, the RCCI closed-loop controller adjusted the PFI ratio on a cycle-by-cycle basis by adjusting the PFI and DI injection duration commands to advance or retard CA50 as needed to match the target value. A flow chart of the closed-loop controller is shown in Figure 3.12

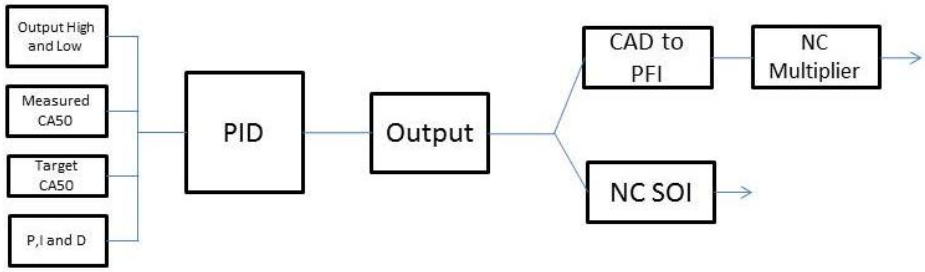

Figure 3.12 Drivven system closed-Loop PID control block diagram

The base values of all the parameters used in the RCCI experiments were saved in 2-D maps based on fueling and engine speed, as shown in Appendix 7.9 and 7.10. These include intake pressure, SOI timing, PFI ratio, CA50, injection number, swirl, rail pressure. All tables were calculated by best practices from results of tests in both MCE and SCE engines [1-9].

Other interesting and/or useful modifications to the Drivven code are the open loop corrections for low coolant temperature operation. Since the steady-state values are saved in the tables, deviations in coolant temperature (i.e., at cold starting) are only applicable for a short part of the engine operating time, but can

account for a large portion of the total mass emissions. As previously discussed, corrections for SOI and PFI fraction were made for coolant temperatures from ambient temperature (25°C to 85°C where the thermostat opens). As seen in the SCE tests, cooler temperatures (intake and or coolant) typically require additional reactive fuel as the autoignition reaction rates are slowed. To accomplish this, the main SOI timing was delayed and the PFI fraction was lowered with lower ECT. Experimental results of these corrections will be shown later. These tables were added to minimize the amount of correction needed with the closed loop controller, as having too much adjustment can lead to erratic and/or dangerous operation.

Chapter 4 Results

For the transient tests, the engine was coupled to a hydrostatic dynamometer capable of rapid speed and load transients [83]. Transient experiments were initiated by changing the accelerator pedal command to the ECU. The ECU interprets the pedal command as a desired torque output and adjusts all the relevant engine parameters accordingly from the stored table data. An example of the pedal command change is seen in Figure 4.1. The desired pedal command was an instantaneous step change, but that was found to be too rapid for the dynamometer to accurately control the engine speed. Thus, the pedal output was slowed using a rate limiting PID controller to simulate the OEM ECU behavior, as shown in Figure 4.1.

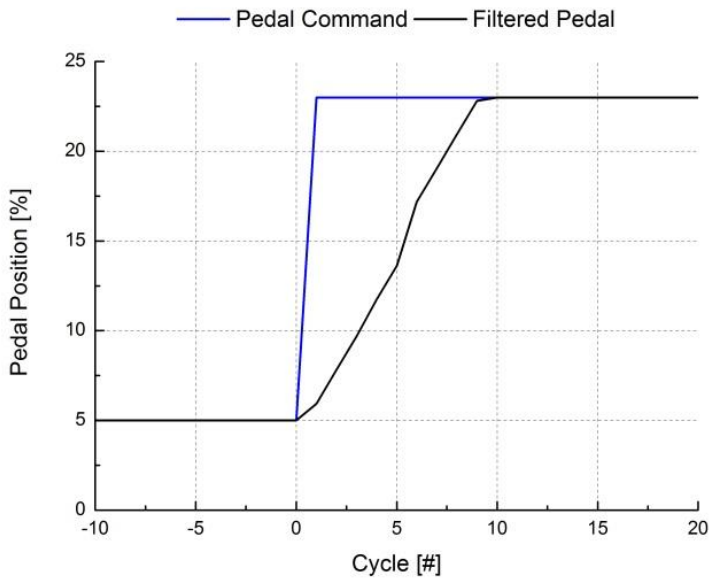

Figure 4.1 Example of commanded and filtered pedal command change for transient engine experiments

4.1 CDC and RCCI Baseline Transient Results

The first part of the transient tests involved operating the engine at steady-state in both combustion modes to establish a baseline for comparison with transient operation. The steady-state runs were conducted in 1 bar increments to establish a baseline for transient tests. Any deviation from these results would indicate conditions that need to be accounted for with additional programming in the ECU as so the deviations are minimized for the lowest level of emissions and performance degradation. Run conditions are shown in Table 4-1, Table 4-2 and Table 4-3, respectfully. Pressure and AHRR traces for both RCCI cases (with and without EGR) and CDC are shown in Figure 4.2, Figure 4.3 and Figure 4.4.

Table 4-1 RCCI w/EGR Run Conditions

	Run 1	Run 2	Run3	Run 4
Engine Speed [rpm]	1,500	1,500	1,500	1,500
Rail Press. [bar]	371	412	453	499
Main SOI [deg. bTDC]	39.5	43	47	52
DI [mg/inj.]	3.42	3.43	2.32	2.28
PFI [mg/inj.]	2.267	4.48	8.32	10.76
Intake Pressure [bar]	1.01	1.02	1.03	1.03
Intake Temp. [°C]	78	88	75	53
PFI Fraction [%]	39.9	55.6	78.1	84.0
EGR [%]	51.5	49.5	35.5	19.51

Table 4-2 RCCI w/o EGR Run Conditions

	Run 1	Run 2	Run3	Run 4
Engine Speed [rpm]	1,500	1,500	1,500	1,500
Rail Press. [bar]	405	421	458	496
Main SOI [deg. bTDC]	42	45	48	53
DI [mg/inj.]	3.52	3.49	3.27	2.94
PFI [mg/inj.]	4.05	5.16	7.48	10.31
Intake Pressure [bar]	1.03	1.02	1.02	1.02
Intake Temp. [°C]	45	45	45	45
PFI Fraction [%]	52.8	58.8	68.7	77.3
EGR [%]	0	0	0	0

Table 4-3 CDC Run Conditions

	Run 1	Run 2	Run3	Run 4
Engine Speed [rpm]	1,500	1,500	1,500	1,500
DI [mg/inj.]	6.15	8.46	10.85	13.7
PFI [mg/inj.]	0	0	0	0
Rail Press. [bar]	458	522	593	676
Main SOI [deg. aTDC]	0	0	0.2	1
Pilot advance [ms]	1.1	1.1	1.1	1.1
Pilot fraction [%]	9.3	8.9	8.5	8.2
Intake Pressure [bar]	1.056	1.08	1.12	1.15
Intake Temp. [°C]	65	68	70	71
EGR [%]	28.9	30.22	26.9	24.0

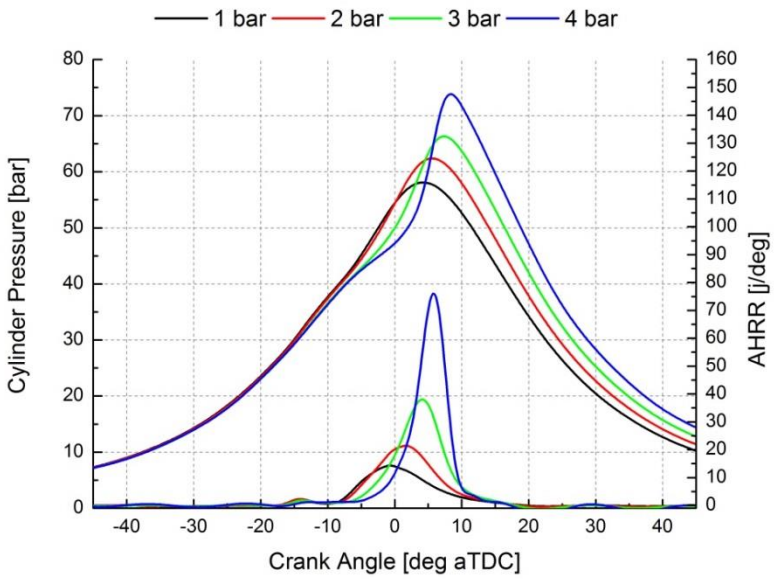

Figure 4.2 RCCI cylinder pressure and apparent heat release rate for the non-EGR steady state cases

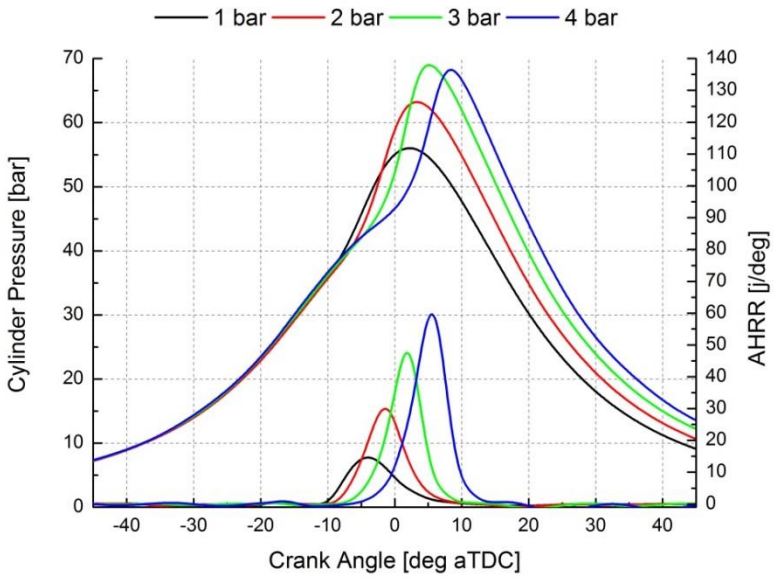

Figure 4.3 RCCI cylinder pressure and apparent heat release rate for the EGR steady state cases

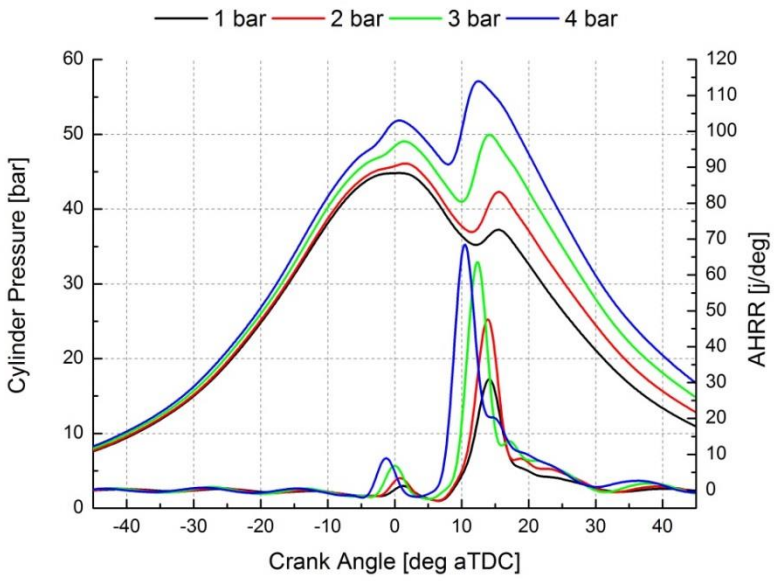

Figure 4.4 CDC cylinder pressure and apparent heat release rate for the steady state cases

Specific operating conditions for the RCCI and CDC cases are shown in Figure 4.5. The CDC values are Drivven's approximation of the OEM EURO IV calibration using a pilot and main injection strategy. Testing has indicated that the emissions and combustion noise are similar to those from the OEM engine using a stock ECU [90].

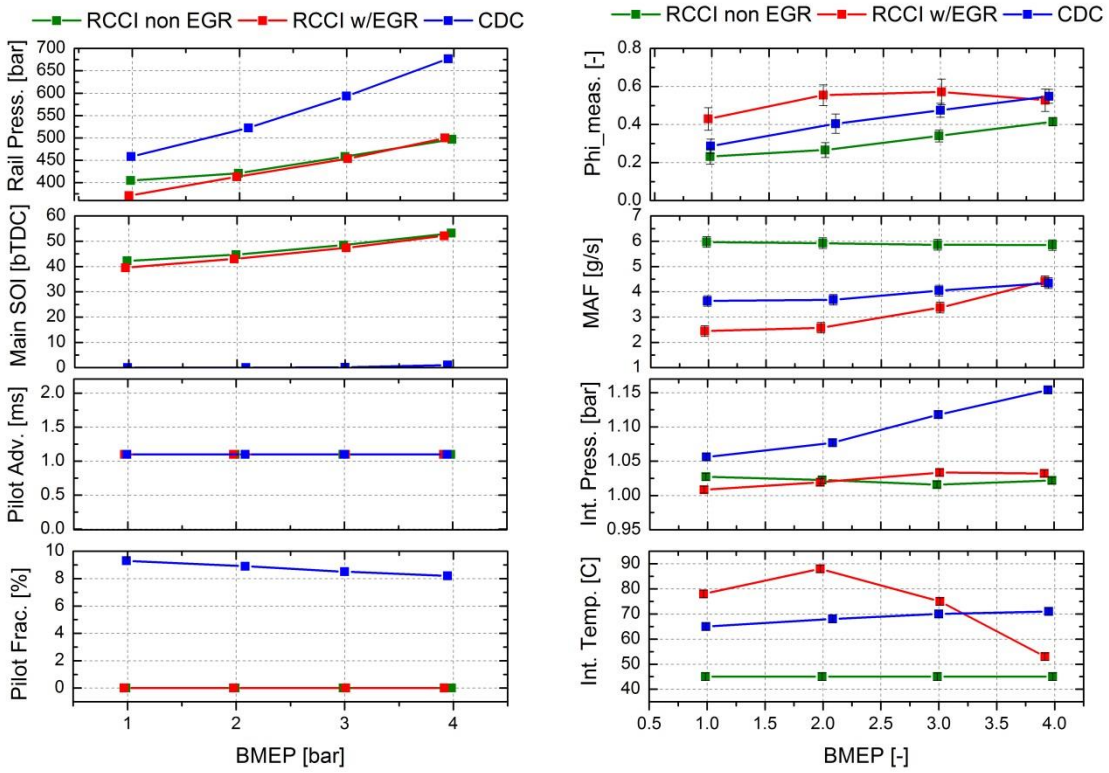

Figure 4.5 Steady-state operating results for RCCI and CDC

The baseline operating conditions for RCCI, such as the fuel injection strategy (actual Start of Injection (SOI) timing, PFI fraction, etc.), EGR and rail pressures were chosen using results from Refs. [1-9,91] and are shown in Table 4-1 and Table 4-2. The OEM CDC values were used as the starting point for the RCCI calibration and then slightly modified to meet emissions targets and to provide the highest BTE as shown in Table 4-3. The emissions targets for RCCI were HC <3,000 ppmC1 (or 80 g/kg-f), NO <10ppm (or 1 g/kg-f), FSN <0.1, with BTE near CDC levels and MPRR <10 bar/deg. Using theses metrics and emissions targets, the intake pressure was set slightly lower than CDC to minimize pumping work, as

less intake pressure is needed for RCCI to achieve low NO and PM emissions as shown in Table 4-1and Table 4-2. Similarly, lower rail pressure was needed as much earlier injection timings are used and less rail pressure is helpful to avoid cylinder wall impingement (see Table 4-1 and Table 4-2).

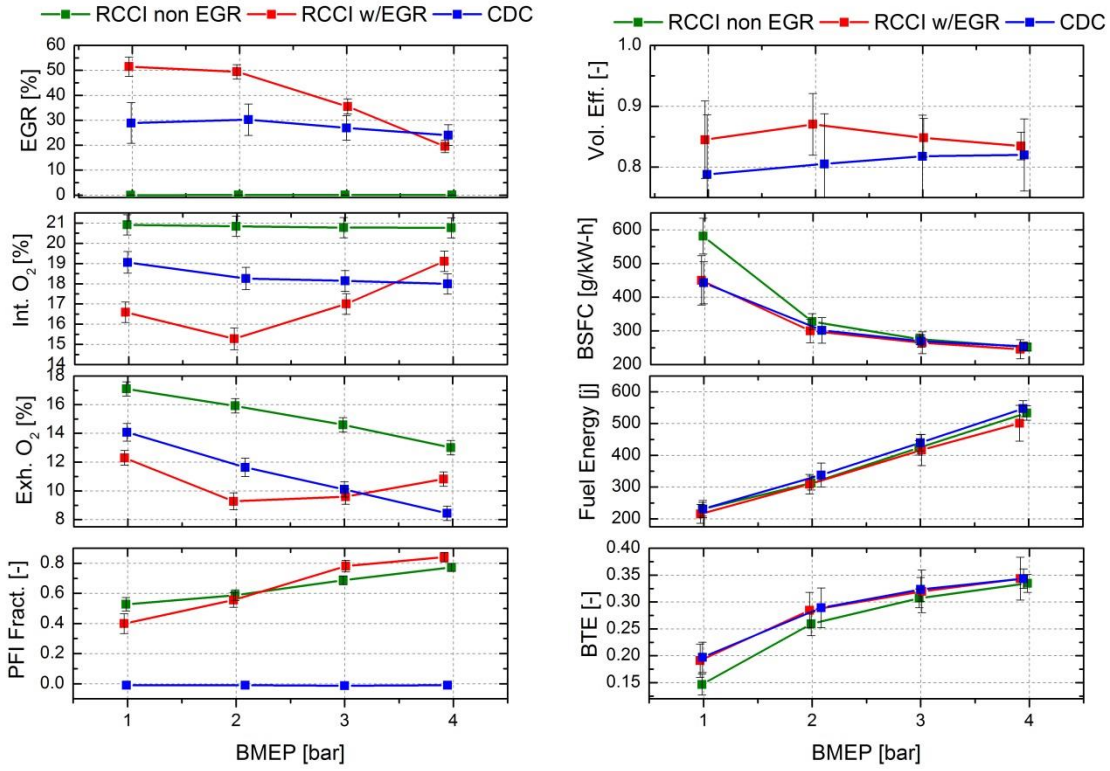

Figure 4.6 Steady-state operating results for RCCI and CDC

Combustion results for both modes are shown in Figure 4.6. As can be seen, the combustion phasing for RCCI is near TDC compared with CDC at nearly 16 deg. aTDC. MPRR for all cases met the noise target, being less than 7 bar/deg. for all cases. Similarly, combustion noise follows MPRR with RCCI being slightly lower than CDC up to the 4 bar BMEP condition.

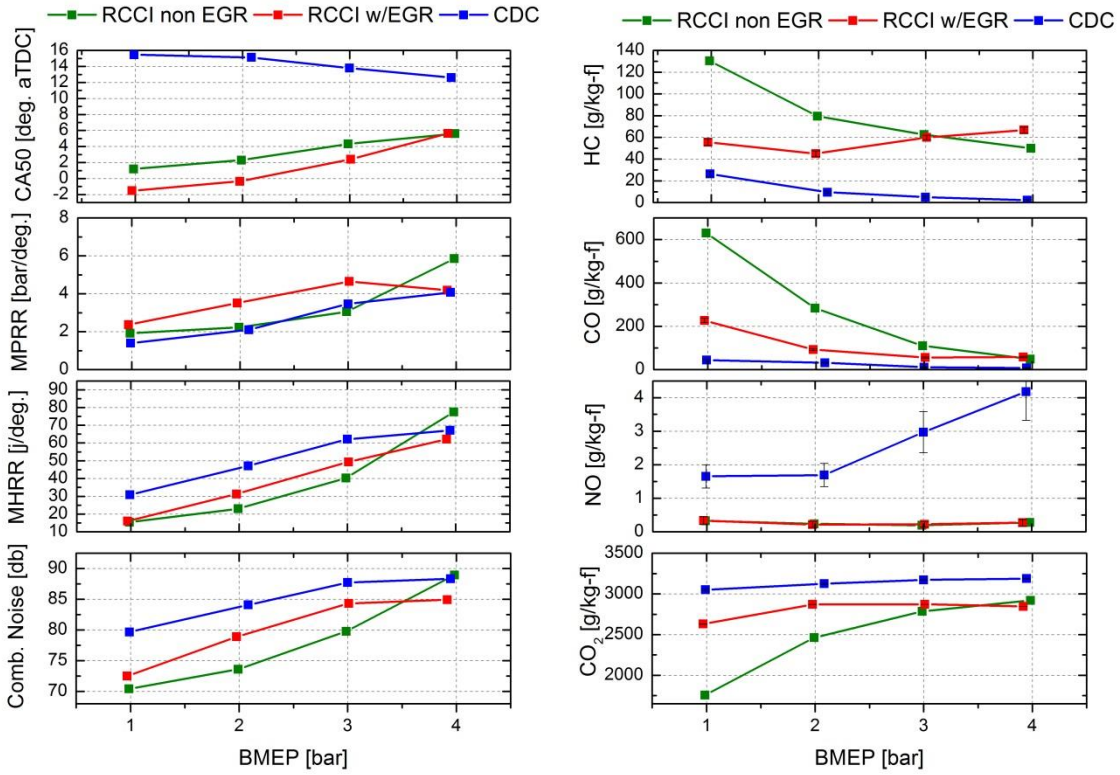

Figure 4.7 Steady-state operating results for RCCI and CDC

The emissions results, as shown in Figure 4.7, for the RCCI cases are also typical of previous single and multi-cylinder engine (SCE and MCE) results (e.g., [1-9]) where NO and PM (the FSN and Opacity) are near zero and HC and CO are elevated over CDC. The BTE of RCCI using EGR was improved over not using EGR and was equal to that of the CDC results. The improvement in BTE can be seen from the reduction in HC and CO when using EGR. The higher intake temperatures with EGR help to increase the oxidation rates and increase the combustion efficiency. With the same BTE between RCCI and CDC, it can be seen that RCCI has lower CO_2 emissions, which is due to the higher H/C ratio of the fuel

mixture. The CDC emissions results are typical of those of a light-duty diesel engine. HC and CO emissions are low with the PM (the FSN and Opacity) and NO emissions being higher than RCCI. Moderate HP EGR was used for NO control for the EURO IV calibration. The moderate rail pressure and use of a single pilot injection are also typical of a EURO IV calibration. Since the OEM engine was equipped with a combination diesel oxidation catalyst/diesel particulate filter (DOC/DPF), it is possible to use both Cambustion HC channels to measure the catalyst efficiency. Shown in Figure 4.8, it was found that the OEM DOC was able to achieve light-off for CDC at 2 bar BMEP, where it was only able to light-off with RCCI at 3 bar with EGR and 4 bar without EGR. The higher exhaust manifold temperature seen when using EGR is likely the reason for the improved catalyst performance. Ideally the catalyst efficiency would be higher at lower loads, so future work to bring the exhaust temperature of RCCI up at 1 and 2 bar will be of critical importance to bring real world drive cycle emissions under the regulated levels.

Finally, in Figure 4.8, a first law balance on all three combustion modes can be seen. As can be interpreted from the HC and CO emissions above, the combustion efficiency is significantly higher for CDC than RCCI due to the higher combustion temperatures. The higher intake pressure used with CDC can be seen to increase the pumping loss compared to RCCI. This higher pumping loss comes from the higher exhaust pressure that is needed to produce the desired intake pressure at this operating condition where the OEM turbocharger efficiency is low.

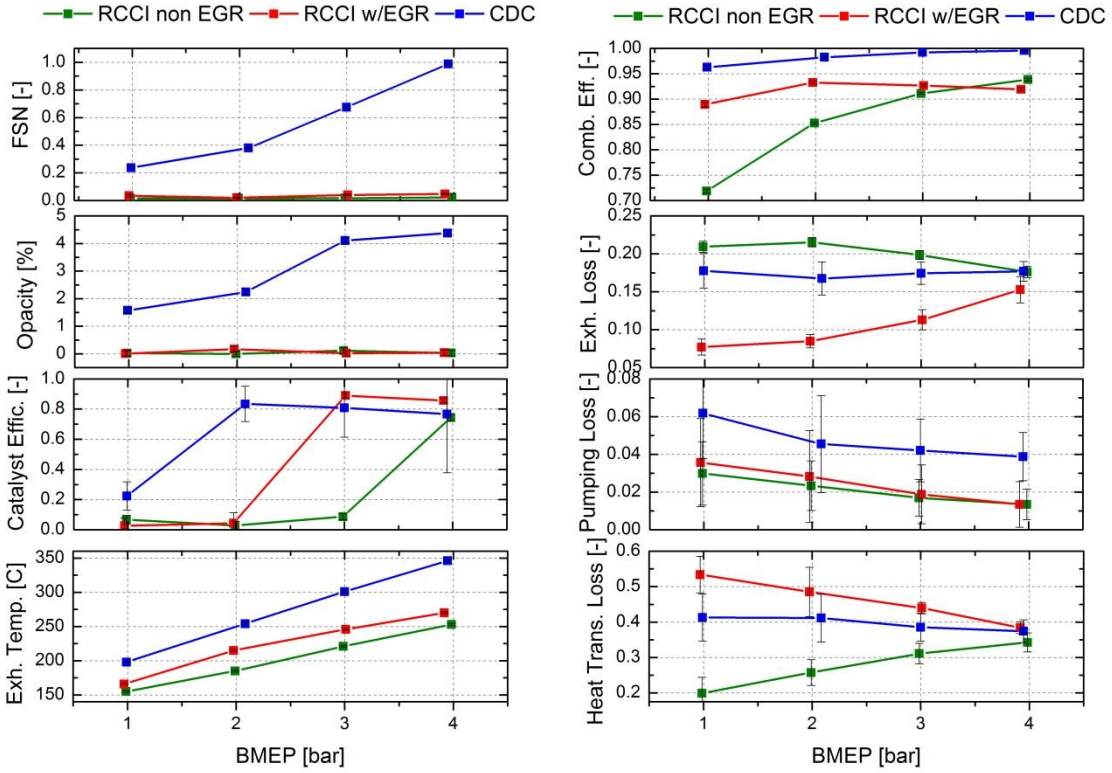

Figure 4.8 Steady-state operating results for RCCI and CDC

The higher exhaust temperature for CDC can be seen to increase the amount of energy lost out the exhaust rather than the cooling system as with RCCI. The higher heat transfer loss of the EGR RCCI cases are due to less mass and energy leaving the system through the exhaust. The heat transfer loss is the remaining losses besides the pumping, exhaust and combustion inefficiency. Thus, if less energy leaves the system through the exhaust, then the remaining energy must be lost to heat transfer to complete the first law balance. This is can be seen in the non-EGR RCCI case where the heat transfer is much lower than the EGR RCCI

case. When not using EGR, more mass and energy leave the system through the exhaust, thus there is less energy to be lost as heat transfer.

4.2 Step Load Change Transient Results

For the first set of transient experiments, a logical choice is to start by investigating how RCCI reacts to step changes in load. The engine was given the above mentioned emulated pedal change to command the engine to operate from 1 to 4 bar BMEP at 1,500 rev/min. These values were chosen from the steady-state values as the highest load that could be achieved at 1,500 rev/min with MPRR less than 10 bar/deg. In this section, RCCI with and without EGR are compared to CDC operation over the step-load change. The steady-state run values for the CDC transient cases were shown in Table 4-3.

Figure 4.9 shows the BMEP as a function of engine cycle number for three different test transient modes. For the up-load RCCI cases it can be seen, the load takes nearly 60 cycles until the load reaches the target of 4 bar BMEP. Conversely, it takes nearly 60 cycles for the load to stabilize at 1 bar for the down speed test. These load excursions are not seen with CDC. It is theorized that the reason for this is intake port wall wetting. During the up-load, the wall film grows with additional gasoline mass being injected, thus less makes it into the cylinder. Conversely, during the down-load this extra wall-film fuel reaches the combustion chamber and adds to the load. This phenomenon is commonly reported in spark-ignition engines in research and well established corrections are used to mitigate this problem [93].

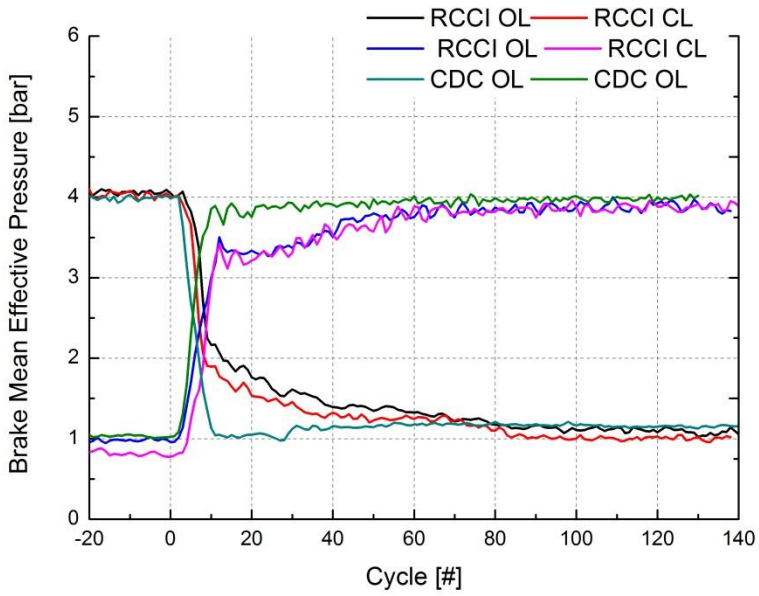

Figure 4.9 RCCI open-loop (OL) and closed-loop (CL) and CDC BMEP over the step load transient

4.3 CDC Load Transient

Figure 4.10 shows the fueling commands and run conditions for CDC during the load step change. As expected for CDC, the main injection timings are near TDC with injection pressure increasing to the final set point following the pedal command. All other relevant parameters such as O_2 concentrations, injection durations and total fueling follow from steady-state point to steady-state point.

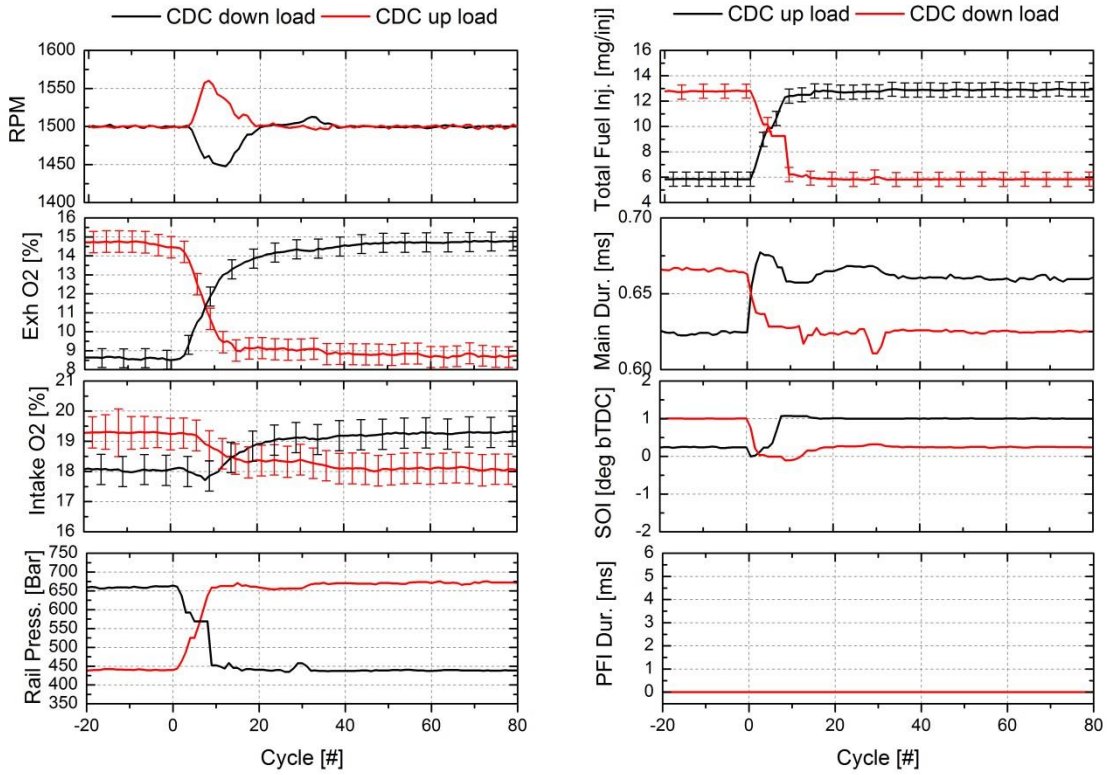

Figure 4.10 CDC open-loop fueling results

Figure 4.12 shows the air system response and combustion performance for CDC over the step load change. Here, the slight turbo lag can be seen as the intake pressure takes nearly 30 cycles to reach its steady state value. This is because the turbocharger efficiency is rather low at this condition as it is sized to provide higher efficiency at full load operation. The intake manifold temperature was constant for both the up and down load tests because the EGR rate is nearly constant, as shown in Figure 4.11. The MAF and equivalence ratio change following their steady-state values, given in Table 4-3.

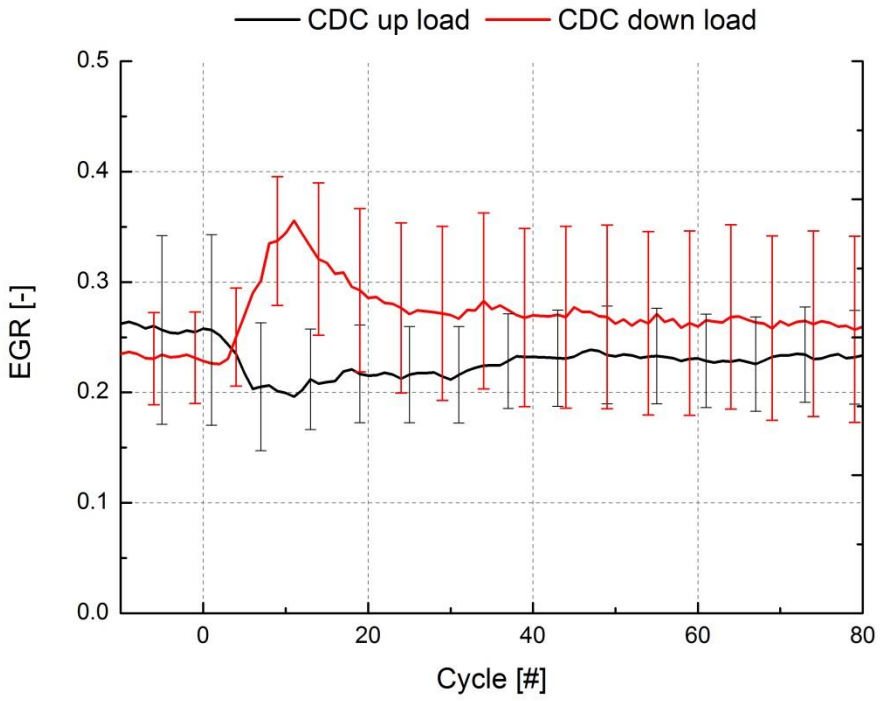

Figure 4.11 CDC load step transient EGR response

The combustion performance results are typical of a light-duty diesel engine. CA50 is nearly constant across the transient as the most of the operating points have late SOI timings to reduce combustion noise and NO, as shown in Figure 4.10. The combustion noise from the EURO IV calibration was fairly high at the 4 bar condition, with high EGR and high intake temperatures allowing for a large premixed spike. Newer engines (i.e., EURO V and VI) are likely to be quieter, but at the expense of increased engine-out PM and lower thermal efficiency.

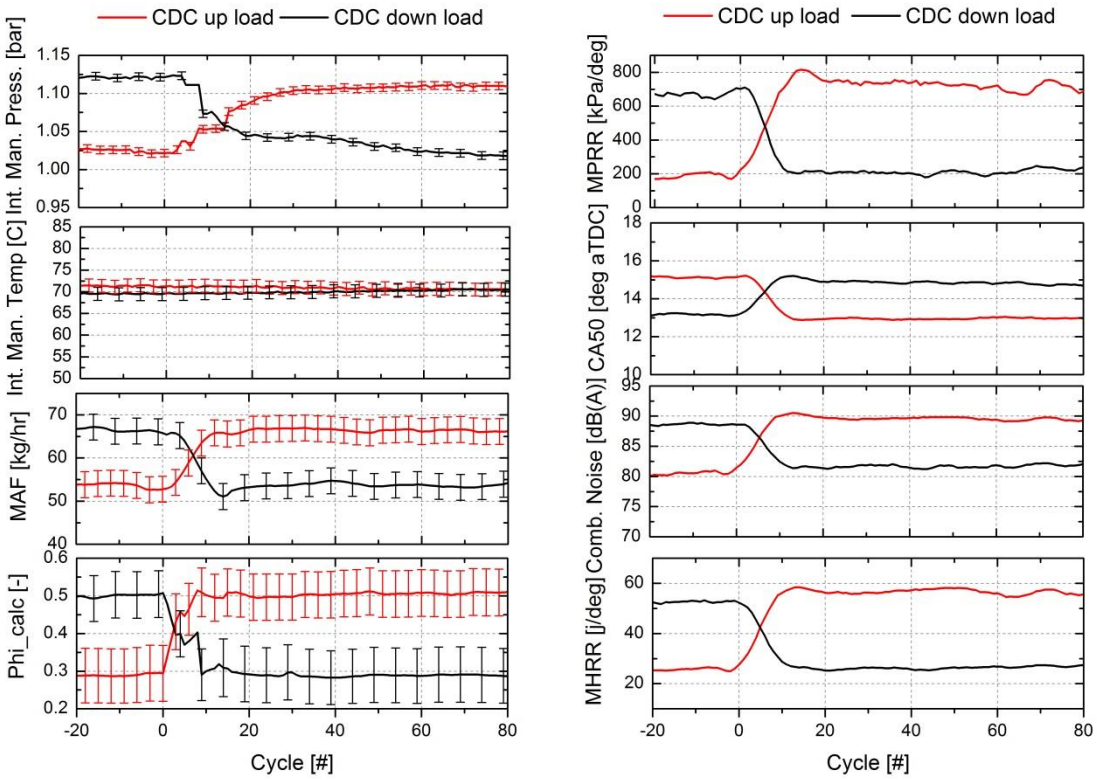

Figure 4.12 CDC open-loop combustion results

Figure 4.13 shows the emissions performance for CDC. As can be expected from a CDC engine, HC emissions are low and PM and NO are fairly high. The main difference is in the NO excursion from the steady-state values. The spike in the up-load NO until cycle 40 is typical of transient CDC, as seen by Glewen et al. [94]. They reported that typically in CDC combustion NO emissions tend to spike during transients as the NO increase is driven by the turbocharger lag and the resulting delay in intake O_2 through the EGR system. The delay in EGR of the up-load cases can be seen until cycle 40 in Figure 4.11.

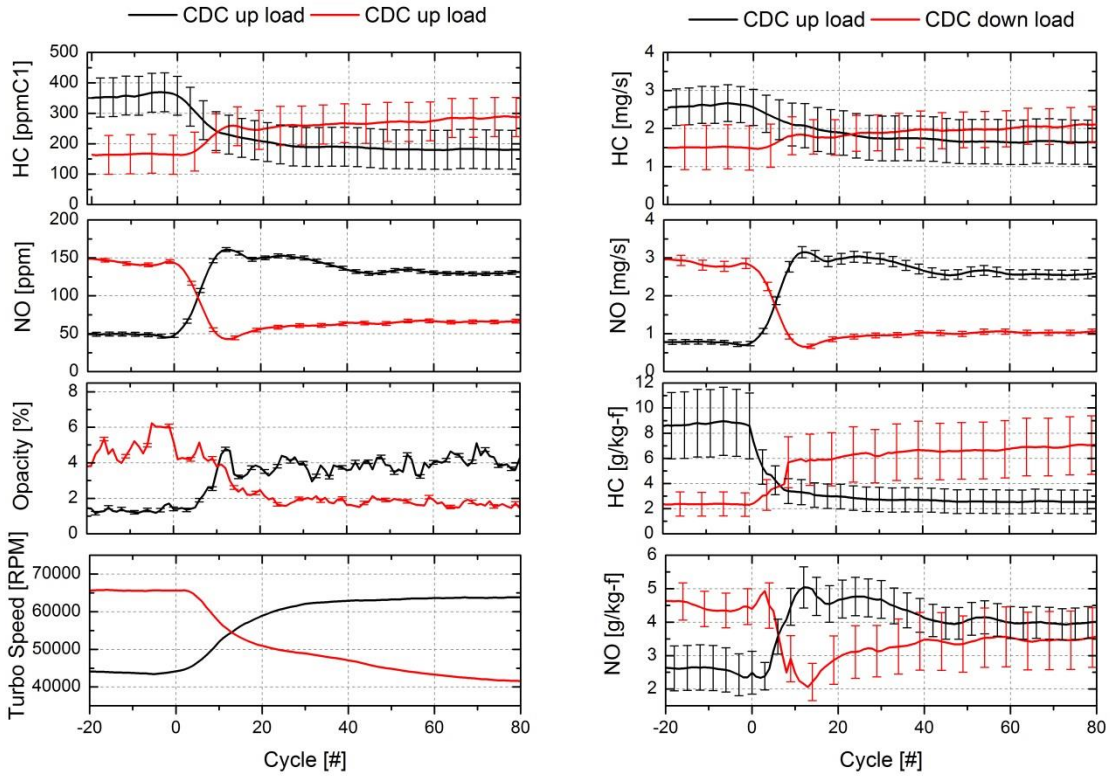

Figure 4.13 CDC open-loop emissions results

4.4 RCCI Load Transient

RCCI transient performance was evaluated in a similar manner to that of CDC, but used both an open- and closed-loop calibration. The open-loop tests were operated using only the steady-state table values to control the engine, while the closed-loop tests adjusted the PFI ratio of each cycle to attempt to reach the steady-state CA50 target value. Figure 4.14 shows the run conditions for the RCCI up and down-load transient tests. Table 4-1, Table 4-2, Table 7-3 and Table 7-4 give all the relevant run conditions for the RCCI load transient cases.

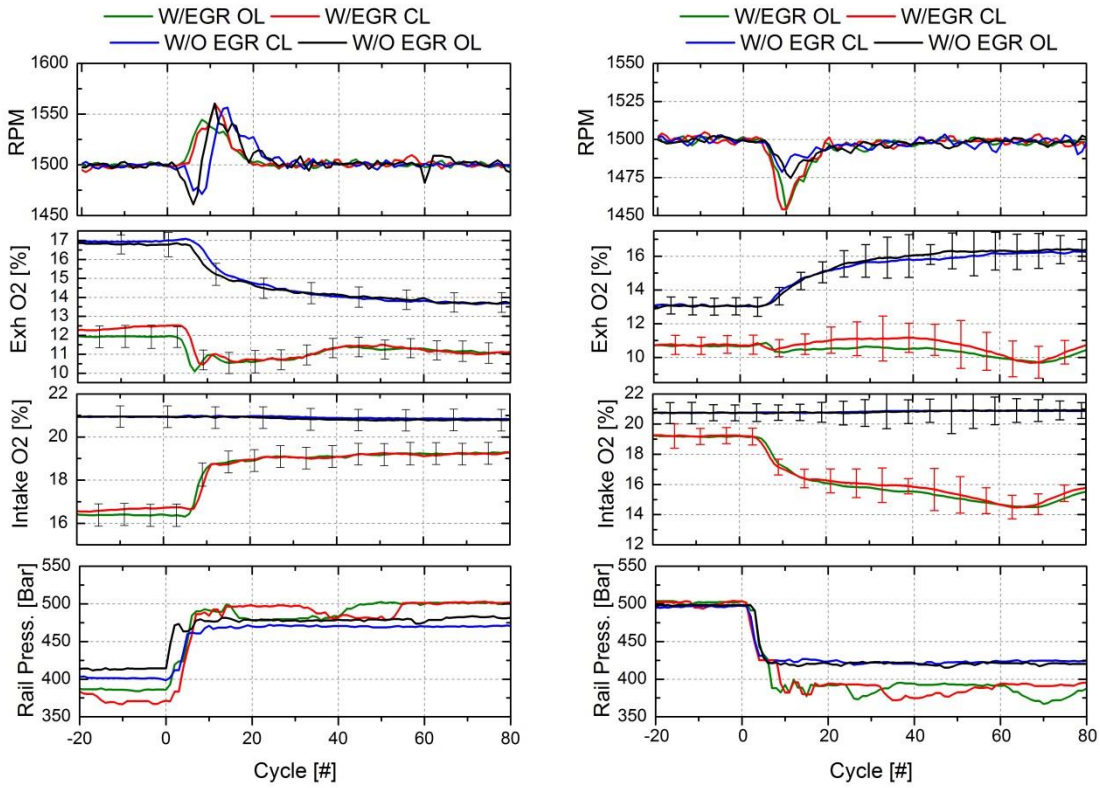

Figure 4.14 EGR and Non-EGR RCCI run conditions

The RCCI transient EGR behavior is shown in Figure 4.15 and Figure 4.16. The up vs. down load performance is slightly different as the down load EGR takes longer to build up. The MAF can be seen to take nearly 60 cycles to reach steady state, both driven by the slow turbocharger response seen in Figure 4.20.

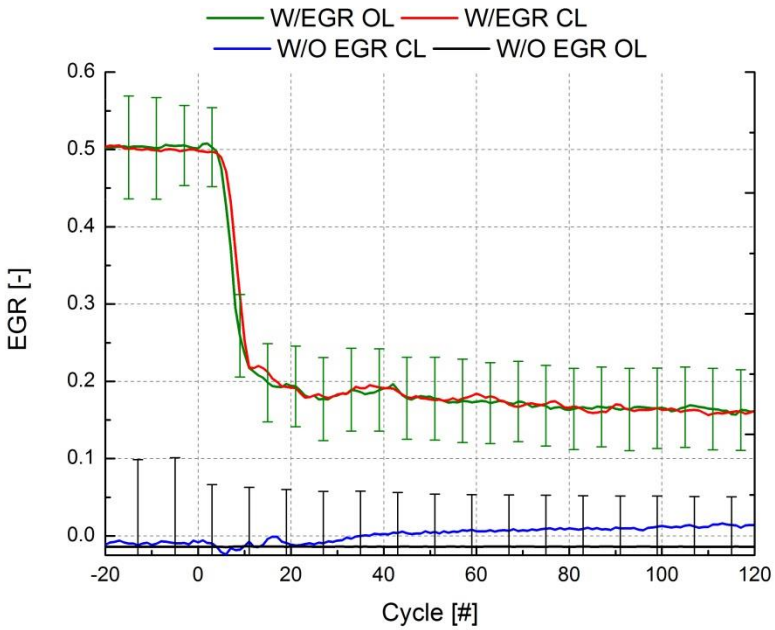

Figure 4.15 EGR response for the up-load RCCI cases

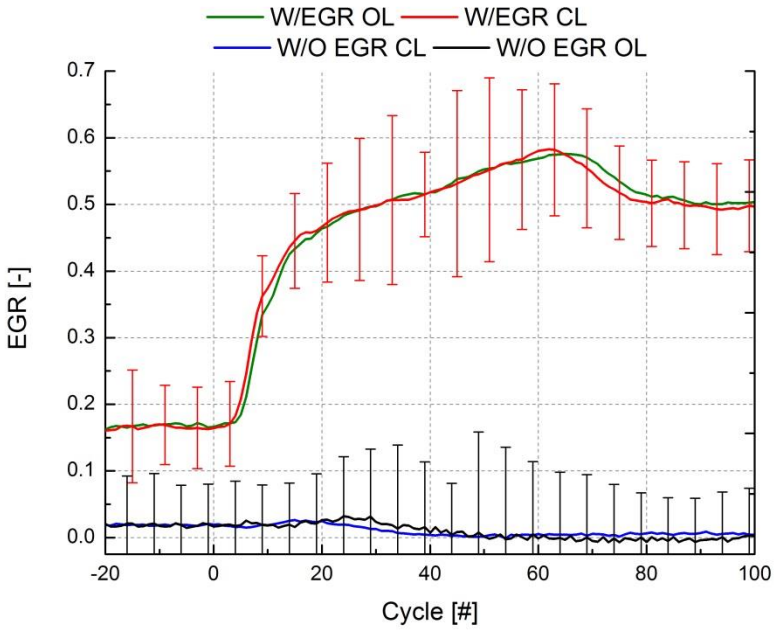

Figure 4.16 EGR response for the down-load RCCI cases

In Figure 4.17, the fueling commands for the open-loop and closed-loop, up- and down-load RCCI transient cases can be seen. As the main SOI timing was not modified by the closed-loop controller, it remained constant between the two modes and load tests. The use of the closed-loop controller can be seen in the main and PFI durations as the need for additional diesel fuel (i.e., lower PFI fraction) was required to reach the requested combustion phasing of 3.5 deg. ATDC at 4 bar BMEP.

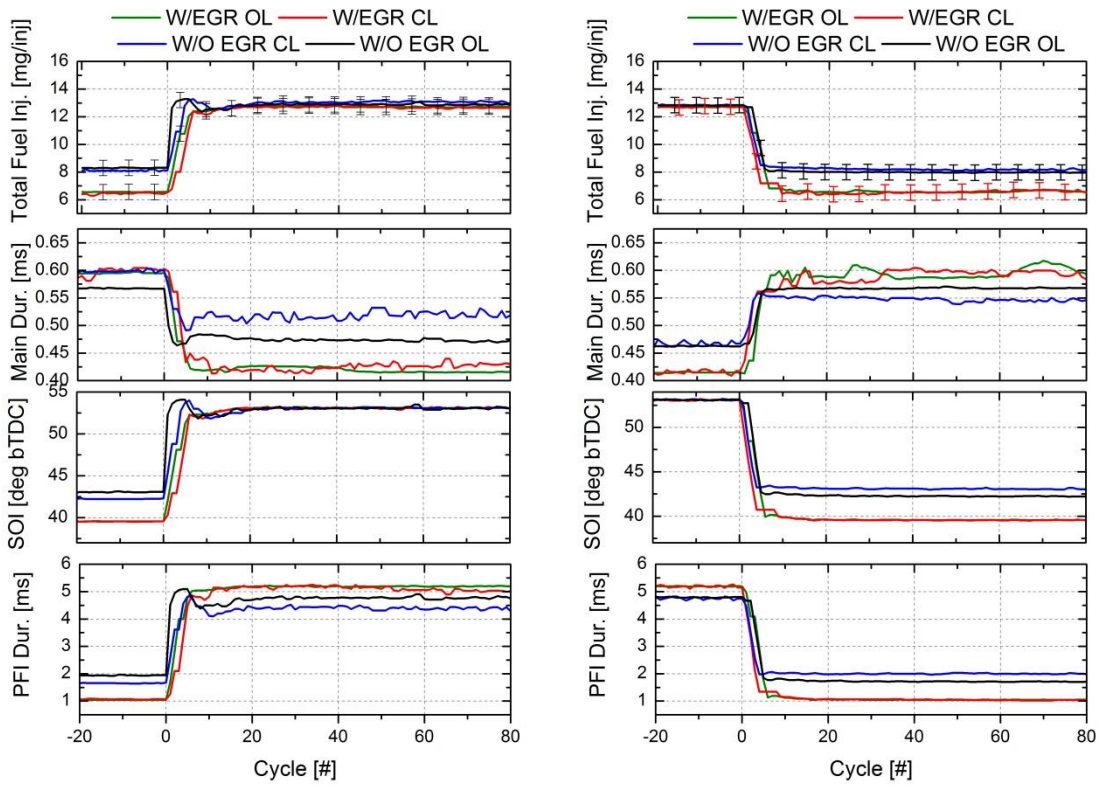

Figure 4.17 RCCI open-loop and closed-loop fuelling commands

Figure 4.18 compares the air system performance between the open-loop and closed-loop RCCI tests. As expected, there were no major differences in the air

system parameters, as they were not affected by the closed-loop controller. The intake pressure and MAF for the EGR and non-EGR case are slightly different from each other. For the non-EGR case, the MAF and intake pressure are nearly constant so there is not much difference across the load change. This is different for the EGR case as the MAF nearly doubles. The slight delay in the air flow rate change combined with the faster fuel flow rate change can be seen in the calculated equivalence ratio becoming higher for about 10 cycles until the MAF reaches its steady state value. Similarly, it can be seen that the Phi drops for about 10 cycles while the MAF is slow to drop to it lower steady-state rate.

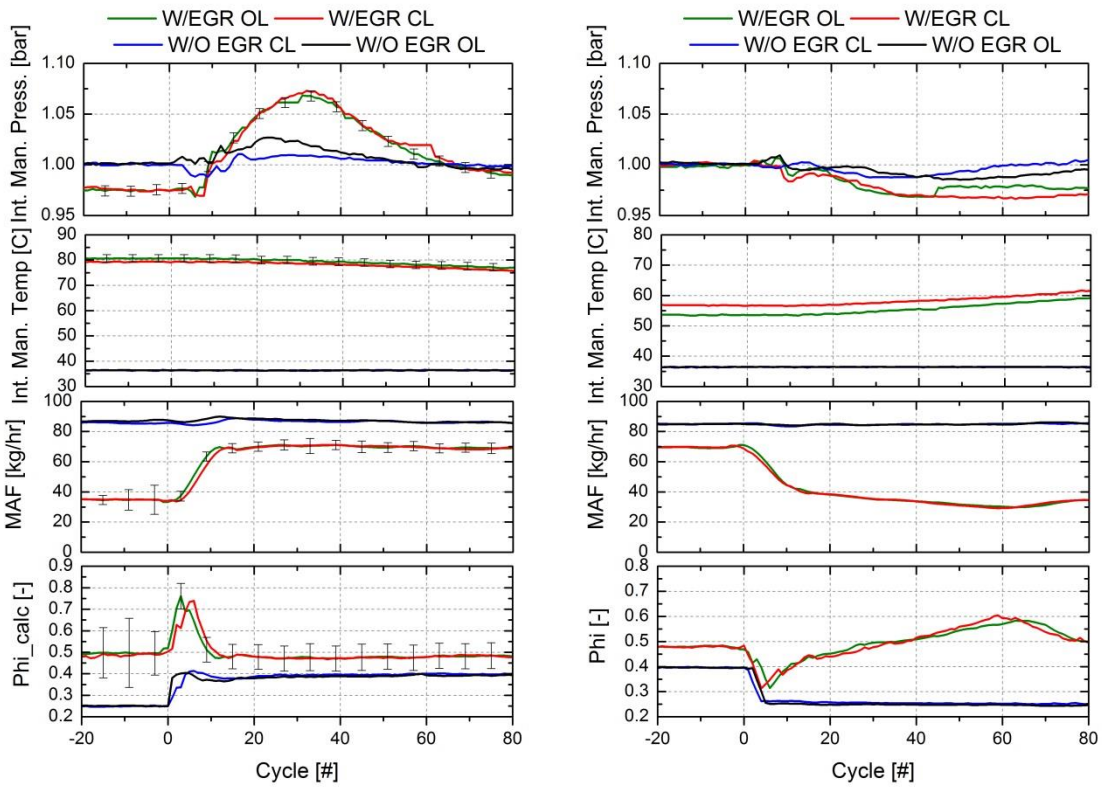

Figure 4.18 RCCI open-loop and closed-loop air system results

In Figure 4.19, the major differences between using and not using feedback control can be seen. For both the EGR and non EGR cases, the closed-loop controller has a quicker response to drive CA50 towards the desired steady-state set point, although it is more pronounced for the non-EGR case. Currently it is unclear why the EGR case had better response, but possibly the higher intake temperature allows the mixture to be more reactive and to respond to the fueling change faster. The faster response to the steady state set point is simultaneously seen in the higher MPRR, combustion noise and MHRR for the closed-loop case after cycle 20 for the non EGR case. The cause of the faster response time is that the closed-loop controller decreased the PFI fraction, which can be seen in Figure 4.17.

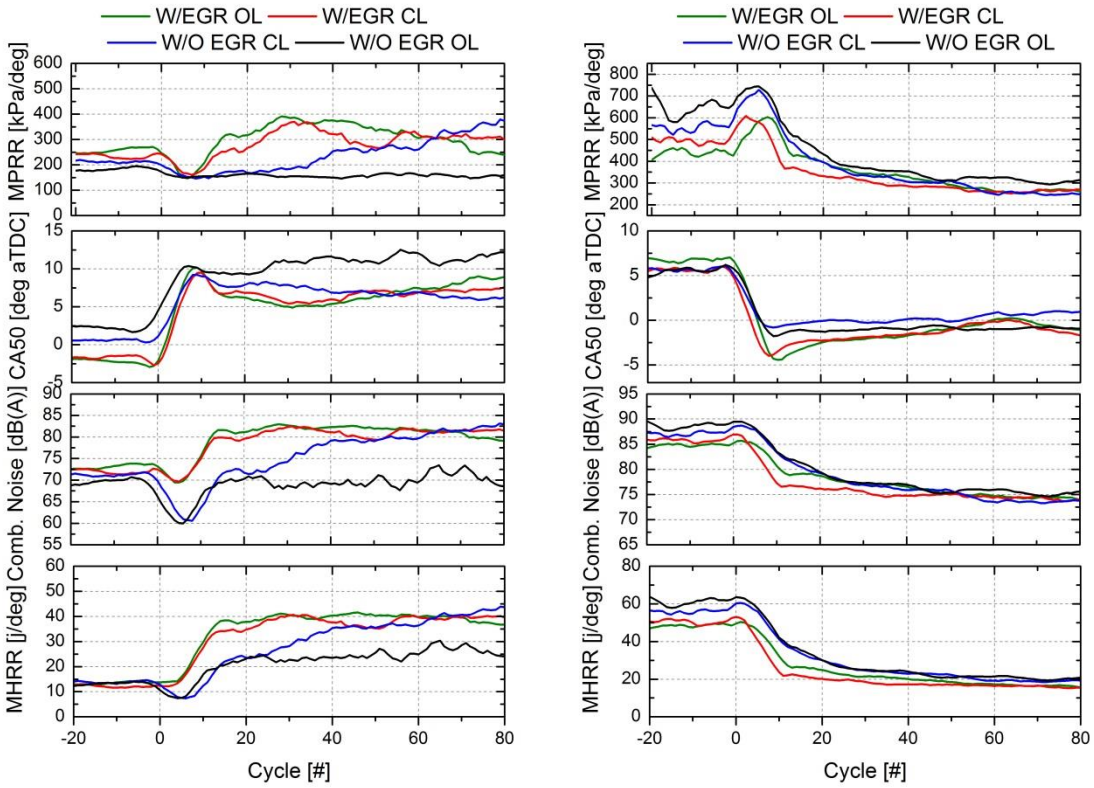

Figure 4.19 RCCI open-loop and closed-loop combustion performance

Comparing the emissions from Figure 4.13 to Figure 4.20, it can be seen that the transient RCCI emissions are different than the CDC results, by having lower NO and PM with higher HC. The closed-loop controller can be seen to improve non-EGR HC emissions over the open loop, up-load condition, to improve NO emissions during the down load test. During the up-load test the closed-loop controller lowered the PFI fraction to advance the combustion phasing and reduce HC emissions. During the down-load, the PFI fraction was increased to delay combustion phasing, which helped reduce NO emissions. The closed-loop controller acted similarly with EGR, but as can be seen, the magnitude of its response was

much lower. Overall, the HC emission was seen to increase during the up-load, and NO increased during the down-load tests.

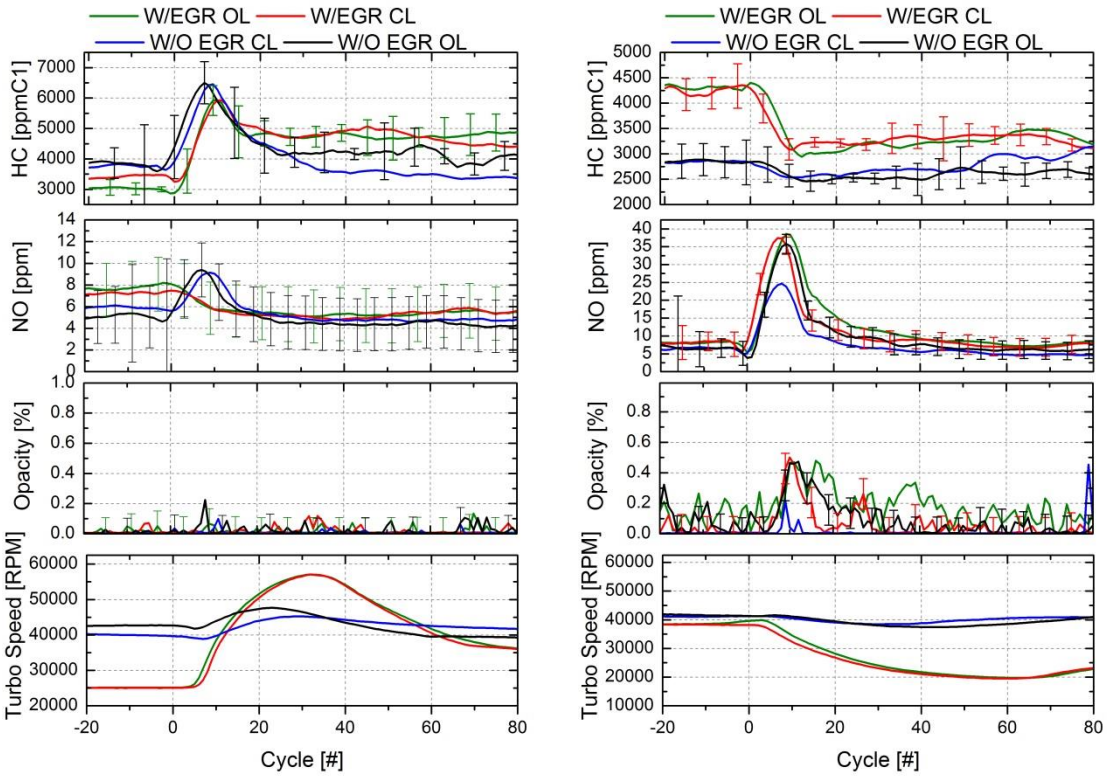

Figure 4.20 RCCI open-loop and closed-loop emissions performance

The cause for the HC spike is not entirely clear, but it may be caused by cooler combustion chamber walls from running at low load, or because of the lack of port-fuel enrichment. Cool cylinder walls typically cause RCCI to delay combustion phasing due to the resulting slower kinetic reaction rates [94, 96] and steady-state maps do not account for different wall temperatures, i.e., high load with cold wall temperatures and low loads with high wall temperatures. However, the more likely explanation for the HC spike is the lack of port-fuel enrichment during transients.

While the closed-loop controller can react to deviations from target values it cannot stop the spike in HC in the first place. This is because it is a feedback controller, which by definition, cannot account for these different boundary conditions and can only react to disturbances. One way to alleviate the HC spike would be to add feed-forward or model-based controls that anticipate the fuel being lost to the intake runner and automatically inject extra fuel to compensate. To inject additional fuel during the transient event to account for the fuel mass lost to the intake runner, various control strategies have been developed, such as Tau-X [93]. EGR lowered the HC mass emissions and the magnitude of the HC spike during the up load. No spike was seen during the down load for either case, as seen in Figure 4.21. This is a result of the higher intake temperatures and lower PFI ratio at 4 bar compared to the non-EGR case. NO increased during the down-load for both and up-load for non-EGR cases. No increased during up-load for EGR case. The Increase during the down load case is thought to be caused by additional port fuel from intake runner walls (as seen in the elevated load in Figure 4.9) combined with increased DI fueling and advanced timings (as seen in Figure 4.17). The cause of the NO increase during the non–EGR, up-load cases is unexplained as no deviations in intake pressure, EGR or fueling were seen. However, the overall magnitude (4-5ppm) is low and at the resolution of the measurement system, see Section 3.18.

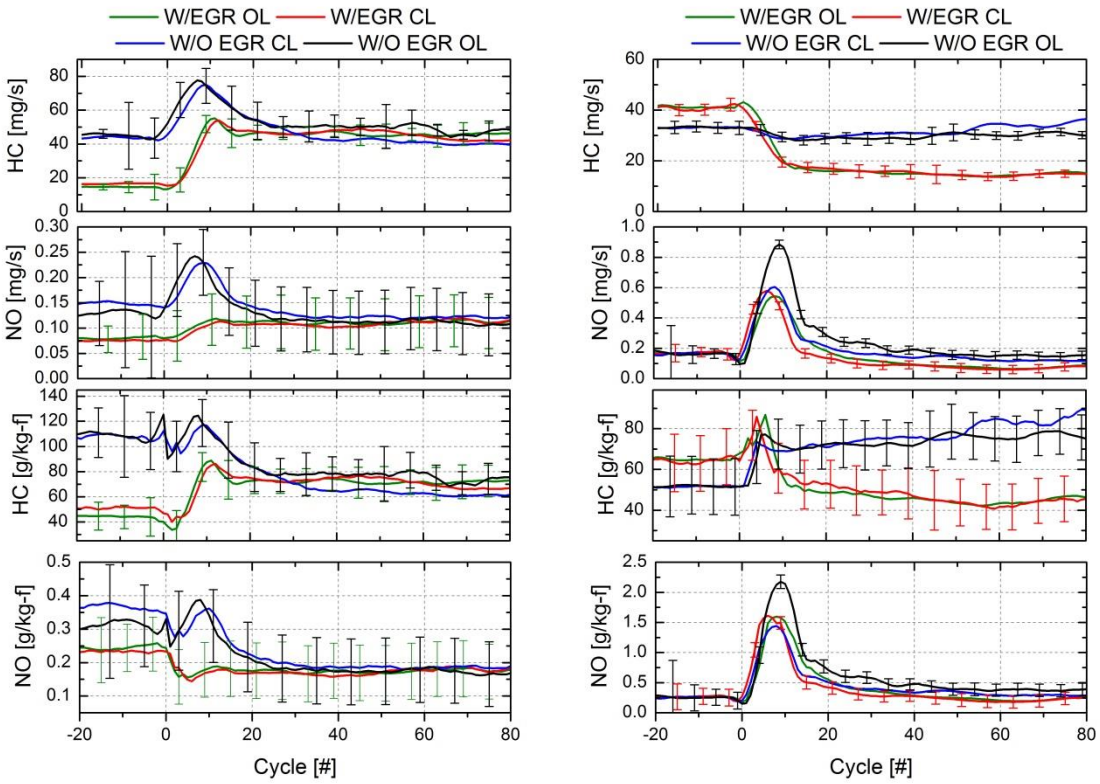

Figure 4.21 RCCI open-loop and closed-loop emissions performance

The turbocharger speed was constant for the non-EGR case as the intake pressure was kept the same for all loads, as shown in Table 4-1, Table 4-2, Table 7-3 and Table 7-4. Deviations in speed can be seen in the up and down-load results for the EGR cases due to the relatively simple control of the Drivven system. An OEM controller would likely have much better control of the turbo speed. The up-load PM was essentially zero for all RCCI cases. The down-load case exhibited a very slight increase during the NO spike but more tests would be needed since the values are near the accuracy limit of the instrument, see the Section 3.18.

4.5 RCCI Biofuel Steady-State Baseline

In this section, common biofuel blends (B20 and E20) are used to replace the EEE and ULSD that were used in the baseline steady state and transient tests. The goal was to investigate whether the RCCI combustion trends, using biofuels, seen in the ORNL steady-state cases will apply under transient operating conditions [70].

The fuels were splash blended on site using 20% by volume of soy methyl ester B100 and 80% ULSD, or 20% by volume E98 and 80% EEE. Fuel properties for the blends are taken as the linear interpolation of the base fuel and the biofuel. Fuel certificates of analysis for the base fuels are shown in the Appendix 7.6. To compare with the transient data, the engine was first calibrated at steady-state; from 1-4 bar BMEP in 1 bar increments with mixtures of E20, B20, ULSD and EEE gasoline. The G/ULSD conditions in the previous section were used as the baseline for combustion phasing. At each load, the emissions and efficiency were optimized with combustion phasing held nearly constant, and only slight changes to the EGR rate, main SOI timing and PFI ratio were made for each fuel combination. General run conditions are shown in Table 4-4, Table 4-5, Table 4-6 and Table 4-7, and detailed run conditions are shown in Appendix 7.1. Figure 4.22 - Figure 4.25 show the cylinder pressure and heat release rate for each load with the 4 fuel combinations.

Table 4-4 G/ULSD RCCI w/EGR Run Conditions

	Run 1	Run 2	Run3	Run 4
Engine Speed [rpm]	1,500	1,500	1,500	1,500
Rail Press. [bar]	371	412	453	499
Main SOI [deg. bTDC]	39.5	43	47	52
DI [mg/inj.]	3.42	3.43	2.32	2.28
PFI [mg/inj.]	2.267	4.48	8.32	10.76
Intake Pressure [bar]	1.01	1.02	1.03	1.03
Intake Temp. [°C]	78	88	75	53
PFI Fraction [%]	39.9	55.6	78.1	84.0
EGR [%]	51.5	49.5	35.5	19.51

Table 4-5 E20/ULSD RCCI w/EGR Run Conditions

	Run 1	Run 2	Run3	Run 4	Run 5
Engine Speed [rpm]	1,500	1,500	1,500	1,500	1,500
Rail Press. [bar]	392	433	482	505	531
Main SOI [deg. bTDC]	38	42.4	45.5	49.1	54.1
DI [mg/inj.]	3.64	5.52	4.59	4.86	4.89
PFI [mg/inj.]	1.85	2.62	6.03	8.3	10.58
Intake Pressure [bar]	1.0	1.01	1.03	1.02	1.08
Intake Temp. [°C]	81	91	83	57	43
PFI Fraction [%]	34.9	33.2	56.3	64.7	69.8
EGR [%]	53.4	53.3	40.9	23.9	14.3

Table 4-6 E20/B20 RCCI w/EGR Run Conditions

	Run 1	Run 2	Run3	Run 4	Run 5
Engine Speed [rpm]	1,500	1,500	1,500	1,500	1,500
Rail Press. [bar]	370	424	466	500	517
Main SOI [deg. bTDC]	41.3	43.6	47.3	52.2	55.3
DI [mg/inj.]	3.08	3.33	3.71	3.36	3.44
PFI [mg/inj.]	3.31	4.99	7.72	10.3	12.9
Intake Pressure [bar]	1.01	1.02	1.02	1.02	1.05
Intake Temp. [°C]	79	86	75	55	43
PFI Fraction [%]	50	60.2	69.1	75.3	78.1
EGR [%]	51.55	47.9	34.8	19.9	11.9

Table 4-7 G/B20 RCCI w/EGR Run Conditions

	Run 1	Run 2	Run3	Run 4
Engine Speed [rpm]	1,500	1,500	1,500	1,500
Rail Press. [bar]	388	418	432	495
Main SOI [deg. bTDC]	43.4	45.2	47.3	52.2
DI [mg/inj.]	2.92	3.49	2.43	1.62
PFI [mg/inj.]	4.1	4.8	7.13	9.84
Intake Pressure [bar]	1.01	1.02	1.03	1.03
Intake Temp. [°C]	82.5	85.5	87.1	56.4
PFI Fraction [%]	46.8	57.1	70.3	86.6
EGR [%]	51.4	49	43.7	18.7

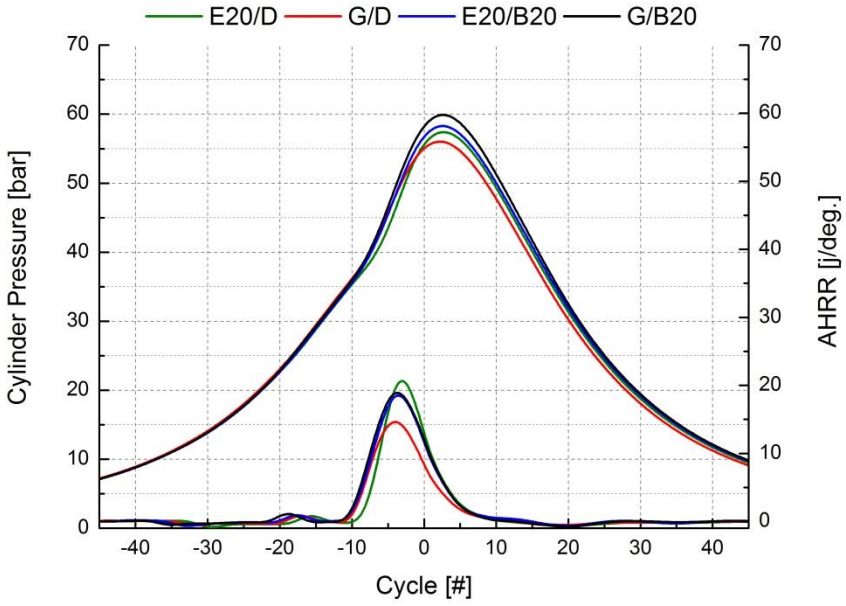

Figure 4.22 1 bar BMEP biofuel cylinder pressure and apparent heat release rates

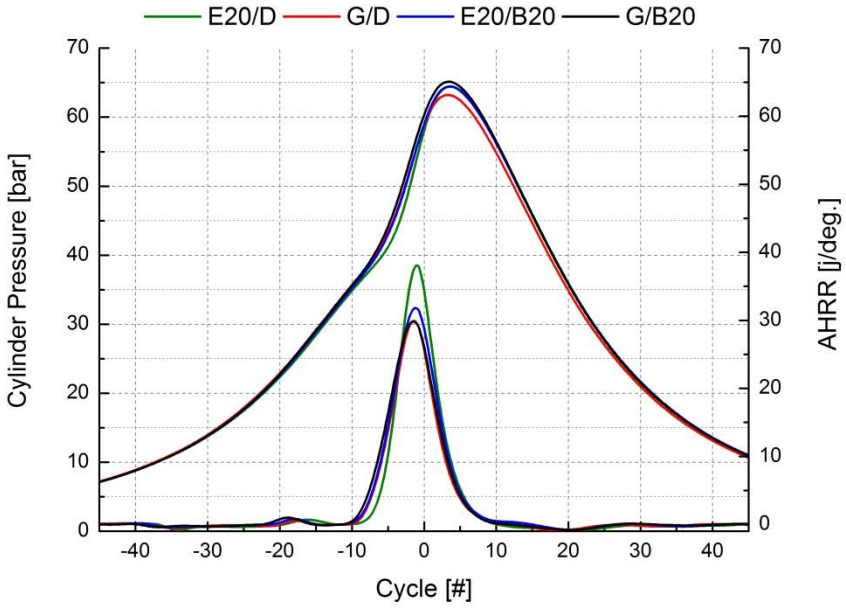

Figure 4.23 2 bar BMEP biofuel cylinder pressure and apparent heat release rates

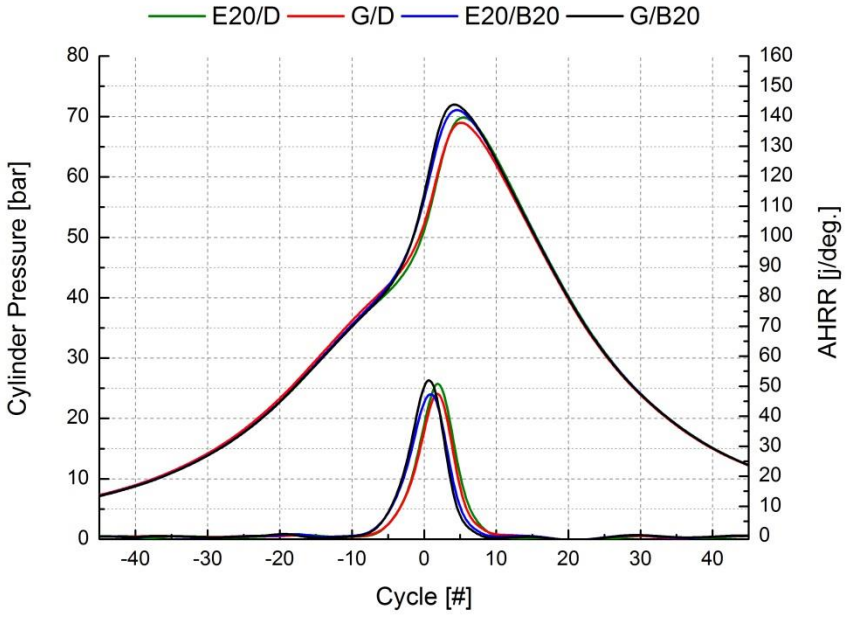

Figure 4.24 3 bar BMEP biofuel cylinder pressure and apparent heat release rates

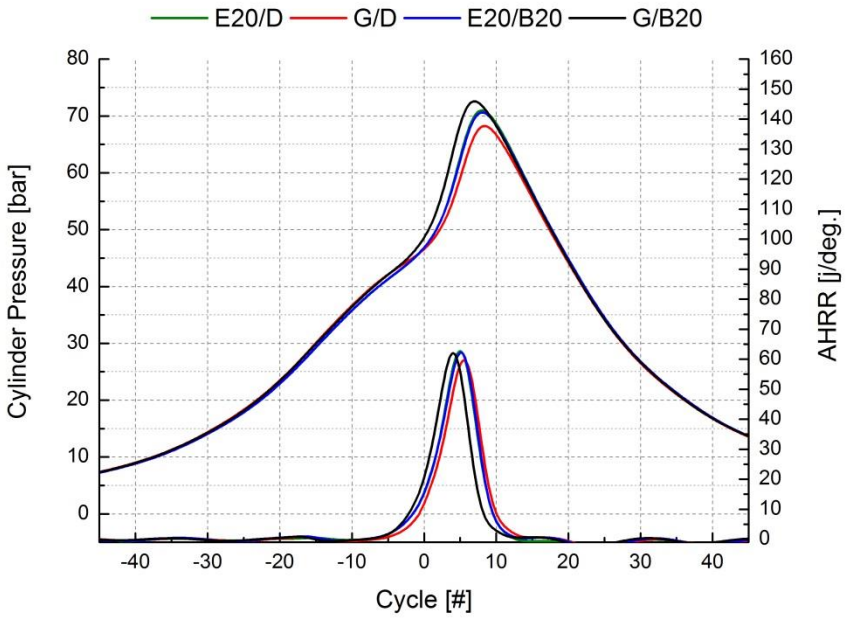

Figure 4.25 4 bar BMEP biofuel cylinder pressure and apparent heat release rates

Figure 4.26 shows the inlet conditions for the different fuel combinations, which were held roughly constant between the different fuels to provide a level comparison. The mass air flow, intake pressure and PFI ratio are seen to increase with load as the EGR level decreases. EGR drops with load as intake conditions require lower inlet temperatures to phase combustion after TDC. A more effective EGR cooler or a low pressure EGR system could increase the amount of EGR that could be tolerated at 3 and 4 bar BMEP by lowering the EGR temperature. The increased PFI fraction is also needed to delay the combustion phasing and to reduce the combustion noise with the elevated intake temperatures.

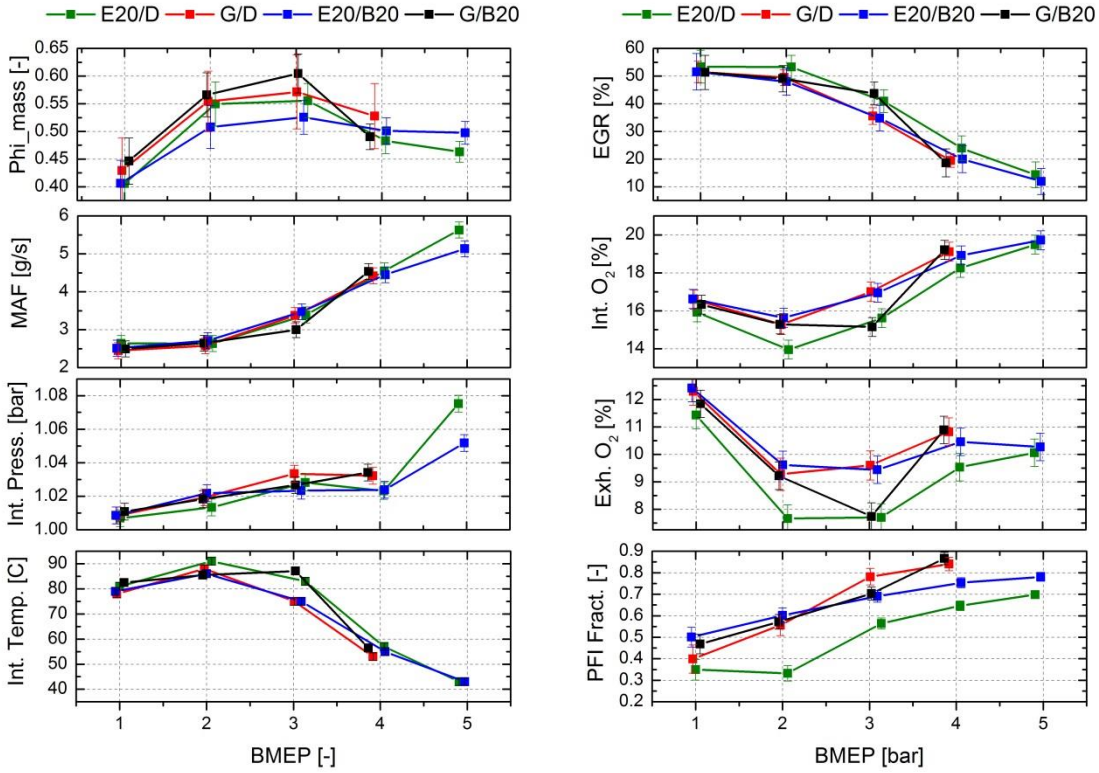

Figure 4.26 General run conditions for the four biofuel combinations

The G/B20 test had 5% higher EGR at 3 bar than the other runs. This lowered the PFI ratio slightly. For the E20/B20 and G/B20 cases, there was a higher PFI fraction over the ULSD baseline. The higher PFI ratio was needed to retard combustion phasing due to the high reactivity (i.e., 48 CN) of B20 compared to ULSD (46 CN). This was not seen in the ORNL data as the CN of that biodiesel was the same as the ULSD [70].

Figure 4.27 shows the emissions results and combustion metrics for the biofuel cases. As with the ORNL experiments, CO and HC emissions drop with load as the combustion temperature increases [70]. HC emissions can be seen to

increase with the EEE fuel blends at 3 and 4 bar BMEP due to the higher PFI ratio, where HC emissions more correlated to unburned fuel originating from the top ring-land crevice. NO increases with load as there was less EGR and dilution, causing higher combustion temperatures. Having a higher efficiency turbocharger would help lower NO at this operating condition due to the higher EGR and intake pressure that could be delivered with minimal impact on the pumping work. CO_2 emissions were lower with the biofuel blends as expected, because the efficiency is high and they have a higher H/C ratio than the petroleum fuels. CA50 delays with load for combustion noise control. The attempt to keep combustion noise low was seen in MPRR which was kept below 6 bar/deg. for all the cases. Keeping the combustion noise low is also very difficult as the MHRR increases with load are directly related to the total fueling amount. Above 5 bar BMEP, additional dilution from higher intake pressure and/or EGR will be needed to continually phase combustion later.

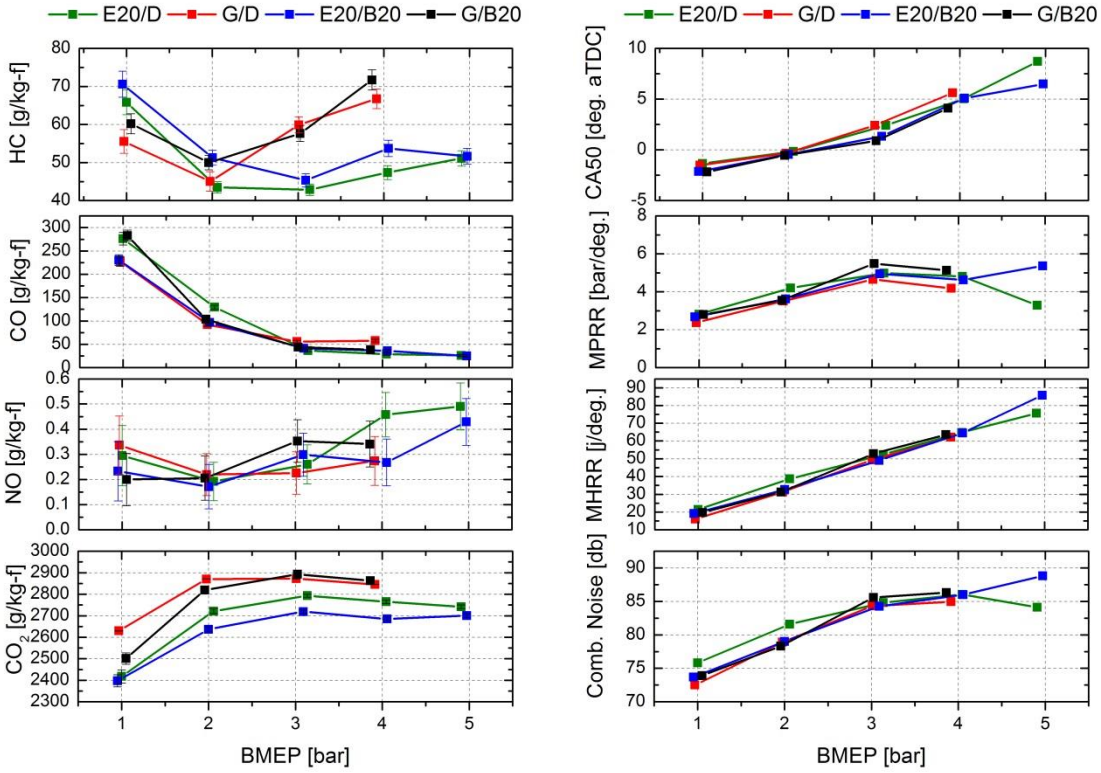

Figure 4.27 Emissions and combustion performance results of the biofuel tests

Figure 4.28 shows the fuel efficiency and a first law energy break down for the biofuel tests. As can be seen, the BTE and fuel energy increase with load. BTE increases with load as friction becomes a smaller fraction of the loss from GTE to BTE. Similarly, BSFC reduces with load, but was slightly higher for the biofuels as they have lower heating value.

Combustion efficiency is seen to increases with increased load and combustion temperature. Pumping losses reduce as the turbocharger becomes more efficient and less EGR is needed. With less EGR, more energy leaves the system out the exhaust, rather than becoming lost through the cooling system.

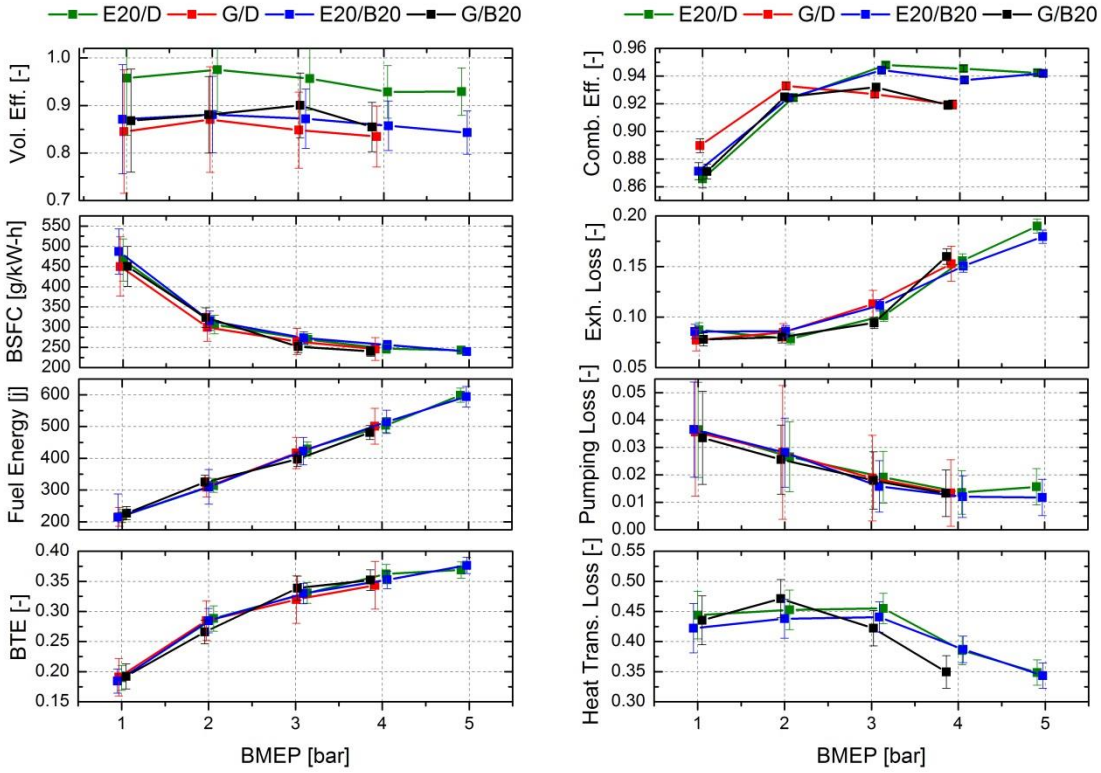

Figure 4.28 Fuel consumption and first law analysis for the biofuel tests

4.6 RCCI Biofuel Up-load Transient Tests

Using the steady-state operating conditions, the engine was operated in a step-load transient by a change in the commanded pedal position, similar to the baseline gasoline/diesel tests. Figure 4.29 shows the load performance for the biofuels with closed-loop controls. Other tests were taken with open-loop control but, for brevity, they are placed in Appendix 7.1 as the differences between open-loop and closed-loop were small.

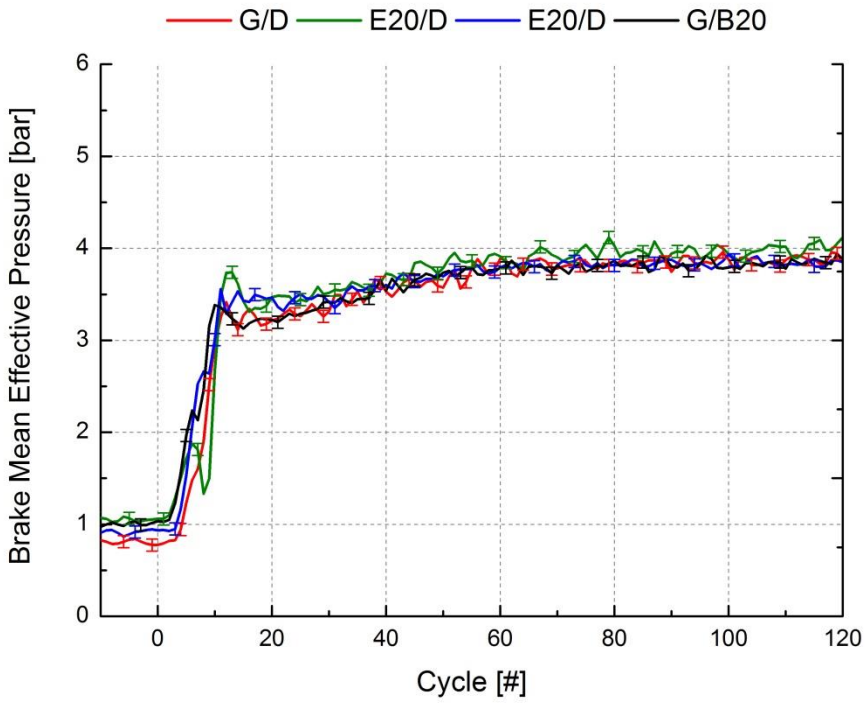

Figure 4.29 BMEP for the biofuel runs during the up-load transient test

Figure 4.30 shows the emissions results of the biofuel tests. As can be seen, HC emissions were lower for the ethanol fuel blends. The steady state tests showed that the ethanol blends had a lower PFI fraction than the EEE tests. The E20 tests were also seen to have a smaller HC spike around cycle 10. The lower PFI fraction seen during the E20 tests was less affected by manifold wall wetting effects likely seen with the gasoline blends as more of the total fuel reached the combustion chamber. NO was roughly constant during the test, except for the E20/D case, which had a large increase in NO around cycle 10. When operating with E20, the combustion phasing was more unstable, as seen in the higher CoV of MPRR, as shown in Figure 4.31.

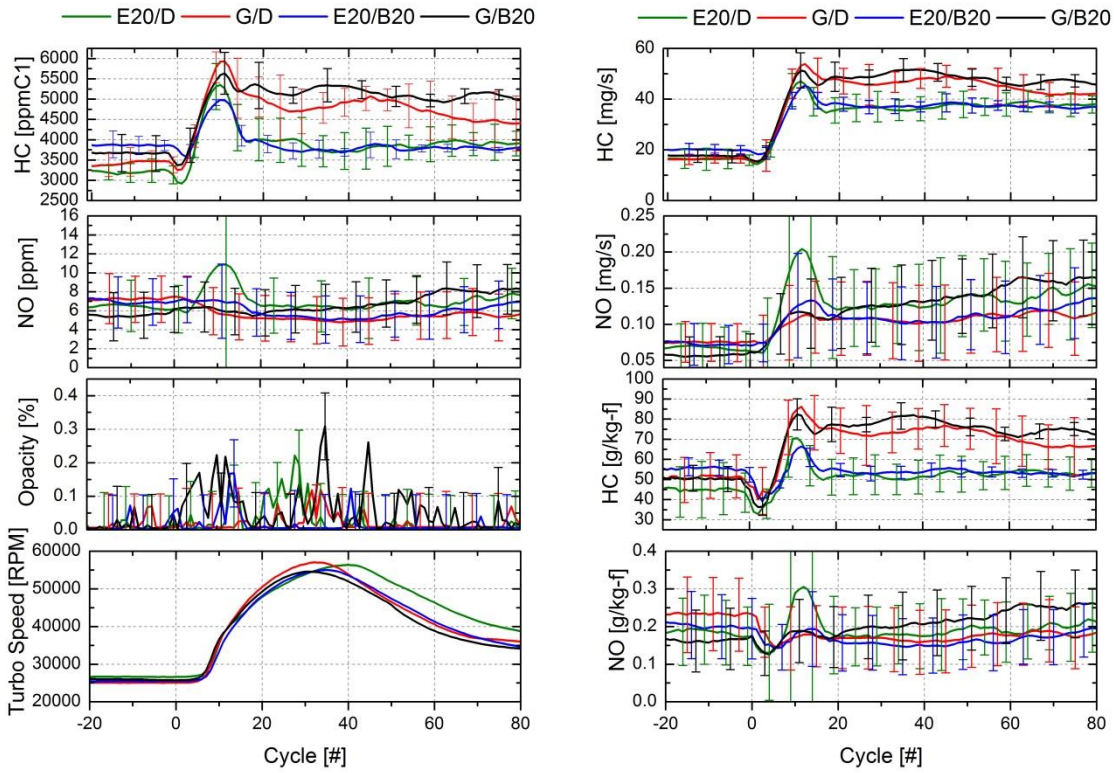

Figure 4.30 Emissions results for the up-load biofuel RCCI tests

Reduced combustion stability became evident when the dynamometer system control could not control the engine speed as accurately as when the combustion stability was higher. The higher engine speed changes seen for E20 cause the engine to operate in areas of the map where the calibration was not optimal, causing increased NO. PM (i.e., Opacity) for all of the biofuels was unaffected by the transient behavior. Closed-loop control offered better performance for HC and control of CA50 during the transient, which can be seen compared to the open-loop tests in Appendix 7.1.

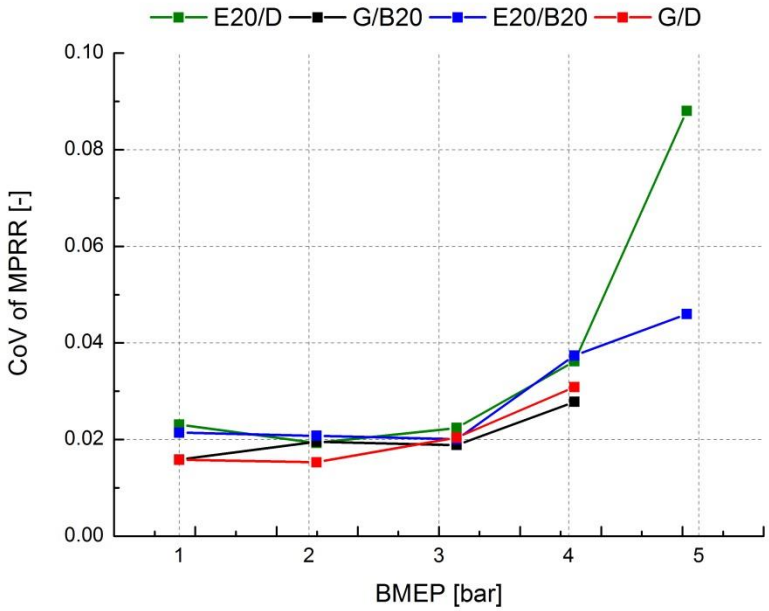

Figure 4.31 CoV of MPRR for the biofuel tests

Figure 4.32 shows the fueling and overall intake conditions for the biofuel RCCI results. The intake pressure can be seen to follow the turbo speed with a slight overshoot of the target pressure around cycle 30. The overshoot in turbocharger speed caused a slightly higher than desired intake pressure due to the slow response of the VGT vane position.

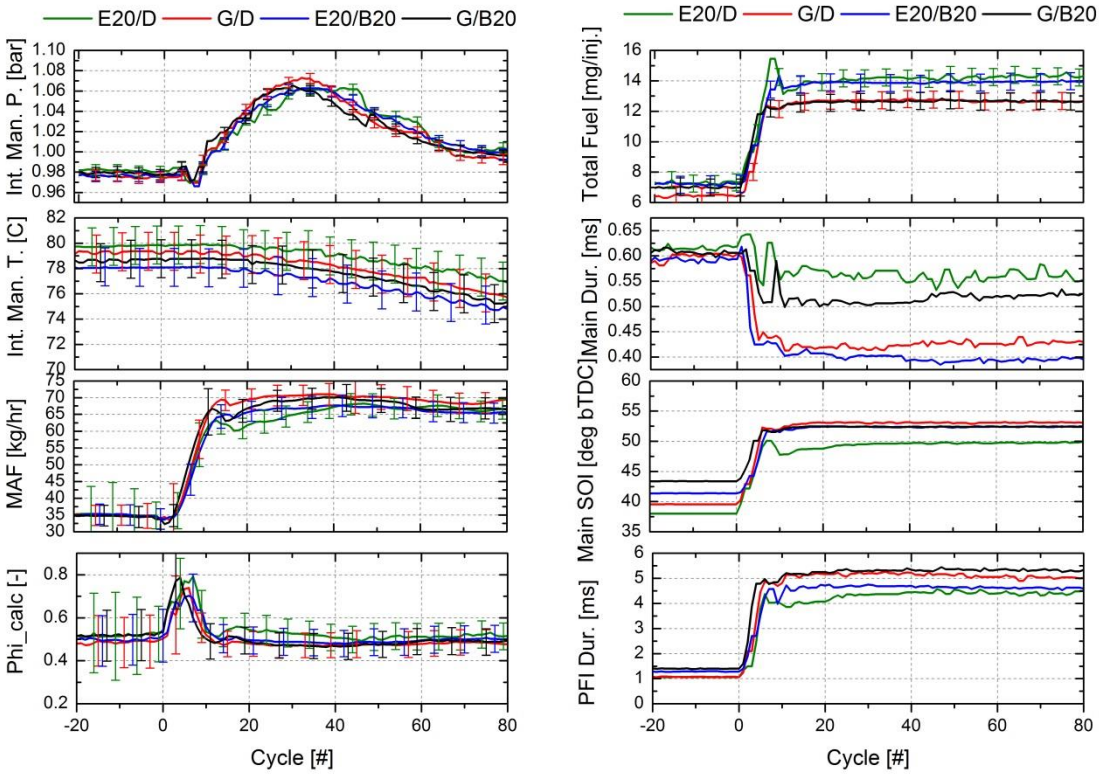

Figure 4.32 Intake and fueling conditions for the biofuel up-load tests

The intake manifold temperatures start high, as the 1 bar condition has high EGR levels, and then drop with decreased levels of EGR, as seen in Figure 4.33. The difference in the PFI ratio of the E20 fuel tests can be seen in the higher main injection duration and lower PFI injection commands. E20 blends also have an increased total fueling due to the lower heating value and the resulting higher injected mass. The slight turbo lag can also be seen in Figure 4.32 where Phi increases for the first 10 cycles before the intake pressure increases. This matches the delay when the turbo speed begins to change, which also occurred around cycle 10, as shown in Figure 4.30.

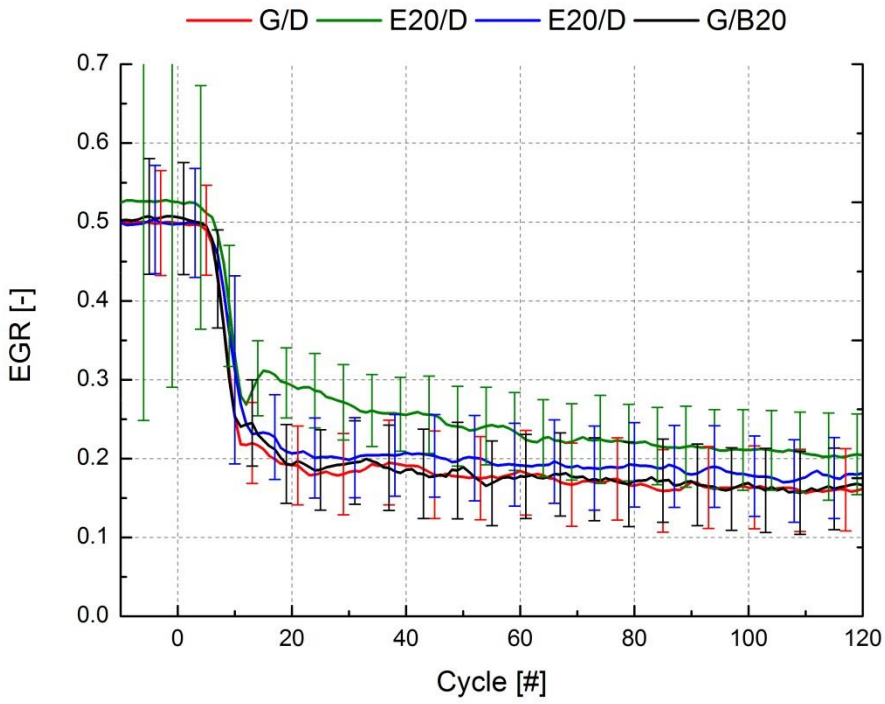

Figure 4.33 EGR response for the up-load RCCI biofuel tests

Figure 4.34 shows combustion and performance metrics for additional run conditions for the up-load RCCI tests. Here, the engine speed deviation for E20 which caused the NO spike can be seen. Otherwise, the intake and exhaust O_2, and the rail pressure follow the steady state values. It can also be seen that the G/D test was much slower to respond to the steady-state value for CA50. Compared to the open-loop tests (shown in Appendix 7.1), the closed-loop control offered faster response to the target steady state values. Interestingly, the G/B20 transient performance was much faster to the CA50 set point. It is unclear as to why this happened, but it is possibly that the higher reactivity offered by the B20 increased the response to the operating condition change.

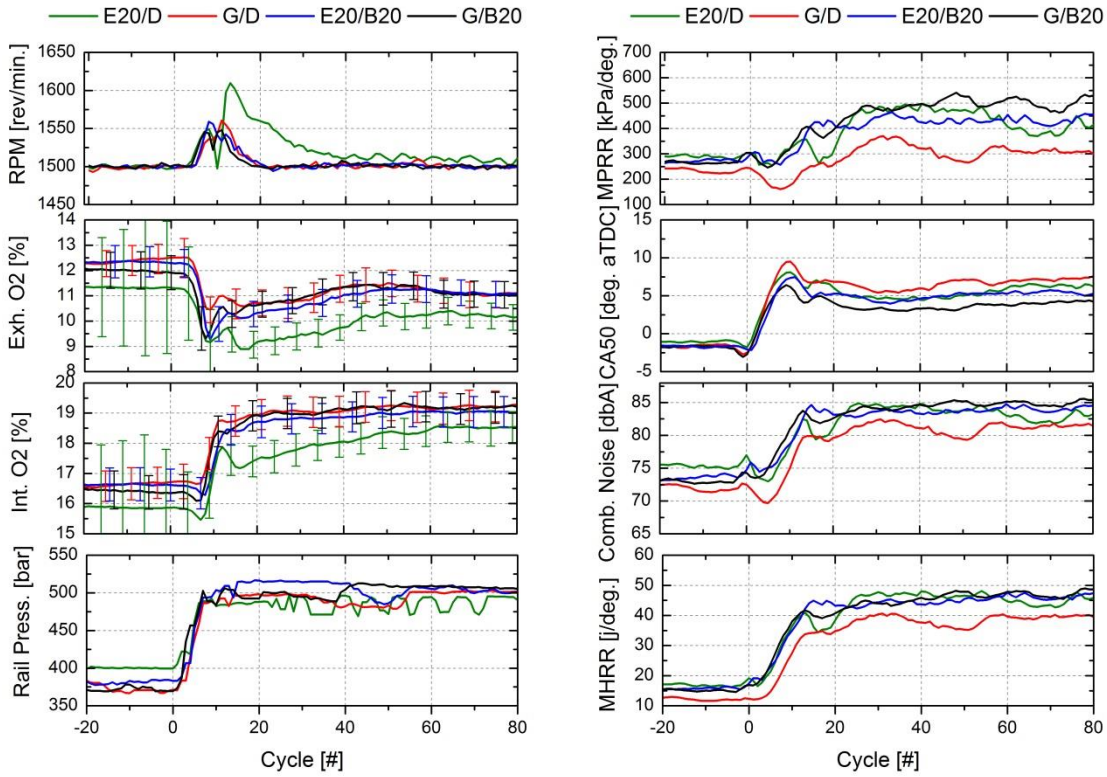

Figure 4.34 Combustion and performance results for the RCCI up-load biofuel tests

4.7 RCCI Biofuel Down-Load Tests

Similar to the baseline RCCI tests, down-load step change tests were performed for the biofuels in the RCCI combustion mode. Figure 4.35 shows the down-load response for the fuels. As can be seen, the load response was much slower that the up-load case, taking 20-40 cycles longer to reach the final value. Additionally, the “missing” fuel from the up-load test can be seen in the elevated load up to cycle 100. For the down-load transients, aggressive temporary fuel cutting could be employed to bring the load to the target value quicker, whereas

with the up-load there needs to be extra fuel added to bring the load response closer to that of CDC.

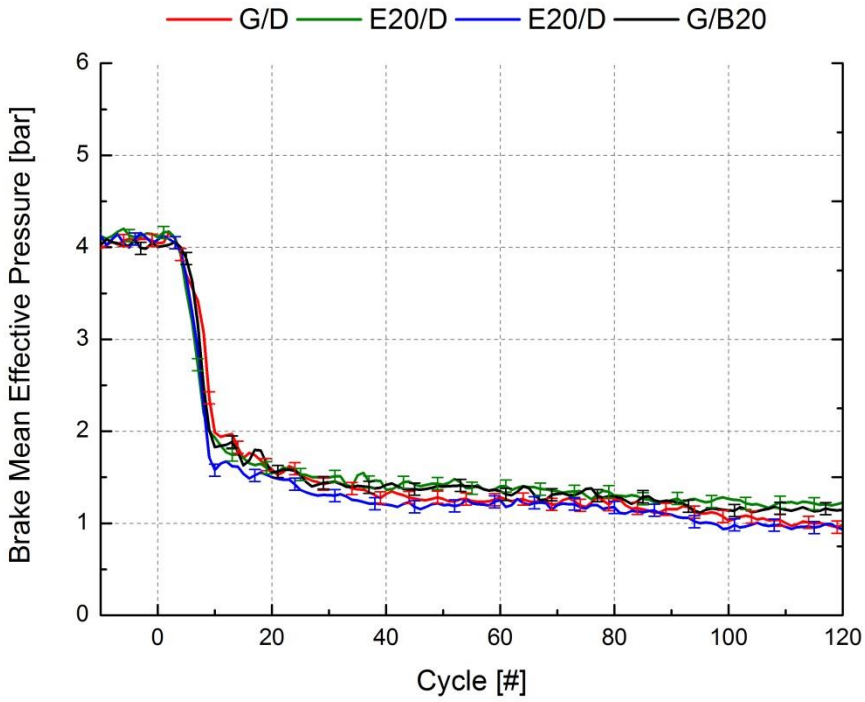

Figure 4.35 BMEP values for the down-load RCCI biofuel tests

Figure 4.36 shows the emissions results for the down-load tests. HC emissions are seen to decrease as the EGR rate increased and the PFI fraction decreases. The most interesting finding of the down-load tests was the NO spike seen for all the fuels. The NO increase seems to be caused by a combination of factors. As seen in Figure 4.35, there was almost 0.5 bar extra load for nearly 40 cycles. This load increase is thought to come from the fuel that was on the intake manifold runner walls. The additional port fuel combined with the earlier DI SOI timings and increased DI fueling can be seen in the advanced CA50 and higher

MPRR, as shown in Figure 4.36. Additionally, there is a delay in EGR for the first 25 cycles, as seen in Figure 4.37.

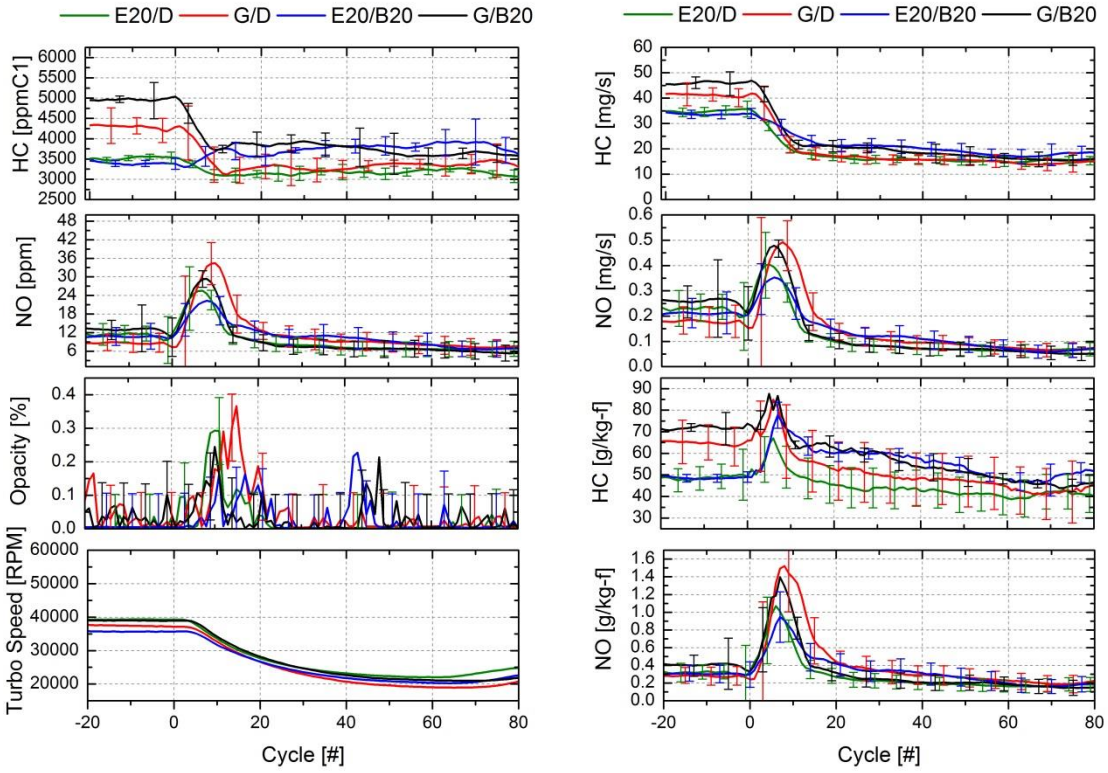

Figure 4.36 Emissions results from the down-load RCCI biofuel tests

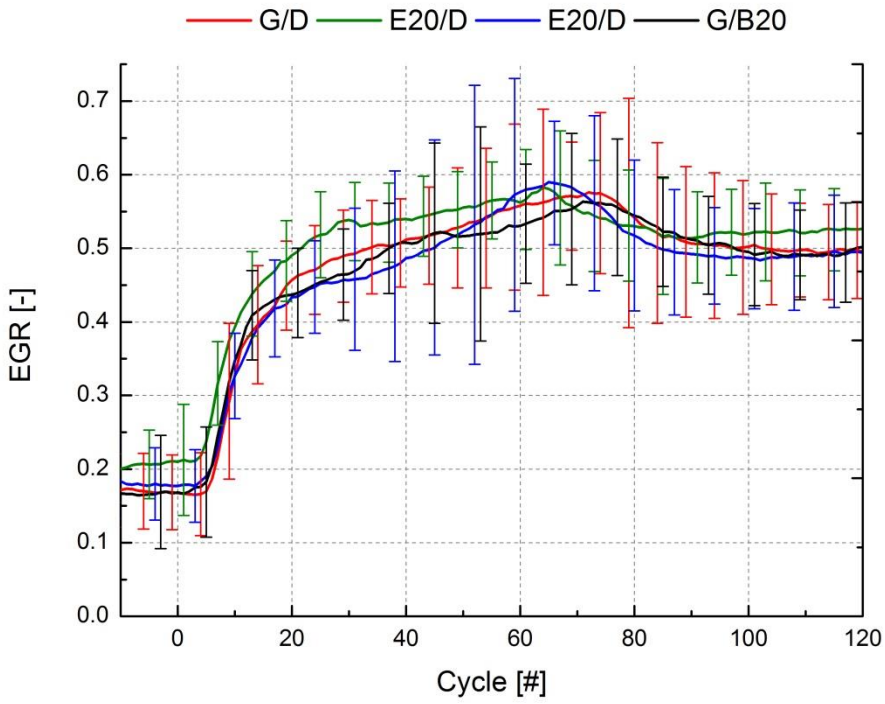

Figure 4.37 EGR response for the down-load RCCI biofuel tests

Intake and fueling parameters are shown in Figure 4.38. Similar to the up-load tests, the total fueling was higher for the E20 tests. The intake temperature is lower than the steady state values as higher loads have less EGR, so the lower intake temperature persists until cycle 80. The intake pressure was better controlled than for the up-load transient with no significant deviation from the steady state value. A slight dip in Phi where the EGR lagged can be seen around cycle 5-10.

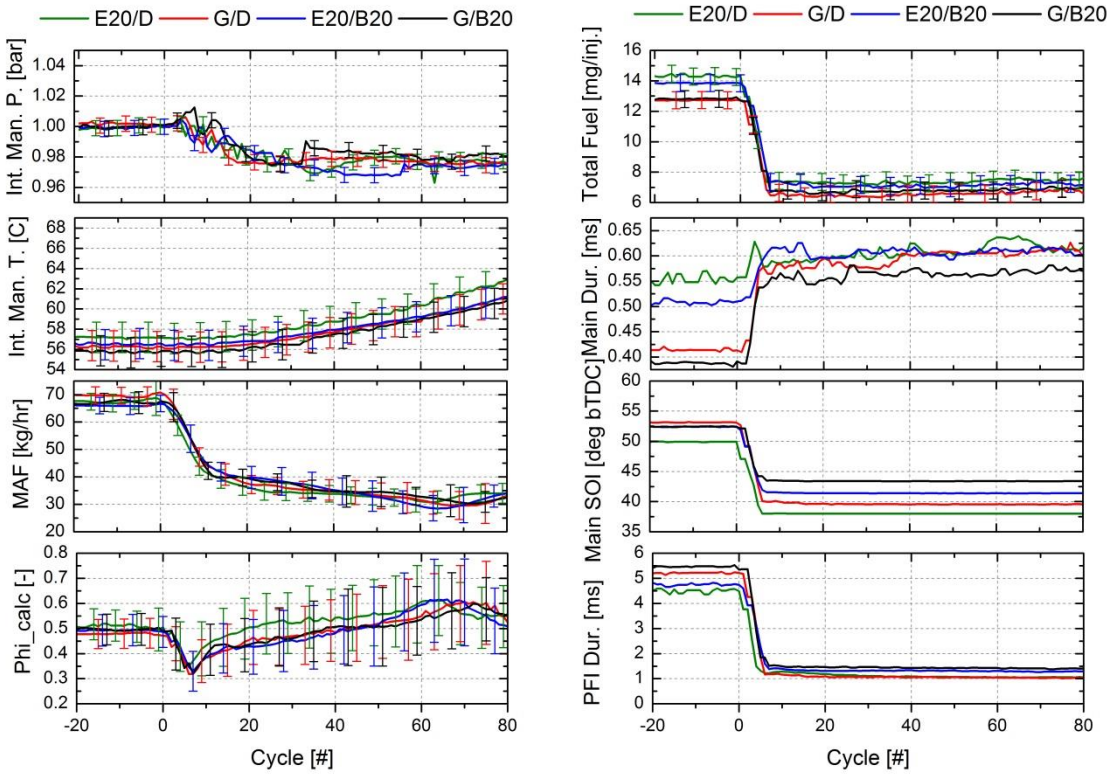

Figure 4.38 Intake and fueling conditions for the up-load biofuel tests

Finally, Figure 4.39 shows the combustion performance and run conditions for the down-load tests. There were not many significant deviations from the steady-state values. Similar to the up-load tests, the engine speed control difficulties seen for E20 were still present for the down-load test. However, this did not affect the NO emissions, as was seen with the up-load test. The only other deviation from steady state was the slight increase in MPRR at cycle 5-10. This rise in MPRR coincides with the EGR dip and NO spike at cycle 10. Here the extra fuel can be seen to increase the MPRR for a few cycles until the EGR builds up to the desired level near cycle 20.

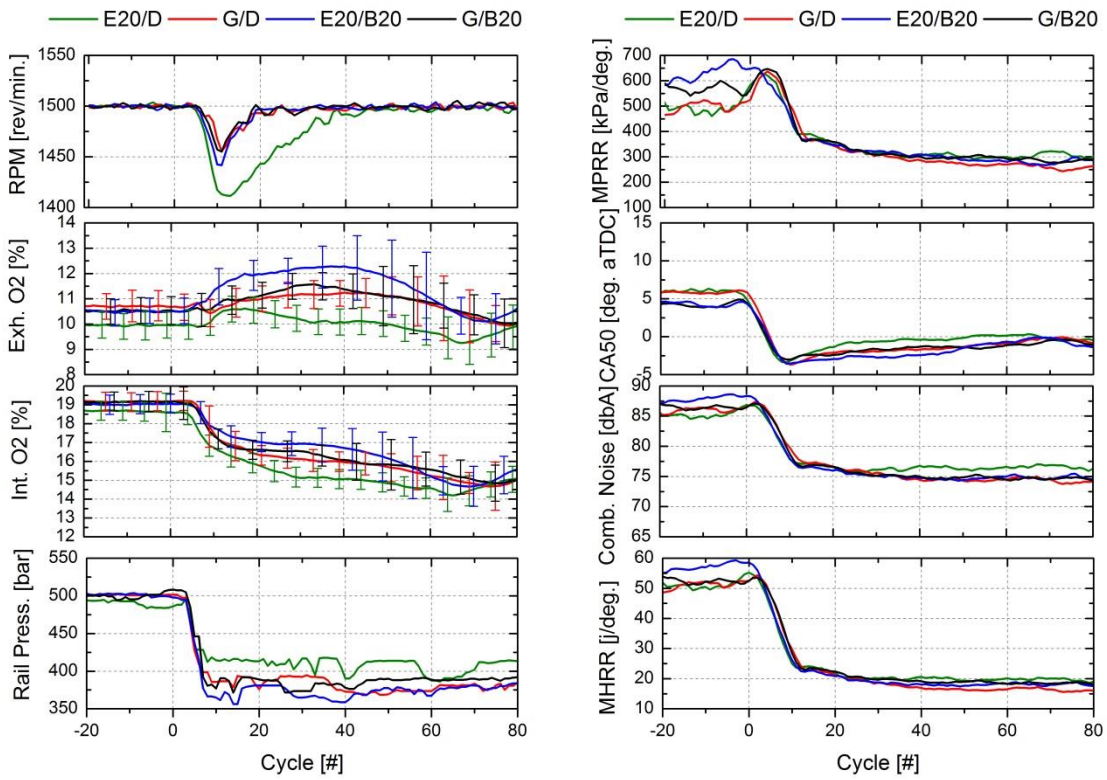

Figure 4.39 Combustion and performance results for the down-load RCCI biofuel tests

4.8 CDC and RCCI Engine Speed Steady-State Baseline

Similar to the load-step tests, transient tests investigating how the engine responds to step-speed changes were performed to determine how the combustion system would respond to real-world conditions. For the speed tests, a step change in pedal position was given (the same as the step-load tests) but the dyno was set to keep torque constant, thus increasing the engine speed. Steady-state operating condition measurements were taken from 1,000 to 2,000 rev/min in 250 rev/min increments so as to compare with the load transient tests, and the results are shown in Table 4-8 and Table 4-9, with the detailed run conditions shown in Appendix 7.7.

Table 4-8 RCCI Run Conditions

	Run 1	Run 2	Run3	Run 4	Run 5
Engine Speed [rpm]	1,000	1,250	1,500	1,750	2,000
DI [mg/inj.]	2.07	2.82	3.33	3.24	3.91
PFI [mg/inj.]	6.65	5.83	4.81	3.59	3.34
Rail Press. [bar]	336	401	418	414	412
PFI Fraction [%]	78	64	58	55	48
Main SOI [deg. bTDC]	35	44	44	45	46
Intake Press. [bar]	1.03	1.02	1.03	1.03	1.03
Intake Temp. [°C]	50	61	82	90	91
EGR [%]	19	33	44	47	45

Table 4-9 CDC Run Conditions

	Run 1	Run 2	Run3	Run 4	Run 5
Engine Speed [rpm]	1,000	1,250	1,500	1,750	2,000
DI [mg/inj.]	7.34	7.15	7.78	8.61	9.34
PFI [mg/inj.]	0	0	0	0	0
Rail Press. [bar]	433	469	507	606	517
Main SOI [deg. bTDC]	-3	-0.3	0	1	1
Pilot advance [ms]	1.1	1.1	1.1	1.09	0.822
Pilot fraction [%]	8.53	8.77	8.67	8.49	8.43
Intake Press. [bar]	1.04	1.03	1.075	1.12	1.17
Intake Temp. [°C]	79	86	75	55	43
EGR [%]	13.8	21.6	26.8	26.8	26

Figure 4.40 shows the intake and fueling commands for both the CDC and RCCI step-speed change tests. The baseline operating conditions for RCCI, including the intake temperature and pressure, EGR rate and rail pressure were chosen using conditions from Refs. [1-9]. The CDC values were Drivven's approximation of the OEM EURO IV calibration using a pilot and main injection strategy. These CDC values were used as the starting point for the RCCI calibration and then modified to meet emissions targets and to provide the highest BTE. The emissions targets for RCCI were NO <10ppm, FSN <0.1, with BTE near CDC levels and MPRR <10 bar/deg. Using these metrics and emissions targets, the intake pressures were set lower than CDC to minimize pumping work, as less intake pressure is needed for RCCI to achieve low NO and PM emissions. Similarly, lower rail pressure was needed as much earlier SOI timings are used, and less rail pressure was needed to avoid cylinder wall impingement. Finally, the PFI fraction was set to bring the combustion phasing (i.e., CA50) to the desired value.

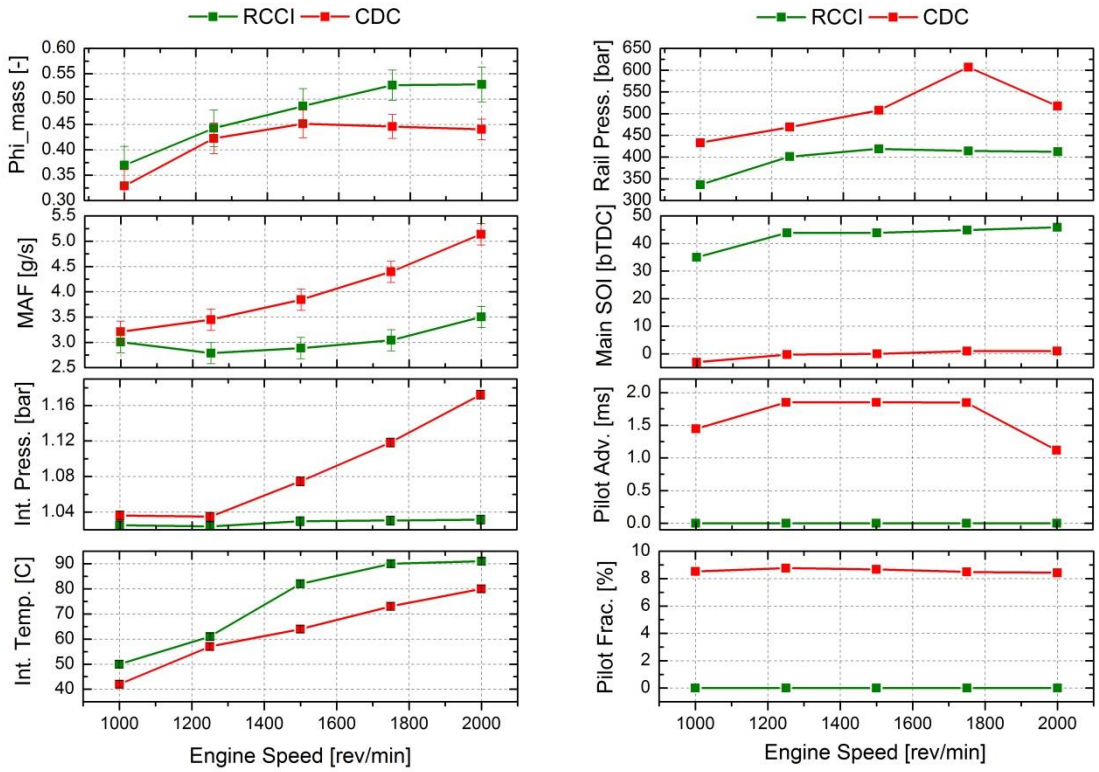

Figure 4.40 Intake and fueling commands for RCCI and CDC step-speed change tests

The combustion results for both combustion modes are shown in Figure 4.41. As can be seen, the combustion phasing was near TDC for all the RCCI cases and near -15 deg. aTDC for the CDC runs. It can be seen that while the MPRR for RCCI is higher and closer to TDC the combustion noise is lower, due to the lower peak heat release rate. However, at 2,000 rev/min, the noise for both runs converges, with RCCI likely getting louder with further increasing engine speed. Regardless, the MPRR for all cases was less than 4.0 bar/deg. and combustion noise was less than 90 dB.

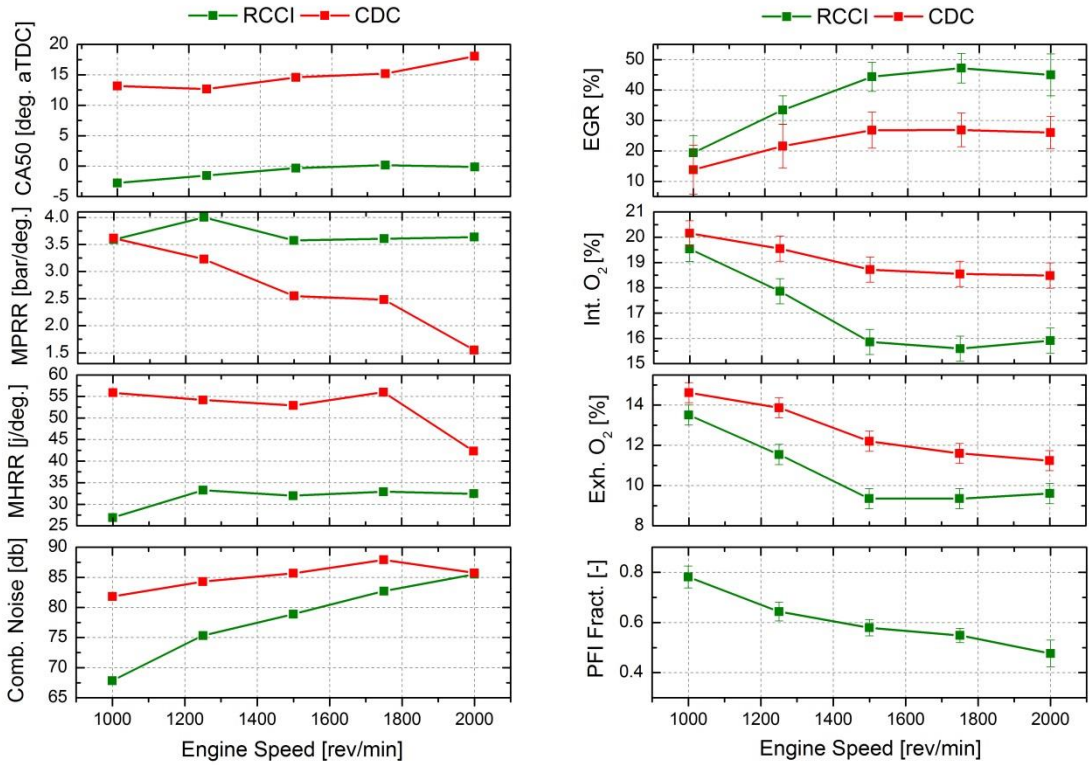

Figure 4.41 Combustion performance results for RCCI and CDC step-speed change tests

EGR was used for both combustion modes, with RCCI employing significantly more as it is more tolerant to the extra dilution and there is no PM trade off with higher EGR levels. The higher resulting intake temperatures aid in decreasing HC emissions for RCCI. The PFI fraction is seen to decrease with engine speed as more reactive fuel is needed to increase the reaction rate due to less residence time being available at higher speeds. The RCCI and CDC steady state operating point's cylinder pressure and AHRR are shown in Figure 4.42 and Figure 4.43.

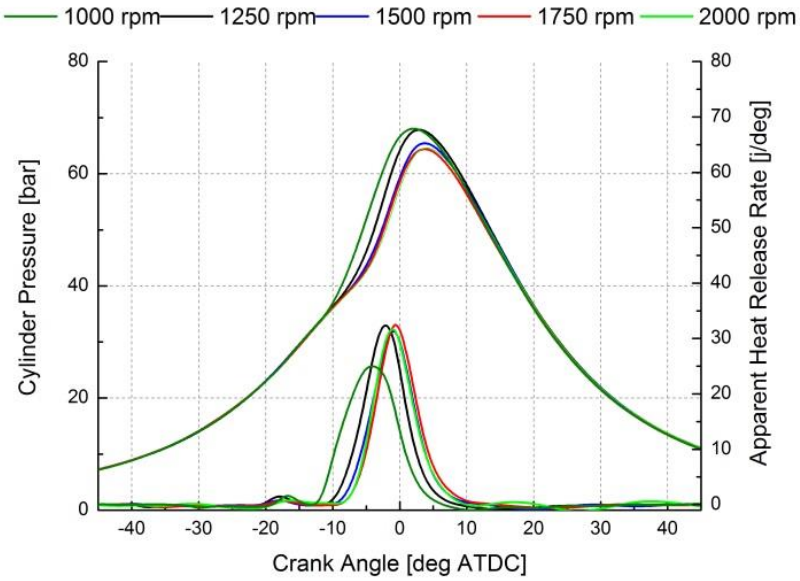

Figure 4.42 RCCI cylinder pressure and apparent heat release rate for the steady state speed sweep cases

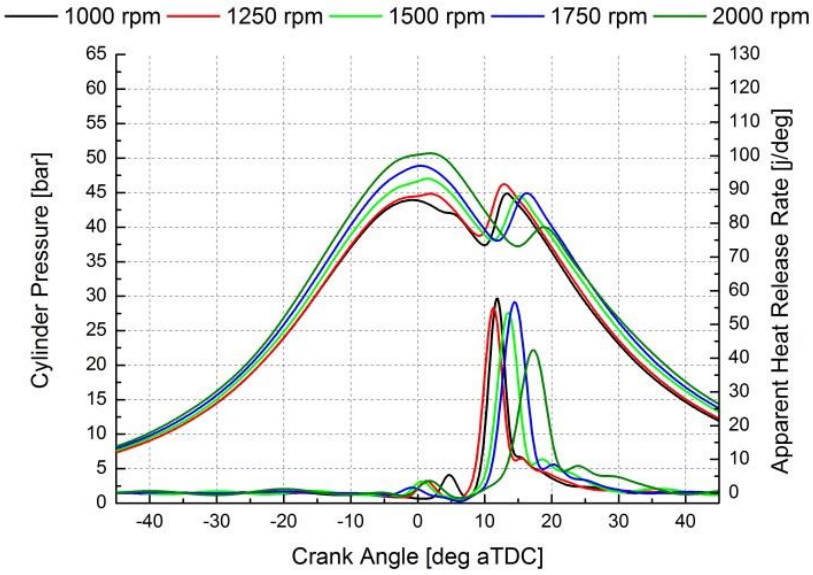

Figure 4.43 CDC cylinder pressure and apparent heat release rate for the steady state speed sweep cases

Emissions results, shown in Figure 4.44, for the RCCI cases are also typical of previous SCE and MCE engine results, where NO and PM are near zero and HC is higher than CDC. NO did not meet the 10 ppm target at 1,000 rpm for RCCI due to the early combustion phasing and lower EGR rate. High HC with RCCI levels likely result from using the stock piston geometry with its large top ring-land crevices [97].

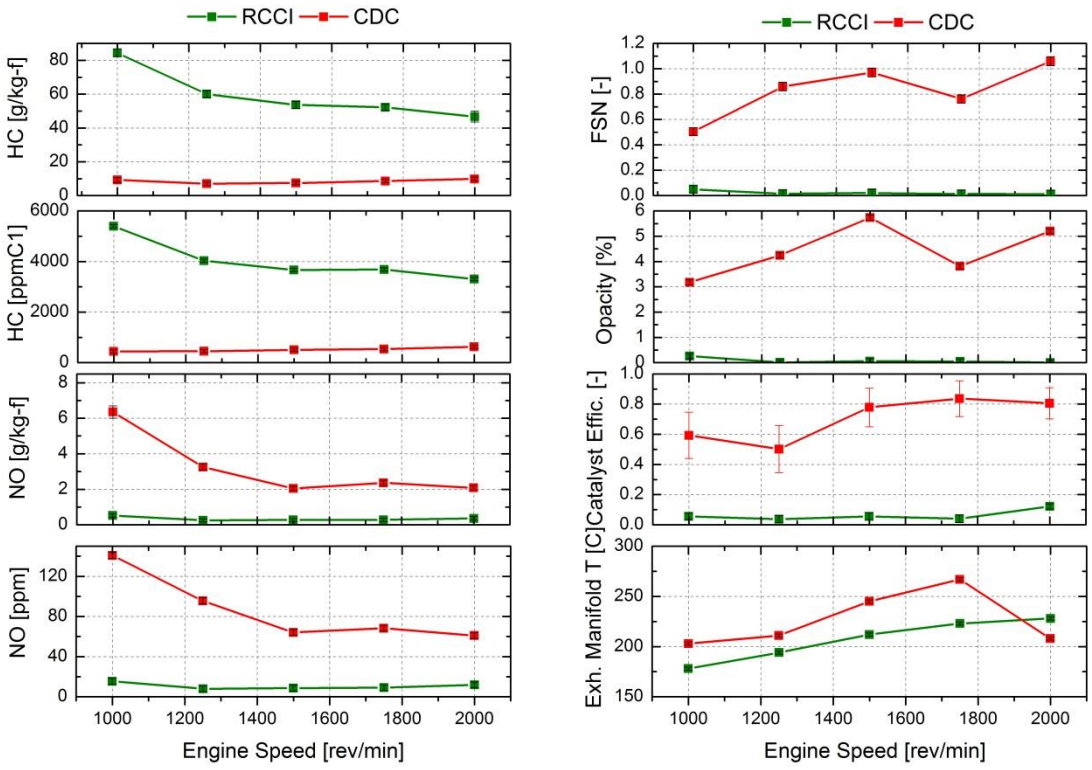

Figure 4.44 Emissions results for RCCI and CDC step-speed change tests

Emissions results from the CDC steady state tests are shown in Figure 4.44 and are typical of those of a light-duty diesel engine. HC emissions are low with the PM and NO emissions being higher than RCCI. Moderate high pressure EGR was

used for NO control for the EURO IV calibration. The moderate rail pressure and use of a single pilot injection, shown in Figure 4.40, are also typical of a EURO IV calibration.

4.9 CDC Speed Transient

Figure 4.45 shows the fueling commands for CDC during the engine speed step change. As expected for CDC, the start of injection timings were near TDC with injection pressure increasing to the final set point following the pedal command. The increase in fueling seen near cycle 20 was required to create a net torque on the crankshaft and caused the engine to accelerate. This load increase happens because the dyno and engine controller do not communicate, thus the dyno can only respond to the engine torque. The additional injected fuel can be seen in Figure 4.46 where the BMEP had to increase to nearly 3 bar before the engine began to change speed. Similarly, to slow the engine speed, the ECU cuts fueling below the steady-state value and thus allows the engine to decrease speed. This can be seen in the fact that the GMEP is roughly equal to the BMEP. The difference in friction between high and low engine speeds can also be seen as higher GMEP is needed at higher engine speed for same BMEP.

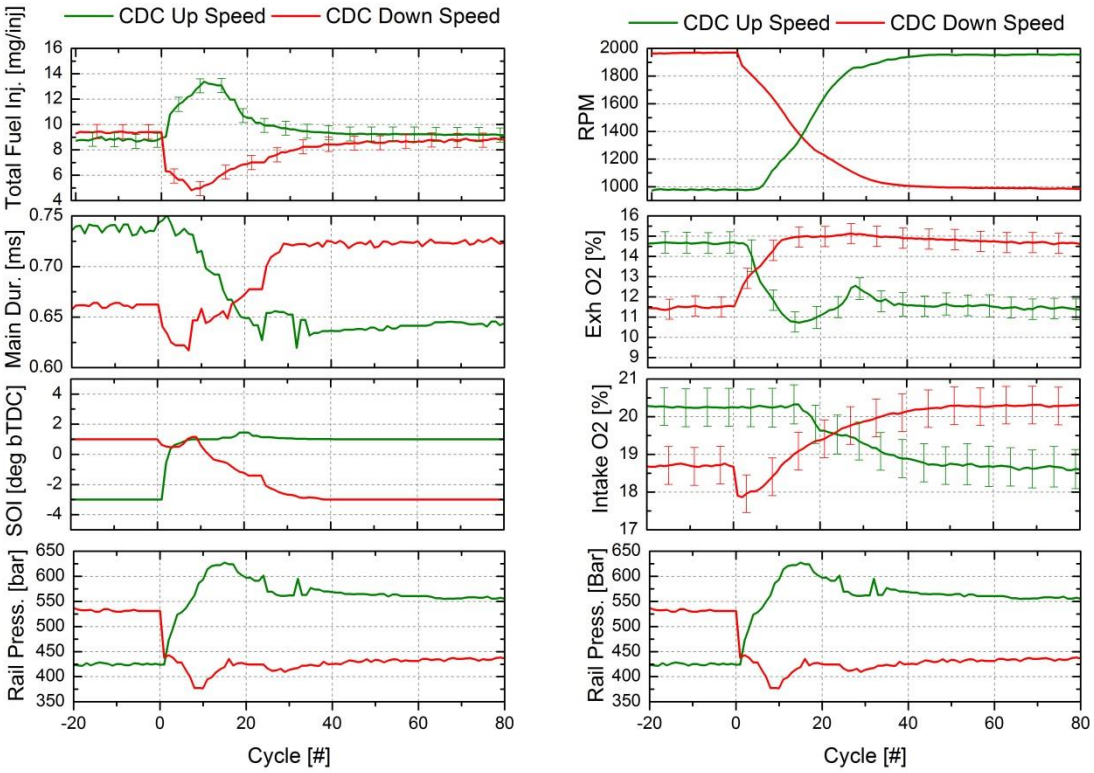

Figure 4.45 CDC speed sweep open-loop operating parameters

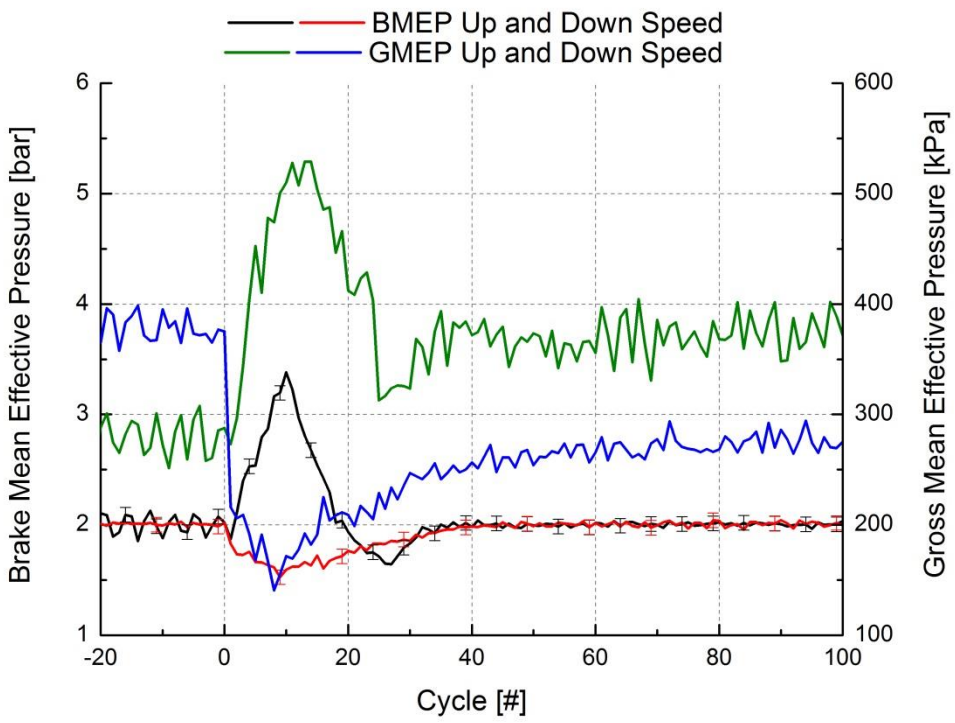

Figure 4.46 CDC Mean effective pressures for the up- and down-speed transient tests

Figure 4.47 shows the air system and combustion performance for CDC operation. The MAF and intake pressure follow their steady-state values. The intake temperature was different for each test, following the value where the transient started, i.e., lower for up-speed and higher for down-speed. There was an increase in equivalence ratio when the fueling increased faster than the manifold pressure. This increase in Phi will later be shown to cause an increase in PM.

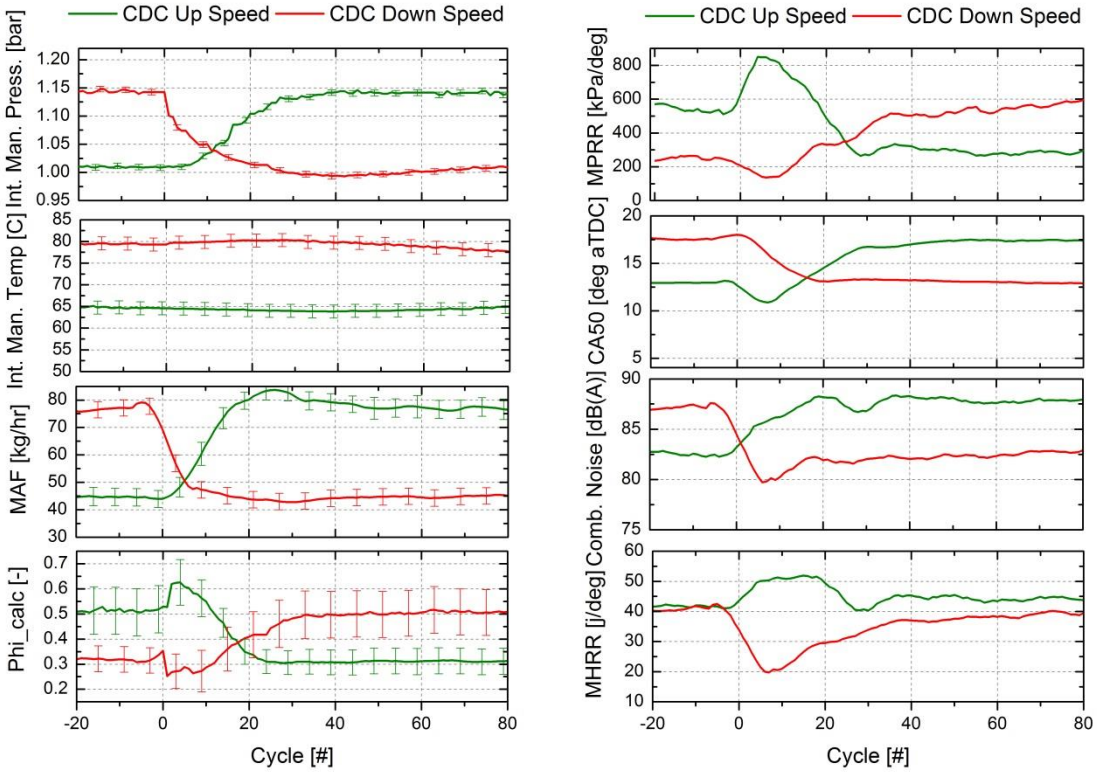

Figure 4.47 CDC open-loop intake system results

As shown in Figure 4.47, the combustion noise and CA50 follow the steady state values as CA50 increases with engine speed. MPRR increases during the up speed following the fueling increase seen near cycle 20, and begins the speed transient. Similarly, the fueling decrease allows MPRR to decrease momentarily and then to return to the steady state value during the down-speed event.

Figure 4.49 shows the emissions performance for CDC. The transient HC emissions follow the steady state values, while the NO and PM emissions do not. Spikes in NO are typical of transient CDC operation, as seen by Glewen et al. [76]. They reported that typically in CDC combustion, NO emissions tend to spike during

transients as the NO increase is driven by the resulting delay in the EGR rate and/or the intake O_2 concentration reaching the cylinder, as shown in Figure 4.48.

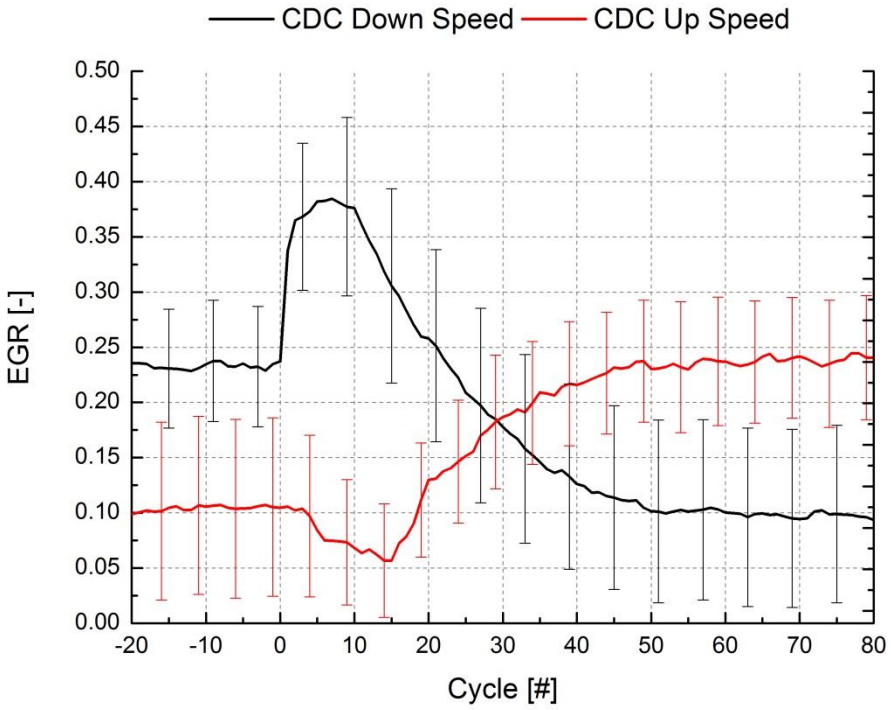

Figure 4.48 CDC transient EGR response for up- and down- speed tests

The PM increase is thought to be caused by the increase in Phi while the intake pressure lagged. Down-speed emissions did not show much deviation from steady-state. As the fueling decreases, so do the requirements for intake pressure and EGR, and thus spikes for NO and PM tend to not occur.

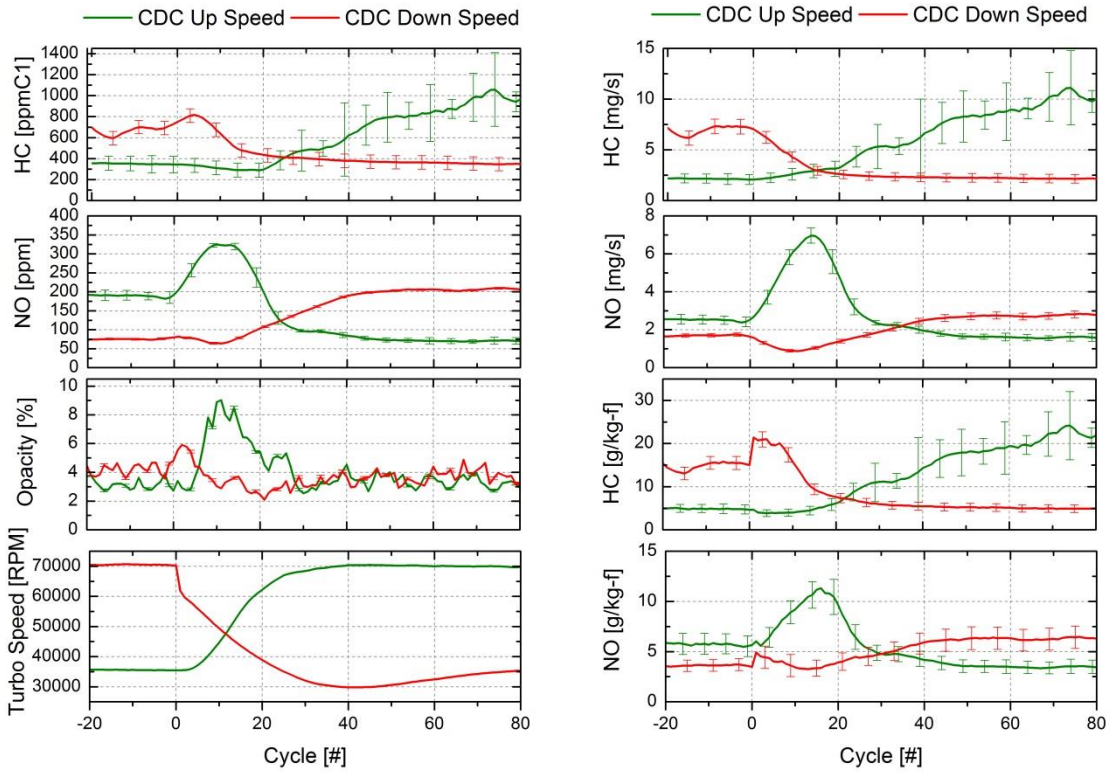

Figure 4.49 CDC open-loop emissions results

4.10 RCCI Speed Transient

RCCI transient performance was evaluated in both the open- and closed-loop calibrations. The open-loop tests were operated using only the steady-state table values to control the engine, while the closed-loop tests adjusted the PFI ratio of each cycle to attempt to reach the steady-state CA50 value.

Similar to the CDC cases, Figure 4.50 and Figure 4.51 show the BMEP and GMEP during the up- and down-speed events. RCCI exhibits similar results as CDC where the load increases to overcome the rotational inertia of the engine and

increase the engine speed. The fueling also decreases during the down-speed event.

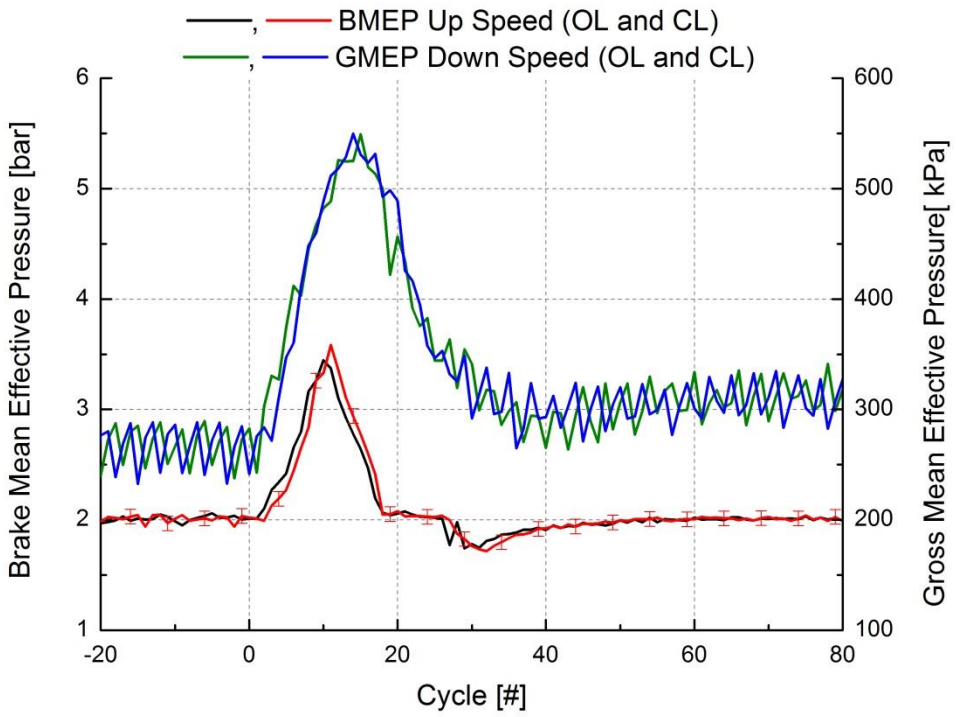

Figure 4.50 RCCI Mean effective pressures for the up speed transient tests

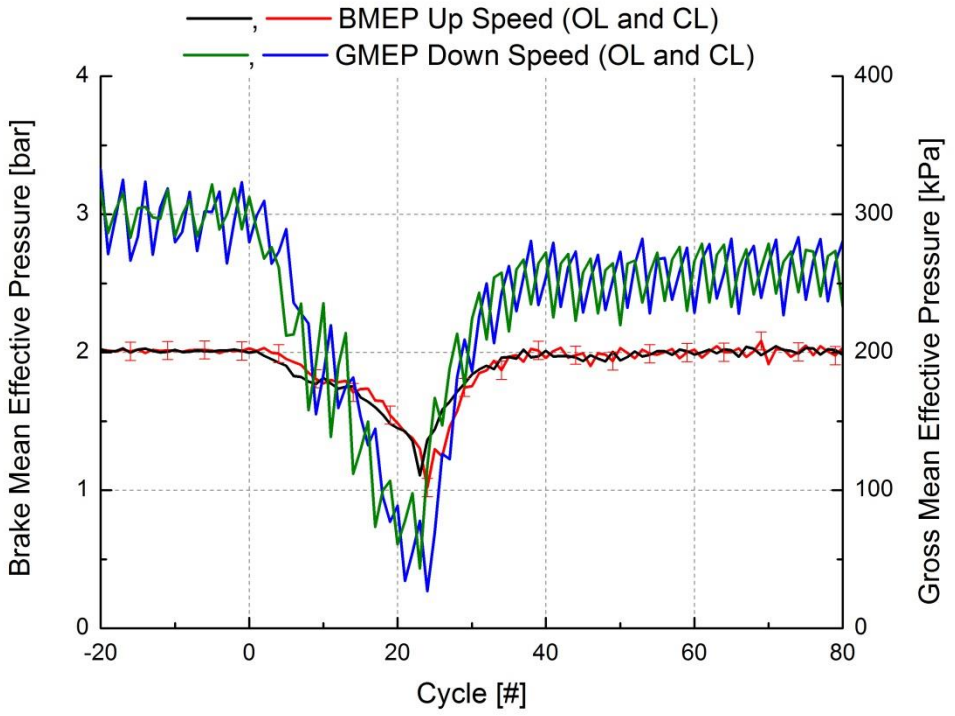

Figure 4.51 RCCI Mean effective pressures for the down-speed transient tests

Figure 4.52 shows additional operating parameters. Here, the change in engine speed can be seen. As will be discussed later, a main finding from the present results is that transient RCCI operation was possible, but some non-ideal fuel injection calibrations did cause some deviations from the steady-state results. It is also interesting to see that RCCI was able to cope with these non-ideal operating conditions and still produce low NO and PM.

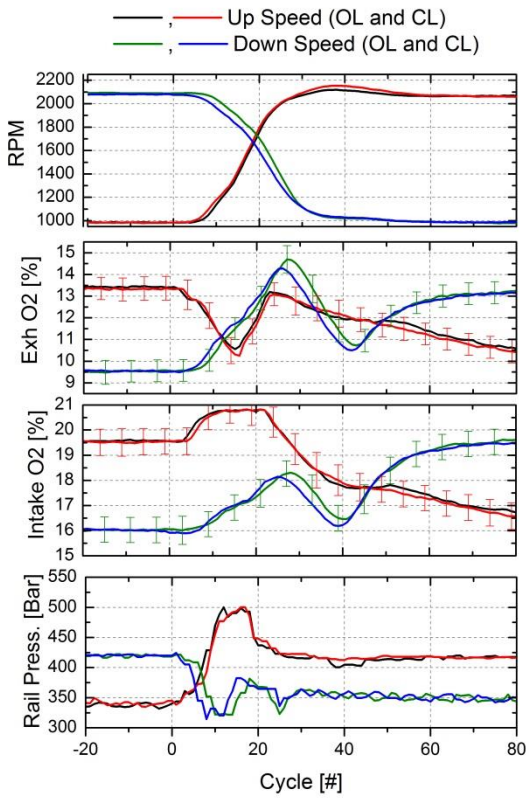

Figure 4.52 Additional RCCI operating parameters

The intake and exhaust O_2 concentration (and EGR, as seen in Figure 4.53) plots show this effect in both the up- and down-speed tests. For the up-speed test, the dip in exhaust O_2 and increase in intake O_2 occurs at the same time as the load increase, so a logical explanation is that the higher load event used more fuel, and hence lower exhaust O_2 , but at a lower EGR rate, hence the higher intake O_2 , as shown in Figure 4.53.

For the down-speed curve, the increase in O_2 concentration near cycle 25 was caused by the reduction in fueling and the corresponding increase in O_2 in the exhaust and intake. The slight dip near cycle 40 is thought to be caused by an

excess of EGR, as shown in Figure 4.53. There were no major corrections seen to be caused by the closed-loop controller, unlike the previous load-step change results, where the large change in port fueling required large adjustments to the PFI ratio to keep CA50 near its calibrated value [98].

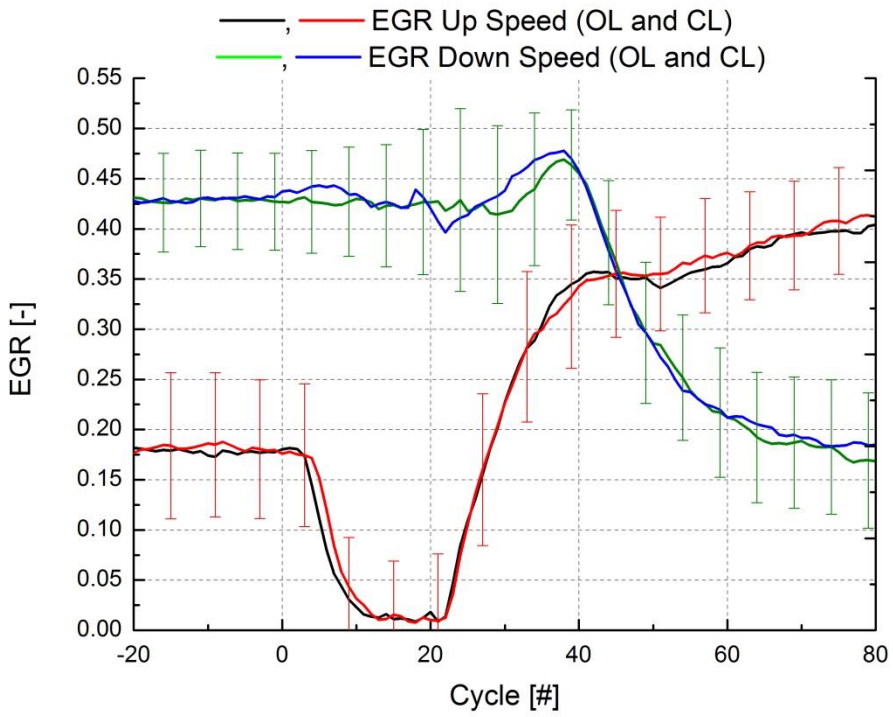

Figure 4.53 RCCI transient EGR response for the up- and down-speed tests

In Figure 4.54, the fueling commands for the open-loop and closed-loop RCCI transient cases can be seen. As the main SOI timing was not modified by the closed-loop controller, it remained constant between the two modes. While the SOI timing followed the calibrated values, it can be seen that the up-load test required very early SOI timing and a larger PFI fraction to keep CA50 after TDC. This is consistent with other high-load RCCI operating conditions [1]. Adjustments from the

closed-loop controller were again minimal for the speed change compared to previous load change results [97]. During the down-speed test, the total fueling decreased more than the steady-state values, similar to the CDC test. The other interesting note is that the PFI ratio decreased as well, especially around cycles 10 to 20. The slight dip was not seen in the steady-state calibration and will later be shown to decrease HC and increase NO emissions. Future work will be needed to perform additional steady-state calibrations at a wider number of pedal positions for a given engine speed to fix these issues.

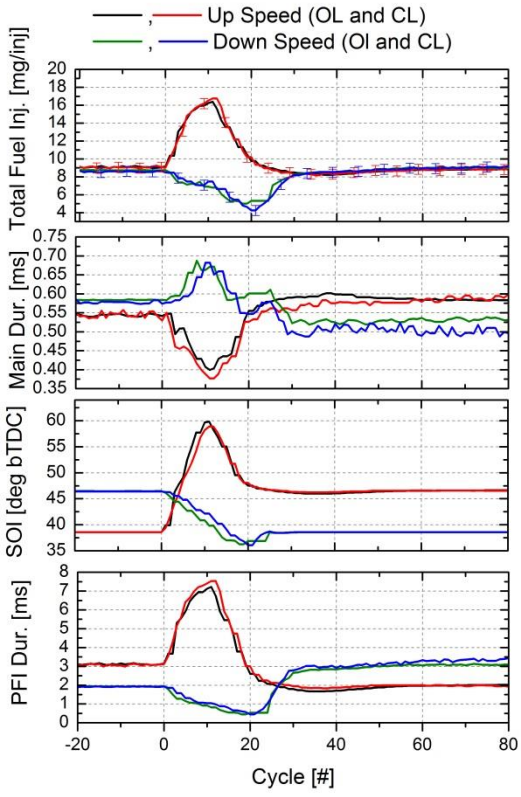

Figure 4.54 RCCI open-loop and closed-loop fuelling commands

Figure 4.55 compares the air system performance between the open-loop and closed-loop RCCI tests. As expected, there were no major differences in the air system parameters, as they were not affected by the closed-loop controller. Similar to CDC operation, the intake temperature is higher for the down-speed compared to the up-speed as the EGR rate is higher at 2,000 than at 1,000 rev/min. During the up-speed test, there was a rise in intake pressure near cycle 20, where the load increased to overcome the inertia of the dyno and begin the speed increase. Currently, it is thought that this increase was caused by a combination of the slow response of the engine controller and that the calibration at the point (roughly 3.5 bar, 1,250 rev/min.) was not fully optimized with lower intake pressure, as for the other 2.0 bar BMEP points. This was not seen during the down-speed test since the engine speed/pedal position path was different, as will be shown in the discussion. Increases in the equivalence ratio can be seen near cycle 5 and cycle 35 where the fueling rate increases faster than the intake pressure for both the up-speed and down-speed tests.

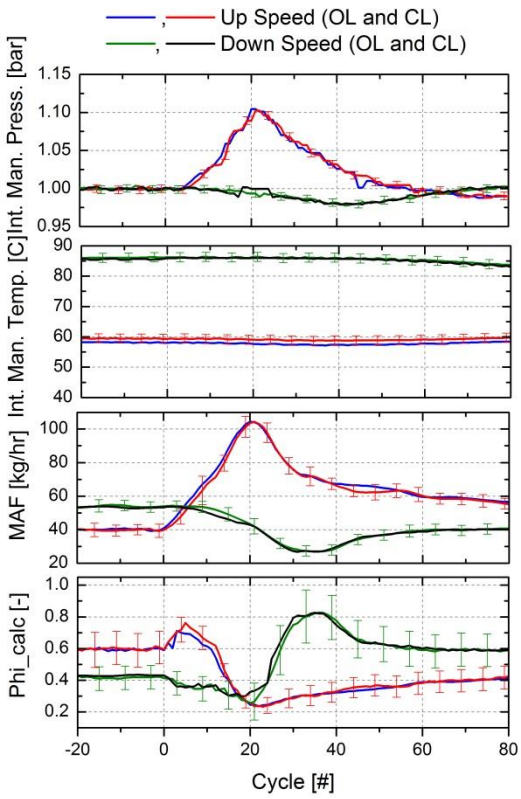

Figure 4.55 RCCI open-loop and closed-loop air system performance

Figure 4.56 compares RCCI combustion performance between open-and closed-loop operation. Again, the difference between open- and closed-loop operation was negligible. Due to the increased load, which occurs near cycle 10 for the up-speed test, occurred at a low engine speed, the MPRR and MHRR increase to near the 10 bar/deg. limit. However, the overall engine noise remained near the steady state value of 85 dB. During this small load excursion, combustion phasings delay to nearly 5 deg. aTDC, similar to other 3.5 bar operating points but then quickly fall to the steady state value of ~0 deg. aTDC. For the down-speed test,

CA50 is too far advanced at cycle 20 because of the lower PFI fraction seen in Figure 4.54.

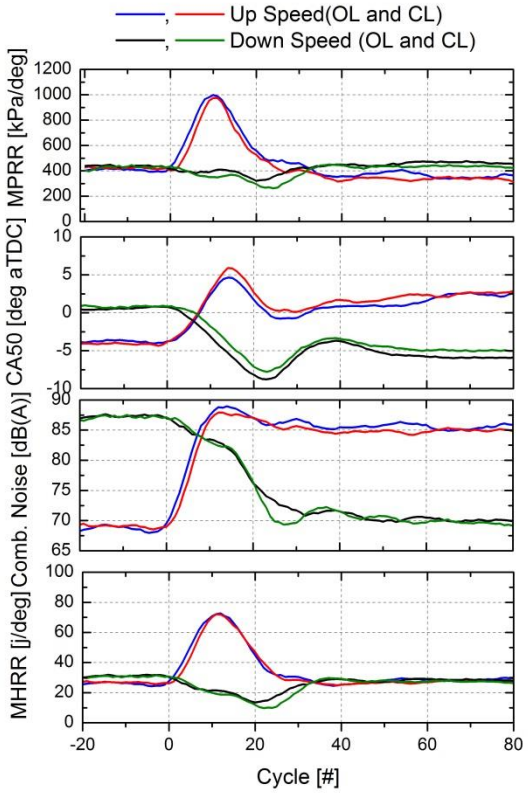

Figure 4.56 RCCI open-loop and closed-loop combustion performance

Emissions results from the RCCI speed transient are shown in Figure 4.57. The results might appear to be different from the previous load transient results seen in [98], but as will be shown, they are actually very similar. During that test the HC concentration was seen to nearly double for a few cycles during the initial phase of the load transient. This was thought to be caused by a combination of turbo lag and a fraction of the port-injected fuel collecting on the intake runner rather than making it into the cylinder, thus causing a delay in combustion phasing.

During the up-speed transient test, the increase in HC concentration was not seen, but as shown in Figure 4.57, the HC mass emissions increase by similar magnitude as seen with a load increase. Since HC emissions are proportional to the PFI fraction [1-3], they are seen to increase around cycle 10, where the PFI fraction increases. The increase in MAF helps to dilute the additional HC mass and keep the concentration nearly constant during the up-speed test. Better control of the intake pressure and EGR rate can help to lower the HC mass emissions. During the down-speed test, HC drops dramatically around cycle 20. This was due to the engine operating outside the calibrated range and the PFI ratio dropped below the optimal level for low NO emissions.

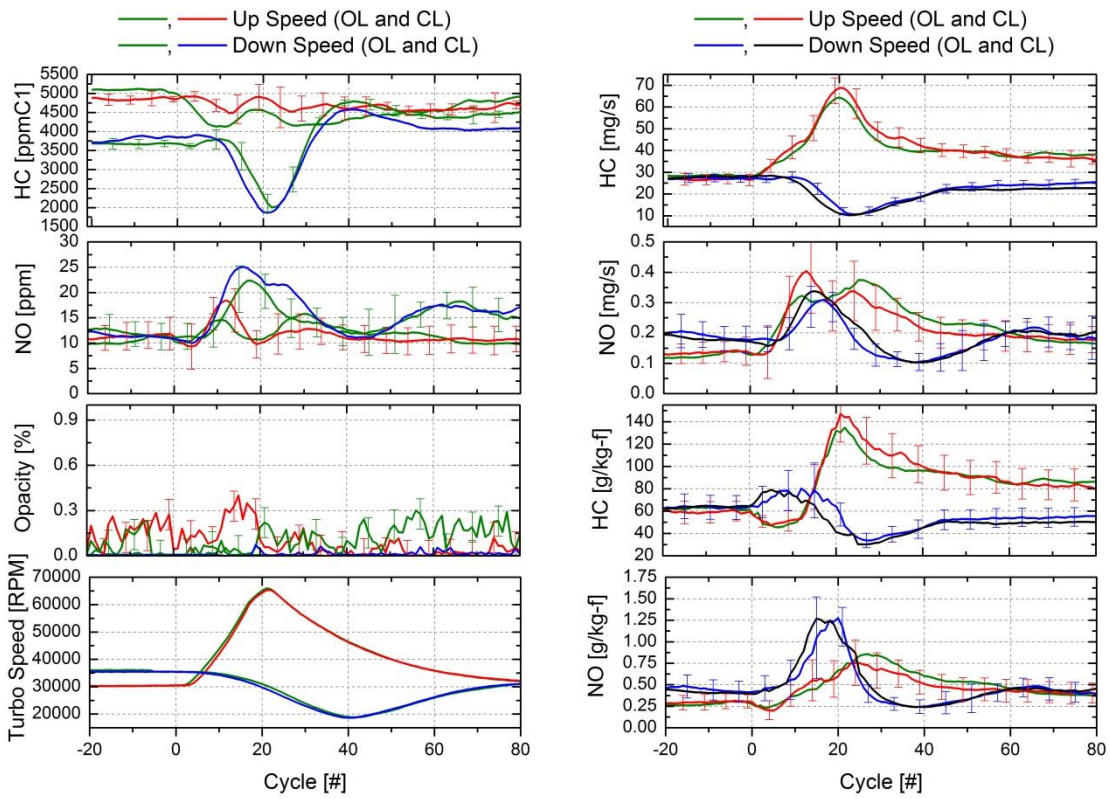

Figure 4.57 RCCI open-loop and closed-loop emissions performance

Figure 4.57 shows the NO mass emission spike corresponding to the fueling increase. It is theorized that the “high” load, low speed condition produced higher levels of NO than desired due to the fairly rich operation of Φ = 0.7. This has been seen in previous RCCI tests, and additional calibration that adds more EGR would help lower the NO [1-9].

During the down-speed test, NO was seen to increase as well. This increase was due to the PFI ratio dropping to a low level from the engine operating in non-calibrated areas. As discussed earlier, when operating at low PFI ratios, HC emissions tends to decrease and NO tends to increase. More work to increase the

PFI ratio in that part of the map should help lower the NO, but at the expense of increased HC. The exhaust opacity for RCCI was near zero, and like the previous load test results [98], no dramatic spikes occurred. Turbocharger speed was seen to increase during the speed change, mirroring the increase in intake pressure seen in Figure 4.55.

4.11 Cold Start Approximation

Vehicles typically operate over a wide variety conditions, which can greatly vary from those tested in laboratories. Even though these conditions are only visited for a short period of time during vehicle operation, they can have a large effect on total emissions, especially for cumulative tests like the EPA FTP75. In this test, the vehicle has to start after sitting overnight for cold start condition. While the vehicle only operates in this condition for the first few minutes of the test until it reaches its operating temperature, a majority of the total emissions are emitted during this phase. The majority of the emissions are emitted because the catalyst/after treatment system has not reached the operating temperature and its efficiency is thus low. Thus, it is of great importance to study engine operation in conditions similar to those seen in the test.

This is usually beyond the scope of most SCE testing, as it as can be difficult to simulate low coolant temperatures for long periods of time. Additionally, most engine controllers used in lab testing lack the appropriate control strategies necessary to account for varying engine coolant temperatures. OEMs spend a majority of engine development on transient and cold starting algorithms, so it is

conceivable that university/research labs would have difficulty doing such tests. However, it was of interest to see how difficult a RCCI cold start would be, and if the closed-loop controller could accommodate conditions that are able to be simulated in the current laboratory.

For this section, a cold start condition was simulated in the lab by operating the engine from 48°C to full operating temperature (85°C) using a combination of open and closed-loop adjustment values. While it is obvious that vehicles would operate in much colder conditions than 48°C, it was not possible to operate the engine as it had difficulty operating colder than this, and 85°C is where the engine's thermostat is set. The test was difficult to conduct as only one test was permitted each day. The HC emissions tended to rapidly foul the instruments. Never the less, the test gives a fairly accurate representation of how such a strategy would work rather than being the optimal or best approach. More work would be required for OEM levels of operation and refinement, but the results showed that it was possible to operate over a wide range of coolant temperatures and offers a path for improved results in future work.

The cold start test was conducted at 1,500 rev/min and 1.0 bar BMEP, which is a difficult point to start and run at when the coolant temperature is cold. The goal for the test was to show what type of control strategy would be needed for an RCCI engine under cold starting conditions. During the test, the pedal position was held constant, and thus engine operated using the predetermined table values for total fueling, EGR, intake manifold temperature and intake pressure. The total time to

reach full operating temperature during the cold start test was approximately 15 minutes, as shown in Figure 4.58.

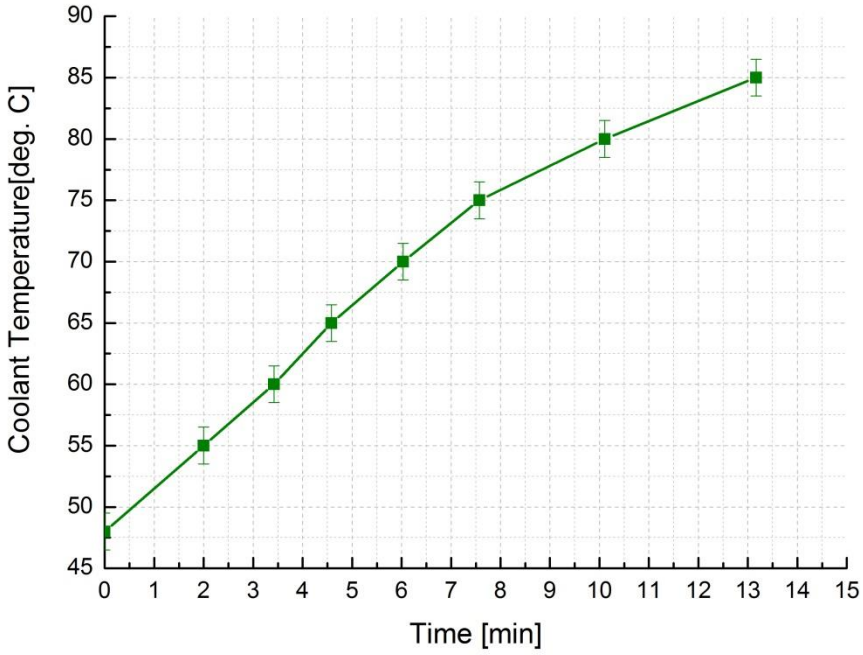

Figure 4.58 Engine coolant temperature as a function of time

The basic operating conditions are shown in Table 4-10, with the detailed run conditions are shown in Appendix 7.7.

Table 4-10 RCCI Engine Coolant Temperature Sweep Parameters

	Run 1
Engine Speed [rpm]	1,500
Rail Press. [bar]	380
Intake Press. [bar]	1.030
Intake Temp. [°C]	45
EGR [%]	1.575
Pedal Position [%]	9.00

To account for the varying engine coolant temperature (ECT), additional code was added to the Drivven base code to automatically change the SOI and PFI ratio as a function of ECT. Values were determined from looking at similar effects such as intake manifold temperature on CA50 [89], but were fine-tuned as there was no direct simulation available for ECT effects. As seen in the experimental setup section and Figure 4.59 and Figure 4.60, the additional code for the ECT adjustments of the table commands were made in-line of the SOI command chain, as shown in the green and red circles.

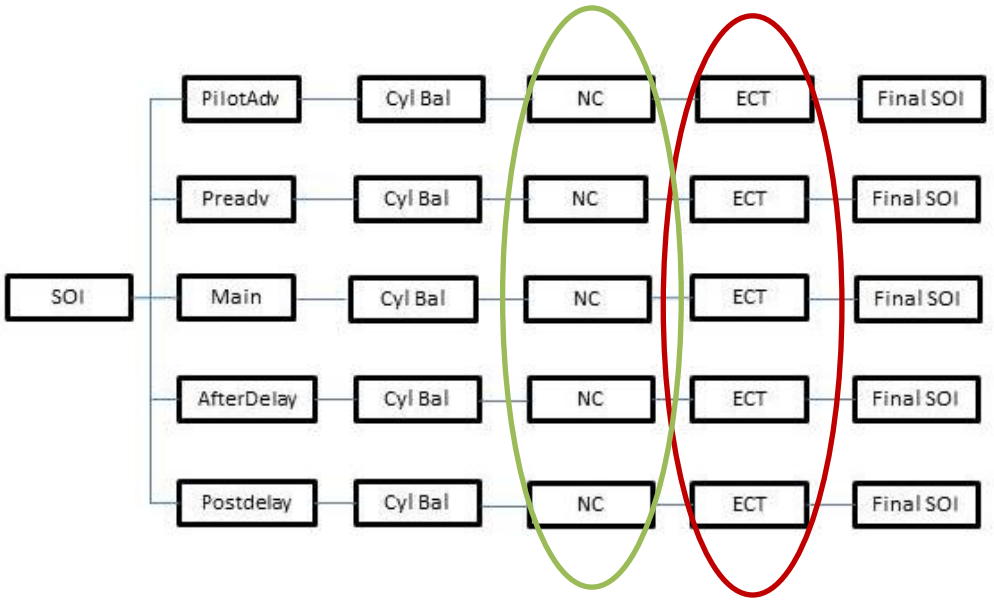

Figure 4.59 Next-cycle and ECT adjustments for the SOI timing for RCCI operation

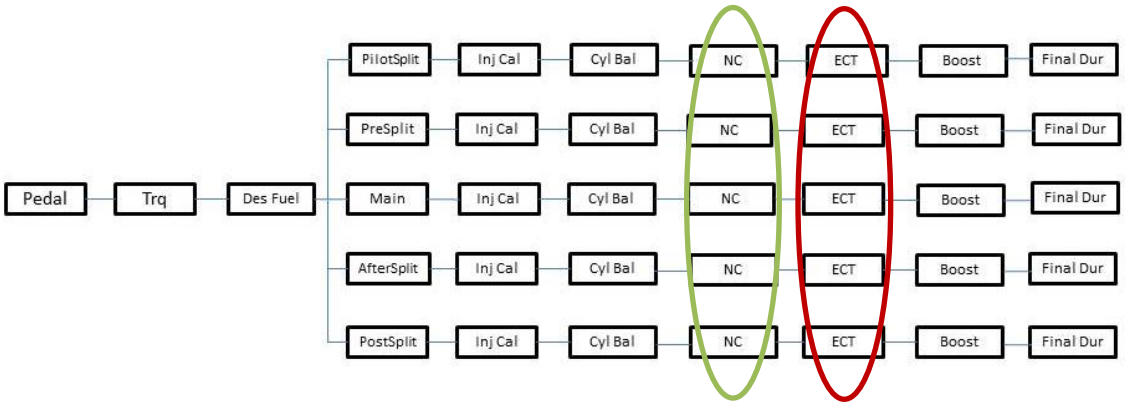

Figure 4.60 Next-cycle and ECT adjustments for the PFI fraction for RCCI operation

As shown in the green circle, the closed-loop controller multiplies the fueling ratio (or the SOI if the CL controller is operating in CDC mode) until the combustion phasing reaches the target value. Next, in red, the ECT based adjustments for SOI and PFI ratio are seen. For these adjustments, custom 1-D tables were made where the main SOI timing was offset a given amount, diminishing to a zero offset at 85°C. Similarly, the PFI ratio uses a 1-D table, but here the PFI ratio was multiplied by a factor also diminishing to unity at the 85°C, steady-state operating ECT. The tables are given in Appendix 7.9 and 7.10.

Figure 4.61 shows the cylinder pressure, apparent heat release rate and injector current traces for the ECT test. Here it can be seen that the closed-loop controller held CA50 constant with the peak AHRR dropping with ECT and increasing PFI ratio.

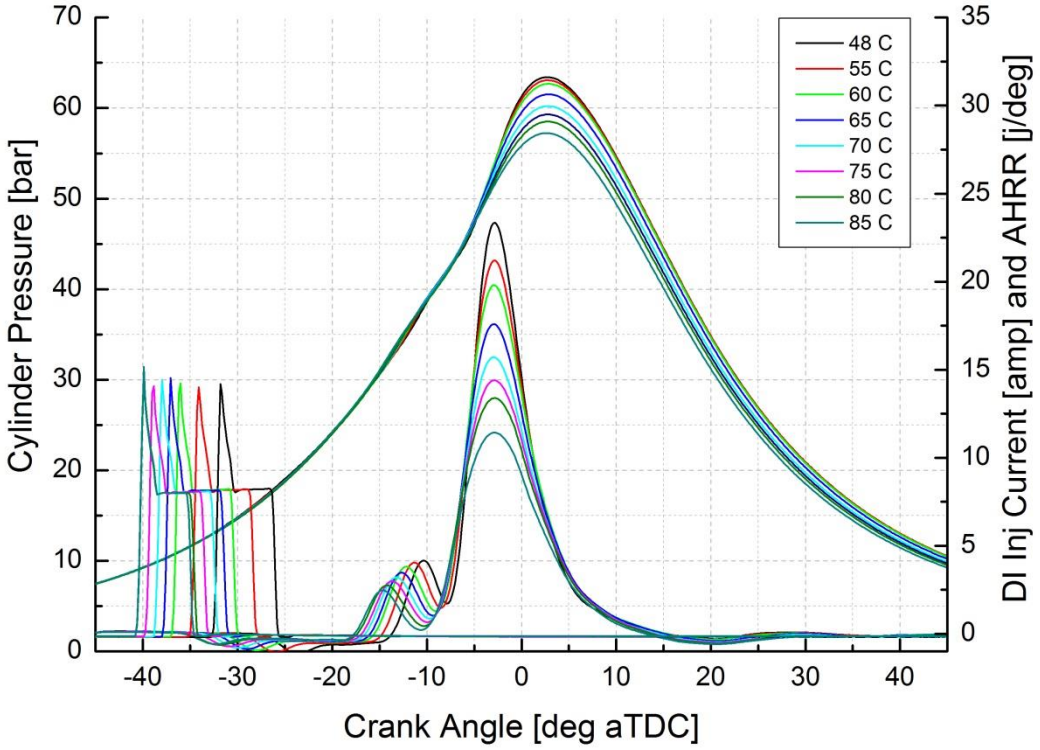

Figure 4.61 Cylinder Pressure, Apparent Heat Release Rate and DI injector Current Traces for the Cold Start Test

Additionally, the SOI timing for the single injection used can be seen. As the ECT drops, the need to increase the local reactivity also increases, thus SOI timing usually needs to advance. The effect is to create higher local temperatures and increase the oxidation rate of the mixture. However, this will be seen to cause higher NO emissions.

Figure 4.62 shows the probability density function (PDF) of CA50 for the ECT test. PDFs can be used to show probability of an event occurring for a set of normally distributed data. Here, the PDF represents a metric for combustion

stability. As the combustion becomes more unstable, the probability of CA50 occurring at a given value decreases, making the curve wider. Typical of most RCCI results, the coupling between late SOI timing and combustion phasing increases. Usually when SOI is advanced towards TDC the combustion stability increases. This increase in stability is usually marked with an increase in NO and PM emissions as the combustion becomes more mixing controlled. Conversely, with HCCI, there is no control of combustion phasing with SOI, so the goal with RCCI is to combine the low emissions of HCCI with the control of the combustion phasing of CDC.

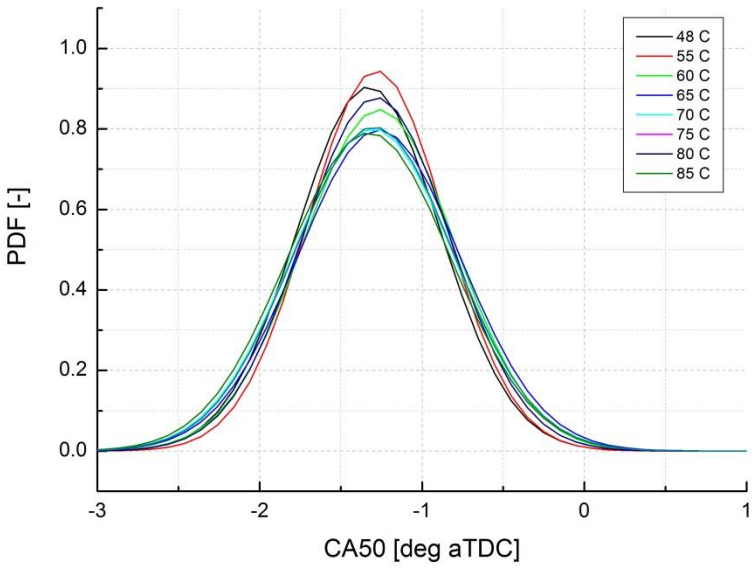

Figure 4.62 Probability Density Function of CA50 for the cold start test

Figure 4.63 shows the emissions and combustion performance of the cold start test. As expected from the control strategy, the PFI ratio is lower at low ECT to

achieve stable combustion and increases with ECT. As the PFI ratio increases, NO decreases and HC increases. Additionally, the BTE is seen to drop with ECT. At first glance this does not make sense, as it should get higher with more RCCI-like combustion, but as will be shown, the total fueling was not constant and thus the load dropped, which caused the BTE to drop, as shown in Figure 4.63.

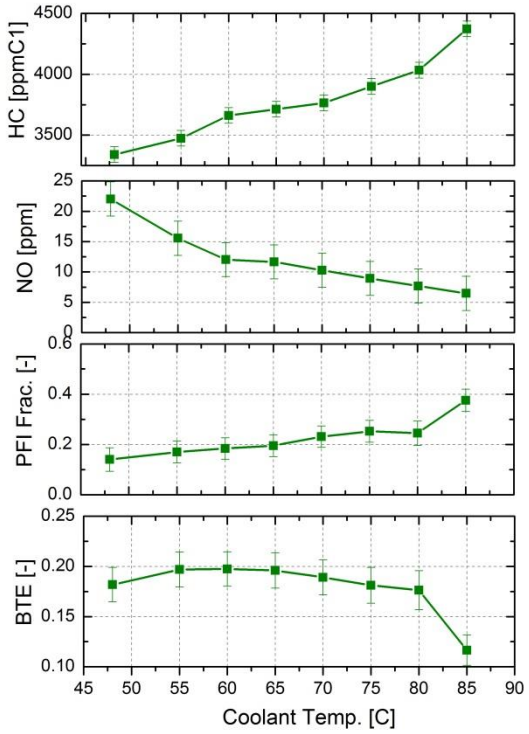

Figure 4.63 Emissions and combustion performance for the RCCI cold start test

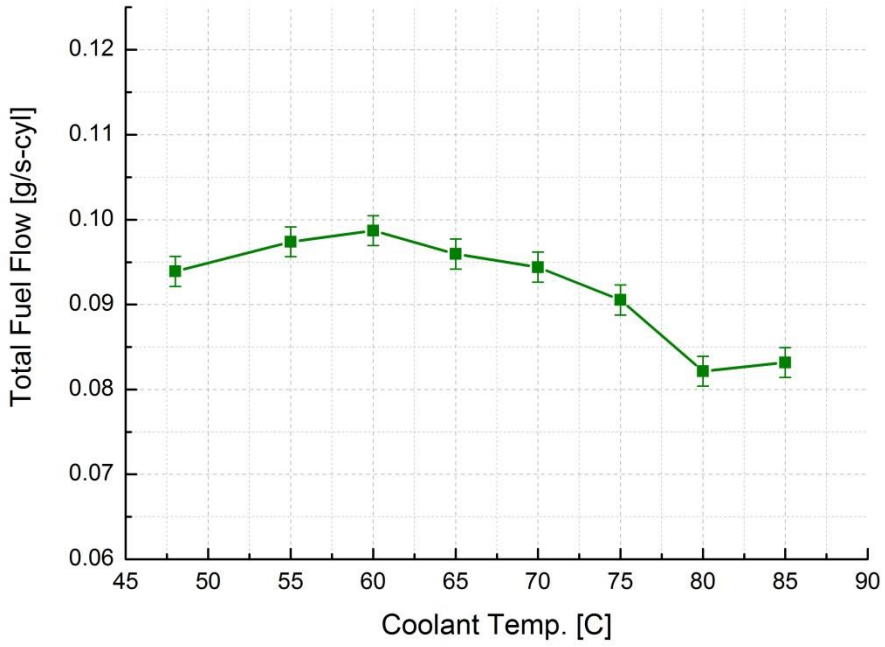

Figure 4.64 Total fuel flow rate as a function of engine coolant temperature

The total fueling was not constant due to the way the PFI fueling is calculated in Drivven. This is accomplished by a function that relates the PFI duration to an injected fuel mass. It is apparent that this correlation is not as accurate as it could be, but the overall conclusion is that the ECT adjustments work the way they were designed to.

In Figure 4.65, the fueling, combustion phasing and noise metrics are shown. The peak AHRR drops with PFI ratio, lowering the combustion noise, while noise is fairly low, <80 dB, it could be lowered at the lower ECT. With the closed-loop controller, the CA50 is a function of pedal position and RPM, so the target

CA50 is constant with ECT. Additional code could be added to delay CA50 at low ECT to lower NO emissions at the expense of increased HC emissions.

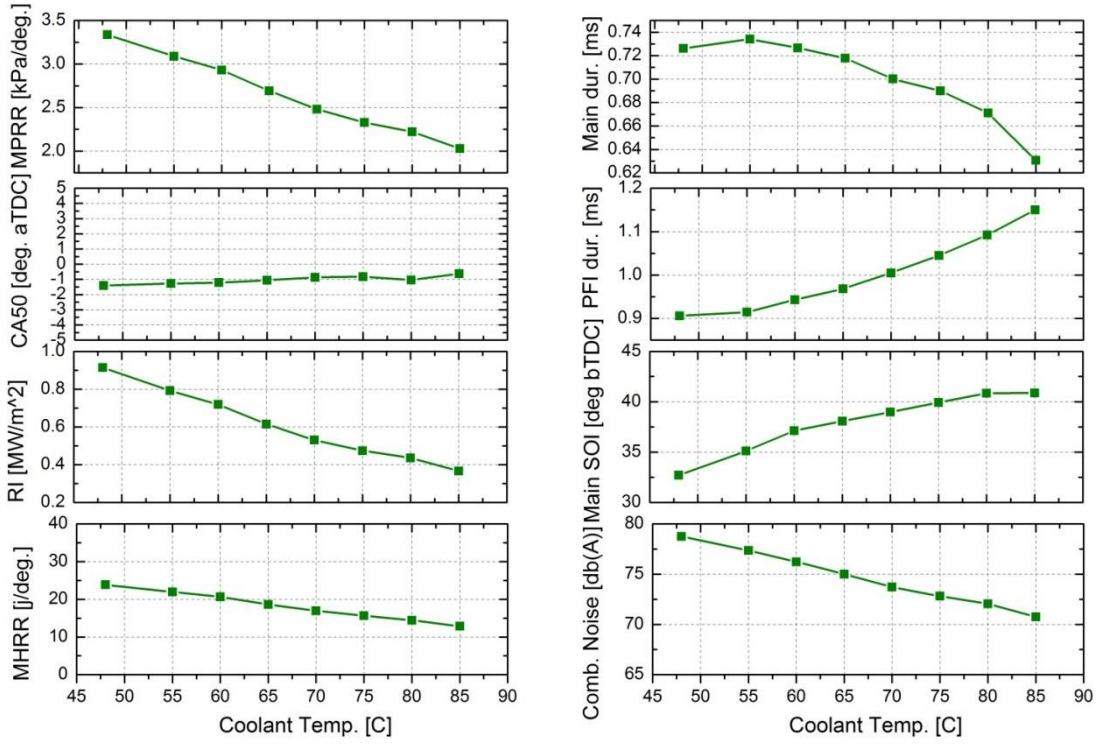

Figure 4.65 Fueling and combustion metrics of the RCCI cold start test

The PFI ratio was also seen to increase with ECT as the correction reaches the steady state condition of no correction. The main SOI timing advances from TDC as the coolant temperature increases as the additional reactivity was not needed for acceptable combustion stability and is needed to lower NO emissions.

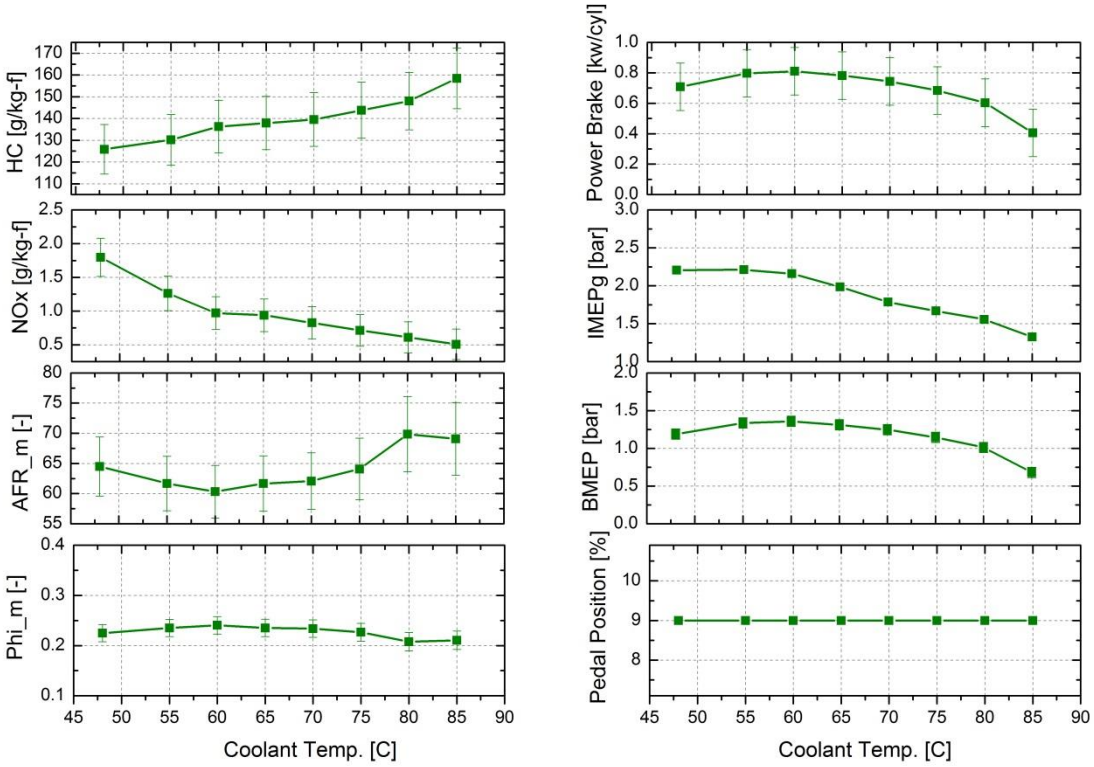

Figure 4.66 Emissions results from the RCCI cold start test

Emissions results from the cold start tests are shown in Figure 4.66. The overall equivalence ratio was fairly constant over the test, but becomes leaner as the PFI ratio increases, indicating that the total fuel was dropping. As the PFI fraction increases, so did the HC emissions, similar to all the results presented so far. NO decreased with PFI fraction as the charge became more premixed. The mean effective pressures can also be seen to drop, additionally indicating lower total fueling.

4.12 Combustion Mode Switching

As seen in the previous results, RCCI has low catalyst efficiency at loads below 3 bar BMEP. The low catalyst efficiency is due to the low exhaust temperatures. Since a large portion of the FTP75 test is at or below this load, methods for increasing catalyst efficiency are needed. As shown in Figure 4.67, the exhaust temperatures for RCCI are much lower than for CDC and do not reach the catalyst light-off temperature until 3 bar BMEP for the EGR case, and 4 bar for the non-EGR case. While future work should involve increasing the exhaust temperature for 1 and 2 bar RCCI.

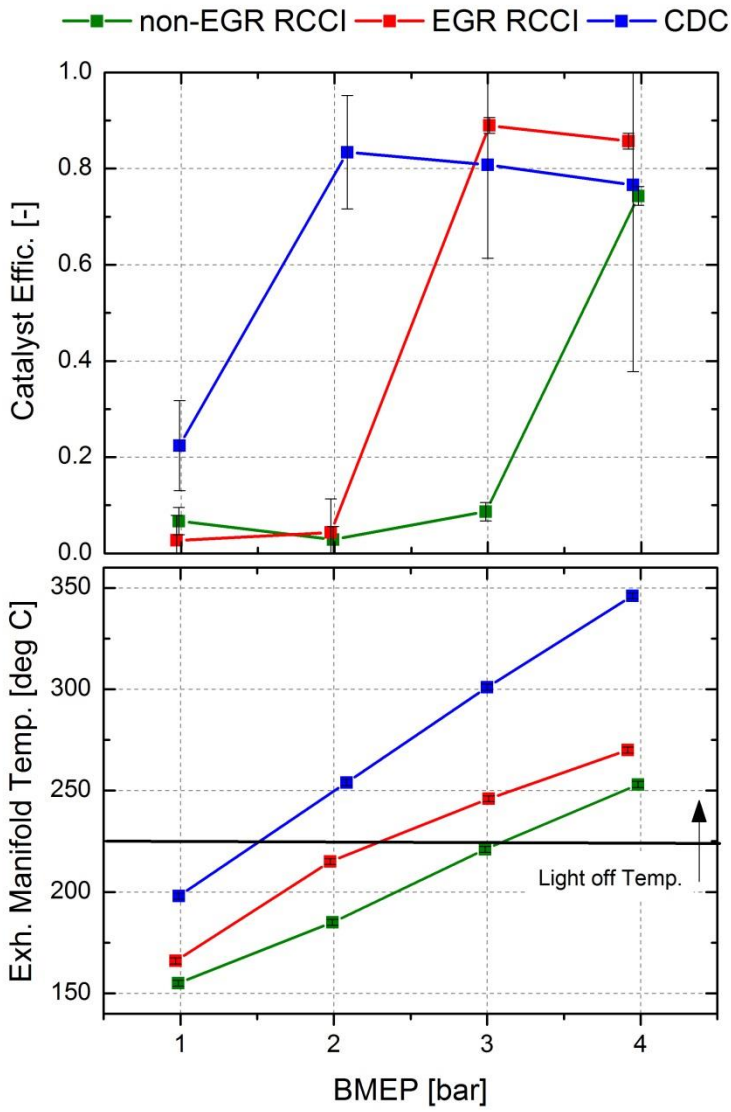

Figure 4.67 Exhaust manifold temperatures and oxidation catalyst efficiency for RCCI and CDC as a function of load

If it is not possible to increase the exhaust temperature for RCCI at these loads, then it might be necessary to operate with a combustion mode that has higher catalyst efficiency (like CDC). So, that asks the question as to whether it is possible to switch between combustion modes during engine operation.

Additionally, since the power density and peak load capability of RCCI can be lower than CDC engines, the use of mode switching from RCCI to CDC at high loads could be used. However, this is beyond the current testing capabilities of the lab and beyond the scope of the work, but the ability to do so will be useful for commercial application of RCCI and should be investigated in future testing.

To allow the ability to switch between combustion modes, the Drivven code was modified so that it was possible to switch between CDC table values and RCCI table values with one master button. This feature was originally implemented to ease switching of maps between RCCI and CDC when the engine was not operating, but it was found to be able to safely switch between RCCI and CDC combustion modes while the engine was firing. In the future, it is hoped that this feature can be made into its own table and used to do mixed-mode transient testing, similar to [80].

The current experiments were done to show the possibility of mixed-mode operation at low loads and to show any flaws in the control strategy. The operating conditions for the test used a fixed swirl ratio (which not found to matter in additional testing), fixed pedal position and use of double direct-injections for both RCCI and CDC, as shown in Table 4-11. For both modes, the pilot advance was kept constant at 1.85 ms. No optimization for the RCCI double injection was performed. The goal was to find what other controls would be needed besides closed-loop control for optimal performance during the mode switch. Similar to the cold start test, the RCCI

fueling and CDC fueling at the same pedal position were not perfectly equal, so the load varied slightly.

Table 4-11 RCCI to CDC Mode Switch Steady-State Run Conditions

	CDC	RCCI
Engine Speed [rpm]	1,500	1,500
DI [mg/inj.]	6.12	2.88
PFI [mg/inj.]	0	3.95
Rail Press. [bar]	450	403
Main SOI [deg. bTDC]	0.65	42.2
Pilot advance [ms]	1.85	1.85
Pilot fraction [%]	9.0	30
Intake Press. [bar]	1.026	0.98
Intake Temp. [°C]	71.5	88.6
EGR [%]	28.5	50.9

The combustion results for CDC and RCCI are shown in Table 4-12. As can be seen, combustion phasing and MPRR were similar to the baseline tests for both modes that were conducted earlier. The BMEP was slightly higher for RCCI given the above mentioned fueling difference.

Table 4-12 RCCI to CDC Mode Switch Combustion Performance

	CDC	RCCI
MPRR [bar/deg.]	2.3	3.2
GMEP [bar]	2.8	2.62
NMEP [bar]	2.5	2.43
BMEP [bar]	1.8	1.99
CA50 [deg. aTDC]	16.2	0.65

The steady-state emissions results are shown in Table 4-13. Similar to the baseline results in the previous tests, RCCI had lower PM and NO at the expense of higher HC.

Table 4-13 Mode Switch Emissions

	CDC	RCCI
Comb. Noise [dB]	81.5	78.1
Phi [-]	0.31	0.5
FSN [-]	0.537	0.02
Opacity [%]	0.98	0.0
HC [ppmC1]	1062	3354
NO [ppm]	42.8	9.25

Figure 4.68 shows the emissions from the mode switch. Interestingly, the results show the only real deviation from the steady-state results was the slight increase in HC for the RCCI to CDC switch.

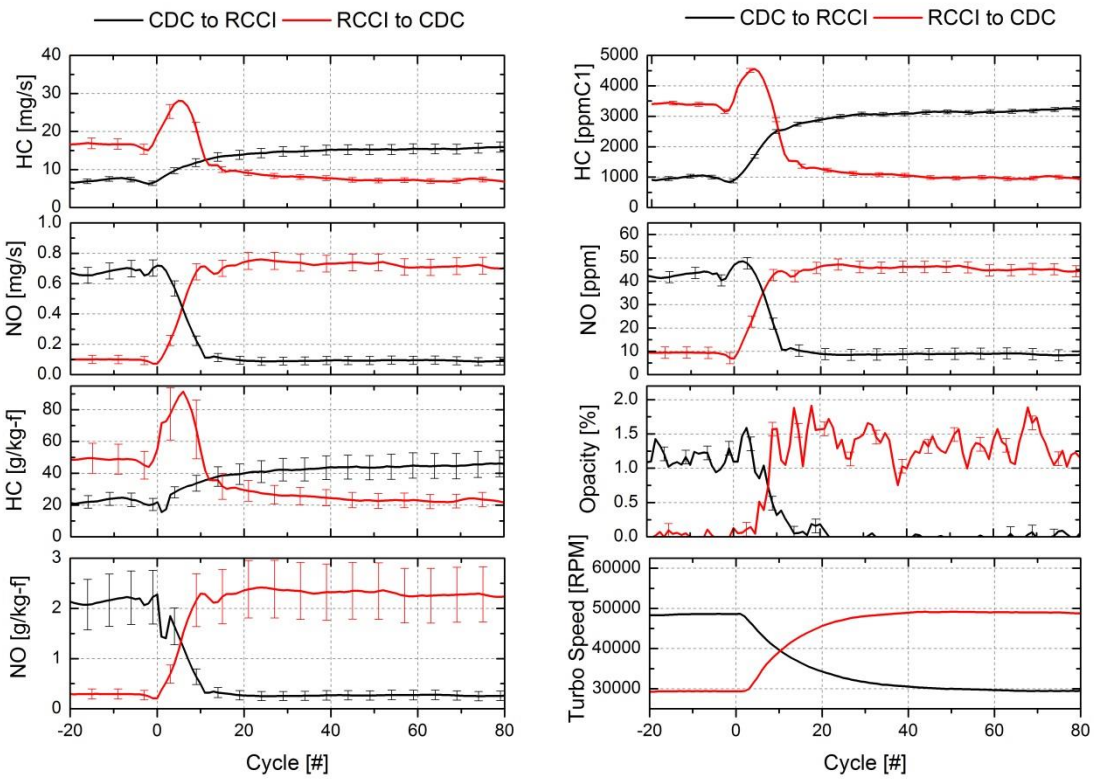

Figure 4.68 Emissions results for the RCCI to CDC mode switch test

This increase is thought to be caused by some of the fuel from the intake runner continuing to enter the engine when the injections switch to CDC. With the main SOI timings used with CDC, the gasoline tends to pass though the engine unburned. The poor combustion could be seen in the BMEP dip in Figure 4.69. The dip in load from CDC to RCCI is smaller and does not increase HC or NO beyond the steady-state values.

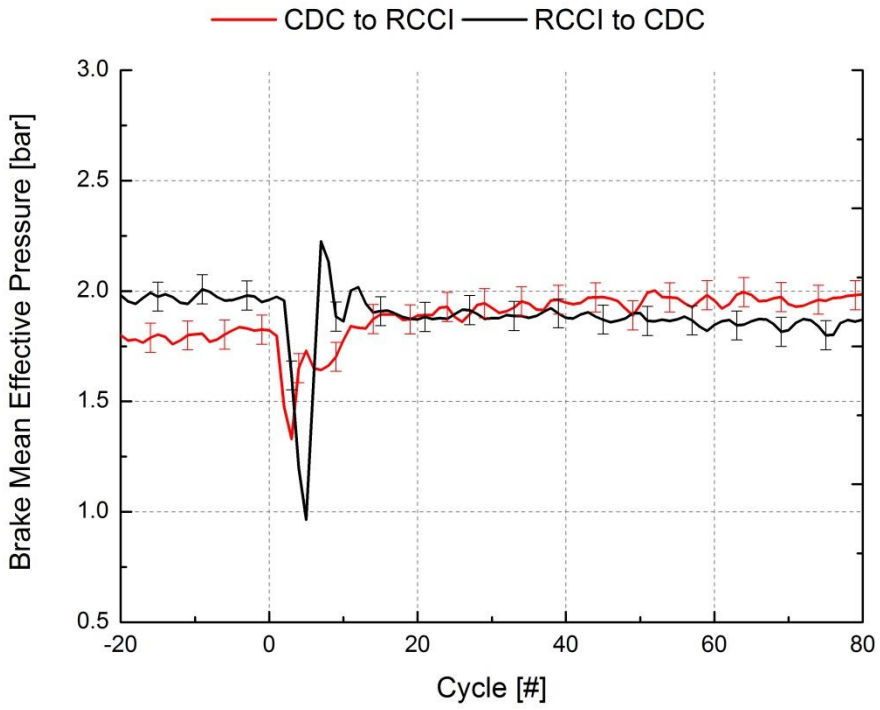

Figure 4.69 BMEP for the RCCI to CDC mode switch test

Figure 4.70 shows the intake and combustion phasing performance. The results follow the steady state results with a small dip in noise for the RCCI to CDC case at the same time as the BMEP dip, around cycle 5-10.

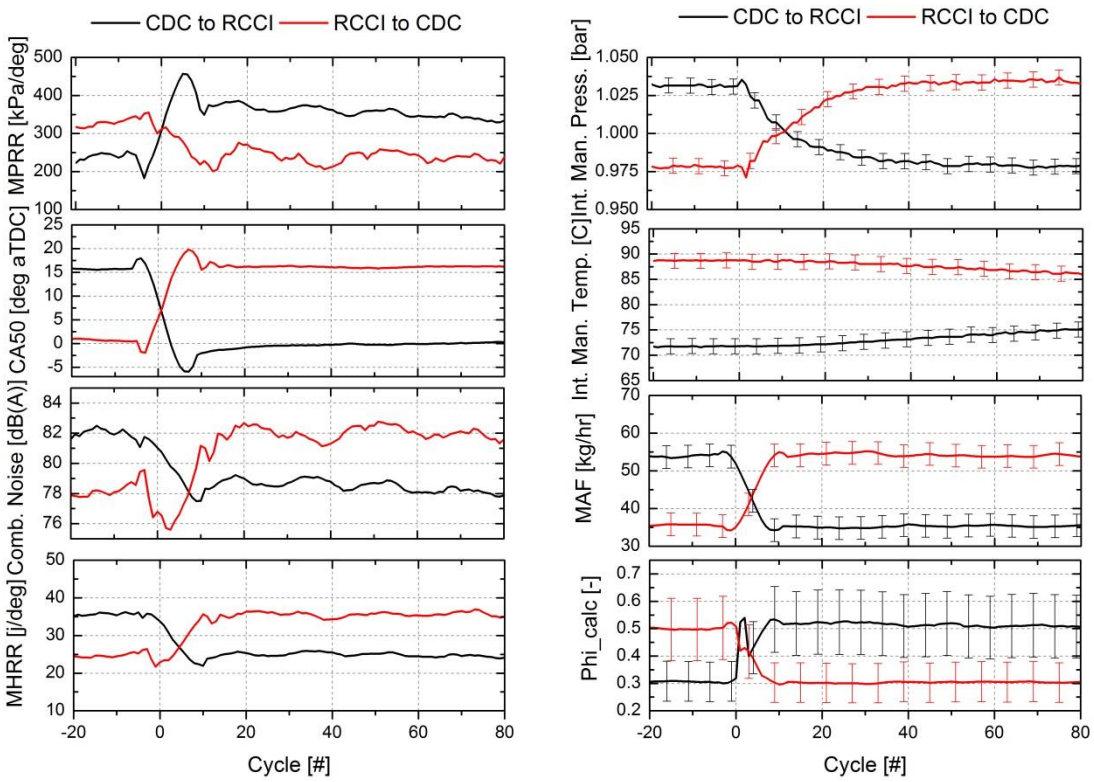

Figure 4.70 Intake and combustion performance results for the RCCI to CDC mode switch test

Figure 4.71 shows fueling commands for both mode switches. Only a slight engine speed disturbance around cycle 5 was seen. This deviation might cause a small change in the total fuel injected.

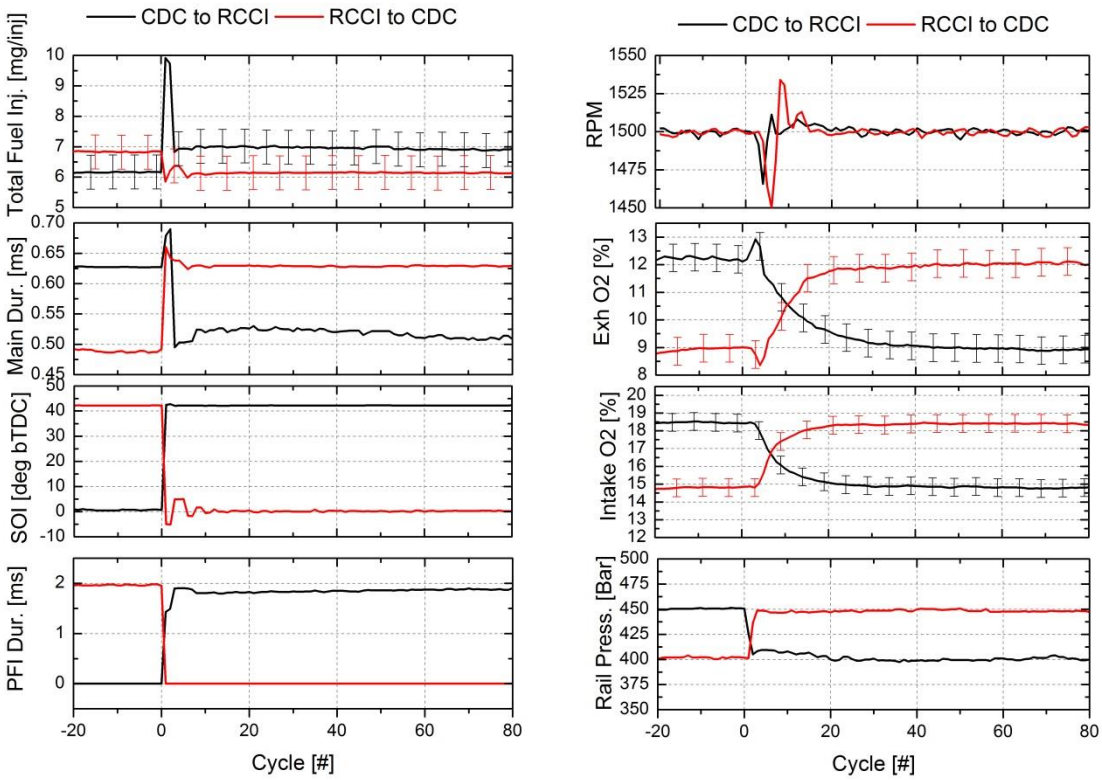

Figure 4.71 Fueling commands for the RCCI to CDC mode switch test

Chapter 5 Conclusions

5.1 General Multi-Cylinder RCCI Conclusions

A General Motors, 2005 model-year, light-duty EURO IV diesel engine was converted to RCCI operation and tested under a number of steady-state and transient operating conditions. Overall, it was found to be possible to adapt RCCI combustion to a multi-cylinder diesel engine with minimal physical modifications. At steady-state operating conditions, similar combustion and performance results to other SCE and MCE engines were seen. RCCI combustion yielded improvements in the engine-out PM and NO emissions compared to CDC operation over most of the presented operating points. However, some of those improvements were met with increased partial combustion products including HC and CO. Additionally, the lower exhaust temperatures with RCCI was shown to decrease aftertreatment performance.

RCCI combustion was found enable modest CO_2 reductions over CDC due to increases in thermal efficiency seen at higher loads [70]. Since the vehicle-out NO, HC, CO and PM emissions will likely be similar between RCCI and CDC engines, the ability to have lower engine-out emissions reduces the reliance on fuel efficiency reducing after-treatment devices (namely the DPF and SCR systems) to lower NO and PM emissions. Reduced use or elimination of these devices can offer thermal efficiency improvements on the order of 5% [27,28] and when combined with the higher thermal efficiencies seen at higher loads with RCCI, can offer efficiency

increases of 10% compared to CDC or upwards of 30% compared to current spark-ignition engines. If it were possible to replace all the light-duty spark-ignition engines in the US with RCCI engines, it could be possible to save 15% of the total 1,500 mmt CO_2 /yr. [18] light duty vehicle CO_2 emissions or roughly 180 mmt CO_2 /yr.

To further lower CO_2 emissions, the use of biofuel blends were investigated, but were shown to offer only modest savings in CO_2 compared to the baseline petroleum fuels. However, the use of biofuels did offer increased peak load, lower HC emissions and higher combustion efficiency with RCCI combustion. The use of E20 decreased combustion stability and had a slight increase in BSFC. Additionally, the net CO_2 gain from the fuel production process was not taken into account, which is beyond the scope of the work. However, an additional benefit of RCCI is that it can allow use of low carbon, gaseous fuels like natural gas, which can offer an additional 15% reduction in the yearly CO_2 emissions. If it were possible to able to implement RCCI natural gas engines in place of current gasoline spark-ignition engines, it could be possible to offer savings of 400 mmt CO_2 or 30% of the total US CO_2 emissions from light duty vehicles.

The use of a closed-loop engine controller was implemented into the Drivven ECU and was shown to offer improved control of the combustion phasing and emissions during transient RCCI operation. The main causes of the differences seen in the emissions and combustion performance when operating over transient vs. steady-state conditions were the engine thermodynamic boundary conditions. However, most of the results with the varying boundary conditions could be

explained from previous steady-state SCE test results [1-9]. Additional effects to the emissions and transient performance were hypothesized to have been due to intake manifold runner wall wetting, as is well known in port-injected gasoline engines.

The last set of testing involved using a closed-loop controller to adapt RCCI combustion to real-word operating conditions that are not normally tested in MCE and SCE laboratories. In one test, the engine was operated in the RCCI mode over a range of coolant temperatures with no outside manual inputs. The purpose of the test was to check the performance of the additional open-loop table corrections needed to keep the combustion phasing stable. Lastly, the possibility of switching between RCCI and CDC while the engine was running was investigated. With the assistance of the closed-loop controller, the combustion was able to be successfully switched from RCCI to CDC and back with minimal impact on emissions.

5.2 RCCI Load Transient Conclusions

For the first set of transient experiments, dual-fuel open-loop and closed-loop controlled RCCI combustion was compared to open-loop CDC at steady-state and in a tip-in step load change operating condition from 1-4 bar BMEP at 1,500 rev/min. Both combustion modes used similar intake conditions but the RCCI tests used with and without EGR. The CDC mode used a EURO IV type pilot-main fuel injection calibration while the RCCI mode was calibrated using best practices from past steady-state engine experiments. During the transient event, combustion performance, emissions were compared. From analyzing the cycle-resolved data, several conclusions were drawn from the work as follows:

1. It was possible to operate the engine in the RCCI mode over a transient load step change without significant issues.
2. Transient RCCI operation was able to be conducted with a relatively simple open-loop steady-state controller.
3. During the transient test, RCCI NO and PM levels were lower than those with CDC; however HC levels were higher than CDC as seen previously in steady-state tests.
4. The addition of a closed-loop controller lowered the HC emissions seen during the RCCI transient event.
5. The RCCI closed-loop controller was able to adjust CA50 towards the desired set point faster than the present open-loop controller could.
6. RCCI combustion minimized transient NO spikes compared to those seen in CDC operation.
7. RCCI combustion noise was the same or lower than that of the present EURO IV CDC engine calibration.
8. RCCI will likely require additional controls to match the CDC load capabilities, including model-based control to account for combustion chamber wall temperatures and PFI fueling transient effects, including fuel build up on the intake runner walls.

5.3 RCCI Load Transient Discussion

From the results it can be seen that RCCI operation was possible for the load transient conditions. While other LTC studies have reported some transient results

[99], strategies such as PPC have little-to-no reported transient results. This is unfortunate as it is important to investigate LTC performance under real-world operating conditions to ensure its practicality. In particular, this is a first RCCI transient study so many of the challenges of MCE operation were seen.

As with previous RCCI SCE tests [1-9], HC emissions were higher than the levels for CDC. Additionally, HC emissions were higher than those seen in SCE results, and were similar to other steady-state MCE results in the literature [76]. Reasons are still unknown why the present MCE had such high HC levels, but the thought is that the high HC levels result from using the stock piston geometry with its large top ring-land crevices, and is one of the main contributors to the reduced thermal efficiency [1-9].

With the observed lower combustion efficiency and increased pumping work, non-EGR RCCI had slightly lower BTE than CDC at low loads. While RCCI typically has lower heat transfer losses than CDC, the result of the reduced combustion efficiency and higher pumping work was a net loss in BTE at low-load conditions. However, when EGR was used with RCCI, the combustion efficiency increased and offered BTE levels that were similar to the CDC values. However, even with the improvement, more work is needed to further improve the low-load RCCI efficiency. The effort should focus on improved piston design and injection strategy optimization.

To address the HC and efficiency issues, future planned work will involve installing custom designed pistons to lower the compression ratio and top ring land

height. Steady-state MCE results with a first generation RCCI optimized piston bowl geometry have been presented by Hanson et al. [76]. They found that an open bowl design could lower MPRR and lead to increases in peak load. However, they did not see reductions in HC levels. A next generation piston design is currently being designed to have a 50% smaller crevice volume to reduce HC emissions while having similar bowl geometry as the first generation piston.

Similarly, due to the OEM re-entrant bowl shape, double direct-injection strategies for RCCI combustion were not found to offer better performance than a single injection in preliminary testing. However, in the work by Hanson et al. [99] the modified bowl shape did offer lower MHRR and emissions with multiple injections. The goal for the future experiments is to combine a smaller crevice volume piston design with a double-injection strategy to improve RCCI steady-state and transient performance.

Finally, the poor turbocharger response and low intake pressure levels seen at 1,500 rev/min. needs to be addressed to improve transient RCCI and CDC performance. Future work will involve installing a better matched turbocharger (and/or a supercharger) to have higher intake pressure and reduced pumping losses at low engine speeds.

5.4 Biofuel RCCI Load Transient Results

During testing with biofuel blends, open-loop and closed-loop controlled RCCI combustion was operated at steady-state and in a tip-in step load change operating condition from 1-4 bar BMEP at 1,500 rev/min. For each fuel, CA50 was held

constant with only changes to the EGR rate, PFI ratio and SOI timing to accommodate each fuel combination. During the transient event, combustion performance and emissions were compared. From analyzing the cycle-resolved data, several conclusions can be drawn from the work as follows:

1. The engine was able to operate with variety of biofuels with only minor changes to the fuel injection and air system parameters.
2. Ethanol fuel blends offered higher peak load, which allowed for a higher peak brake thermal efficiency.
3. Ethanol fuel blends also offered lower PFI ratios due to the need for an increased DI fuel fraction. This was shown to reduce HC during both steady-state and transient testing. The lower HC emissions were shown to offer increased combustion efficiency at higher loads.
4. B20 had an increased PFI ratio due to its higher CN than the baseline ULSD.
5. B20 was also shown to increase the transient response of the combustion phasing.
6. The use of biofuels showed to increase BSFC due to the lower heating values of the oxygenated fuels. However, the biofuels were shown to have higher BTE at high loads. They also were shown to have lower CO_2 emissions at all operating conditions.
7. Finally, E20 blends were shown to offer lower NO spike during transient testing due the lower PFI fractions.

5.5 Biofuel RCCI Load Transient Discussion

As with any kinetically controlled combustion mode, fuel properties are an important factor in the combustion and emissions performance. For biofuels, the main difference is their increased and decreased reactivity compared with petroleum fuels. Ethanol has a much lower reactivity compared with gasoline and that tends to slow the reaction rate and allow for higher loads and peak efficiency. Biodiesel usually has higher CN than ULSD which was shown to cause an increase in the PFI ratio to reduce the overall fuel reactivity. Both of these effects can cause slight changes to the emissions, typically increased NO with the lower PFI ratio when using ethanol blends and increased HC from increased PFI ratios when using high CN biodiesel. One side effect of using biofuels is that they tend to have oxygen in their chemical makeup which reduces the heating value, thus increasing the volumetric fuel consumption. This can be a hindrance to consumers as they are used to buying fuels priced on petroleum energy density. In addition, mass market biofuel will have to be price competitive with petroleum fuels on an energy basis.

Another impact of using biofuels is that the latent heat of vaporization can be much different than gasoline, which can cause some changes in the combustion event. While not reported, higher ethanol blends (E85) were initially investigated but were found to be difficult to use because of decreased combustion stability. While currently not fully understood, it is thought that the variation in intake temperature, when using a fuel with high latent heat of vaporization can cause cyclic variation in the cycle-by-cycle intake temperature which has been shown to influence of the

combustion phasing. Additional future work will be needed to investigate this phenomenon. Certain biofuels maybe way to reduce net CO_2 emissions from combustion sources, but that depends on their method of production, a discussion of which is beyond the scope of this work. Lastly, the presented biofuel tests did not have any significant drawbacks on the measured regulated emissions. Biofuels have been seen to cause partial combustion products, like the aldehydes to increase, but they also have less aromatics, like toluene and benzene. In future work, it is recommended to investigate these intermediate combustion products.

5.6 RCCI and CDC Speed Transient Conclusions

In this section, open-loop and closed-loop controlled RCCI combustion was operated in a tip-in speed load change from 1,000 to 2,000 rev/min. at 2.0 bar BMEP. During the transient event, combustion performance and emissions were compared to CDC. From analyzing the cycle-resolved data, several conclusions can be drawn from the work as follows:

1. It was possible to operate the engine satisfactorily using RCCI combustion during speed transient conditions.
2. Engine speed transient RCCI operation was able to be conducted with either an open or closed-loop controller.
3. During the speed transients, NO and PM levels were considerably lower than those possible with CDC.
4. Conversely, during the speed transients, HC levels were considerably higher than those seen with CDC.

5. RCCI was capable of operating over a wide variety of engine operating conditions for engine speed, pedal position, MAF, EGR, intake temperature and intake pressure.
6. RCCI operation will likely require additional controls to match the CDC load performance, including model-based control to account for combustion chamber wall temperatures and PFI fueling transient effects.

5.7 RCCI and CDC Speed Transient Discussion

While it can be seen that RCCI combustion was able to operate over engine speed transients, there are some points of interest to be discussed. First, it was interesting to see how well RCCI responded to engine speed changes, but as Glewen [76] showed, an engine speed transient acts a lot like a step-up and then a step-down load transient. Future work should look at load transients as a more fundamental test of transient engine performance.

Second, it should be noted that this work was a first attempt at transient RCCI operation and future results will almost certainly be improved. The reason for some of the poorer results seen was that a majority of the operating points used were calibrated at steady-state for exact pedal positions. During the transient tests, at certain engine speeds, the pedal position could differ by +/-5 % from the steady-state values, as shown in Figure 5.1 and Figure 5.2. This was unexpected and only seen during post processing of the data. However, the present results are representative enough to show that RCCI can be operated satisfactorily over engine speed transients. Better calibration of specific operating points in the low engine

speed, high pedal position, and high engine speed, low pedal position, ranges should be able to improve NO and HC emissions with better control of the PFI ratio, intake pressure and EGR rate.

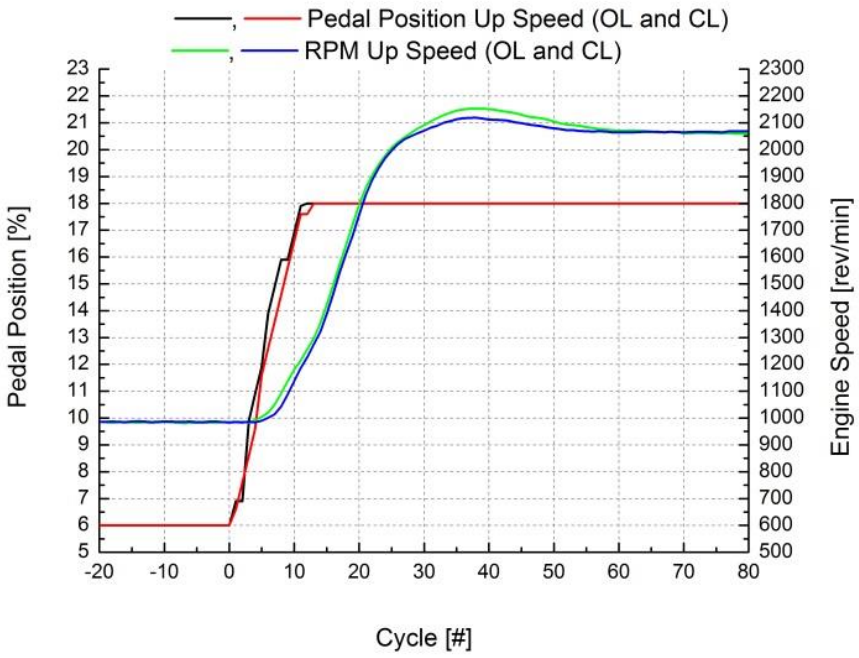

Figure 5.1 RCCI up-speed engine speed and pedal position

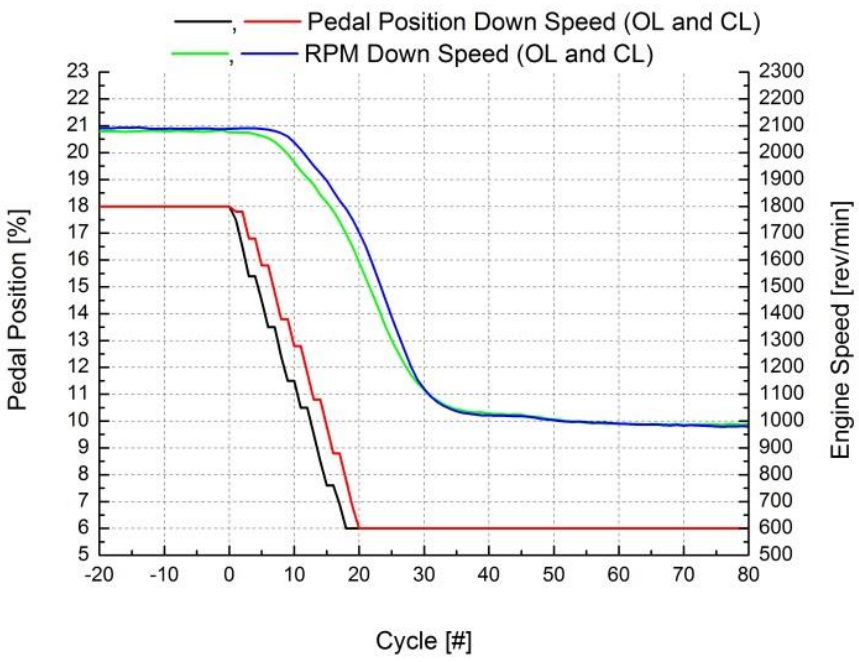

Figure 5.2 RCCI down-speed engine speed and pedal position

High overall HC emissions are still present and new solutions are being considered and implemented. As mentioned above, future work will involve installing custom designed pistons to optimize RCCI [97] by lowering the compression ratio and top ring land height. However, even when constrained by the OEM setup, the current RCCI setup was able to offer low NO and near zero PM with high thermal efficiency.

Additional future work could be done to investigate the feasibility of adding port-fuel enrichment and/or wall temperature model-based controls to the controller in order to correct some of the transient emission issues. Further feed forward and/or model based controls will likely be needed to operate at higher loads and when doing larger load transients.

5.8 RCCI Cold Start Results

To test the real-world application of RCCI and the closed-loop combustion phasing controller, RCCI was tested by operating at much cooler coolant temperatures than normal. The only adjustments made were made to the closed-loop controller and additional coolant temperature based tables. The test condition was 1,500 rev/min. at 1.0 bar BMEP to simulate operation just after cranking when the engine is cold. From analyzing the cycle-resolved data, several conclusions can be drawn from the work as follows:

1. The open-loop tables modified SOI timing and PFI ratio as designed, and allowed RCCI to be operated from 48°C to 85°C. More development of the controller table values will likely add improved performance at even lower temperatures.
2. HC emissions increased with ECT and PFI ratio.
3. NO was lower than expected and decreased with ECT and PFI ratio.
4. MPRR dropped with ECT from the higher PFI ratio and SOI timing changes.

5.9 RCCI Cold Start Discussion

This test was a first attempt and much was learned and the results could be improved. Use of open-loop tables to limit the range of the closed-loop adjustment is a method used by OEMs and could provide a basic starting point for an RCCI cold start strategy. Due to the way the gasoline fueling is calculated, more work is

needed to ensure that the total fueling is the same between RCCI and CDC for the same pedal position.

For future tests, the use of non-standard injection timings could be used with late or post injections. If it were possible to bypass the EGR cooler, a larger quantity of hot EGR should help increase the combustion efficiency, as seen in the baseline G/D tests. Increasing the charge gas temperature by using variable cam timing to increase the trapped residual and/or reducing the trapped mass could also be helpful. Cold starting is a complex problem that OEMs spend significant amounts of money and time on, but it can be seen that using the prescribed method of the present study is a good starting point.

5.10 RCCI to CDC Mode Switch Results

For the final RCCI tests, closed-loop RCCI and CDC combustion modes were switched between while the engine was firing at 1,500 rev/min. 2.0 bar BMEP. From analyzing the cycle-resolved data, several conclusions can be drawn from the work as follows:

1. It was possible to switch combustion modes readily while the engine was running with just the closed-loop controller.
2. Most emissions followed the steady-state values, except for HC, which spiked when RCCI was switched to CDC.
3. There was a slight BMEP drop during the RCCI to CDC transition, which caused the high HC emissions.

5.11 RCCI to CDC Mode Switch Discussion

This test was conducted more easily than expected, especially since the only code used was to instantaneously flip between the stored table values. Switching between RCCI and CDC during a transient speed and load test would be of interest. Mode switching may be very important if low temperature oxidation catalysts are not available. Without appropriate oxidation catalysts, commercial implementation of RCCI may be difficult. Another use could be at high load where the combustion noise is limiting for RCCI. Switching to CDC could increase the power density of the engine in areas where the engine emission regulations are less stringent.

Chapter 6 References

1. Hanson, R., Kokjohn, S., Splitter, D., and Reitz, R., "An Experimental Investigation of Fuel Reactivity Controlled PCCI Combustion in a Heavy-Duty Engine," SAE Int. J. Engines 3(1):700-716, 2010, doi:10.4271/2010-01-0864.
2. Splitter, D., Reitz, R., and Hanson, R., "High Efficiency, Low Emissions RCCI Combustion by Use of a Fuel Additive," *SAE Int. J. Fuels Lubr.* 3(2):742-756, 2010, doi:10.4271/2010-01-2167.
3. Kokjohn, S., Hanson, R., Splitter, D., and Reitz, R., "Experiments and Modeling of Dual-Fuel HCCI and PCCI Combustion Using In-Cylinder Fuel Blending," *SAE Int. J. Engines* 2(2):24-39, 2010, doi:10.4271/2009-01-2647.
4. Hanson, R., Kokjohn, S., Splitter, D., and Reitz, R., "Fuel Effects on Reactivity Controlled Compression Ignition (RCCI) Combustion at Low Load," *SAE Int. J. Engines* 4(1):394-411, 2011, doi:10.4271/2011-01-0361.
5. Kokjohn, S., Hanson, R., Splitter, D., Kaddatz, J. et al., "Fuel Reactivity Controlled Compression Ignition (RCCI) Combustion in Light- and Heavy-Duty Engines," *SAE Int. J. Engines* 4(1):360-374, 2011, doi:10.4271/2011-01-0357.
6. Splitter, D., Hanson, R., Kokjohn, S., and Reitz, R., "Reactivity Controlled Compression Ignition (RCCI) Heavy-Duty Engine Operation at Mid-and High-Loads with Conventional and Alternative Fuels," SAE Technical Paper 2011-01-0363, 2011, doi:10.4271/2011-01-0363.
7. Splitter, D., Hanson, R., Kokjohn, S., Wissink, M. et al., "Injection Effects in Low Load RCCI Dual-Fuel Combustion," SAE Technical Paper 2011-24-0047, 2011, doi:10.4271/2011-24-0047.
8. Curran, S., Prikhodko, V., Cho, K., Sluder, C. et al., "In-Cylinder Fuel Blending of Gasoline/Diesel for Improved Efficiency and Lowest Possible Emissions on a Multi-Cylinder Light-Duty Diesel Engine," SAE Technical Paper 2010-01-2206, 2010, doi:10.4271/2010-01-2206.
9. Curran, S., Hanson, R., and Wagner, R., "Effect of E85 on RCCI Performance and Emissions on a Multi-Cylinder Light-Duty Diesel Engine," SAE Technical Paper 2012-01-0376, 2012, doi:10.4271/2012-01-0376.
10. Heywood, J., "Internal Combustion Engines Fundamentals", McGraw-Hill, Inc., St. Louis, 1988.
11. Kittelson, D. B., Engines and nanoparticles: a review, Journal of Aerosol Science, Volume 29, Issues 5–6, 1 June 1998, Pages 575-588, ISSN 0021-8502, 10.1016/S0021-8502(97)10037-4.
12. Solomon, A., S., D. Qin, M. Manning, R.B. Alley, T. Berntsen, N.L. Bindoff, Z. Chen, A. Chidthaisong, J.M. Gregory, G.C. Hegerl, M. Heimann, B. Hewitson, B.J. Hoskins, F. Joos, J. Jouzel, V. Kattsov, U. Lohmann, T. Matsuno, M. Molina, N. Nicholls, J., Overpeck, G. Raga, V. Ramaswamy, J. Ren, M. Rusticucci, R. Somerville, T.F. Stocker, P. Whetton, R.A. Wood and D. Wratt, 2007: Technical Summary. In: Climate Change 2007: The Physical Science Basis. Contribution of Working Group I to the Fourth

Assessment Report of the Intergovernmental Panel on Climate Change [Solomon, S., D. Qin, M. Manning, Z. Chen, M. Marquis, K.B. Averyt, M. Tignor and H.L. Miller (eds.)].Cambridge University Press, Cambridge, United Kingdom and New York, NY, USA.

13. CFR, 2012. US Code of Federal Regulations, Title 40, Part 86, Appendix I, Revised as of July 1, 2012, 543-610, http://www.gpo.gov/fdsys/pkg/CFR-2012-title40-vol20/pdf/CFR-2012-title40-vol20.pdf.
14. Samulski, M. and Jackson, C., "Effects of Steady-State and Transient Operation on Exhaust Emissions from Nonroad and Highway Diesel Engines," SAE Technical Paper 982044, 1998, doi: 10.4271/982044.
15. Swain, D., Jackson, C., Lindhjem, C., and Hoffman, G., "A Method for Comparing Transient NOx Emissions With Weighted Steady State Test Results," SAE Technical Paper 980408, 1998, doi: 10.4271/980408.
16. Shindell D., *et. al.,"*Simultaneously Mitigating Near-Term Climate Change and Improving Human Health and Food Security", *Science* 335, 183 (2012); DOI: 10.1126/science.1210026.
17. US EPA, Report to Congress on Black Carbon, 2010.
18. US Energy Information Agency, International Energy Outlook, 2013.
19. Edwards, K. D., "Defining Engine Efficiency Limits", DEER Conference 2011.
20. Caton, J., "Thermodynamic Advantages of Low Temperature Combustion (LTC) Engines Using Low Heat Rejection (LHR) Concepts," SAE Technical Paper 2011-01-0312, 2011, doi:10.4271/2011-01-0312.
21. Arias, D., Shedd, T., and Jester, R., "Theoretical Analysis of Waste Heat Recovery from an Internal Combustion Engine in a Hybrid Vehicle," SAE Technical Paper 2006-01-1605, 2006, doi:10.4271/2006-01-1605.
22. Ringler, J., Seifert, M., Guyotot, V., and Hübner, W., "Rankine Cycle for Waste Heat Recovery of IC Engines," *SAE Int. J. Engines* 2(1):67-76, 2009, doi:10.4271/2009-01-0174.
23. Foster, D. E., "Pragmatic Thermodynamic Efficiency Limits for IC Engines", Combustion Engine Efficiency Colloquium, 2010.
24. Killingsworth, N., Rapp, V., Flowers, D., Aceves, S., Chen, J. and Dibble, R., "Increased Efficiency in SI Engine with Air Replaced by Oxygen in Argon Mixture", 33rd Intl. Symposium on Combustion, Beijing, China, 2010.
25. Dec, J., "A Conceptual Model of DI Diesel Combustion Based on Laser-Sheet Imaging", SAE Paper, 970873
26. Turns, S., "An Introduction to Combustion Concepts and Applications", McGraw-Hill, ISBN 0-07-911812-7, 1996.
27. Johnson, T., "Diesel Emission Control in Review," SAE Technical Paper 2007-01-0233, 2007, doi:10.4271/2007-01-0233.
28. Stanton, D., "Technology Development for High Efficiency Clean Diesel Engines and a Pathway to 50% Thermal Efficiency", presentation at US Department of Energy Directions in Engine Efficiency and Emissions Research (DEER) Conference, Dearborn, Michigan, August 2009.

29. Musculus, M., Miles, P., and Pickett, L., “Conceptual Models for Partially Premixed Low-temperature diesel Combustion”, Progress in Energy and Combustion Science, Volume 39, Issues 2–3, April–June 2013, Pages 246–283, http://dx.doi.org/10.1016/j.pecs.2012.09.001.
30. Onishi, S., Jo, S., Shoda, K., Jo, P. et al., "Active Thermo-Atmosphere Combustion (ATAC) - A New Combustion Process for Internal Combustion Engines," SAE Technical Paper 790501, 1979, doi:10.4271/790501.
31. Najt, P. and Foster, D., "Compression-Ignited Homogeneous Charge Combustion," SAE Technical Paper 830264, 1983, doi:10.4271/830264.
32. Thring, R., "Homogeneous-Charge Compression-Ignition (HCCI) Engines," SAE Technical Paper 892068, 1989, doi:10.4271/892068.
33. Sjöberg, M. and Dec, J., "Effects of Engine Speed, Fueling Rate, and Combustion Phasing on the Thermal Stratification Required to Limit HCCI Knocking Intensity," SAE Technical Paper 2005-01-2125, 2005, doi:10.4271/2005-01-2125.
34. Dec, J., Yang, Y., and Dronniou, N., "Boosted HCCI - Controlling Pressure-Rise Rates for Performance Improvements using Partial Fuel Stratification with Conventional Gasoline," *SAE Int. J. Engines* 4(1):1169-1189, 2011, doi:10.4271/2011-01-0897.
35. Krasselt, J., Foster, D., Ghandhi, J., Herold, R. et al., "Investigations into the Effects of Thermal and Compositional Stratification on HCCI Combustion – Part I: Metal Engine Results," SAE Technical Paper 2009-01-1105, 2009, doi:10.4271/2009-01-1105.
36. Dec, J., Hwang, W., Sjöberg, M., “An Investigation of Thermal Stratification in HCCI Engines Using Chemiluminescence Imaging”, SAE Paper, 2006-01-1518.
37. Dec, J., Sjöberg, M., ” Smoothing HCCI Heat-Release Rates Using Partial Fuel Stratification with Two-Stage Ignition Fuels”, SAE Paper, 2006-01-0629.
38. Hanson, R., Splitter, D., and Reitz, R., "Operating a Heavy-Duty Direct-Injection Compression-Ignition Engine with Gasoline for Low Emissions," SAE Technical Paper 2009-01-1442, 2009, doi:10.4271/2009-01-1442.
39. Loeper, P., “Experimental Investigation of Gasoline Compression Ignitino Combustion in a Light Duty Diesel Engine”, Ph.D. Thesis University of Wisconsin-Madison, 2013.
40. Manente, V., Zander, C., Johansson, B., Tunestal, P. et al., "An Advanced Internal Combustion Engine Concept for Low Emissions and High Efficiency from Idle to Max Load Using Gasoline Partially Premixed Combustion," SAE Technical Paper 2010-01-2198, 2010, doi:10.4271/2010-01-2198.
41. Kalghatgi, G., Risberg, P., Ångström, H.-E., ”Partially Pre-Mixed Auto-Ignition of Gasoline to Attain Low Smoke and Low NOx at High Load in a Compression Ignition Engine and Comparison with a Diesel Fuel”, SAE Paper, 2007-01-0006.

42. Inagaki, K., Fuyuto, T., Nishikawa, K., Nakakita, K. et al., "Dual-Fuel PCI Combustion Controlled by In-Cylinder Stratification of Ignitability," SAE Technical Paper 2006-01-0028, 2006, doi:10.4271/2006-01-0028.
43. Kokjohn, S., Hanson, R., Splitter, D. and Reitz, R., "Fuel reactivity controlled compression ignition (RCCI): a pathway to controlled high-efficiency clean combustion", *International Journal of Engine Research 2011 12:209-226; doi:10.1177/1468087411401548.*
44. Prikhodko, V., Curran, S., Barone, T., Lewis, S. et al., "Emission Characteristics of a Diesel Engine Operating with In-Cylinder Gasoline and Diesel Fuel Blending," *SAE Int. J. Fuels Lubr.* 3(2):946-955, 2010, doi:10.4271/2010-01-2266.
45. Prikhodko, V., Curran, S., Barone, T., Lewis, S., Storey, J., Cho, K., Wagner, R., Parks, J., et al., "Diesel Oxidation Catalyst Control of Hydrocarbon Aerosols From Reactivity Controlled Compression Ignition Combustion", Paper No. IMECE2011-64147, pp. 273-278; 6 pages doi:10.1115/IMECE2011-6414
46. Ando, H., Yasuyuki, S., "Universal Rule of Hydrocarbon Oxidation", SAE Paper, 2009-01-0948.
47. Sun, Y., "Diesel Combustion Optimization and Emissions Reduction Using Adaptive Injection Strategies (AIS) with Improved Numerical Models", PhD Thesis, University of Wisconsin--Madison, 2007.
48. Kamimoto, T. and Bae, M., "High Combustion Temperature for the Reduction of Particulate in Diesel Engines," SAE Technical Paper 880423, 1988, doi:10.4271/880423.
49. Erlandsson, O., Johansson, B., and Silversand, F., "Hydrocarbon (HC) Reduction of Exhaust Gases from a Homogeneous Charge Compression Ignition (HCCI) Engine Using Different Catalytic Mesh-Coatings," SAE Technical Paper 2000-01-1847, 2000, doi:10.4271/2000-01-1847.
50. Epping, K., Aceves, S., Bechtold, R., and Dec, J., "The Potential of HCCI Combustion for High Efficiency and Low Emissions," SAE Technical Paper 2002-01-1923, 2002, doi:10.4271/2002-01-1923.
51. http://www.msnbc.msn.com/id/15233556/ns/us_news-environment/t/renewable-energy-has-icon-henry-ford/#.T2pVItV1zcs
52. http://www.radford.edu/wkovarik/papers/fuel.html
53. Yanowitz, J., and McCormick, R., "Effect of E85 on Tailpipe Emissions from Light-Duty Vehicles", ISSN:1047-3289 J. Air & Waste Manage. Assoc. 59:172–182 DOI:10.3155/1047-3289.59.2.172.
54. http://www.biodiesel.org/what-is-biodiesel/biodiesel-basics, ASTM D 6751
55. http://lipidlibrary.aocs.org/history/Diesel/index.htm
56. US Environmental Protection Agency, "A Comprehensive Analysis of Biodiesel Impacts on Exhaust Emissions", EPA420-P-02-001 October 2002.

57. Mueller, C., Boehman, A., and Martin, G., "An Experimental Investigation of the Origin of Increased NO_x Emissions When Fueling a Heavy-Duty Compression-Ignition Engine with Soy Biodiesel," *SAE Int. J. Fuels Lubr.* 2(1):789-816, 2009, doi:10.4271/2009-01-1792.
58. Tran, H., "Investigation of Fuel Property and Biodiesel Effects In a Highly Dilute Low Temperature Combustion Regime with a Light-Duty Diesel Engine", M.S. Thesis, University of Wisconsin-Madison 2010.
59. Zheng, M., Wang, M., Reader, G., Mulenga, M. et al., "An Improvement on Low Temperature Combustion in Neat Biodiesel Engine Cycles," *SAE Int. J. Fuels Lubr.* 1(1):1120-1132, 2009, doi:10.4271/2008-01-1670.
60. Veltman, M., Karra, P., and Kong, S., "Effects of Biodiesel Blends on Emissions in Low Temperature Diesel Combustion," SAE Technical Paper 2009-01-0485, 2009, doi:10.4271/2009-01-0485.
61. Northrop, W., Bohac, S., and Assanis, D., "Premixed Low Temperature Combustion of Biodiesel and Blends in a High Speed Compression Ignition Engine," *SAE Int. J. Fuels Lubr.* 2(1):28-40, 2009, doi:10.4271/2009-01-0133.
62. Brakora, J. and Reitz, R., "Investigation of NOx Predictions from Biodiesel-fueled HCCI Engine Simulations Using a Reduced Kinetic Mechanism," SAE Technical Paper 2010-01-0577, 2010, doi:10.4271/2010-01-0577.
63. Szybist, J., McFarlane, J., and Bunting, B., "Comparison of Simulated and Experimental Combustion of Biodiesel Blends in a Single Cylinder Diesel HCCI Engine," SAE Technical Paper 2007-01-4010, 2007, doi:10.4271/2007-01-4010
64. Bunting, B., Eaton, S., Crawford, R., Xu, Y. et al., "Performance of Biodiesel Blends of Different FAME Distributions in HCCI Combustion," SAE Technical Paper 2009-01-1342, 2009, doi:10.4271/2009-01-1342.
65. Olsson, J., Tunestål, P., Haraldsson, G., and Johansson, B., "A Turbo Charged Dual Fuel HCCI Engine," SAE Technical Paper 2001-01-1896, 2001, doi:10.4271/2001-01-1896.
66. Sjoberg, M. and Dec, J., "Ethanol Autoignition Characteristics and HCCI Performance for Wide Ranges of Engine Speed, Load and Boost," *SAE Int. J. Engines* 3(1):84-106, 2010, doi:10.4271/2010-01-0338.
67. Curran, S., Hanson R. and Wagner, R., "Reactivity controlled compression ignition combustion on a multi-cylinder light-duty diesel engine", International Journal of Engine Research 1468087412442324, first published on April 26, 2012 doi:10.1177/1468087412442324.
68. Flowers, D., Aceves, S., and Frias, J., "Improving Ethanol Life Cycle Energy Efficiency by Direct Utilization of Wet Ethanol in HCCI Engines," SAE Technical Paper 2007-01-1867, 2007, doi:10.4271/2007-01-1867.

69. Dempsey, A., Adhikary, B. Das, Viswanathan, S. and Reitz, R., "Reactivity Controlled Compression Ignition (RCCI) Using Premixed Hydrated Ethanol and Direct Injection Diesel", ASME Conf. Proc. 2011, 963 (2011), DOI:10.1115/ICEF2011-60235
70. Hanson, R., Curran, S., Wagner, R., and Reitz, R., "Effects of Biofuel Blends on RCCI Combustion in a Light-Duty, Multi-Cylinder Diesel Engine," *SAE Int. J. Engines* 6(1):488-503, 2013, doi:10.4271/2013-01-1653.
71. Chadwell, C. and Mehta, D., "Development of a Transient-Capable Multi-Cylinder HCCI Engine," SAE Technical Paper 2010-01-1244, 2010, doi:10.4271/2010-01-1244.
72. Stanglmaier, R., Ryan, T., and Souder, J., "HCCI Operation of a Dual-Fuel Natural Gas Engine for Improved Fuel Efficiency and Ultra-Low NOx Emissions at Low to Moderate Engine Loads," SAE Technical Paper 2001-01-1897, 2001, doi:10.4271/2001-01-1897.
73. Dahl, D. and Denbratt, I., "HCCI/SCCI Load Limits and Stoichiometric Operation in a Multi-cylinder Naturally Aspirated Spark Ignition Engine Operated on Gasoline and E85", International Journal of Engine Research February 1, 2011 12: 58-68, doi:10.1177/14680874JER392450.
74. Final Report for Caterpillar/DOE Heavy Truck Clean Diesel Cooperative Research Program DOE contract No. DE-FC05-00OR22806
75. CFR, 2012. US Code of Federal Regulations, Title 40, Part 86, Appendix I, Revised as of July 1, 2012, 543-610, http://www.gpo.gov/fdsys/pkg/CFR-2012-title40-vol20/pdf/CFR-2012-title40-vol20.pdf.
76. Eastwood, P., Tufail, K., Winstanley, T., Darlington, A. et al., "Estimation of Deviations in NO and Soot Emissions Between Steady- State and EUDC Transient Operation of a Common-Rail Diesel Engine," *SAE Int. J. Engines* 2(2):648-659, 2010, doi:10.4271/2009-24-0147.
77. Lindgren, A., Larsson, G., and Hansson, P.A., "Evaluation of factors influencing emissions from tractors and construction equipment during realistic work operations using diesel fuel and bio-fuels as substitute," Biosystems Engineering, 107, pp 123-130, 2010.
78. Hagena, J., Filipi, Z., and Assanis, D., "Transient Diesel Emissions: Analysis of Engine Operation During a Tip-In," SAE Technical Paper 2006-01-1151, 2006, doi:10.4271/2006-01-1151.
79. Glewen, W., "Experimental Investigation of Transient Operation and Low Temperature Combustion in a Light Duty Diesel Engine", Ph.D. Thesis University of Wisconsin-Madison, 2012.
80. Lapuerta, M., Martos, F. J., Cardenas, M. D., "Determination of Light Extinction Efficiency of Diesel Soot from Smoke Opacity Measurements," Measurement Science and Technology 16, 2048-2055, 2005.
81. AVL. "Smoke Measurement," AVL LIST GMBH. Graz. 2001.
82. Burton, J.L., "Investigation of Transient Emissions and Mixed Mode Combustion for a Light Duty Diesel Engine," MS. Thesis, Engine Research Center, Dept. of Mechanical Engineering, University of Wisconsin - Madison, 2008.

83. Feist, M., “Implementation of a Transient Hydrostatic Engine Dynamometer,” MS Thesis. University of Wisconsin, Madison, 2001.
84. Williams, D.R., “Transient Effect of Speed and Load on Low Temperature Diesel Combustion”, M.S. Thesis, Department of Mechanical Engineering, University of Wisconsin, Madison, 2008.
85. Chang, K., Lavoie, G., Babajimopoulos, A., Filipi, Z. et al., "Control of a Multi-Cylinder HCCI Engine During Transient Operation by Modulating Residual Gas Fraction to Compensate for Wall Temperature Effects," SAE Technical Paper 2007-01-0204, 2007, doi:10.4271/2007-01-0204.
86. Shahlari, A., Hocking, C., Kurtz, E., and Ghandhi, J., "Comparison of Compression Ignition Engine Noise Metrics in Low-Temperature Combustion Regimes," *SAE Int. J. Engines* 6(1):541-552, 2013, doi:10.4271/2013-01-1659.
87. Stivender, D., "Development of a Fuel-Based Mass Emission Measurement Procedure," SAE Technical Paper 710604, 1971, doi:10.4271/710604.
88. Ghandi, J., Private Communication.
89. Dempsey, A., "Dual-Fuel Reactivity Controlled Compression Ignition (RCCI) with Alternative Fuels." Order No. 3591404 The University of Wisconsin - Madison, 2013. Ann Arbor: *ProQuest.* Web. 12 Nov. 2013.
90. Kokjohn, Sage L., "Reactivity Controlled Compression Ignition (RCCI) Combustion," Ph.D. Thesis, Engine Research Center, Dept. of Mechanical Engineering, University of Wisconsin - Madison, 2012.
91. Curran, S., Hanson, R., Wagner, R., and Reitz, R., "Efficiency and Emissions Mapping of RCCI in a Light-Duty Diesel Engine," SAE Technical Paper 2013-01-0289, 2013, doi:10.4271/2013-01-0289.
92. Splitter, D.A., Hanson, R.M. , Kokjohn, S.L., Reitz, R.D., "Improving Engine Performance by Optimizing Fuel Reactivity with a Dual Fuel PCCI Strategy", Thiesel 2010 Conference, 2010.
93. Shan, X., Burl, J., Jankovic, M., and Cooper, S., "Transient Fuel X-Tau Parameter Estimation Using Short Time Fourier Transform," SAE Technical Paper 2008-01-1305, 2008, doi:10.4271/2008-01-1305.
94. Wilhelmsson, C., Vressner, A., Tunestål, P., Johansson, B. et al., "Combustion Chamber Wall Temperature Measurement and Modeling During Transient HCCI Operation," SAE Technical Paper 2005-01-3731, 2005, doi:10.4271/2005-01-3731.
95. Glewen, W., Heuwetter, D., Foster, D., Andrie, M. et al., "Analysis of Deviations from Steady State Performance During Transient Operation of a Light Duty Diesel Engine," *SAE Int. J. Engines* 5(3):2012, doi: 10.4271/2012-01-1067.
96. Chang, K., Lavoie, G., Babajimopoulos, A., Filipi, Z. et al., "Control of a Multi-Cylinder HCCI Engine During Transient Operation by Modulating Residual Gas Fraction to Compensate for Wall Temperature Effects," SAE Technical Paper 2007-01-0204, 2007, doi:10.4271/2007-01-0204.
97. Hanson, R., Curran, S., Wagner, R., Kokjohn, S. et al., "Piston Bowl Optimization for RCCI Combustion in a Light-Duty Multi-Cylinder Engine," *SAE Int. J. Engines* 5(2):286-299, 2012, doi:10.4271/2012-01-0380.

98. Splitter, D., Wissink, M., DelVescovo, D., and Reitz, R., "RCCI Engine Operation Towards 60% Thermal Efficiency," SAE Technical Paper 2013-01-0279, 2013, doi:10.4271/2013-01-0279.
99. Hanson, R. and Reitz, R., "Transient RCCI Operation in a Light-Duty Multi-Cylinder Engine," *SAE Int. J. Engines* 6(3):1694-1705, 2013, doi:10.4271/2013-24-0050.

Chapter 7 Appendix

7.1 RCCI Biofuel Up-Load Changes OL

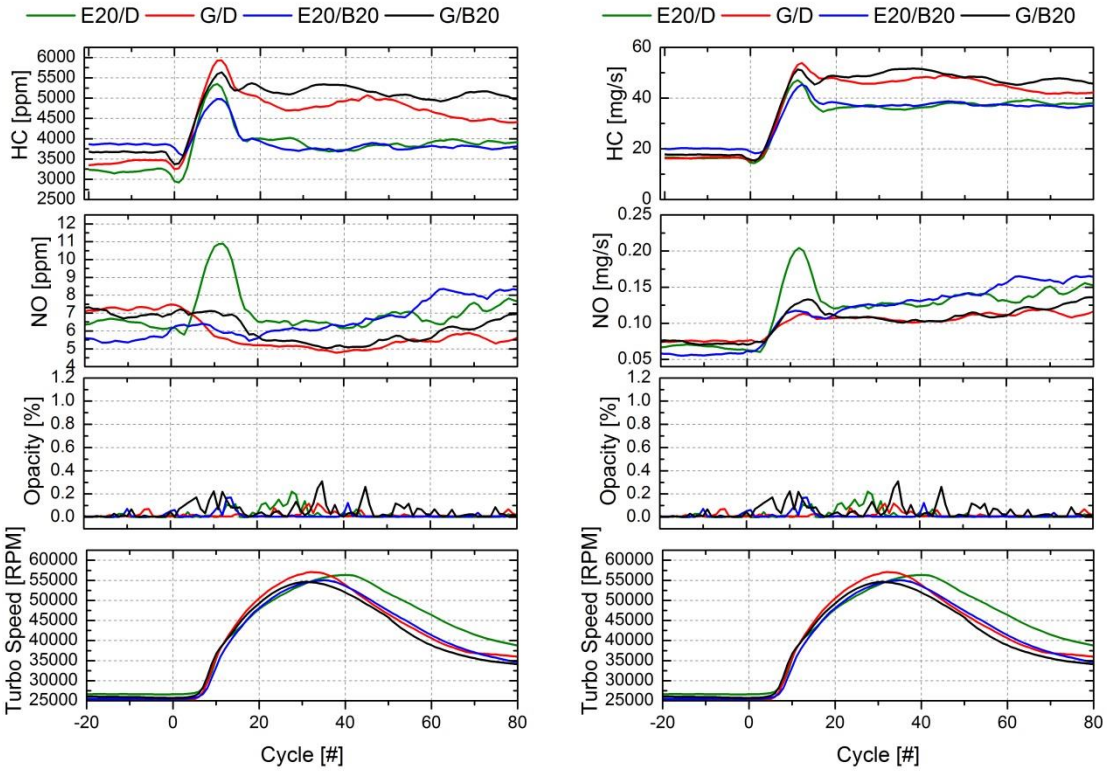

Figure 7.1 Up-load transient biofuel RCCI OL emissions results

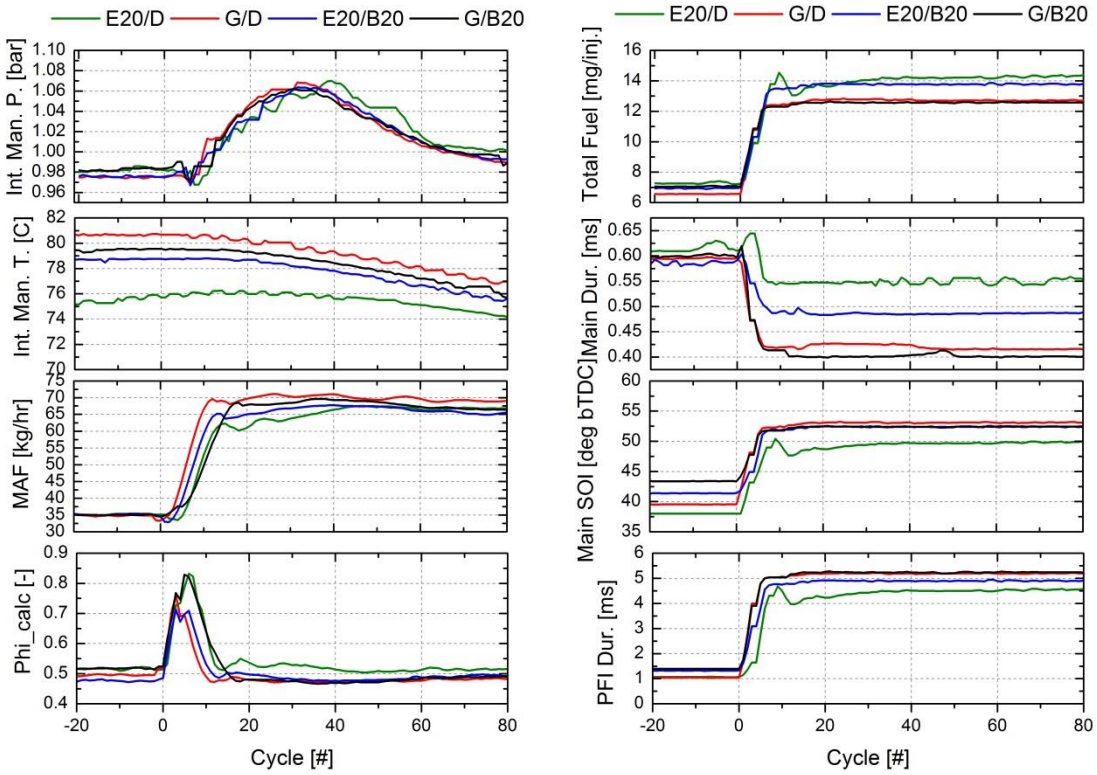

Figure 7.2 Up-load transient biofuel RCCI OL air and fuel system results

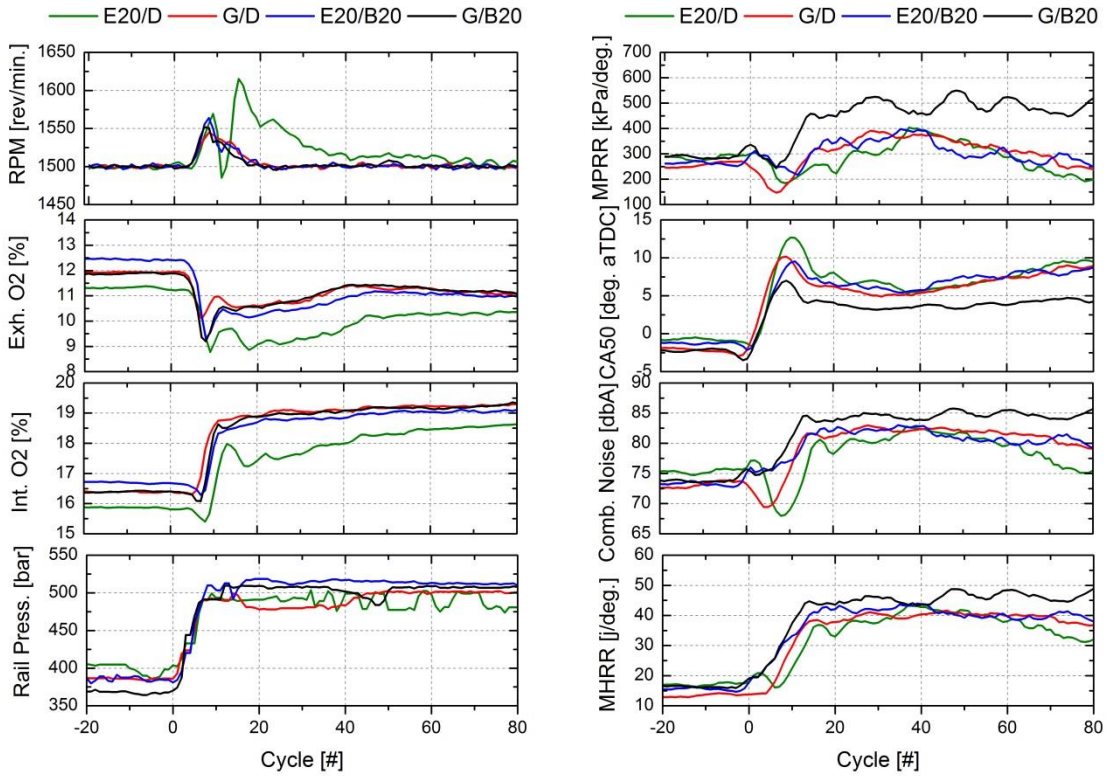

Figure 7.3 Up-load transient biofuel RCCI OL combustion performance results

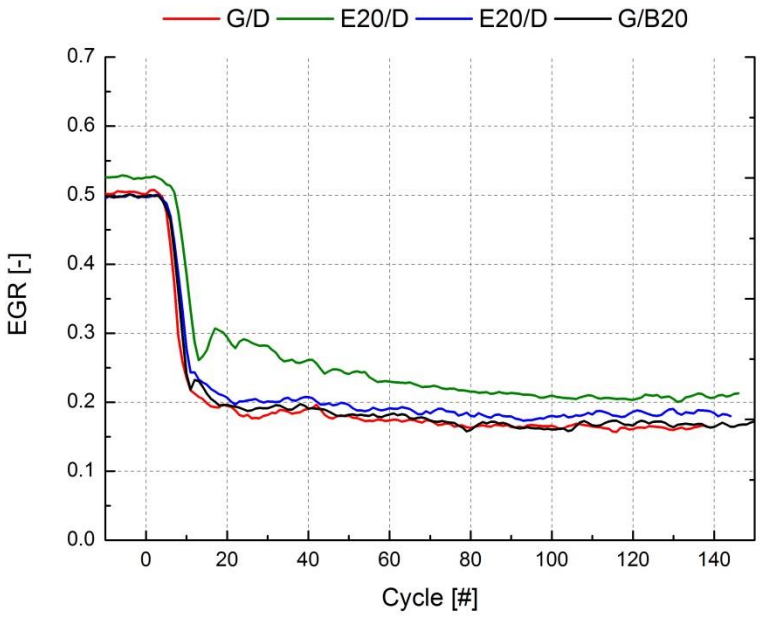

Figure 7.4 Up-load transient biofuel RCCI OL EGR performance

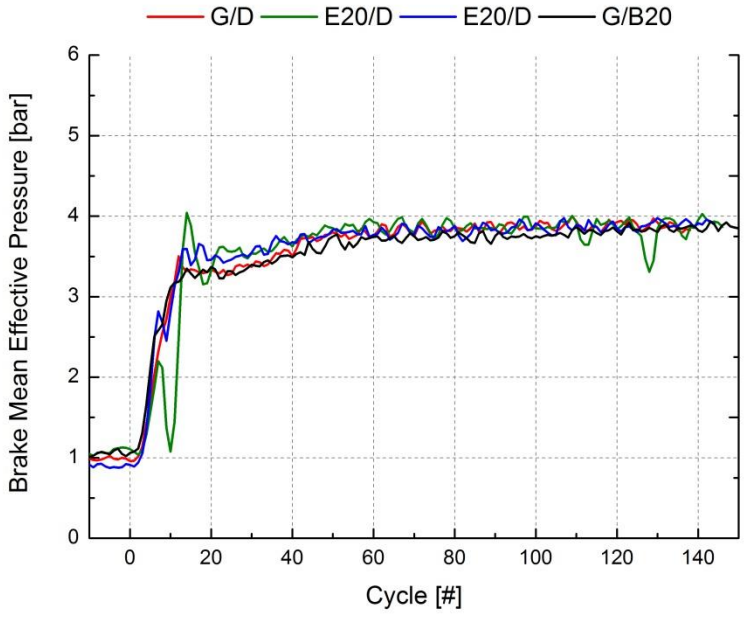

Figure 7.5 Up-load transient biofuel RCCI OL BMEP results

7.2 Down-Load RCCI Biofuel OL Tests

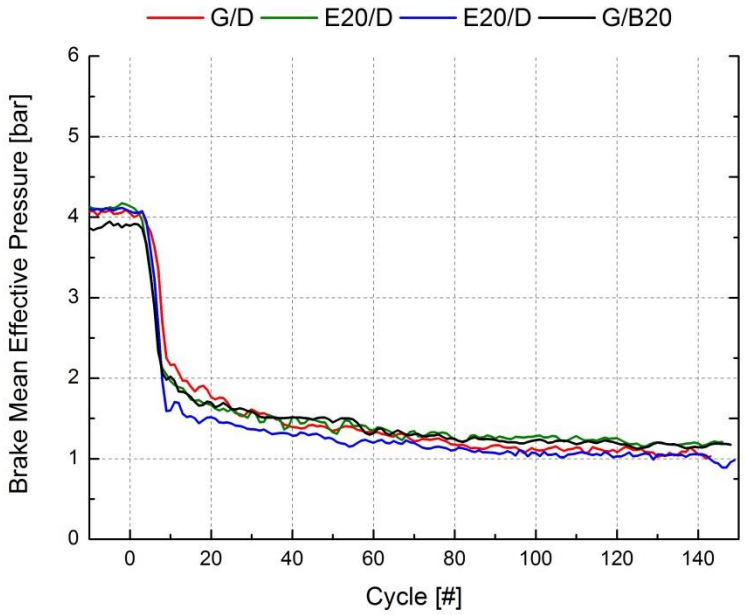

Figure 7.6 Down-load transient biofuel RCCI OL BMEP results

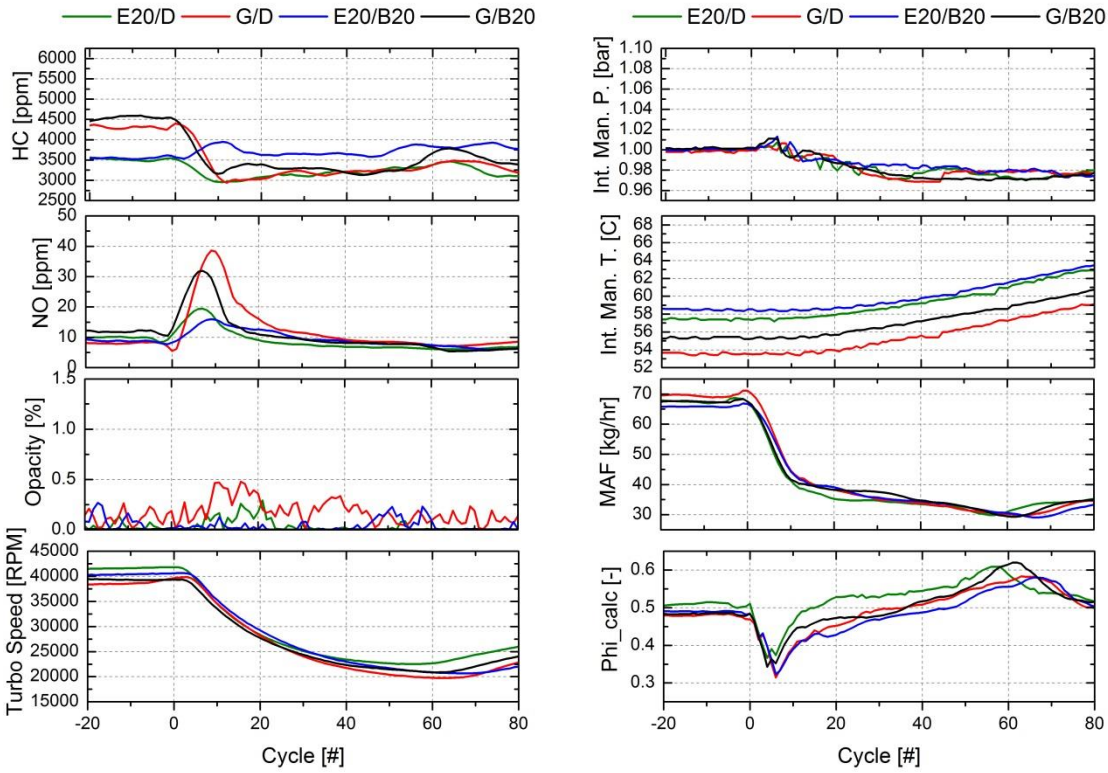

Figure 7.7 Down-load transient biofuel RCCI OL emissions and intake results

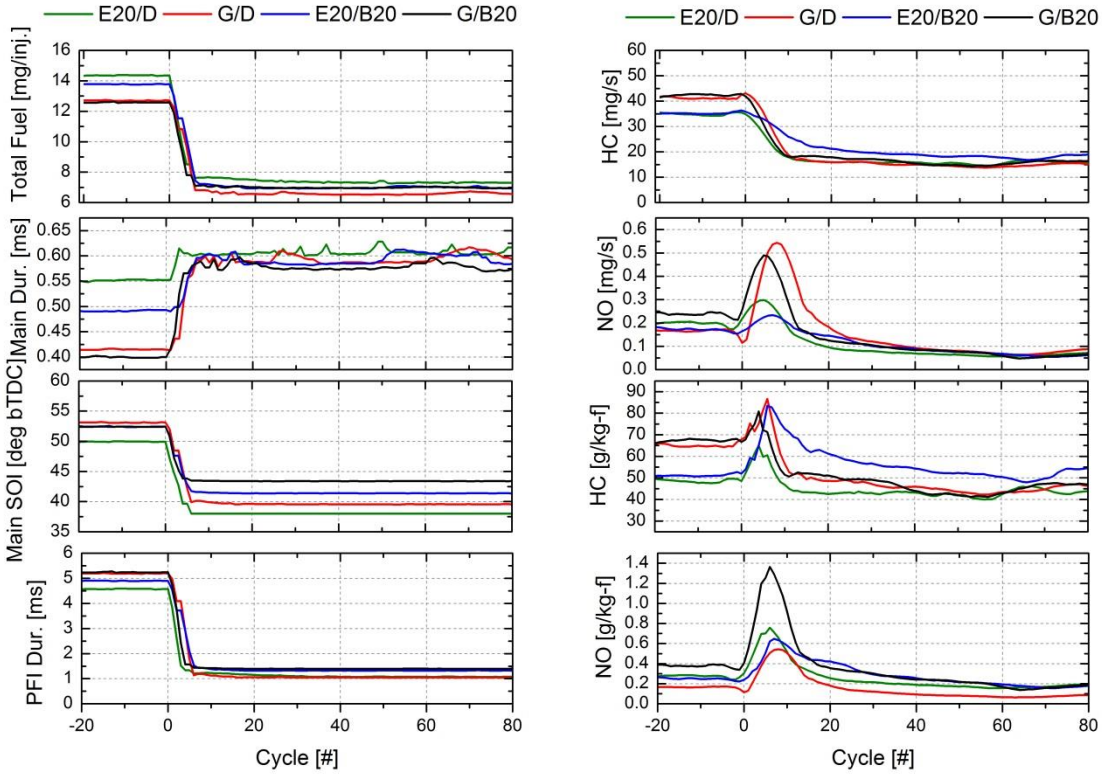

Figure 7.8 Down-load transient biofuel RCCI OL fuelling and emissions results

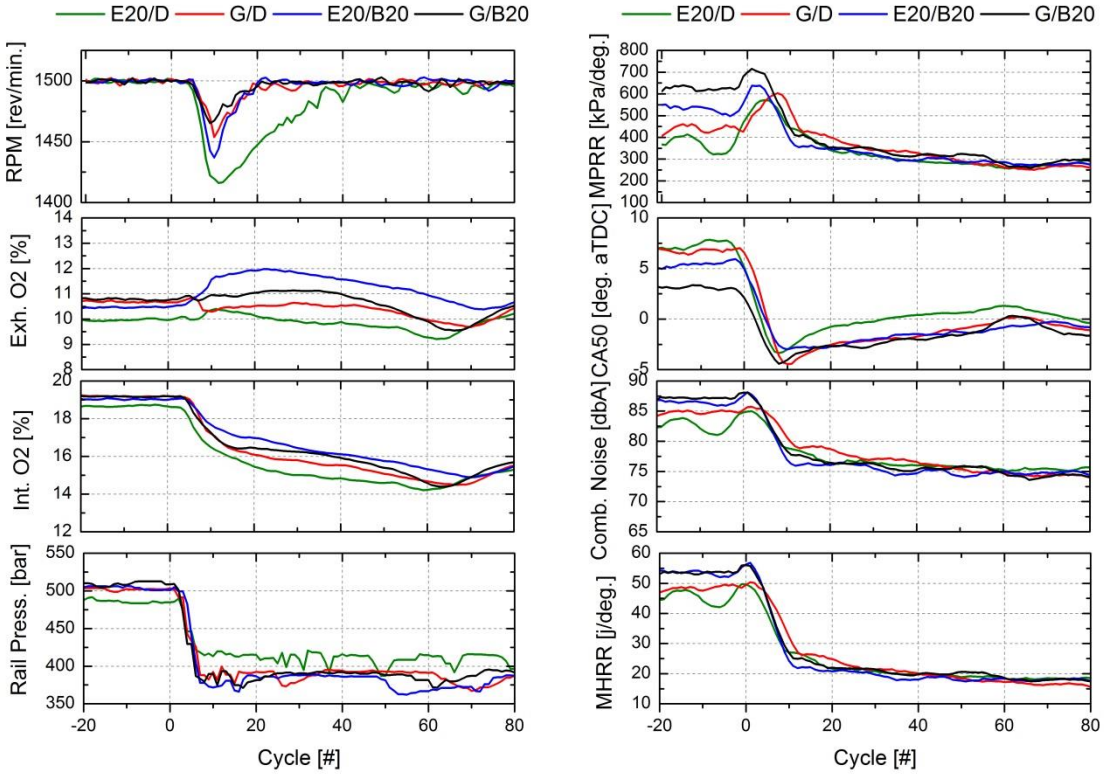

Figure 7.9 Down-load transient biofuel RCCI OL combustion performance results

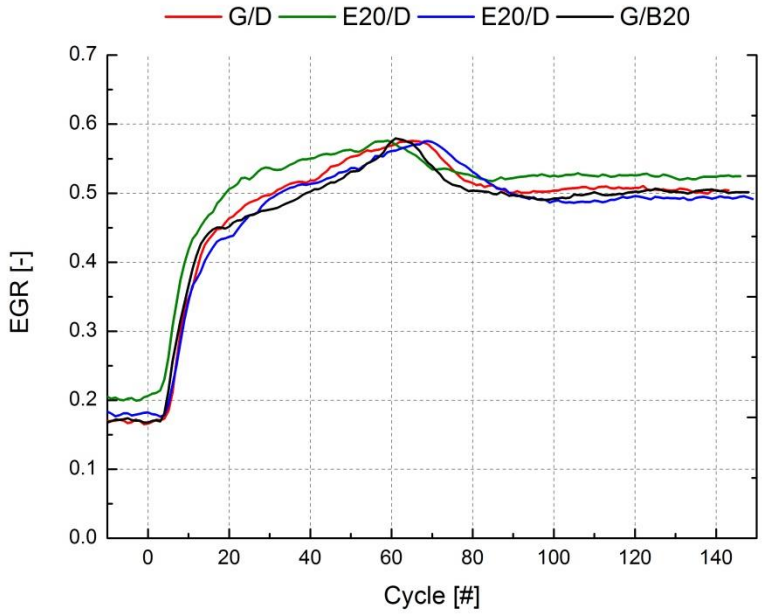

Figure 7.10 Down-load transient biofuel RCCI OL EGR performance results

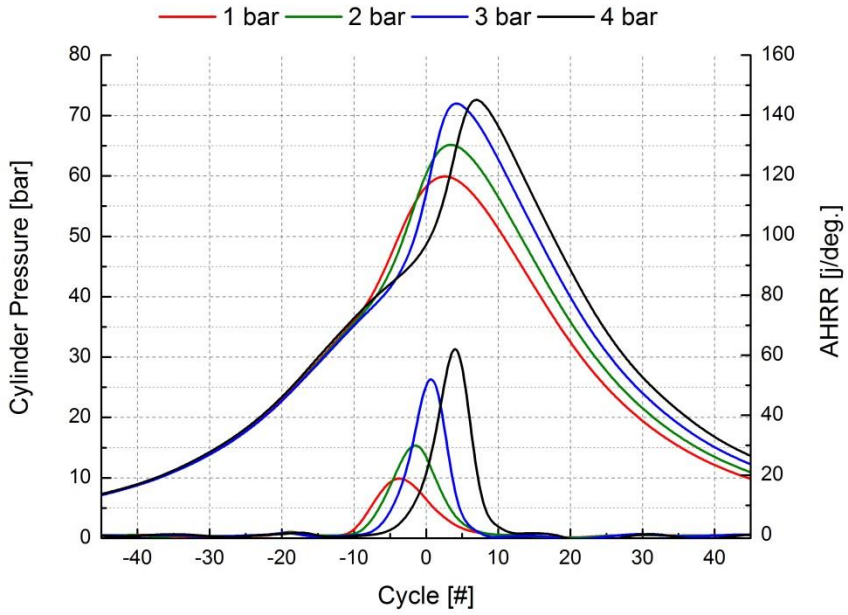

Figure 7.11 Steady-state gas/diesel RCCI results

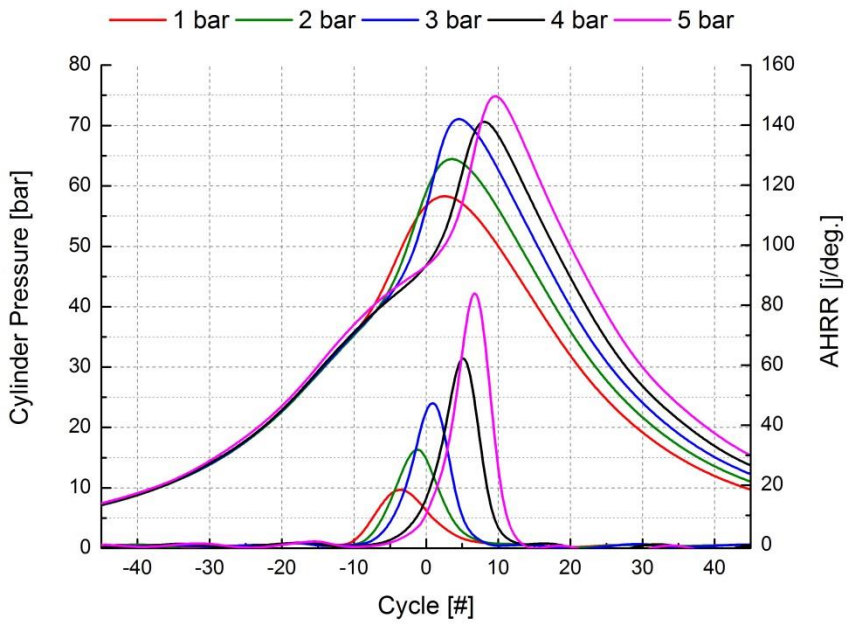

Figure 7.12 Steady-state E20/diesel RCCI results

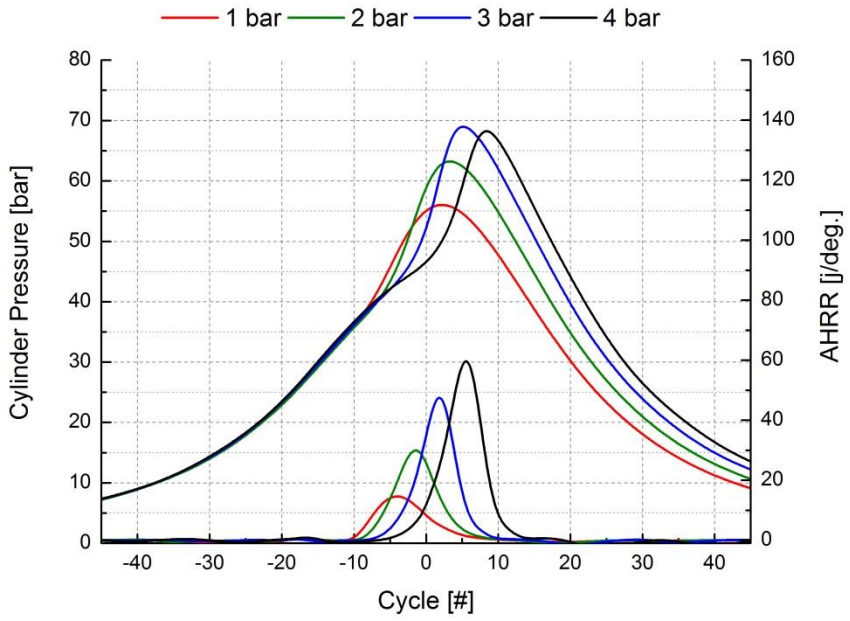

Figure 7.13 Steady-state gas/B20 RCCI results

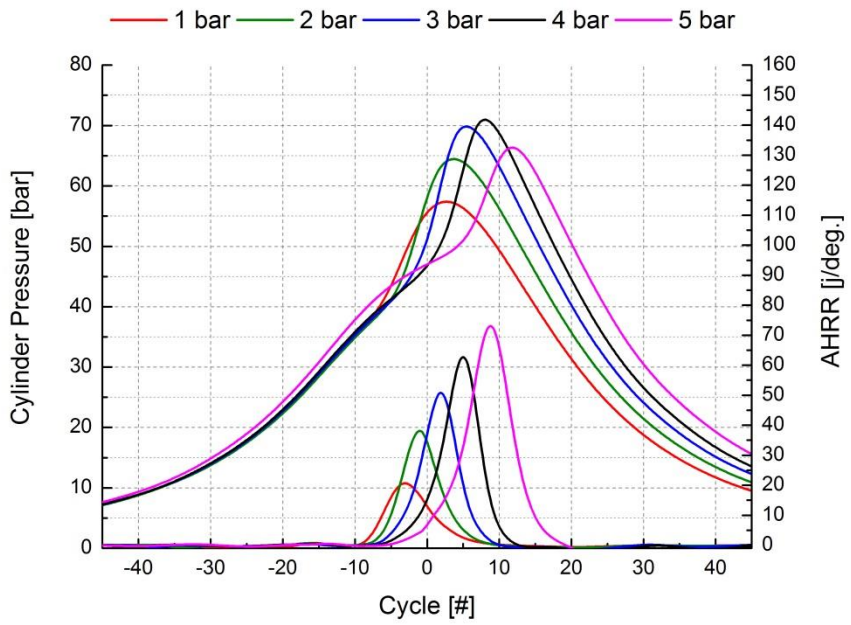

Figure 7.14 Steady-state E20/B20 RCCI results

7.3 Emissions Calculation Codes

Found using the standard methods seen in Heywood [10]

AFR carbon and O_2

$$AF_{Carbon} = \frac{MW_{air}}{MW_{fuel}} \cdot (n_{exh,wet} - 0.5 \cdot (n_{CO} + n_{H2O} + n_{H2}) - n_{HC})$$

$$AF_{O2} = \frac{MW_{air}}{MW_{fuel}} \cdot 4.76 \cdot n_{air,oxygen}$$

Phi cabin and O_2

$$f_m = \frac{AFR_{stoich}}{AFR_m}$$

$$f_{O2} = \frac{AFR_{stoich}}{AF_{O2}}$$

Emissions Index

$$\dot{EINOx} = \frac{MW_{NO}}{MW_{fuel}} \cdot \frac{NO_{PPM}}{1000000} \cdot n_{exh,dry} \cdot \left| 1000 \cdot \frac{g}{kg} \right|$$

Brake Specific Emissions

$$BS_{NO} = \frac{MW_{NO}}{MW_{fuel}} \cdot \frac{NO_{PPM}}{1000000} \cdot n_{exh,dry} \cdot \left| 1000 \cdot \frac{g}{kg} \right| \cdot \frac{BSFC}{1000}$$

Brake Thermal Efficiency

$$Q_{hfv} = \frac{\dot{m}_{PFI} \cdot LHV_{PFI} + \dot{m}_{DI} \cdot LHV_{DI}}{fuel_{flow,metric}}$$

$$BTE = \frac{kw \cdot 4}{fuel_{flow,kgs} \cdot Q_{hfv}}$$

Combustion efficiency

$$\dot{yCO} = EICO \cdot \left[\frac{\frac{fuel_{flow,metric}}{1000}}{int_{airflowrate,kghr} + fuel_{flow,metric}} \right]$$

$$\dot{yHC} = EIHC \cdot \left[\frac{\frac{fuel_{flow,metric}}{1000}}{int_{airflowrate,kghr} + fuel_{flow,metric}} \right]$$

$$top = yCO \cdot LHV_{CO} + yHC \cdot LHV_{HC}$$

$$\dot{bot} = Q_{hfv} \cdot \left[\frac{fuel_{flow,metric}}{int_{airflowrate,kghr} + fuel_{flow,metric}} \right]$$

$$h_{comb} = 1 - \frac{top}{bot}$$

7.4 Additional MCE Lab Uncertainties

Table 7-1 Additional UW MCE Lab Emissions Measurement Uncertainties

Measurement	Linearity	Noise	Repeatability	Temperature	Full Scale	Total [%]	Uncertainty
Torque	0.01	0.01	0.002	0.001 and 0.002	500 [n-m]	0.002476	1.23 [n-m]
Int and Exh O_2	0.01	-	-		1.75 [%]		0.05 [lambda]
Airflow	0.01				300 [kg/h]	0.03	3 [kg/hr.]
Smoke							0.005*FSN+3%
Opacity	0.01				10 [%]	0.1	0.1 [%]
Temperature							1.5 [deg. C]
Pressure					2.1 [bar]	0.0025	0.00525 [bar]

7.5 Post Processing Codes

```
% emission_calc.m
% Calculates emissions balances and AFRs

function [AFR,phi,emissions,EGR,fuel,ms,eta] =
emission_calc(emissions,phi,geom,...
    mdot,temp,pressure,Pn,Pg,Pb,...
    P_FMEP,Etas_mode,HC1,HC2,NO1,NO2,pint,pexh,ms,RPM,opts)

omega = 0;      % mass specific humidity of air

% EGR% based on CO2 at intake and exhaust
% -------------fix for different cases (ORNL vs UW)----------------------
%EGR = max(100*(emissions.CO2in.ppm - 388)/(emissions.CO2ex.ppm - 388),0);
EGR = max(100*(emissions.O2in.ppm/1E4 - 20.9)/(emissions.O2ex.ppm/1E4 -
20.9),0);

% calculate fuel mixture properties on molar basis
y_DI = geom.HtoC_DI;
y_PFI = geom.HtoC_PFI;
z_DI = geom.OtoC_DI;
z_PFI = geom.OtoC_PFI;
H2Ofrac_DI = geom.H2Ofrac_DI;           % mass fraction of H2O in DI
H2Ofrac_PFI = geom.H2Ofrac_PFI;         % mass fraction of H2O in PFI
MW_DI = 12.01 + 1.008*y_DI+z_DI*16;     %g/mol
MW_PFI = 12.01 + 1.008*y_PFI+z_PFI*16;  %g/mol
ndot.DI = (1-H2Ofrac_DI)*mdot.DI/MW_DI;     % molar flowrate of DI fuel
ndot.PFI = (1-H2Ofrac_PFI)*mdot.PFI/MW_PFI; % molar flowrate of PFI fuel
y = (ndot.DI*y_DI+ndot.PFI*y_PFI)/(ndot.DI+ndot.PFI);    %H/C ratio
z = (ndot.DI*z_DI+ndot.PFI*z_PFI)/(ndot.DI+ndot.PFI);    %O/C ratio
emissions.z=z;
MW_fuel = 12.01 + 1.008*y+z*16; %g/mol
MW_PFI = 12.01 + 1.008*y_PFI+z_PFI*16; %g/mol
MW_DI = 12.01 + 1.008*y_DI+z_DI*16; %g/mol
MW_H2O = 18.01528;              %g/mol
MW_O2 = 32;                     %g/gmol
ndot.H2O.DI = H2Ofrac_DI*mdot.DI/MW_H2O;    % molar flowrate of H2O in DI
ndot.H2O.PFI = H2Ofrac_PFI*mdot.PFI/MW_H2O; % molar flowrate of H2O in PFI
n_H2O_f = (ndot.H2O.DI + ndot.H2O.PFI)/(ndot.DI+ndot.PFI); % moles H2O per
mole carbon
fuel.MW = MW_fuel;
fuel.HtoC = y;
fuel.OtoC = z;
fuel.mfH2O = (H2Ofrac_DI*mdot.DI +
H2Ofrac_PFI*mdot.PFI)/(mdot.DI+mdot.PFI);
emissions.PFI_frac=mdot.PFI/(mdot.PFI+mdot.DI);

% Gas properties
MW_air = 28.97;     %g/mol
R_air = 8.314/MW_air*1000;   %J/kg-K
MW_CO2 = 44.01;     %g/mol
```

```
MW_CO = 28.01;      %g/mol
MW_NO2 = 46;        %g/mol
MW_NO = 30.01;      %g/mol
MW_HC = 83.25/2;    %g/mol (from GM test code)

% calculation of rho for use in specific PM calc
T = temp.turbine.out + 273.15;   %K
P = pressure.ambient*6894.75729+101325; %Pa %change to press.exh once
hooked up
rho = P/(R_air*T); %kg/m^3

% total fueling rate
mdot.fuel = (1-H2Ofrac_DI)*mdot.DI + (1-H2Ofrac_PFI)*mdot.PFI;

% indicated specific fuel consumption
[ISFCn,ISFCg,BSFC,ISFC_FMEP,BSFC_diesel] =
ISFC_calc(mdot,Pn,Pg,Pb,P_FMEP,geom);

%Catalyst Effic
eta.catalyst=(HC1-HC2)/HC1;

% measured concentrations
emissions.HC.ppm = mean(HC1); %pick one based on setup or day
%emissions.HC.ppm = mean(HC2);
emissions.HC_corrected.ppm = emissions.HC.ppm/(1-((1-
.74)*(0.608*(z/.5)^2)+(0.092*(z/.5))));

%HCwet = HC2/1e6; % wet basis uses HC2 head from cambustion
HCwet = emissions.HC.ppm/1e6; % wet basis

COdry = emissions.CO.ppm/1e6;
CO2exdry = emissions.CO2ex.ppm/1e6;
%CO2indry = emissions.CO2in.ppm/1e6;    %not used in MCE

%emissions.NOx.ppm = mean(NO1); %pick one based on setup or day
emissions.NOx.ppm = mean(NO2);

NOdry = emissions.NOx.ppm/1e6;
%NOdry = NO2/1e6; %uses NO2 head from cambustion

% compute dry moles of exhaust per mole of fuel based on carbon balance,
% hydrogen balance, and CO/H2 relation
beta = 7.65*omega/(2*4.76+7.65*omega);
% n_exh_dry = (1/HCwet - (y/2)/(1+(y/2)*HCwet))/...
%     ((1-(y/4)*COdry)/(1+(y/2)*HCwet) + (COdry + CO2exdry)/HCwet);
n_exh_dry = (1/HCwet - (y/2+n_H2O_f*(1-beta)-
beta*z)/(1+(y/2)*HCwet+beta*(2*HCwet-1)))/...
    ((1-(y/4)*COdry+beta*(1-(2+y)*COdry/2))/(1+(y/2)*HCwet+beta*(2*HCwet-
1)) + (COdry + CO2exdry)/HCwet);

% dry to wet conversion (based on hydrogen balance and CO/H2 relation)
```

```
n_exh_wet = (1-n_exh_dry*(COdry+CO2exdry))/HCwet;

% number of moles
n_HC = HCwet*n_exh_wet; % wet basis
n_CO = COdry*n_exh_dry;
n_CO2ex = CO2exdry*n_exh_dry;
%n_CO2in = CO2indry*n_exh_dry; %not used in MCE
n_CO2in = 0; %not used in MCE
n_NO = NOdry*n_exh_dry;

% CO/H2 relation
n_H2 = 0.25*y*n_CO;
% Moles of water
n_H2O = n_exh_wet - n_exh_dry;
% Moles of air, carbon-based
n_air_carbon = (2*n_exh_wet - 2*n_HC - 2*n_H2 - n_CO - n_H2O - z -
n_H2O_f)/...
    (2*4.76 + 7.65*omega);

%Air/Fuel Ratios
% AFR.carbon = (MW_air/MW_fuel)*(n_exh_wet - 0.5*(n_CO + n_H2O + n_H2) -
n_HC);
% AFR.carbon = (MW_air/MW_fuel)*(n_exh_wet - 0.5*(n_CO + n_H2O + z) - n_H2
- n_HC);
AFR.carbon = (MW_air/MW_fuel)*4.76*n_air_carbon;
%AFR.mass = mdot.air*(1000/60)/mdot.fuel;
AFR.mass = mdot.air/mdot.fuel;
alpha = (2+y/2-z)/2;
AFR.stoich.total = alpha*4.76*MW_air/MW_fuel;
AFR.stoich.PFI = alpha*4.76*MW_air/MW_PFI;
AFR.stoich.DI= alpha*4.76*MW_air/MW_DI;

%Phi
phi.charge=AFR.stoich.total/((mdot.air/(1-EGR/100))/mdot.fuel);
phi.carbon = AFR.stoich.total/AFR.carbon;
phi.mass = AFR.stoich.total/AFR.mass;

%Oxygen balance
if isfield(emissions,'O2ex')
    n_O2 = emissions.O2ex.ppm*n_exh_dry/1e6;
    n_air_oxygen = (2*n_CO2ex+ n_CO + n_H2O + 2*n_O2 + n_NO - z -
n_H2O_f)/...
        (2 + 7.65*omega);
    AFR.oxygen = (MW_air/MW_fuel)*4.76*n_air_oxygen;
    phi.oxygen = AFR.stoich.total/AFR.oxygen;
end

% Check lambda meter mode
if Etas_mode % 0 = Lambda mode, 1 = O2% mode
    phi.meter = AFR.stoich.total/AFR.oxygen;
else
    if exist('phi.meter','var')
```

```
        AFR.meter = AFR.stoich.total/phi.meter;
    end
end

AFR_fields = fields(AFR);
AFR_sum = 0;
for i=1:length(AFR_fields)
    if ~strcmpi(AFR_fields(i),'stoich')
        AFR_sum = AFR_sum + AFR.(AFR_fields{i});
    end
end
AFR.mean = AFR_sum/sum(~strcmpi(AFR_fields,'stoich'));
clear AFR_sum

phi.mean = AFR.stoich.total/AFR.mean;

% Fuel Specific Emissions Index Equations
%emissions.NOx.g_kgfuel =
(MW_NO2/MW_fuel)*(emissions.NOx.ppm/1e6)*n_exh_dry*1000;
emissions.NOx.g_kgfuel =
(MW_NO/MW_fuel)*(emissions.NOx.ppm/1e6)*n_exh_dry*1000;
emissions.CO.g_kgfuel =
(MW_CO/MW_fuel)*(emissions.CO.ppm/1e6)*n_exh_dry*1000;
emissions.CO2ex.g_kgfuel =
(MW_CO2/MW_fuel)*(emissions.CO2ex.ppm/1e6)*n_exh_dry*1000;
%emissions.CO2in.g_kgfuel =
(MW_CO2/MW_fuel)*(emissions.CO2in.ppm/1e6)*n_exh_dry*1000;
emissions.O2in.g_kgfuel =
(MW_O2/MW_fuel)*(emissions.O2in.ppm/1e6)*n_exh_dry*1000;
emissions.O2ex.g_kgfuel =
(MW_O2/MW_fuel)*(emissions.O2ex.ppm/1e6)*n_exh_dry*1000;
emissions.HC.g_kgfuel =
(MW_fuel/MW_fuel)*(emissions.HC.ppm/1e6)*n_exh_dry*1000;

%PM emissions from Will, EI and soot rates
emissions.opacity.g_kgfuel =
(8.314/28.96)*(298/100)/1000*(1+AFR.mass)*emissions.opacity.mgmm3;
emissions.FSN.g_kgfuel =
(8.314/28.96)*(298/100)/1000*(1+AFR.mass)*emissions.FSN.mgmm3;

emissions.opacity.kghr = emissions.opacity.g_kgfuel/AFR.mass*mdot.air*4;
%air flow in g/s for total engine
emissions.FSN.kghr = emissions.FSN.g_kgfuel/AFR.mass*mdot.air*4;    %air
flow in g/s for total engine

%MS emissions rate and EI
emissions.EINO1=1000*NO1/1e6*MW_NO/MW_air*(1+AFR.mass);
emissions.EINO2=1000*NO2/1e6*MW_NO/MW_air*(1+AFR.mass);

emissions.EIHC1=1000*HC1/1e6*MW_fuel/MW_air*(1+AFR.mass);
emissions.EIHC2=1000*HC2/1e6*MW_fuel/MW_air*(1+AFR.mass);
```

```
%call HSinterp
[phi,emissions,ms,AFR] =
HSinterp(emissions,phi,ms,AFR,MW_NO,MW_air,MW_fuel,MW_PFI,MW_DI,opts);
%can put HSInterp code here

if isfield(emissions,'PM')
    if isfield(emissions.PM,'g_kgfuel')
        emissions.PM.g_kgfuel =
emissions.PM.mg_m3*mdot.air/60/rho/mdot.fuel;
    end
end

% Power Specific Emissions Index Equations
emissions.NOx.g_kWhr = emissions.NOx.g_kgfuel*ISFCg/1000;
emissions.CO.g_kWhr = emissions.CO.g_kgfuel*ISFCg/1000;
emissions.CO2ex.g_kWhr = emissions.CO2ex.g_kgfuel*ISFCg/1000;
%emissions.CO2in.g_kWhr = emissions.CO2in.g_kgfuel*ISFCg/1000;
emissions.O2in.g_kWhr = emissions.O2in.g_kgfuel*ISFCg/1000;
emissions.O2ex.g_kWhr = emissions.O2ex.g_kgfuel*ISFCg/1000;
emissions.HC.g_kWhr = emissions.HC.g_kgfuel*ISFCg/1000;
if isfield(emissions,'PM')
if isfield(emissions.PM,'g_kgfuel')
    emissions.PM.g_kWhr = emissions.PM.g_kgfuel*ISFCg/1000;
end
end


end
```

```
function [Output]=mce_trans_uncert(run1,run2,run3)

%MCE uncertainty calc
%intput NO, HC and MAF vectors

T_stat=4.808;
N=3;

HC_inst=64;
NO_inst=2.41;
MAF_inst=300*0.01;
O2_inst=0.5;
Opacity_inst=0.1;

cyc(:,1)=run1(:,36);
cyc(:,2)=run2(:,36);
cyc(:,3)=run3(:,36);

ind1=find(cyc==max(cyc(1,:)));
ind2=find(cyc==min(cyc(end,:)));

[a,b]=size(cyc);
cyc2=zeros(ind2(1)-ind1(1)+1,b);

O2i(:,1)=run1(:,7);
O2i(:,2)=run2(:,7);
O2i(:,3)=run3(:,7);

O2e(:,1)=run1(:,8);
O2e(:,2)=run2(:,8);
O2e(:,3)=run3(:,8);

Opacity(:,1)=run1(:,10);
Opacity(:,2)=run2(:,10);
Opacity(:,3)=run3(:,10);

HC1(:,1)=run1(:,12);
HC1(:,2)=run2(:,12);
HC1(:,3)=run3(:,12);

HC2(:,1)=run1(:,13);
HC2(:,2)=run2(:,13);
HC2(:,3)=run3(:,13);

NO1(:,1)=run1(:,14);
NO1(:,2)=run2(:,14);
NO1(:,3)=run3(:,14);

NO2(:,1)=run1(:,15);
NO2(:,2)=run2(:,15);
NO2(:,3)=run3(:,15);
```

```
MAF(:,1)=run1(:,19);
MAF(:,2)=run2(:,19);
MAF(:,3)=run3(:,19);

DImgtrans(:,1)=run1(:,26);
DImgtrans(:,2)=run2(:,26);
DImgtrans(:,3)=run3(:,26);

PFImgtrans(:,1)=run1(:,27);
PFImgtrans(:,2)=run2(:,27);
PFImgtrans(:,3)=run3(:,27);

MWfuel(:,1)=run1(:,43);
MWfuel(:,2)=run2(:,43);
MWfuel(:,3)=run3(:,43);

DItrans(:,1)=run1(:,44);
DItrans(:,2)=run2(:,44);
DItrans(:,3)=run3(:,44);

PFItrans(:,1)=run1(:,45);
PFItrans(:,2)=run2(:,45);
PFItrans(:,3)=run3(:,45);

for ii=1:b
 cyc2(:,ii)=cyc(ind1(ii):ind2(ii));
 HC3(:,ii)=HC1(ind1(ii):ind2(ii));
 HC4(:,ii)=HC2(ind1(ii):ind2(ii));
 NO3(:,ii)=NO1(ind1(ii):ind2(ii));
 NO4(:,ii)=NO2(ind1(ii):ind2(ii));
 MAF2(:,ii)=MAF(ind1(ii):ind2(ii));
 O2exh(:,ii)=O2e(ind1(ii):ind2(ii));
 O2int(:,ii)=O2i(ind1(ii):ind2(ii));
 Opacity2(:,ii)=Opacity(ind1(ii):ind2(ii));

 DImgtrans2(:,ii)=DImgtrans(ind1(ii):ind2(ii));
 PFImgtrans2(:,ii)=PFImgtrans(ind1(ii):ind2(ii));
 MWfuel2(:,ii)=MWfuel(ind1(ii):ind2(ii));
 DItrans2(:,ii)=DItrans(ind1(ii):ind2(ii));
 PFItrans2(:,ii)=PFItrans(ind1(ii):ind2(ii));
end

%Mean values
HC1mean=mean(HC3,2);
HC2mean=mean(HC4,2);

NO1mean=mean(NO3,2);
NO2mean=mean(NO4,2);

MAFmean=mean(MAF2,2);
```

```
O2exhmean=mean(O2exh,2);
O2intmean=mean(O2int,2);

Opacitymean=mean(Opacity2,2);

DImgtransmean=mean(DImgtrans2,2);
PFImgtransmean=mean(PFImgtrans2,2);
MWfuelmean=mean(MWfuel2,2);
DItransmean=mean(DItrans2,2);
PFItransmean=mean(PFItrans2,2);

for i=1:length(HC1mean)
    HC1stddev(i,:)=std(HC3(i,:))';
    HC1precision(i,:)=T_stat*(HC1stddev(i)/sqrt(N));
    HC1_ux(i,:)=sqrt(HC1precision(i)^2+HC_inst^2);

    HC2stddev(i,:)=std(HC4(i,:))';
    HC2precision(i,:)=T_stat*(HC2stddev(i)/sqrt(N));
    HC2_ux(i,:)=sqrt(HC2precision(i)^2+HC_inst^2);
end

for i=1:length(NO1mean)
    NO1stddev(i,:)=std(NO3(i,:))';
    NO1precision(i,:)=T_stat*(NO1stddev(i)/sqrt(N));
    NO1_ux(i,:)=sqrt(NO1precision(i)^2+NO_inst^2);

    NO2stddev(i,:)=std(NO4(i,:))';
    NO2precision(i,:)=T_stat*(NO2stddev(i)/sqrt(N));
    NO2_ux(i,:)=sqrt(NO2precision(i)^2+NO_inst^2);
end

for i=1:length(MAFmean)
    MAFstddev(i,:)=std(MAF2(i,:))';
    MAFprecision(i,:)=T_stat*(MAFstddev(i)/sqrt(N));
    MAF_ux(i,:)=sqrt(MAFprecision(i)^2+MAF_inst^2);
end

for i=1:length(O2exhmean)
    O2exhstddev(i,:)=std(O2exh(i,:))';
    O2exhprecision(i,:)=T_stat*(O2exhstddev(i)/sqrt(N));
    O2exh_ux(i,:)=sqrt(O2exhprecision(i)^2+O2_inst^2);

    O2intstddev(i,:)=std(O2int(i,:))';
    O2intprecision(i,:)=T_stat*(O2intstddev(i)/sqrt(N));
    O2int_ux(i,:)=sqrt(O2intprecision(i)^2+O2_inst^2);
end

for i=1:length(Opacitymean)
    Opacitystddev(i,:)=std(Opacity2(i,:))';
    Opacityprecision(i,:)=T_stat*(Opacitystddev(i)/sqrt(N));
```

```
    Opacity_ux(i,:)=sqrt(Opacityprecision(i)^2+Opacity_inst^2);
end

figure(1)
plot(HC3,'DisplayName','HC2','YDataSource','HC2');figure(gcf)
hold on
plot(HC1mean,'b')
plot(HC1mean+HC1_ux,'r--')
plot(HC1mean-HC1_ux,'r--')

figure(2)
plot(HC4,'DisplayName','HC2','YDataSource','HC2');figure(gcf)
hold on
plot(HC2mean,'b')
plot(HC2mean+HC2_ux,'r--')
plot(HC2mean-HC2_ux,'r--')

% figure(3)
% plot(NO3,'DisplayName','NO2','YDataSource','NO2');figure(gcf)
% hold on
% plot(NO1mean+NO1_ux,'r--')
% plot(NO1mean-NO1_ux,'r--')

figure(4)
plot(NO4)
hold on
plot(NO2mean,'b--')
plot(NO2mean+NO2_ux,'r--')
plot(NO2mean-NO2_ux,'r--')

figure(5)
plot(MAF2)
hold on
plot(MAFmean,'b--')
plot(MAFmean+MAF_ux,'r--')
plot(MAFmean-MAF_ux,'r--')

%Output files

Output(:,1)=HC1mean(:,1);
Output(:,2)=HC2mean(:,1);
Output(:,3)=NO1mean(:,1);
Output(:,4)=NO2mean(:,1);
Output(:,5)=MAFmean(:,1);
Output(:,6)=O2exhmean(:,1);
Output(:,7)=O2intmean(:,1);

Output(:,8)=HC1_ux(:,1);
Output(:,9)=HC2_ux(:,1);
Output(:,10)=NO1_ux(:,1);
Output(:,11)=NO2_ux(:,1);
Output(:,12)=MAF_ux(:,1);
```

```
Output(:,13)=O2exh_ux(:,1);
Output(:,14)=O2int_ux(:,1);

Output(:,15)=DImgtransmean(:,1);
Output(:,16)=PFImgtransmean(:,1);
Output(:,17)=MWfuelmean(:,1);
Output(:,18)=DItransmean(:,1);
Output(:,19)=PFItransmean(:,1);


end
```

```
%%HSinterp
 function [phi,emissions,ms,AFR] =
HSinterp(emissions,phi,ms,AFR,MW_NO,MW_air,MW_fuel,MW_PFI,MW_DI,opts)
%function [] = HSinterp()

%located in emiss_calc lin 181

load HSInterp2.mat

%MS emissions

%EGR
ms.EGR = (ms.O2in - 20.9)./(ms.O2ex - 20.9);

% SS inputs
ms.pfi_dur_final_avg=mean(ms.pfi_dur_final);
ms.main_dur_final_avg=mean(ms.main_dur_final);
ms.rail_p_avg=mean(ms.rail_p);
ms.MAF_avg=mean(ms.MAF);
ms.BMEP_avg=mean(ms.BMEP);
ms.rps=ms.RPM/60;

% Transient fuel calculations
if opts(6)==0       %select diesel HRR for using double inj when executing
the run
%use for single inj
ms.DI_trans=interp2(X1_single,Y1_single,Z_DI_single,ms.rail_p,ms.main_dur_
final); %interp use for single inj kg/hr
ms.DI_ss=interp2(X1_single,Y1_single,Z_DI_single,ms.rail_p_avg,ms.main_dur
_final_avg); % use for single inj interp kg/hr, interp SS durations
ms.DI_mg_trans=interp2(X1_single,Y1_single,Z_DI_single_mg,ms.rail_p,ms.mai
n_dur_final); %interp use for single inj kg/hr
    else
    %use for double

ms.DI_trans=interp2(X1_double,Y1_double,Z_DI_double,ms.rail_p,ms.main_dur_
final); % use for double inj interp kg/hr

ms.DI_ss=interp2(X1_double,Y1_double,Z_DI_double,ms.rail_p_avg,ms.main_dur
_final_avg); % use for double inj interp kg/hr, interp SS durations

ms.DI_mg_trans=interp2(X1_double,Y1_double,Z_DI_double_mg,ms.rail_p,ms.mai
n_dur_final); % use for double inj interp kg/hr, interp SS durations
end

if isnan(ms.DI_ss(1,1))
   ms.DI_ss=ms.DI/1000*3600*4; %convert ms.DI to kg/hr
    else
    ms.DI_ss=ms.DI_ss;
end

if isnan(ms.DI_trans(1,1))
```

```
    ms.DI_trans=ms.DI*4/1000*3600;
    else
    ms.DI_trans=ms.DI_trans;
end

if isnan(ms.DI_mg_trans(1,1))
    ms.DI_mg_trans=(ms.DI/1000*3600*4)./ms.rps*0.5/3600*1000*1000;
    else
    ms.DI_mg_trans=ms.DI_mg_trans;
end

ms.PFI_ss=0.0999*ms.pfi_dur_final_avg+0.0013; %interp ss
ms.PFI_trans=0.0999*ms.pfi_dur_final+0.0013; %interp transient
ms.PFI_mg_trans=1.998*ms.pfi_dur_final+0.027;    %g/s to mg/inj

%ms.DI_mg_trans=ms.DI_trans*277.8/rps*0.5; %kg/hr to mg/inj
%ms.DI_mg.trans_double=ms.DI.trans_double*277.8/rps*0.5; %kg/hr to mg/inj

ms.PFI_mg_m=ms.PFI.*3600/1000*4./ms.rps*2.0/3600*1000*1000/4;    %g/s to
mg/inj measured
ms.PFI_mg_ss=ms.PFI_ss./ms.rps*2.0/3600*1000*1000;    %g/s to mg/inj
ms.PFI_mg_transt=ms.PFI_trans./ms.rps*0.5*1000;    %g/s to mg/inj

ms.DI_mg_m=ms.DI.*3600/1000*4./ms.rps*2.0/3600*1000*1000/4;    %g/s to
mg/inj
ms.DI_mg_ss=ms.DI_ss./ms.rps*2.0/3600*1000*1000/4;    %g/s to mg/inj
ms.DI_mg_transt=ms.DI_trans./ms.rps*0.5/3600*1000*1000;    %g/s to mg/inj

ms.total_mg_ss=ms.PFI_mg_ss+ms.DI_mg_ss;  %total mg/inj ss
ms.total_mg_trans=ms.PFI_mg_trans+ms.DI_mg_trans;  %total mg/inj

ms.total_kgh_ss=ms.PFI_ss.*3600./1000.+ms.DI_ss;   %g/s to kg/hr
ms.total_kgh_trans=ms.PFI_trans.*3600./1000.+ms.DI_trans;   %g/s to kg/hr

ms.AFR_ss = ms.MAF_avg./ms.total_kgh_ss;  % kh/hr ss
ms.AFR_trans = ms.MAF./ms.total_kgh_trans;  % kh/hr transient

ms.PFI_fract_ss=ms.PFI_mg_ss./ms.total_mg_ss;
ms.PFI_fract_trans=ms.PFI_mg_trans./ms.total_mg_trans;
ms.AFR.stoich_ss=(ms.PFI_fract_ss*AFR.stoich.PFI)+((1-
ms.PFI_fract_ss)*AFR.stoich.DI);
ms.AFR.stoich_trans=(ms.PFI_fract_trans*AFR.stoich.PFI)+((1-
ms.PFI_fract_trans)*AFR.stoich.DI);
ms.phi_ss=ms.AFR.stoich_ss./ms.AFR_ss;
ms.phi_trans=ms.AFR.stoich_trans./ms.AFR_trans;

ms.MW_fuel_trans=MW_PFI*ms.PFI_fract_trans+(1-ms.PFI_fract_trans)*MW_DI;

%MS emissions rate and EI
ms.EINO1=1000*ms.NO1./1e6*MW_NO/MW_air.*(1+ms.AFR_trans);
ms.EINO2=1000*ms.NO2./1e6*MW_NO/MW_air.*(1+ms.AFR_trans);
```

```
ms.EIHC1=1000*ms.HC1./1e6.*ms.MW_fuel_trans/MW_air.*(1+ms.AFR_trans);
ms.EIHC2=1000*ms.HC2./1e6.*ms.MW_fuel_trans/MW_air.*(1+ms.AFR_trans);

%Emissions rate
ms.NO1_rate=ms.EINO1./ms.AFR_trans.*ms.MAF*1000/3600; %mg/s
ms.NO2_rate=ms.EINO2./ms.AFR_trans.*ms.MAF*1000/3600;

ms.HC1_rate=ms.EIHC1./ms.AFR_trans.*ms.MAF*1000/3600; %mg/s
ms.HC2_rate=ms.EIHC2./ms.AFR_trans.*ms.MAF*1000/3600;

%PM emissions from Will, EI and soot rates
ms.opacity.FSN=0.486.*ms.opacity.pcnt.^0.6194; %opacity to FSN
ms.opacity.mgmm3=1/0.405*5.32.*ms.opacity.FSN.*exp(0.3062.*ms.opacity.FSN)
; %mg/mm3 from opacity
ms.opacity.g_kgfuel =
(8.314/28.96)*(298/100)/1000.*(1+ms.AFR_trans).*ms.opacity.mgmm3;
ms.opacity.kghr = ms.opacity.g_kgfuel./ms.AFR_trans.*ms.MAF*1000/3600;
%air flow in g/s for total engine

%find offset
%ms.offset = find(ms.pedal>ms.pedal(1,1),1, 'first');

ms.offset1 = find(ms.pedal>ms.pedal(1,1),1, 'first');
ms.offset2 = find(ms.pedal<ms.pedal(1,1),1, 'first');

 if isempty(ms.offset1)
    if isempty(ms.offset2)
        ms.offset = 1;
    else
        ms.offset = ms.offset2;
    end
    else
    ms.offset = ms.offset1;
 end

ms.x_axis=linspace(1,200,200);
ms.x_axis=ms.x_axis-(ms.offset-1);
```

"Emissions uncertainy delta calulator
delta finder uncert 3"

t_stat=1.98
N=200

HC_instrument=63.4
NO_instrument=2.81
CO_instrument=75
CO2_instrument=0.234
kw_instrument=0.156/4
P_instrument=0.05*convert(bar,kpa)
T_instrument=1.5
Opacity_instrument=0.1
fuel_flow_intrument=0.02/4
O2_instrument=0.5
INTFLOW_instrument=300*convert(kg/hr,g/s)*.01/4

sdCO=CO*CO_COV
sdCO2=EXHCO2*CO2_COV
sdFUELFLOW1=FUELFLOW1*FUELFLOW1_COV
sdFUELFLOW2=FUELFLOW2*FUELFLOW2_COV
sdHC=HC*HC_COV
sdINTFLOW=INTFLOW*INITFLOW_COV
sdINTO2=INTO2*INTO2_COV
sdKWb=KWb*KWb_COV
{sdKWn=KWn*KWb_COV
sdKWg=KWg*KWb_COV}
sdNO=NO*NO_COV
sdEXHO2=EXHO2*EXHO2_COV
sdOpacity=Opacity*Opacity_COV

DELTAFSN=0.005*FSN+0.03
DELTACO=sqrt(CO_instrument^2+t_stat*(sdCO/sqrt(N))^2)
DELTACO2=sqrt(CO2_instrument^2+t_stat*(sdCO2/sqrt(N))^2)
DELTAFUELFLOW1=sqrt(fuel_flow_intrument^2+t_stat*(sdFUELFLOW1/sqrt(N))^2)
DELTAFUELFLOW2=sqrt(fuel_flow_intrument^2+t_stat*(sdFUELFLOW2/sqrt(N))^2)
DELTAHC=sqrt(HC_instrument^2+t_stat*(sdHC/sqrt(N))^2)
DELTAINTFLOW=(INTFLOW_instrument^2+t_stat*(sdINTFLOW/sqrt(N))^2) "actually MAF cov"
{DELTAINTFLOW=0.21}
DELTAINTO2=sqrt(O2_instrument^2+t_stat*(sdINTO2/sqrt(N))^2)
DELTAKWb=sqrt(KW_instrument^2+t_stat*(sdKWb/sqrt(N))^2)
DELTAP=0.05*convert(bar,kpa)
DELTANO=sqrt(NO_instrument^2+t_stat*(sdNO/sqrt(N))^2)
DELTAEXHO2=sqrt(O2_instrument^2+t_stat*(sdEXHO2/sqrt(N))^2)
DELTAOPACITY=sqrt(Opacity_instrument^2+t_stat*(sdOPACITY/sqrt(N))^2)

{Pin=1
Pexh=1
Tin=1
Texh=1
HC2=1}

```
"Trans uncert v1
UW MCE transient uncertainty calculator"

"Constants"
MW_NO=30.01                                   [kg/kmol]
MW_air=28.97                                  [kg/kmol]
AFR_stoich_PFI=14.42                          "from fuel props, no error"
AFR_stoich_DI=14.58
Pbrake=1

"Inputs"
{MW_fuel=14.8                                 [kg/kmol]

DI_mg_trans=5                                 "mg"
PFI_mg_trans=5                                "mg"

PFI_trans=0.75                                "convert to kg/h"
DI_trans=0.75                                 "kg/h"


MAF=50                                        "kg/h"

NO1=10*convert(PPM,-)                         "ppm, error from matlab, assume const"
NO2=10*convert(PPM,-)

HC1=1000*convert(PPM,-)                       "ppm, error from matlab, assume const"
HC2=1000*convert(PPM,-)}

{DELTAHC1=1
DELTAHC2=1
DELTANO1=1
DELTANO2=1
DELTAMAF=1
DELTAO2exh=1
DELTAO2int=1
DELTATrq=0.039}

"Calcs"

NO1_new=NO1*convert(PPM,-)                    "ppm, error from matlab, assume const"
NO2_new=NO2*convert(PPM,-)

HC1_new=HC1*convert(PPM,-)                    "ppm, error from matlab, assume const"
HC2_new=HC2*convert(PPM,-)

total_mg_trans=PFI_mg_trans+DI_mg_trans       "mg"
total_kgh_trans=PFI_trans*convert(g/s,kg/hr)+DI_trans  "kg/h"

PFI_fract_trans=PFI_mg_trans/total_mg_trans
AFR_stoich_trans=(PFI_fract_trans*AFR_stoich_PFI)+((1-PFI_fract_trans)*AFR_stoich_DI)

AFR_trans = MAF/total_kgh_trans
```

```
phi_trans=AFR_stoich_trans/AFR_trans

EINO1=1000[g/kg]*NO1_new*MW_NO/MW_air*(1+AFR_trans)
EINO2=1000[g/kg]*NO2_new*MW_NO/MW_air*(1+AFR_trans)

EIHC1=1000[g/kg]*HC1_new*MW_fuel/MW_air*(1+AFR_trans)
EIHC2=1000[g/kg]*HC2_new*MW_fuel/MW_air*(1+AFR_trans)

NO1_rate=EINO1/AFR_trans*(MAF*convert(kg/h,g/s))
NO2_rate=EINO2/AFR_trans*(MAF*convert(kg/h,g/s))

HC1_rate=EIHC1/AFR_trans*(MAF*convert(kg/h,g/s))
HC2_rate=EIHC2/AFR_trans*(MAF*convert(kg/h,g/s))

"EGR"
Amb_O2=20.91
EGR=(Amb_O2-Int_O2)/(Amb_O2-O2_%)

{Int_O2=18
O2_%=10}

"BMEP"
{BMEPrun=1}
{RPM=1500
BMEP2*convert(bar,pa)=(2*trq*2*Pi)/Vd}

{Vd=0.0004774 [m^3]
BMEP=((2*trq*2*Pi)/Vd)*convert(pa,bar)}


$CHECKUNITS Off
"! Assumes all dry measurements"

"!Molecular Weights"
MW_air = MOLARMASS(AIR)
MW_C = molarmass(C)
MW_O = molarmass(O)
MW_H = molarmass(H)
MW_CO2 = MOLARMASS(CO2)
MW_CO = MOLARMASS(CO)
MW_NO2 = MOLARMASS(NO2)
MW_NO = MOLARMASS(NO)
MW_HC ={13} 83.25/2                    "Per GM Test code"

"Inputs"
omega=0

bore=0.082 [m]
stroke = 0.0904 [m]
RPM=1500 [1/min]

"Fuel inputs"
```

```
LHV_PFI=42866
LHV_DI=41280

y_PFI=1.86
y_DI=1.702

z_PFI=0
z_DI=0

N=200                                   "number of cycles"
T_statistic=1.98                        "Student T statistic 1.92 or 4.303"

INT_CO2_%=0.1349 [%]
{PM_mg\m3=103 [mg/m^3]}

"Emissions Inputs"
{EXH_CO2_%=4.42 [%]
CO1_PPM=6000 [PPM]
O2_%=12.3 [%]
HC_PPM=2961 [PPM]
HC2=2500 [ppm]
NO_PPM=8.289 [ppm]
mdotPFI=0.04344 [g/s]
mdotDI=0.02883 [g/s]
int_O2=16.59 [%]
int_airflowrate=2.447 [g/s]
kw=0.5783 [kw]

kw_gross=0.844 [kw]
kw_net=0.735 [kw]

T_exh=166 [C]
P_exh=103 [kPa]

T_int=78 [C]
P_int=101.325 [kPa]

FSN=1
Opacity=1}

"Add precision error for all measurements"

{COV_EXHCO2=0.02
COV_CO=0.02}

{COV_O_2=0.02
COV_HC_PPM=0.02
COV_NO_PPM=0.02
{COV_INTCO2=0.02}
{COV_PM=0.02}
COV_FUELFLOW2=0.02
COV_FUELFLOW=0.02
```

```
COV_int_O2=0.02
COV_INTFLOW=0.02
COV_KW=0.02
COV_Opacity=0.02
CO2_error=0.02
CO_error=0.02}

"Instrument Uncertainties"
{Instrument_EXHCO2=0.234
Instrument_CO=75}
Instrument_O_2=0.5
Instrument_HC_PPM=63.4
Instrument_NO_PPM=2.41

{Instrument_PM=0.234}
Instrument_FUELFLOW2=0.005
Instrument_FUELFLOW=0.005
Instrument_int_O2=0.005
Instrument_INTFLOW=0.21
Instrument_KW=0.0375

"Delta functions"
{DELTAEXHCO2=CO2_error
DELTACO=CO_error
DELTAO_2=SQRT(Instrument_O_2^2+(T_statistic*(COV_O_2*O2_%))^2)
DELTAHC_PPM=SQRT(Instrument_HC_PPM^2+(T_statistic*(COV_HC_PPM*HC_PPM))^2)
DELTANO_PPM=SQRT(Instrument_NO_PPM^2+(T_statistic*(COV_NO_PPM*NO_PPM))^2)
{DELTAINTCO2=SQRT(Instrument_EXHCO2^2+(T_statistic*(COV_EXHCO2*EXH_CO2_%))^2)}
{DELTAPM=SQRT(Instrument_EXHCO2^2+(T_statistic*(COV_EXHCO2*EXH_CO2_%))^2)}
DELTAFUELFLOW2=SQRT(Instrument_FUELFLOW2^2+(T_statistic*(COV_FUELFLOW2*mdotPFI)
)^2)
DELTAFUELFLOW=SQRT(Instrument_FUELFLOW^2+(T_statistic*(COV_FUELFLOW*mdotDI))^2)
DELTAint_O2=SQRT(Instrument_int_O2^2+(T_statistic*(COV_int_O2*int_O2))^2)
DELTAINTFLOW=Instrument_INTFLOW
DELTAKW=SQRT(Instrument_kw^2+(T_statistic*(COV_kw*kw))^2)
DELTAOpacity=SQRT(Instrument_opacity^2+(T_statistic*(COV_opacity*opacity))^2)}

"Calcs"
m_dot_PFI=(mdotPFI*convert(g/s,kg/hr))*4                    "g/s to kg/hr"
m_dot_DI=(mdotDI*convert(g/s,kg/hr))*4
fuel_flow_metric =(m_dot_PFI+m_dot_DI)

int_airflowrate_kghr=(int_airflowrate*convert(g/s,kg/hr))*4

MW_PFI=12.01 + 1.008*y_PFI+z_PFI*16
MW_DI= 12.01 + 1.008*y_DI+z_DI*16

N_dot_DI = m_dot_DI/MW_DI
N_dot_PFI= m_dot_PFI/MW_PFI

y= (N_dot_DI*y_DI+N_dot_PFI*y_PFI)/(N_dot_PFI+N_dot_DI)
z = (N_dot_DI*z_DI+N_dot_PFI*z_PFI)/(N_dot_PFI+N_dot_DI)
```

```
MW_fuel = 12.01 + 1.008*y+z*16

"Mole concentrations"
HCwet=HC_PPM/(1*10^6)
COdry=CO1_PPM/(1*10^6)
NOdry=NO_PPM/(1*10^6)
Exh_CO2_dry=Exh_CO2_%/(100)
Int_CO2_dry=Int_CO2_%/(100)
O2dry=O2_%/(100)
{n_N2=3.76*n_air}
{beta=(7.65*omega)/(2*4.76+7.65*omega)}

"Mole fractions"
HCdry=n_HC/n_exh_dry
HCwet=n_HC/n_exh_wet
COdry=n_CO/n_exh_dry
Exh_CO2_dry=n_exh_CO2/n_exh_dry
Int_CO2_dry=n_int_CO2/n_exh_dry
O2dry=n_O2/n_exh_dry
NOdry=n_NO/n_exh_dry
H2Odry=n_H2O/n_exh_dry
H2dry=n_H2/n_exh_dry

{n_exh_dry=(1/HCwet - (y/2+0-beta*z)/(1+(y/2)*HCwet+beta*(2*HCwet-1)))/((1-(y/4)*COdry+beta*(1-
(2+y)*COdry/2))/(1+(y/2)*HCwet+beta*(2*HCwet-1))+(COdry+Exh_CO2_dry)/HCwet)}

{n_exh_dry=(1/HCwet - (y/2)/(1+(y/2)*HCwet))/((1-
(y/4)*COdry))/((1+(y/2)*HCwet)+(COdry+Exh_CO2_dry)/HCwet)
n_exh_wet=(1-n_exh_dry*(COdry+Exh_CO2_dry))/(HCwet)}

{n_exh_dry2=n_HC+n_exh_CO2+n_CO+n_NO+n_O2+n_H2+n_N2
n_exh_wet2=n_exh_dry2+n_H2O}

{H2Odry+1=dry_to_wet}
{H2Odry=y*(COdry+EXH_CO2_dry)/(2*(COdry/(3.8*EXH_CO2_dry)+1))}

"!Hydrogen calculation"
n_H2=0.25*y*n_CO
n_H2O=n_exh_wet-n_exh_dry

"Balance"
{n_air_carbon=(2*n_exh_wet-2*n_HC-2*n_H2-n_CO-n_H2O-z-0)/(2*4.76+7.65*omega)
n_air_oxygen = (2*n_exh_CO2+ n_CO + n_H2O + 2*n_O2 + n_NO - z)/(2 + 7.65*omega)}

"!Carbon balance"
1= n_CO +n_exh_CO2+ n_HC
"!Hydrogen balance"
y=2*n_H2O + 2*n_H2 + y*n_HC
"!Oxygen balance"
2*n_air  = 2*n_exh_CO2+ n_CO + n_H2O + 2*n_O2 + n_NO-z
```

```
"!Hydrogen calculation"
{n_H2=0.25*y*n_CO}
{n_H2=0.5*y*n_CO}

"Carbon in" "add in EGR later....."
{EGR=Int_CO2_%/Exh_CO2_%}

"Carbon bal"
{C_in= fuel_flow_metric/(MW_C + HoCf*MW_H + z*MW_O)}

C_in= fuel_flow_metric/(MW_C + y*MW_H + z*MW_O)
C_out_dry=(int_airflowrate_kghr)/MW_air*(n_CO/n_exh_dry+ n_HC/n_exh_dry +
n_exh_CO2/n_exh_dry)
C_out_wet=(int_airflowrate_kghr)/MW_air*(n_CO/n_exh_wet+ n_HC/n_exh_wet +
n_exh_CO2/n_exh_wet)

C_bal_dry=C_in/C_out_dry
C_bal_wet=C_in/C_out_wet

"!Air-fuel ratio calculations"
AFR_m= int_airflowrate/(mdotPFI+mdotDI)
AF_Carbon = (MW_air/MW_fuel)*(n_exh_wet - 0.5*(n_CO + n_H2O + n_H2) - n_HC)
AF_JBG = (MW_air/MW_fuel) * 4.76 * (n_air)
AF_O2= (MW_air/MW_fuel) *
4.76*(n_exh_CO2+n_CO/2+n_H2O/2+n_NO/2+n_O2)/(n_HC+n_CO+n_exh_Co2)

"Heywood"
{K=3.65{(COdry*H2Odry)/(EXH_CO2_dry*H2dry)}
n_H2Oh=0.5*y*(n_exh_CO2+n_CO)/(n_CO/(K*n_exh_CO2)+1)}

AF_C_heywood= (h1) * ((ht/100)/(hb/100)-y/2)
h1=MW_air/MW_fuel
ht=1+HCdry-COdry/2+3*H2Odry/2
hb=HCdry+COdry+exh_CO2_dry

{AF_Carbon2= (MW_air/MW_fuel)*4.76*(n_air_carbon)
AF_O2= (MW_air/MW_fuel) * 4.76 * (n_air_oxygen)}

"Phi"
alpha = (2+y/2-z)/2
AFR_stoich = alpha*4.76*(MW_air/MW_fuel)
Phi_m = AFR_stoich/AFR_m
Phi_c = AFR_stoich/AF_Carbon
Phi_O2 = AFR_stoich/AF_O2

"!Emissions Index Equations"
EINOx = (MW_NO/MW_fuel)*(NO_ppm/1e6)*n_exh_dry*convert(kg,g)
EICO = (MW_CO/MW_fuel)*(CO1_ppm/1e6)*n_exh_dry*convert(kg,g)
EIEXHCO2 = (MW_CO2/MW_fuel)*(exh_CO2_%/100)*n_exh_dry*convert(kg,g)
EIINTCO2 = (MW_CO2/MW_fuel)*(int_CO2_%/100)*n_exh_dry*convert(kg,g)
EIHC = (MW_fuel/MW_fuel)*(HC_ppm/1e6)*n_exh_dry*convert(kg,g)
```

```
"BS Emissions"
BSFC=(mdotDI+mdotPFI)*convert(g/s,g/hr)*(1/(kw))

BS_NO= (MW_NO/MW_fuel)*(NO_ppm/1e6)*n_exh_dry*convert(kg,g)*BSFC/1000
BS_CO=EICO*BSFC/1000
BS_HC = EIHC*BSFC/1000
BS_Exh_CO2= EIEXHCO2*BSFC/1000

"Comb Effic"
yCO = EICO*fuel_flow_metric/1000/(int_airflowrate_kghr+fuel_flow_metric)
yHC = EIHC*fuel_flow_metric/1000/(int_airflowrate_kghr+fuel_flow_metric)

LHV_CO = 10100                                          [kj/kg]
LHV_HC = 43800                                          [kj/kg]

Q_hfv = (m_dot_PFI*LHV_PFI + m_dot_DI*LHV_DI)/fuel_flow_metric
top = yCO*LHV_CO + yHC*LHV_HC
bot = Q_hfv*fuel_flow_metric/(int_airflowrate_kghr+fuel_flow_metric)

eta_comb = 1 - (top/bot)

Qfuel=((mdotDI*convert(g/s,kg/s)*60*(1/RPM)*2)+(mdotPFI*convert(g/s,kg/s)*60*(1/RPM)*2))*eta_co
mb*Q_hfv*1000

"BTE"
fuel_flow_kgs=(mdotDI+mdotPFI)*convert(g/s,kg/s)
BTE=(kw)/(fuel_flow_kgs*Q_hfv)

"EGR"
Amb_O2=20.91
EGR=(Amb_O2-Int_O2)/(Amb_O2-O2_%)

"Delta FSN"
{DELTAFSN=0.03*FSN+0.005}

"Catalyst Effic"
eta_cat=(HC_PPM-HC2)/HC_PPM

"First Law Eqns"
GTE=(kw_gross)/(fuel_flow_kgs*Q_hfv)
NTE=(kw_net)/(fuel_flow_kgs*Q_hfv)

cp_exh=cp(air,T=T_exh)
cp_int=cp(air,T=T_int)

E_exh=(int_airflowrate*convert(g/s,kg/s))*cp_exh*(converttemp(C,K,T_exh))
E_int=(int_airflowrate*convert(g/s,kg/s))*cp_int*(converttemp(C,K,T_int))

E_fuel=(mdotPFI+mdotDI)*convert(g/s,kg/s)*Q_hfv

eta_exh=(E_exh-E_int)/E_fuel
eta_pump=(kw_gross-kw_net)/E_fuel
```

```
eta_HT=1-(NTE+(1-eta_comb)+eta_exh+eta_pump)

sum=eta_HT+(1-eta_comb)+eta_exh+eta_pump+NTE

"PFI frac"
PFI_frac=mdotPFI/(mdotPFI+mdotDI)

"VE"
rho_air=density(air,T=T_int,P=P_int)
Vd=(Pi/4)*bore^2*stroke

VE= (int_airflowrate*convert(g/s,kg/min))/(1-EGR)/(rho_air*(RPM/2)*Vd)
```

7.6 Fuel Specification Data Sheets

haltermannsolutions
fueling the world, one solution at a time

Product Information

Telephone: (800) 969-2542 FAX: (281) 457-1469

Johann Haltermann Ltd.

PRODUCT: EPA TIER II EEE
FEDERAL REGISTER

PRODUCT CODE: HF0437

Batch No.: AK1921LT20
TMO No.: MTS
Tank No.: 105
Date: 11/26/2012

TEST	METHOD	UNITS	HALTERMANN Specs			RESULTS
			MIN	TARGET	MAX	
Distillation - IBP	ASTM D86	°F	75		95	88
5%		°F				110
10%		°F	120		135	125
20%		°F				147
30%		°F				171
40%		°F				201
50%		°F	200		230	222
60%		°F				233
70%		°F				244
80%		°F				264
90%		°F	305		325	320
95%		°F				341
Distillation - EP		°F			415	411
Recovery		vol %		Report		97.0
Residue		vol %		Report		1.0
Loss		vol %		Report		2.0
Gravity	ASTM D4052	°API	58.7		61.2	59.2
Density	ASTM D4052	kg/l	0.734		0.744	0.742
Reid Vapor Pressure	ASTM D5191	psi	8.7		9.2	9.1
Carbon	ASTM D3343	wt fraction		Report		0.8646
Carbon	ASTM E191	wt fraction		Report		0.8626
Hydrogen	ASTM E191	wt fraction		Report		0.1347
Hydrogen/Carbon ratio	ASTM E191	mole/mole		Report		1.860
Stoichiometric Air/Fuel Ratio				Report		14.598
Oxygen	ASTM D4815	wt %			0.05	None Detected
Sulfur	ASTM D5453	wt %	0.0025		0.0035	0.0028
Lead	ASTM D3237	g/gal			0.01	None Detected
Phosphorous	ASTM D3231	g/gal			0.005	None Detected
Silicon	ASTM 5184	mg/kg			4	None Detected
Composition, aromatics	ASTM D1319	vol %			35	28
Composition, olefins	ASTM D1319	vol %			10	1
Composition, saturates	ASTM D1319	vol %		Report		72
Particulate matter	ASTM D5452	mg/l			1	0.5
Oxidation Stability	ASTM D525	minutes	240			1000+
Copper Corrosion	ASTM D130				1	1a
Gum content, washed	ASTM D381	mg/100mls			5	<0.5
Fuel Economy Numerator/C Density	ASTM E191		2401		2441	2424
C Factor	ASTM E191			Report		1.0001
Research Octane Number	ASTM D2699		96.0			96.4
Motor Octane Number	ASTM D2700			Report		88.5
Sensitivity			7.5			7.8
Net Heating Value, btu/lb	ASTM D3338	btu/lb		Report		18492
Net Heating Value, btu/lb	ASTM D240	btu/lb		Report		18429
Color	VISUAL			Report		Undyed

Figure 7.15 EEE certification gasoline fuel specification

Southwest Research Institute
Test Summary Report
for
University of Wisconsin - Madison
July 13, 2012

ASTM Method	*Test Property*	*DIESEL Rec'd 6-18-12*
D240 GROSS	Heat of Combustion by Bomb Calorimeter	
	BTU/lb	17058
	MJ/kg	39.678
	cal/g	9476.9
D240 NET	Heat of Combustion by Bomb Calorimeter	
	BTU/lb	15976
	MJ/kg	37.159
	cal/g	8875.3
D2622_07	Sulfur by X-Ray (ppm)	< 10
D4052	API Gravity at 60°F	28.4
	Specific Gravity at60°F	0.8852
	Density at 15°C (grams/L)	884.8
D445	Viscosity at 40°C (cSt)	4.139
D5291	Instrumental Determination of C, H	
	Carbon (Weight %)	76.93
	Hydrogen (Weight %)	11.87
D613	Cetane Number	56.3

Figure 7.16 Soy methyl ester fuel specification test sheet

haltermannsolutions
fueling the world, one solution at a time

Product Information

Telephone: (800) 969-2542 **FAX: (281) 457-1469**

Johann Haltermann Ltd.

PRODUCT: **2007 Certification Diesel** **Batch No.:** ZI0121HW10

PRODUCT CODE: **HF0582** **Tank No.:** 54

Analysis Date: 9/28/2011

TEST	METHOD	UNITS	SPECIFICATIONS			RESULTS
			MIN	TARGET	MAX	Remix
Distillation - IBP	ASTM D86	°F	340		400	365
5%		°F				406
10%		°F	400		460	418
20%		°F				439
30%		°F				458
40%		°F				476
50%		°F	470		540	497
60%		°F				516
70%		°F				533
80%		°F				553
90%		°F	560		630	577
95%		°F				599
Distillation - EP		°F	610		690	628
Recovery		vol %		Report		98.0
Residue		vol %		Report		1.3
Loss		vol %		Report		0.7
Gravity	ASTM D4052	°API	32.0		37.0	34.7
Specific Gravity	ASTM D4052		0.840		0.865	0.851
Flash Point	ASTM D93	°F	130			167
Cloud Point	ASTM D2500	°F		Report		-13
Pour Point	ASTM D97	°F		Report		-22
Viscosity, 40°C	ASTM D445	cSt	2.0		3.2	2.5
Sulfur	ASTM D5453	ppm	7		15	12
Carbon	ASTM D5291	wt %		Report		86.80
Hydrogen	ASTM D5291	wt %		Report		12.40
Composition, aromatics	ASTM D5186	wt %		Report		28.9
Composition, aromatics	ASTM D1319	vol %	27			28
Composition, olefins	ASTM D1319	vol %		Report		3
Composition, saturates	ASTM D1319	vol %		Report		69
Cetane Number	ASTM D613		40.0		50.0	44.4
Cetane Index	ASTM D4737		40.0		50.0	44.0
Net heat content	ASTM D240	btu/lb		Report		17747
HFRR @60° C	ASTM D6079	mm		Report		0.600

APPROVED BY:

Figure 7.17 ULSD fuel specification sheet

7.7 Experimental Run Data Tables

Table 7-2 CDC Steady-State Run Conditions

Test Date:	7/10/2013			
Run #	18	19	20	21
RPM	1499.676	1499.71	1499.83	1499.801
IMEPg (bar)	1.870698	2.90851	4.008656	5.113041
IMEPn (bar)	1.560422	2.580885	3.618603	4.667087
BMEP (bar)	0.989915	2.082645	2.999422	3.947297
FMEP (bar)	0.570508	0.49824	0.619181	0.71979
BMEP_CF (bar)	0.707359	1.722726	2.74504	3.764855
FMEP_CF (bar)	0.853064	0.858159	0.873563	0.902232
CA50 (ATDC)	15.46552	15.13548	13.79307	12.61239
COV of IMEPg	0.011141	0.006207	0.005008	0.003907
COV of PPRR	0.0442	0.03938	0.029288	0.029068
Gross Power (kW)	1.116107	1.735332	2.391914	3.050828
Net Power (kW)	0.930989	1.539858	2.159174	2.784739
Brake Power (kW)	0.590609	1.242588	1.789717	2.355257
Torque (ft-lb)	11.09364	23.33951	33.61352	44.23604
EGR %	28.90853	30.22811	26.91897	24.04428
Fuel 1	EEE	EEE	EEE	EEE
Fuel 2	ULSD	ULSD	ULSD	ULSD
Fuel1 Flow (g/s)	-0.000732	-0.0011	-0.00182	-0.00166
Fuel2 Flow (g/s)	0.073382	0.105232	0.135971	0.167921
Fuel1 Fraction	-0.010079	-0.01053	-0.01355	-0.00997
Fuel2 Fraction	1.010079	1.010534	1.013553	1.00997
Fuel Energy (J/cyc)	230.9766	337.8634	439.4027	546.7079
Fuel H/C	1.699838	1.69974	1.699093	1.699861
Fuel O/C	0	0	0	0
Fuel MW/C	13.72344	13.72334	13.72269	13.72346
Fuel mf H2O	0	0	0	0
RI (MW/m^2)	0.227507	0.527772	1.381031	1.737142
Peak HRR (J/deg)	30.86138	47.09565	62.10632	67.09734
Peak PRR (bar/deg)	1.400774	2.106496	3.465578	4.071944
PP (bar)	44.82225	46.09381	49.93706	57.10619
LPP (ATDC)	0.703125	1.582031	14.23828	12.48047
P Orifice (bar)				
P Intake (bar)	1.056154	1.0768	1.117824	1.153891
P Exhaust (bar)	1.209124	1.259451	1.356028	1.440324
T Orifice (C)				
T Intake (C)	65	68	70	71
T Exhaust Port (C)	198	254	301	346
T Exhaust Tank (C)	178	226	268	307
Gross Therm Eff	0.372308	0.40385	0.432149	0.44468

Net Therm Eff	0.310557	0.358359	0.390099	0.405895
Brake Therm Eff	0.197014	0.289178	0.323349	0.343295
Brake Therm Eff (CF)	0.140779	0.239202	0.295926	0.327428
Turbo Eff	0.122784	0.142537	0.169242	0.177133
Vol Eff	0.788108	0.805178	0.817776	0.820099
Comb Eff	0.9629	0.982663	0.992227	0.99595
Exhaust Loss	0.177644	0.167465	0.174446	0.176996
Pumping Loss	0.061751	0.045491	0.042049	0.038784
Heat Transfer Loss	0.412947	0.411348	0.385632	0.374274
ISFCg	234.3301	216.0323	201.9091	196.1923
ISFCn	280.9246	243.4561	223.6731	214.939
BSFC	442.827	301.699	269.8467	254.1332
BSFC_CF	619.7154	364.7312	294.8533	266.4482
HC (ppm)	1063.045	546.6866	332.8183	168.2774
NOx (ppm)	30.49629	44.21488	90.49793	143.0946
CO2ex (ppm)	38400	55700	65880	74400
O2in (ppm)	189434.8	180767.1	179698.3	179447.8
CO (ppm)	870	889.4293	370	270
PM (mg/m^3)				
HC (g/kg-fuel)	26.33376	9.563777	4.997159	2.248227
NOx (g/kg-fuel)	1.652006	1.691476	2.97154	4.180613
CO2ex (g/kg-fuel)	3050.57	3124.912	3172.356	3187.682
O2in (g/kg-fuel)	10942.29	7373.957	6291.74	5590.349
CO (g/kg-fuel)	43.98766	31.7582	11.33944	7.362539
PM (g/kg-fuel)				
HC (g/ikW-hr)	6.170793	2.066085	1.008972	0.441085
NOx (g/ikW-hr)	0.387115	0.365413	0.599981	0.820204
CO2ex (g/ikW-hr)	714.8406	675.0821	640.5274	625.3986
O2in (g/ikW-hr)	2564.108	1593.013	1270.36	1096.783
CO (g/ikW-hr)	10.30763	6.860797	2.289537	1.444473
PM (g/ikW-hr)				
HC (g/bkW-hr)	11.6613	2.885382	1.348467	0.571349
NOx (g/bkW-hr)	0.731553	0.510317	0.80186	1.062432
CO2ex (g/bkW-hr)	1350.875	942.7831	856.0497	810.0959
O2in (g/bkW-hr)	4845.541	2224.716	1697.806	1420.693
CO (g/bkW-hr)	19.47892	9.581417	3.059912	1.871065
PM (g/bkW-hr)				
Air Flow (g/s-cyl)	3.637822	3.686313	4.047561	4.342104
AFR mass	50.07371	35.3992	30.17133	26.11578
AFR carbon	53.05692	37.75958	32.56506	29.0845
AFR oxygen	48.95535	34.38835	29.31925	25.82574
AFR Lambda meter				
AFR Average	50.69533	35.84904	30.68521	27.00867
AFR Stoich	14.31842	14.31828	14.31733	14.31845

Phi mass	0.285947	0.40448	0.474534	0.548268
Phi carbon	0.269869	0.379196	0.439653	0.492305
Phi oxygen	0.292479	0.41637	0.488325	0.554426
Phi Lambda meter	0.292479	0.41637	0.488325	0.554426
Phi Average	0.282441	0.399405	0.466587	0.530143
CA5 (ADTC)	11.09123	10.59173	3.785189	3.649857
CA10 (ADTC)	11.98295	11.69736	10.38504	8.560053
CA25 (ADTC)	13.48002	13.22533	11.85534	10.16933
CA75 (ADTC)	20.94456	21.12159	20.1698	19.75204
CA90 (ADTC)	30.24491	31.07866	32.48539	34.06902
CA95 (ADTC)	54.94907	53.27169	51.14518	49.97283
CA10-90 (deg)	18.26195	19.38131	22.10036	25.50897
CA5-90 (deg)	19.15368	20.48694	28.7002	30.41917
dBA	79.67385	84.09364	87.72481	88.35366
DI (mg/inj-cyl)	6.147365	8.4669	10.85639	13.70978
PFI (mg/inj-cyl)	-0.165362	-0.17247	-0.17371	-0.17263
eta cat (-)	0.224258	0.833921	0.807941	0.76604
FSN (-)	0.238	0.38	0.675	0.987
Rail Press. (bar)	458.2506	522.5446	593.5161	676.9519
Main SOI (deg BTDC)	0.000919	-0.0013	0.159558	1.008559
Opacity (%)	1.573838	2.241775	4.10784	4.377544
PFI (ms)	0	0	0	0
Main dur (ms)	0.622296	0.646534	0.658554	0.6565
Pedal (%)	10	14	18.5	21.5
O2 int (%)	19.05389	18.2645	18.13832	17.98944
O2 exh (%)	14.07673	11.63684	10.10163	8.445036
Phi_charge(-)	0.203284	0.282213	0.346795	0.416441
Pre Adv(ms)	1.1	1.1	1.1	1.1

Table 7-3 RCCI EGR Run Conditions

Test Date:	7-10-13				
Run #	1	2	3	4	5
RPM	1499.837	1499.708	1499.678	1499.752	1499.792
IMEPg (bar)	1.413785	2.690067	2.516493	3.521575	4.365141
IMEPn (bar)	1.232964	2.484152	2.320844	3.34436	4.211938
BMEP (bar)	0.969151	2.152455	1.975212	3.010145	3.916598
FMEP (bar)	0.263814	0.331698	0.345631	0.334215	0.295341
BMEP_CF (bar)	0.335055	1.552375	1.39418	2.394681	3.265212
FMEP_CF (bar)	0.897909	0.931778	0.926664	0.949679	0.946727
CA50 (ATDC)	-1.5161	-0.01292	-0.34359	2.403849	5.634033
COV of IMEPg	0.009196	0.006006	0.005588	0.00425	0.004569
COV of PPRR	0.015806	0.016098	0.015291	0.020409	0.030873
Gross Power (kW)	0.843591	1.604998	1.501408	2.101169	2.604557
Net Power (kW)	0.735697	1.482142	1.384678	1.995433	2.513146
Brake Power (kW)	0.578283	1.284238	1.178465	1.796022	2.336924
Torque (ft-lb)	10.86095	24.12184	22.13555	33.73369	43.892
EGR %	51.50679	47.49821	49.47341	35.53699	19.51434
Fuel 1	EEE	EEE	EEE	EEE	EEE
Fuel 2	ULSD	ULSD	ULSD	ULSD	ULSD
Fuel1 Flow (g/s)	0.028827	0.060952	0.054597	0.103219	0.134253
Fuel2 Flow (g/s)	0.043438	0.042259	0.04358	0.028864	0.025452
Fuel1 Fraction	0.398905	0.590558	0.556112	0.781472	0.840633
Fuel2 Fraction	0.601095	0.409442	0.443888	0.218528	0.159367
Fuel Energy (J/cyc)	215.5093	326.2821	308.9445	416.4607	500.6556
Fuel H/C	1.76459	1.794867	1.789415	1.82516	1.834575
Fuel O/C	0	0	0	0	0
Fuel MW/C	13.78871	13.81923	13.81373	13.84976	13.85925
Fuel mf H2O	0	0	0	0	0
RI (MW/m^2)	0.544955	1.251858	1.129661	1.902764	1.56539
Peak HRR (J/deg)	16.01336	33.97205	31.28289	49.3643	62.1461
Peak PRR (bar/deg)	2.376247	3.721394	3.512802	4.654371	4.185413
PP (bar)	56.02318	64.49866	63.22203	68.97107	68.2305
LPP (ATDC)	2.285156	3.515625	3.339844	5.097656	8.4375
P Orifice (bar)					
P Intake (bar)	1.008558	1.025472	1.019304	1.033464	1.032252
P Exhaust (bar)	1.030604	1.082424	1.064224	1.071184	1.048381
T Orifice (C)					
T Intake (C)	78	86	88	75	53
T Exhaust Port (C)	166	218	215	246	270
T Exhaust Tank (C)	143	190	190	226	249
Gross Therm Eff	0.278519	0.368352	0.362718	0.374134	0.382711
Net Therm Eff	0.242897	0.340156	0.334518	0.355306	0.369279

Brake Therm Eff	0.190925	0.294736	0.2847	0.319799	0.343385
Brake Therm Eff (CF)	0.066007	0.212567	0.200952	0.254412	0.286276
Turbo Eff	-1.38707	0.021751	-0.06136	0.12191	0.194244
Vol Eff	0.845088	0.867456	0.870351	0.848304	0.834751
Comb Eff	0.889308	0.935851	0.932755	0.926783	0.919445
Exhaust Loss	0.077148	0.085731	0.084877	0.113059	0.15276
Pumping Loss	0.035622	0.028196	0.0282	0.018827	0.013432
Heat Transfer Loss	0.533641	0.481768	0.48516	0.43959	0.383974
ISFCg	308.391	231.5029	235.4032	226.302	220.7429
ISFCn	353.6181	250.6924	255.2479	238.2936	228.7721
BSFC	449.8769	289.3247	299.9123	264.7512	246.0232
BSFC_CF	1301.274	401.1649	424.9024	332.7956	295.103
HC (ppm)	2961.048	3328.39	3316.993	4411.326	4380.825
NOx (ppm)	8.289136	7.772059	7.483115	7.703057	8.34992
CO2ex (ppm)	44200	67700	66780	66910	59110
O2in (ppm)	164357.7	153818.3	151932.2	168872.6	189219.6
CO (ppm)	6000	2950	3370	2040	1890
PM (mg/m^3)					
HC (g/kg-fuel)	55.57068	44.86607	45.02491	59.90817	66.75832
NOx (g/kg-fuel)	0.338573	0.227511	0.220671	0.226675	0.275523
CO2ex (g/kg-fuel)	2647.588	2906.298	2887.986	2887.467	2860.369
O2in (g/kg-fuel)	7158.411	4801.293	4777.459	5298.878	6657.726
CO (g/kg-fuel)	228.7394	80.60003	92.75563	56.02965	58.20826
PM (g/kg-fuel)					
HC (g/ikW-hr)	17.13749	10.38662	10.59901	13.55734	14.73643
NOx (g/ikW-hr)	0.104413	0.052669	0.051947	0.051297	0.06082
CO2ex (g/ikW-hr)	816.4921	672.8163	679.8412	653.4397	631.4061
O2in (g/ikW-hr)	2207.589	1111.513	1124.629	1199.147	1469.646
CO (g/ikW-hr)	70.54118	18.65914	21.83497	12.67962	12.84906
PM (g/ikW-hr)					
HC (g/bkW-hr)	24.99996	12.98086	13.50353	15.86076	16.4241
NOx (g/bkW-hr)	0.152316	0.065825	0.066182	0.060012	0.067785
CO2ex (g/bkW-hr)	1191.088	840.8636	866.1426	764.4603	703.7171
O2in (g/bkW-hr)	3220.404	1389.132	1432.819	1402.884	1637.955
CO (g/bkW-hr)	102.9046	23.31958	27.81856	14.83392	14.32058
PM (g/bkW-hr)					
Air Flow (g/s-cyl)	2.447135	2.70333	2.580189	3.374684	4.420763
AFR mass	33.8631	26.19212	26.28106	25.54972	27.68083
AFR carbon	39.9066	28.95663	29.14807	29.09885	32.526
AFR oxygen	35.72673	25.96621	26.11793	26.36893	29.60285
AFR Lambda meter					
AFR Average	36.49881	27.03832	27.18235	27.00583	29.93656
AFR Stoich	14.41253	14.45624	14.44838	14.49977	14.51326
Phi mass	0.425612	0.551931	0.549764	0.567512	0.524307

Phi carbon	0.361157	0.499238	0.495689	0.498293	0.446205
Phi oxygen	0.40341	0.556733	0.553198	0.549881	0.490266
Phi Lambda meter	0.40341	0.556733	0.553198	0.549881	0.490266
Phi Average	0.394877	0.534657	0.531535	0.536912	0.4848
CA5 (ADTC)	-9.99925	-6.48466	-6.81173	-4.09719	-1.39014
CA10 (ADTC)	-7.67821	-4.83788	-5.222	-2.25431	0.744022
CA25 (ADTC)	-5.01587	-2.52104	-2.91461	0.139538	3.349836
CA75 (ADTC)	4.889117	3.877069	3.667248	5.530058	7.994271
CA90 (ADTC)	21.6981	15.33008	15.06182	15.95851	12.40425
CA95 (ADTC)	47.18689	37.16433	38.05161	32.9915	16.87146
CA10-90 (deg)	29.37631	20.16796	20.28382	18.21282	11.66023
CA5-90 (deg)	31.69735	21.81475	21.87355	20.0557	13.79439
dBA	72.49833	79.87283	78.90107	84.33444	84.95212
DI (mg/inj-cyl)	3.424863	3.415929	3.437102	2.318321	2.278128
PFI (mg/inj-cyl)	2.26724	4.965911	4.479183	8.320262	10.76179
eta cat (-)	0.027081	0.03318	0.043494	0.889755	0.857043
FSN (-)	0	0	0	0	0
Rail Press. (bar)	371.2036	421.0938	412.9161	453.5754	499.8232
Main SOI (deg BTDC)	39.53238	43.88211	43.03263	47.37072	52.15234
Opacity (%)	0.008225	0.008267	0.166799	0.02207	0.041949
PFI (ms)	1.040074	2.334472	2.031045	3.839038	5.014099
Main dur (ms)	0.612451	0.547075	0.56087	0.458927	0.414456
Pedal (%)	8	11	10.5	13	15.5
O2 int (%)	16.5944	15.42505	15.27639	17.00291	19.10887
O2 exh (%)	12.30032	9.18526	9.275109	9.597019	10.82352
Phi_charge(-)	0.206393	0.289774	0.277777	0.365835	0.421992
Pre Adv(ms)	1.85	1.85	1.85	1.85	1.842383

Table 7-4 Non-EGR RCCI Run Conditions

Test Date:	11-May-13			
Run #	4	5	6	7
RPM	1499.71	1499.733	1499.734	1499.77
IMEPg (bar)	2.086788	2.920252	3.908454	4.994366
IMEPn (bar)	1.885839	2.740744	3.743474	4.833955
BMEP (bar)	0.985697	1.991308	2.986962	3.982616
FMEP (bar)	0.900142	0.749436	0.756512	0.851339
BMEP_CF (bar)	0.97971	1.817479	2.804434	3.864801
FMEP_CF (bar)	0.906129	0.923265	0.93904	0.969153
CA50 (ATDC)	1.19373	2.297579	4.327776	5.618712
COV of IMEPg	0.011835	0.00808	0.005259	0.003537
COV of PPRR	0.020639	0.02564	0.031104	0.032746
Gross Power (kW)	1.245061	1.742364	2.331976	2.979955
Net Power (kW)	1.125167	1.635261	2.233541	2.884243
Brake Power (kW)	0.588106	1.188111	1.782168	2.376281
Torque (ft-lb)	11.04638	22.31592	33.47389	44.63185
EGR %	0	0	0	0
Fuel 1	EEE	EEE	EEE	EEE
Fuel 2	ULSD	ULSD	ULSD	ULSD
Fuel1 Flow (g/s)	0.050105	0.063604	0.093774	0.128503
Fuel2 Flow (g/s)	0.044825	0.044564	0.042702	0.0378
Fuel1 Fraction	0.527808	0.588009	0.68711	0.772705
Fuel2 Fraction	0.472192	0.411991	0.31289	0.227295
Fuel Energy (J/cyc)	230.6829	312.7421	423.3916	533.3057
Fuel H/C	1.86784	1.874468	1.885393	1.894843
Fuel O/C	0	0	0	0
Fuel MW/C	13.89278	13.89946	13.91048	13.92
Fuel mf H2O	0	0	0	0
RI (MW/m^2)	0.282229	0.42597	0.7381	2.635721
Peak HRR (J/deg)	15.39261	23.01582	40.28039	77.44449
Peak PRR (bar/deg)	1.918835	2.235364	3.053201	5.849997
PP (bar)	58.08626	62.36877	66.31258	73.83857
LPP (ATDC)	4.21875	5.625	7.382813	8.4375
P Orifice (bar)				
P Intake (bar)	1.027323	1.022614	1.015998	1.021851
P Exhaust (bar)	0.971491	0.957048	0.940184	0.941392
T Orifice (C)				
T Intake (C)	45	45	45	45
T Exhaust Port (C)	155	185	221	253
T Exhaust Tank (C)	154	178	206	222
Gross Therm Eff	0.310402	0.380224	0.401605	0.419598
Net Therm Eff	0.280511	0.356851	0.384653	0.406121
Brake Therm Eff	0.146619	0.259273	0.306919	0.334597

Brake Therm Eff (CF)	0.145728	0.23664	0.288164	0.324699
Turbo Eff	-0.049895	0.007058	0.049461	0.009728
Vol Eff	1.194112	0.929692	1.066345	1.026082
Comb Eff	0.718745	0.852941	0.911277	0.93852
Exhaust Loss	0.209291	0.215332	0.198545	0.176293
Pumping Loss	0.02989	0.023372	0.016952	0.013477
Heat Transfer Loss	0.199052	0.257385	0.311127	0.342628
ISFCg	274.4847	223.4928	210.6853	200.9054
ISFCn	303.733	238.1307	219.9705	207.5723
BSFC	581.1028	327.7521	275.6827	251.9437
BSFC_CF	584.6539	359.0991	293.6257	259.6239
HC (ppm)	3484.263	2912.052	2836.047	2836.952
NOx (ppm)	4.074997	4.074683	4.105004	7.432549
CO2ex (ppm)	14800	28480	39900	52500
O2in (ppm)	198120.4	206462.4	197432.5	196941
CO (ppm)	8350	5150	2480	1385
PM (mg/m^3)				
HC (g/kg-fuel)	130.5162	79.50601	62.56993	49.88932
NOx (g/kg-fuel)	0.329729	0.240194	0.195384	0.281786
CO2ex (g/kg-fuel)	1756.214	2462.035	2785.06	2918.952
O2in (g/kg-fuel)	17094	12977.58	10020.26	7961.639
CO (g/kg-fuel)	630.6146	283.35	110.173	49.00937
PM (g/kg-fuel)				
HC (g/ikW-hr)	35.82471	17.76902	13.18256	10.02303
NOx (g/ikW-hr)	0.090506	0.053682	0.041165	0.056612
CO2ex (g/ikW-hr)	482.054	550.2471	586.7711	586.4331
O2in (g/ikW-hr)	4692.042	2900.396	2111.121	1599.536
CO (g/ikW-hr)	173.0941	63.32669	23.21182	9.846247
PM (g/ikW-hr)				
HC (g/bkW-hr)	75.84335	26.05826	17.24945	12.5693
NOx (g/bkW-hr)	0.191607	0.078724	0.053864	0.070994
CO2ex (g/bkW-hr)	1020.541	806.9371	767.7928	735.4116
O2in (g/bkW-hr)	9933.371	4253.429	2762.412	2005.885
CO (g/bkW-hr)	366.4519	92.86855	30.37278	12.3476
PM (g/bkW-hr)				
Air Flow (g/s-cyl)	5.969501	5.924654	5.858422	5.848649
AFR mass	62.88279	54.77256	42.92644	35.16874
AFR carbon	77.89558	57.27886	46.5921	37.36241
AFR oxygen	72.21313	54.12313	44.28039	35.71407
AFR Lambda meter				
AFR Average	70.99717	55.39152	44.59964	36.08174
AFR Stoich	14.56077	14.57022	14.58576	14.59918
Phi mass	0.231554	0.266013	0.339785	0.415118
Phi carbon	0.186927	0.254373	0.313052	0.390745
Phi oxygen	0.201636	0.269205	0.329395	0.408779

Phi Lambda meter	0.201636	0.269205	0.329395	0.408779
Phi Average	0.20509	0.263041	0.327038	0.404614
CA5 (ADTC)	-10.70395	-9.19752	-5.95571	-3.47683
CA10 (ADTC)	-6.16976	-4.95125	-2.32866	0.194387
CA25 (ADTC)	-2.731273	-1.33005	1.320388	3.444416
CA75 (ADTC)	6.233783	6.501958	7.527583	7.573425
CA90 (ADTC)	12.77327	12.64371	12.96706	11.15305
CA95 (ADTC)	17.47081	17.46122	17.39397	14.95541
CA10-90 (deg)	18.94303	17.59497	15.29572	10.95866
CA5-90 (deg)	23.47721	21.84123	18.92277	14.62987
dBA	70.43005	73.62609	79.79578	88.94388
DI (mg/inj-cyl)	3.521043	3.495019	3.272188	2.949333
PFI (mg/inj-cyl)	4.052795	5.168994	7.481251	10.31211
eta cat (-)	0.066871	0.028652	0.086876	0.743067
FSN (-)	0.016	0.016	0.017	0.023
Rail Press. (bar)	405.0391	421.1349	458.3379	496.6853
Main SOI (deg BTDC)	42.21849	44.68102	48.43826	53.19876
Opacity (%)	0.023392	0.003803	0.11733	0.030211
PFI (ms)	1.706648	2.439444	3.556751	4.817597
Main dur (ms)	0.576709	0.55138	0.505028	0.462305
Pedal (%)	10	11.5	13.5	16
O2 int (%)	20.91124	20.84138	20.7771	20.76173
O2 exh (%)	17.09899	15.91514	14.59189	13.00928
Phi_charge(-)	0.172441	0.253694	0.281183	0.354358
Pre Adv(ms)	1.1	1.1	1.1	1.1

Table 7-5 E20/D RCCI Run Conditions

Test Date:	18-Jul-13				
Run #	1	2	3	4	5
RPM	1499.8694	1499.951	1499.886	1499.716	1499.734
IMEPg (bar)	1.7646244	2.807554	3.714531	4.51461	5.374385
IMEPn (bar)	1.5722702	2.617889	3.532342	4.363001	5.165885
BMEP (bar)	1.0013642	2.057432	3.137565	4.044233	4.907519
FMEP (bar)	0.570906	0.560457	0.394777	0.318768	0.258367
BMEP_CF (bar)	0.6688982	1.68626	2.579152	3.405372	4.226759
FMEP_CF (bar)	0.903372	0.931628	0.95319	0.957629	0.939127
CA50 (ATDC)	-1.346048	-0.16504	2.419533	5.020678	8.711992
COV of IMEPg	0.0161359	0.006297	0.003115	0.003181	0.005022
COV of PPRR	0.0230644	0.019291	0.022397	0.036209	0.088025
Gross Power (kW)	1.0529566	1.675367	2.216496	2.693606	3.206622
Net Power (kW)	0.9381783	1.562187	2.107782	2.603149	3.082221
Brake Power (kW)	0.597517	1.227742	1.872215	2.412959	2.928067
Torque (ft-lb)	11.221954	23.05695	35.16164	45.32237	54.99693
EGR %	53.414484	53.27518	40.9291	23.92709	14.31451
Fuel 1	E20	E20	E20	E20	E20
Fuel 2	ULSD	ULSD	ULSD	ULSD	ULSD
Fuel1 Flow (g/s)	0.027	0.034743	0.079084	0.106968	0.138045
Fuel2 Flow (g/s)	0.0503472	0.069766	0.061141	0.058487	0.059632
Fuel1 Fraction	0.3490752	0.332439	0.563981	0.646508	0.698334
Fuel2 Fraction	0.6509248	0.667561	0.436019	0.353492	0.301666
Fuel Energy (J/cyc)	218.14094	314.9528	429.4114	503.7031	598.6316
Fuel H/C	1.8326546	1.831535	1.847504	1.853403	1.857165
Fuel O/C	0.0323637	0.030764	0.053577	0.062004	0.067379
Fuel MW/C	14.375135	14.34841	14.72952	14.8703	14.96009
Fuel mf H2O	0	0	0	0	0
RI (MW/m^2)	0.7183041	1.53186	2.084309	1.944179	0.955276
Peak HRR (J/deg)	21.47716	38.66843	52.37121	64.81098	75.6281
Peak PRR (bar/deg)	2.8131844	4.197396	4.980367	4.813814	3.288784
PP (bar)	57.386835	64.44569	69.84018	70.96094	66.33429
LPP (ATDC)	2.6367188	3.691406	5.449219	8.085938	11.77734
P Orifice (bar)					
P Intake (bar)	1.0069419	1.013367	1.028222	1.023153	1.075257
P Exhaust (bar)	1.0383958	1.051177	1.067133	1.033945	1.144764
T Orifice (C)					
T Intake (C)	81	91	83	57	43
T Exhaust Port (C)	167	211	248	270	298
T Exhaust Tank (C)	154	184	216	246	270
Gross Therm Eff	0.3343045	0.393411	0.391471	0.404518	0.403896
Net Therm Eff	0.2978634	0.366834	0.37227	0.390934	0.388226

Brake Therm Eff	0.1897064	0.2883	0.330665	0.362371	0.36881
Brake Therm Eff (CF)	0.1267214	0.236289	0.271815	0.305128	0.317649
Turbo Eff	-0.750038	-0.22289	0.063793	-0.01192	0.232881
Vol Eff	0.9574664	0.974963	0.956317	0.928438	0.929191
Comb Eff	0.8656475	0.924439	0.947946	0.94538	0.942354
Exhaust Loss	0.0873495	0.078398	0.101383	0.155733	0.189979
Pumping Loss	0.0364411	0.026577	0.019201	0.013585	0.015669
Heat Transfer Loss	0.4439935	0.452629	0.455091	0.385128	0.348479
ISFCg	264.44584	224.5683	227.7518	221.1293	221.9273
ISFCn	296.79858	240.8382	239.4987	228.8133	230.8845
BSFC	466.01185	306.444	269.633	246.8484	243.0399
BSFC_CF	697.63611	373.897	328.0113	293.1582	282.1838
HC (ppm)	3381.913	3493.099	3402.4	3335.886	3415.443
NOx (ppm)	7.2503471	7.38279	10.12803	15.96064	16.33965
CO2ex (ppm)	40560	71300	74200	65800	62300
O2in (ppm)	158725.56	138278.1	155277.5	181910.8	193503.2
CO (ppm)	7280	5330	1533	1080	930
PM (mg/m^3)					
HC (g/kg-fuel)	65.848643	43.46829	42.86703	47.37063	51.09534
NOx (g/kg-fuel)	0.2947116	0.192152	0.25998	0.457398	0.490353
CO2ex (g/kg-fuel)	2417.8079	2721.44	2793.217	2765.385	2741.824
O2in (g/kg-fuel)	6879.6973	3837.613	4250.185	5558.875	6192.107
CO (g/kg-fuel)	276.19573	129.4786	36.72863	28.88785	26.04931
PM (g/kg-fuel)					
HC (g/ikW-hr)	17.4134	9.761601	9.763044	10.47503	11.33945
NOx (g/ikW-hr)	0.0779353	0.043151	0.059211	0.101144	0.108823
CO2ex (g/ikW-hr)	639.37923	611.1492	636.1603	611.5077	608.4857
O2in (g/ikW-hr)	1819.3073	861.8062	967.9874	1229.23	1374.198
CO (g/ikW-hr)	73.038811	29.0768	8.365012	6.387951	5.781054
PM (g/ikW-hr)					
HC (g/bkW-hr)	30.686248	13.3206	11.55837	11.69337	12.41821
NOx (g/bkW-hr)	0.1373391	0.058884	0.070099	0.112908	0.119175
CO2ex (g/bkW-hr)	1126.7271	833.969	753.1437	682.6311	666.3727
O2in (g/bkW-hr)	3206.0205	1176.014	1145.99	1372.2	1504.929
CO (g/bkW-hr)	128.71048	39.67796	9.903252	7.130921	6.331022
PM (g/bkW-hr)					
Air Flow (g/s-cyl)	2.6367438	2.635858	3.390866	4.550345	5.629485
AFR mass	34.089703	25.22122	24.18156	27.50214	28.4782
AFR carbon	39.589502	25.72289	25.45844	28.328	29.6183
AFR oxygen	33.340419	21.86815	21.84622	25.1106	26.25611
AFR Lambda meter					
AFR Average	35.673208	24.27075	23.82874	26.98025	28.11754
AFR Stoich	13.832583	13.86334	13.43523	13.28264	13.18682

Phi mass	0.4057701	0.54967	0.555598	0.482968	0.46305
Phi carbon	0.3494003	0.53895	0.527732	0.468888	0.445225
Phi oxygen	0.4148893	0.633951	0.614991	0.528966	0.502238
Phi Lambda meter	0.4148893	0.633951	0.614991	0.528966	0.502238
Phi Average	0.3877583	0.571195	0.563825	0.49231	0.468989
CA5 (ADTC)	-7.167146	-5.27729	-3.60764	-1.93156	0.348498
CA10 (ADTC)	-5.956107	-4.096	-2.00037	0.144975	2.862898
CA25 (ADTC)	-3.970479	-2.27511	0.226392	2.788196	6.117016
CA75 (ADTC)	2.9435563	2.825005	5.185858	7.226128	11.15204
CA90 (ADTC)	13.267585	10.20184	13.94287	10.61413	89.67812
CA95 (ADTC)	37.678284	30.83337	32.55188	15.353	44.87587
CA10-90 (deg)	19.223692	14.29785	15.94324	10.46915	86.81522
CA5-90 (deg)	20.434732	15.47913	17.55051	12.54568	89.32962
dBA	75.809731	81.60302	84.81778	86.04673	84.14502
DI (mg/inj-cyl)	3.6488428	5.519381	4.593274	4.86252	4.897262
PFI (mg/inj-cyl)	1.8475381	2.622787	6.036053	-0.17387	10.57717
eta cat (-)	0.0794091	0.042825	0.834661	0.793217	0.762734
FSN (-)	0.03	0.036	0.02	0.025	0.044
Rail Press. (bar)	392.96744	433.8556	482.2032	505.4689	531.2986
Main SOI (deg BTDC)	38	42.43511	45.51339	49.13256	54.05862
Opacity (%)	0.0057869	0.153781	0.219437	0.213499	0.376165
PFI (ms)	1.0698645	1.508025	3.195752	4.358189	5.542964
Main dur (ms)	0.6210628	0.64192	0.566903	0.540927	0.531257
Pedal (%)	9	12.5	15	17.5	21
O2 int (%)	15.917368	13.95101	15.61228	18.26006	19.48499
O2 exh (%)	11.426545	7.659324	7.705079	9.531235	10.05492
Phi_charge(-)	0.1890301	0.256832	0.328197	0.367408	0.396766

Table 7-6 E20/B20 Run Conditions

1-Aug-13				
1	2	3	8	5
1499.819	1499.791	1499.775	1499.783	1499.782
1.877385	2.813229	3.673774	4.597198	5.53306
1.688682	2.615511	3.525635	4.458343	5.377331
0.953052	2.000694	3.090058	4.054694	4.972944
0.73563	0.614817	0.435577	0.403648	0.404388
0.781731	1.683939	2.567567	3.502074	4.404142
0.906951	0.931572	0.958068	0.956269	0.973189
-2.1304	-0.45052	1.346886	5.089267	6.494117
0.012599	0.007339	0.003514	0.003636	0.002855
0.021413	0.020783	0.020043	0.037374	0.045969
1.120204	1.678574	2.192014	2.743003	3.301401
1.007608	1.560601	2.103625	2.660152	3.208483
0.56867	1.193757	1.843731	2.419308	2.967197
10.68054	22.42111	34.62925	45.4396	55.73012
51.55196	47.96308	34.81798	19.96884	11.94093
E20	E20	E20	E20	E20
B20	B20	B20	B20	B20
0.038552	0.06312	0.096719	0.129716	0.154387
0.038416	0.041713	0.043351	0.042449	0.043341
0.500885	0.602103	0.690504	0.75344	0.780806
0.499115	0.397897	0.309496	0.24656	0.219194
214.9912	310.0094	422.4698	514.7449	593.8818
1.80538	1.821494	1.835826	1.846181	1.850723
0.05914	0.067109	0.074197	0.079318	0.081564
14.77606	14.91981	15.04767	15.14004	15.18056
0	0	0	0	0
0.675315	1.181616	2.091422	1.868066	2.428352
19.20211	32.73974	49.08008	64.48728	85.73903
2.679774	3.619517	4.945523	4.629416	5.360245
58.28476	64.4418	71.06689	70.61661	74.84684
2.636719	3.515625	4.570313	8.085938	9.667969
1.008641	1.021863	1.023352	1.023835	1.051726
1.022932	1.055787	1.018313	1.008176	1.064088
79	86	75	55	43
167	212	242	269	303
153	185	218	248	277
0.363227	0.400391	0.391999	0.399573	0.418964
0.326717	0.372251	0.376192	0.387505	0.407172

0.184392	0.284748	0.329715	0.352421	0.376552
0.151245	0.239666	0.273965	0.304389	0.333482
21.77865	-0.02863	0.00354	-0.01574	0.356401
0.870986	0.880899	0.871972	0.85742	0.842929
0.871283	0.924205	0.94424	0.937151	0.941945
0.085778	0.08588	0.111499	0.150471	0.179475
0.036509	0.02814	0.015807	0.012069	0.011792
0.422278	0.437933	0.440742	0.387107	0.343506
247.3537	224.8332	230.0396	225.9542	215.611
274.9943	241.8294	239.7053	232.9916	221.8551
487.2535	316.144	273.4944	256.1861	239.8958
594.0379	375.6118	329.1495	296.6118	270.8787
3662.958	3571.44	3248.088	3556.019	3437.846
5.945818	5.944854	10.72614	8.941018	14.44714
41760	62260	66640	61150	62000
164821.8	154792.8	169391.1	188193.1	196275.5
6310	3600	1590	1290	910
70.60243	51.28446	45.31427	53.71722	51.66078
0.232759	0.171706	0.298433	0.267717	0.429175
2397.403	2637.179	2719.095	2685.161	2701.033
6880.087	4767.382	5025.491	6008.64	6217.315
230.5535	97.04983	41.29032	36.05166	25.2314
17.46377	11.53045	10.42408	12.13763	11.13863
0.057574	0.038605	0.068651	0.060492	0.092535
593.0064	592.9255	625.4995	606.7235	582.3723
1701.815	1071.866	1156.062	1357.678	1340.521
57.02824	21.82002	9.498409	8.146027	5.440166
34.40128	16.21327	12.3932	13.76161	12.3932
0.113413	0.054284	0.08162	0.068585	0.102957
1168.143	833.7284	743.6572	687.901	647.9665
3352.346	1507.179	1374.444	1539.33	1491.508
112.338	30.68172	11.29267	9.235936	6.052907
2.512801	2.711492	3.473265	4.451037	5.133637
32.64715	25.86484	24.79673	25.85336	25.96322
38.12729	28.42916	27.48505	29.50888	29.29855
33.63044	24.80247	24.41522	26.48531	26.08338
34.80163	26.36549	25.56567	27.28252	27.11505
13.26868	13.14124	13.02994	12.9507	12.91625
0.406427	0.508074	0.52547	0.500929	0.497482

0.34801	0.462245	0.474074	0.438875	0.440849
0.394544	0.529836	0.533681	0.488977	0.495191
0.394544	0.529836	0.533681	0.488977	0.495191
0.381266	0.498426	0.509666	0.474689	0.47635
-8.81979	-6.63038	-5.10767	-2.27411	-0.48428
-7.33456	-5.16505	-3.35583	-0.00372	1.633004
-5.00859	-2.92908	-0.96799	2.765464	4.310914
1.896759	2.780239	4.216215	7.34813	8.443091
10.20478	10.72136	14.38295	11.28437	10.61626
25.59422	26.14716	30.80668	16.0489	13.12965
17.53933	15.8864	17.73879	11.28809	8.983259
19.02457	17.35174	19.49063	13.55848	11.10054
73.69868	79.02545	84.26939	86.01276	88.80878
3.078507	3.338298	3.714468	3.356034	3.44344
3.309801	4.993504	7.718816	10.26052	12.87372
0.092735	0.024805	0.865046	0.865224	0.859528
0.034	0.019	0.01	0.02	0.026
370.1469	424.3415	466.674	500.0049	517.1221
41.39779	43.60141	47.32048	52.17853	55.34896
0.069059	0.09398	0.109023	0.048644	0.075837
1.328308	2.408052	3.656043	4.844232	6.000471
0.603607	0.562683	0.517467	0.493365	0.484738
8	11.5	14	16.8	20
16.62424	15.62673	16.94533	18.92281	19.72345
12.41438	9.612939	9.436866	10.45356	10.2667
0.196906	0.264386	0.342512	0.400899	0.438078
1.85	1.85	1.85	1.713385	1.6

Table 7-7 G/B20 Run Conditions

8/8/2013			
1	2	3	4
1499.731	1499.765	1499.775	1499.793
1.956169	2.749104	3.709418	4.49388
1.772988	2.560776	3.548855	4.347896
1.051019	1.957691	3.023794	3.861385
0.721969	0.603085	0.525061	0.486511
0.859589	1.626438	2.587152	3.383777
0.913399	0.934338	0.961703	0.964119
-2.18205	-0.54212	0.897367	4.109754
0.009415	0.006688	0.003783	0.003906
0.015821	0.019529	0.01887	0.027808
1.167144	1.640284	2.213282	2.681376
1.05785	1.527916	2.11748	2.594271
0.627088	1.168079	1.804194	2.303983
11.77842	21.93919	33.88665	43.27325
51.35851	49.07643	43.74426	18.65282
EEE	EEE	EEE	EEE
B20	B20	B20	B20
0.03675	0.06	0.088875	0.13325
0.041667	0.045	0.0375	0.02058
0.46865	0.571429	0.703264	0.866216
0.53135	0.428571	0.296736	0.133784
227.285	325.0806	397.172	481.2933
1.791431	1.804783	1.821847	1.842842
0.01153	0.009285	0.006416	0.002885
14.00025	13.97778	13.94907	13.91375
0	0	0	0
0.727791	1.129867	2.55771	2.227164
19.73101	31.31109	52.85496	63.54056
2.796556	3.554186	5.493776	5.131317
59.90249	65.13513	71.97561	72.57856
2.636719	3.515625	4.21875	7.03125
1.010882	1.018276	1.02669	1.034111
1.026886	1.052507	1.035547	1.031765
82.5	85.5	87.1	56.4
167	212	242	269
153	185	218	248
0.357911	0.37343	0.415498	0.409716
0.324395	0.347848	0.397513	0.396406

0.1923	0.265927	0.3387	0.35205
0.157275	0.220931	0.289791	0.308506
-2.37614	-0.10672	0.153443	0.68637
0.86808	0.880472	0.900325	0.854781
0.87107	0.924961	0.931871	0.919147
0.077851	0.080307	0.094257	0.15988
0.033516	0.025582	0.017985	0.01331
0.435308	0.471224	0.422116	0.349552
241.8724	230.4478	205.5545	206.5312
266.8621	247.3957	214.8545	213.4656
450.1759	323.6083	252.1625	240.361
550.4295	389.5169	294.7207	274.2871
3539.384	3476.313	4186.105	4846.048
5.482474	6.650024	11.92162	10.67399
46760	62260	66640	61150
162345.4	152411.2	151403.8	190220.9
8310	3600	1590	1290
60.22351	49.99209	57.60173	71.72745
0.199961	0.205321	0.352924	0.340758
2501.086	2819.062	2893.12	2862.868
6313.828	5017.774	4779.329	6475.327
282.8895	103.7432	43.93295	38.43761
14.56641	11.52057	11.84029	14.81396
0.048365	0.047316	0.072545	0.070377
604.9437	649.6467	594.6938	591.2716
1527.141	1156.335	982.4124	1337.357
68.42317	23.9074	9.030613	7.938565
27.11117	16.17785	14.52499	17.24048
0.090018	0.066444	0.088994	0.081905
1125.929	912.2718	729.5363	688.122
2842.333	1623.793	1205.167	1556.416
127.3501	33.57217	11.07824	9.238903
2.495057	2.64652	3.000893	4.536255
31.81794	25.20495	23.74594	29.48877
35.5921	30.44543	29.27847	31.49615
32.10103	26.43613	23.84015	29.11785
33.17036	27.36217	25.62152	30.03426
14.20407	14.27091	14.35664	14.4626
0.446417	0.566195	0.604593	0.490444

0.399079	0.468737	0.490348	0.459186
0.44248	0.539826	0.602204	0.496692
0.44248	0.539826	0.602204	0.496692
0.428216	0.521556	0.560335	0.481537
-8.91708	-7.33617	-4.6885	-2.2969
-7.47891	-5.68855	-3.2621	-0.4455
-5.13826	-3.253	-1.15288	1.969685
1.877485	3.226234	3.168016	6.329988
10.2721	13.54292	10.41732	11.12955
29.35371	31.48018	29.00897	16.53641
17.75102	19.23147	13.67942	11.57505
19.18918	20.87909	15.10582	13.42646
73.89286	78.32436	85.60075	86.32998
2.923426	3.488419	2.432022	1.628278
4.098621	4.780961	7.130486	9.842294
0.11762	0.053696	0.430663	0.906221
0.034	0.019	0.01	0.02
388.2065	418.3567	432.2845	495.0587
43.38669	45.11546	47.34342	52.1188
0.005084	0.022566	0.02612	0.011242
1.394305	2.298664	3.803478	5.207067
0.577301	0.561893	0.482514	0.401615
8	11	13	15.5
16.32326	15.28693	15.1458	19.21243
11.84349	9.218131	7.735327	10.8888
0.217144	0.288326	0.340119	0.398963
1.85	1.85	1.85	1.842575

Table 7-8 CDC Speed Transient Run Conditions

Test Date:	20-Aug-13				
Run #	1	2	3	4	5
RPM	999.8345	1249.844	1499.776	1749.702	1999.701
IMEPg (bar)	2.762975	2.9734	3.25388	3.342054	3.394104
IMEPn (bar)	2.555446	2.775195	2.927023	2.901394	2.857782
BMEP (bar)	1.985292	2.027465	2.091484	2.031816	2.09019
FMEP (bar)	0.570155	0.74773	0.835539	0.869577	0.767592
BMEP_CF (bar)	1.829504	1.9804	2.065228	1.967358	1.851198
FMEP_CF (bar)	0.725942	0.794795	0.861795	0.934036	1.006584
CA50 (ATDC)	13.15988	12.67556	14.5964	15.21107	18.06823
COV of IMEPg	0.004901	0.005046	0.00708	0.007863	0.011307
COV of PPRR	0.026833	0.027471	0.030068	0.034326	0.031309
Gross Power (kW)	1.099031	1.478474	1.94148	2.326389	2.700194
Net Power (kW)	1.016482	1.37992	1.746455	2.019647	2.27352
Brake Power (kW)	0.789691	1.008124	1.247917	1.414338	1.66286
Torque (ft-lb)	22.2485	22.72113	23.43856	22.76989	23.42407
EGR %	13.8132	21.58697	26.8362	26.88999	26.07725
Fuel 1	EEE	EEE	EEE	EEE	EEE
Fuel 2	ULSD	ULSD	ULSD	ULSD	ULSD
Fuel1 Flow (g/s)	0	0	0	0	0
Fuel2 Flow (g/s)	0.072917	0.100694	0.119792	0.135417	0.15625
Fuel1 Fraction	0	0	0	0	0
Fuel2 Fraction	1	1	1	1	1
Fuel Energy (J/cyc)	354.5725	393.4552	390.1257	377.3478	380.5074
Fuel H/C	1.81	1.81	1.81	1.81	1.81
Fuel O/C	0	0	0	0	0
Fuel MW/C	13.83448	13.83448	13.83448	13.83448	13.83448
Fuel mf H2O	0	0	0	0	0
RI (MW/m^2)	0.680745	0.854123	0.773394	0.989046	0.482128
Peak HRR (J/deg)	55.87011	54.18036	52.89242	55.99737	42.29786
Peak PRR (bar/deg)	3.61367	3.227173	2.549164	2.480171	1.549996
PP (bar)	44.86732	46.24725	46.9986	48.8905	50.68416
LPP (ATDC)	13.35938	12.83203	1.40625	0.527344	1.933594
P Orifice (bar)					
P Intake (bar)	1.036195	1.034808	1.074633	1.118328	1.172367
P Exhaust (bar)	1.10153	1.084086	1.23081	1.356975	1.469438
T Orifice (C)					
T Intake (C)	79	86	75	55	43
T Exhaust Port (C)	167	212	242	269	303
T Exhaust Tank (C)	153	185	218	248	277
Gross Therm Eff	0.365126	0.355687	0.392615	0.41617	0.418635
Net Therm Eff	0.337702	0.331978	0.353176	0.361296	0.352484

Brake Therm Eff	0.262356	0.242532	0.252359	0.253012	0.257808
Brake Therm Eff (CF)	0.241769	0.236902	0.249191	0.244985	0.22833
Turbo Eff	-0.11543	-0.07567	0.705385	0.359235	0.333722
Vol Eff	0.913132	0.88122	0.818532	0.727389	0.676191
Comb Eff	0.981489	0.985881	0.986015	0.984267	0.983076
Exhaust Loss	0.112257	0.110187	0.139508	0.182488	0.219456
Pumping Loss	0.027425	0.02371	0.039439	0.054873	0.066151
Heat Transfer Loss	0.504106	0.520007	0.453892	0.385609	0.344986
ISFCg	238.8468	245.1852	222.1244	209.5522	208.3184
ISFCn	258.2437	262.6963	246.9288	241.3788	247.4137
BSFC	332.4085	359.5788	345.5758	344.6841	338.2727
BSFC_CF	360.714	368.1244	349.9692	355.9774	381.9441
HC (ppm)	444.9966	452.6675	506.2212	539.3672	625.0774
NOx (ppm)	140.892	95.54108	64.14503	68.2945	60.93921
CO2ex (ppm)	46760	62260	66640	61150	62000
O2in (ppm)	200298.4	193691.9	185325.7	184059.8	183648.2
CO (ppm)	900	900	900	900	910
PM (mg/m^3)					
HC (g/kg-fuel)	9.246872	7.113124	7.436013	8.613415	9.832837
NOx (g/kg-fuel)	6.35079	3.256674	2.04393	2.365809	2.079433
CO2ex (g/kg-fuel)	3091.016	3112.28	3114.034	3106.532	3102.596
O2in (g/kg-fuel)	9627.262	7040.114	6296.84	6798.874	6682.19
CO (g/kg-fuel)	37.86439	28.63346	26.76657	29.09937	28.98255
PM (g/kg-fuel)					
HC (g/ikW-hr)	2.208586	1.744033	1.65172	1.80496	2.048361
NOx (g/ikW-hr)	1.516866	0.798488	0.454007	0.495761	0.433184
CO2ex (g/ikW-hr)	738.2793	763.085	691.703	650.9807	646.3278
O2in (g/ikW-hr)	2299.441	1726.132	1398.682	1424.719	1392.023
CO (g/ikW-hr)	9.04379	7.0205	5.945508	6.097838	6.037599
PM (g/ikW-hr)					
HC (g/bkW-hr)	3.073739	2.557728	2.569706	2.968908	3.32618
NOx (g/bkW-hr)	2.111056	1.171031	0.706333	0.815457	0.703415
CO2ex (g/bkW-hr)	1027.48	1119.11	1076.135	1070.772	1049.524
O2in (g/bkW-hr)	3200.184	2531.475	2176.035	2343.464	2260.403
CO (g/bkW-hr)	12.58645	10.29598	9.249877	10.03009	9.804007
PM (g/bkW-hr)					
Air Flow (g/s-cyl)	3.209511	3.449332	3.843044	4.395694	5.138142
AFR mass	44.01615	34.25543	32.08106	32.46051	32.88411
AFR carbon	44.38555	33.79515	31.65087	34.32521	33.82116
AFR oxygen	44.45882	35.9027	31.95742	32.75237	31.75582
AFR Lambda meter					
AFR Average	44.28684	34.65109	31.89645	33.17936	32.82036
AFR Stoich					
Phi mass	0.328925	0.422648	0.451295	0.446019	0.440274

Phi carbon	0.326187	0.428405	0.457428	0.421789	0.428075
Phi oxygen	0.32565	0.403257	0.45304	0.442045	0.455917
Phi Lambda meter	0.32565	0.403257	0.45304	0.442045	0.455917
Phi Average	0.326914	0.417822	0.453906	0.436356	0.441129
CA5 (ADTC)	5.073105	-8.62878	-1.44857	-5.17779	-7.0158
CA10 (ADTC)	9.904163	8.567201	10.40645	11.69508	10.87425
CA25 (ADTC)	11.39567	10.67888	12.63752	13.45276	15.65418
CA75 (ADTC)	19.37849	19.50306	20.59755	19.10873	23.82724
CA90 (ADTC)	33.02035	33.04265	33.50749	27.4076	33.06945
CA95 (ADTC)	50.29112	50.93624	49.56871	39.99174	48.35408
CA10-90 (deg)	23.11618	24.47545	23.10104	15.71252	22.1952
CA5-90 (deg)	27.94724	41.67143	34.95606	32.58539	40.08525
dBA	81.82632	84.30266	85.66702	87.90701	85.72667
DI (mg/inj-cyl)	7.340127	7.158114	7.782679	8.606102	9.337582
PFI (mg/inj-cyl)	-0.26477	-0.21086	-0.17734	-0.15094	-0.13247
eta cat (-)	0.592722	0.501793	0.77791	0.836254	0.805298
FSN (-)	0.504	0.86	0.971	0.762	1.06
Rail Press. (bar)	433.1068	469.0817	507.6253	606.8886	517.2239
Main SOI (deg BTDC)	-3	-0.27633	-6E-05	1.05057	0.998733
Opacity (%)	3.179309	4.243861	5.736726	3.813728	5.197746
PFI (ms)	0	0	0	0	0
Main dur (ms)	0.732739	0.687593	0.667115	0.60843	0.666667
Pedal (%)	8.5	11	14.5	19	22
O2 int (%)	20.15579	19.54739	18.7195	18.54733	18.48446
O2 exh (%)	14.61922	13.86752	12.20013	11.59786	11.23743

Table 7-9 RCCI Speed Transient Run Conditions

Test Date:	11-Nov-13					
Run #	1	13	9	10	11	12
RPM		999.7166	1249.947	1499.658	1749.967	1999.875
IMEPg (bar)		2.650253	2.822446	2.800324	2.838016	2.731842
IMEPn (bar)		2.488485	2.643434	2.599897	2.651571	2.541104
BMEP (bar)		1.974243	2.000702	2.124048	2.046056	1.967763
FMEP (bar)		0.514242	0.642732	0.475849	0.605516	0.573341
BMEP_CF (bar)		1.669929	1.762307	1.664412	1.654628	1.479628
FMEP_CF (bar)		0.818556	0.881127	0.935485	0.996943	1.061476
CA50 (ATDC)		-2.76006	-1.53179	-0.31265	0.155111	-0.1338
COV of IMEPg		0.016692	0.012696	0.008683	0.00649	0.010009
COV of PPRR		0.042461	0.034483	0.021962	0.020127	0.024653
Gross Power (kW)		1.054069	1.403531	1.670727	1.975829	2.173518
Net Power (kW)		0.98973	1.314513	1.551148	1.846026	2.021762
Brake Power (kW)		0.785203	0.994899	1.267248	1.424466	1.565598
Torque (ft-lb)		22.12468	22.4212	23.8035	22.92946	22.05207
EGR %		19.36117	33.43673	44.37244	47.20143	44.98251
Fuel 1		EEE	EEE	EEE	EEE	EEE
Fuel 2		ULSD	ULSD	ULSD	ULSD	ULSD
Fuel1 Flow (g/s)		0.05947	0.054477	0.055802	0.060419	0.060729
Fuel2 Flow (g/s)		0.016617	0.030144	0.040558	0.049769	0.066655
Fuel1 Fraction		0.781607	0.64378	0.579098	0.548328	0.476739
Fuel2 Fraction		0.218393	0.35622	0.420902	0.451672	0.523261
Fuel Energy (J/cyc)		337.5286	308.2868	295.2987	289.4435	294.833
Fuel H/C		1.895827	1.880614	1.873487	1.870098	1.862222
Fuel O/C		0	0	0	0	0
Fuel MW/C		13.92099	13.90566	13.89847	13.89506	13.88712
Fuel mf H2O		0	0	0	0	0
RI (MW/m^2)		0.476984	0.985679	1.14501	1.642896	2.216831
Peak HRR (J/deg)		26.92283	33.26942	31.98984	32.89109	32.44197
Peak PRR (bar/deg)		3.589762	4.000615	3.574449	3.605272	3.636491
PP (bar)		68.02817	67.82357	65.42863	64.60001	64.39581
LPP (ATDC)		2.109375	2.988281	3.691406	4.042969	3.691406
P Orifice (bar)						
P Intake (bar)		1.025093	1.023978	1.029718	1.030432	1.031565
P Exhaust (bar)		1.059654	1.064382	1.07934	1.047899	1.035489
T Orifice (C)						
T Intake (C)		50	61	82	90	91
T Exhaust Port (C)		178	194	212	223	228
T Exhaust Tank (C)		168	173	190	199	207
Gross Therm Eff		0.325815	0.392096	0.410875	0.425423	0.405906
Net Therm Eff		0.305928	0.367228	0.381468	0.397474	0.377565

Brake Therm Eff		0.242708	0.277939	0.311649	0.306707	0.292376
Brake Therm Eff (CF)		0.205297	0.244821	0.24421	0.248031	0.219848
Turbo Eff		0.031224	0.009266	0.070061	0.170427	0.393238
Vol Eff		0.847769	0.788645	0.861107	0.83709	0.81084
Comb Eff		0.869178	0.89709	0.907564	0.908832	0.917613
Exhaust Loss		0.139999	0.112924	0.100976	0.094237	0.09912
Pumping Loss		0.019887	0.024868	0.029407	0.027948	0.028341
Heat Transfer Loss		0.403363	0.39207	0.395713	0.389172	0.412588
ISFCg		259.8613	217.0494	207.6328	200.765	210.9865
ISFCn		276.754	231.7479	223.6393	214.8818	226.8235
BSFC		348.8417	306.1976	273.7411	278.4745	292.9123
BSFC_CF		412.4117	347.6183	349.336	344.3519	389.5453
HC (ppm)		5392.975	4036.487	3667.784	3683.472	3305.049
NOx (ppm)		15.45146	7.995692	8.659587	9.112516	11.80036
CO2ex (ppm)		52000	57000	59000	61000	62000
O2in (ppm)		194771.3	177651	158990.3	154138.6	158112.6
CO (ppm)		6200	6000	5500	5700	5200
PM (mg/m^3)						
HC (g/kg-fuel)		84.4306	60.00943	53.6383	52.17132	46.74497
NOx (g/kg-fuel)		0.521479	0.256535	0.273443	0.278752	0.360667
CO2ex (g/kg-fuel)		2573.688	2681.949	2732.169	2736.499	2778.995
O2in (g/kg-fuel)		7009.325	6077.737	5353.339	5027.772	5153.011
CO (g/kg-fuel)		195.3017	179.6754	162.0988	162.7429	148.341
PM (g/kg-fuel)						
HC (g/ikW-hr)		21.94025	13.02501	11.13707	10.47418	9.862559
NOx (g/ikW-hr)		0.135512	0.055681	0.056776	0.055964	0.076096
CO2ex (g/ikW-hr)		668.8021	582.1155	567.2878	549.3932	586.3306
O2in (g/ikW-hr)		1821.452	1319.169	1111.529	1009.401	1087.216
CO (g/ikW-hr)		50.75136	38.99845	33.65704	32.67308	31.29796
PM (g/ikW-hr)						
HC (g/bkW-hr)		29.45291	18.37474	14.68301	14.52838	13.69218
NOx (g/bkW-hr)		0.181914	0.07855	0.074853	0.077625	0.105644
CO2ex (g/bkW-hr)		897.8099	821.2064	747.9067	762.0452	814.0019
O2in (g/bkW-hr)		2445.145	1860.989	1465.429	1400.106	1509.38
CO (g/bkW-hr)		68.12938	55.01618	44.37311	45.31975	43.4509
PM (g/bkW-hr)						
Air Flow (g/s-cyl)		3.005248	2.787276	2.887147	3.042147	3.503304
AFR mass		39.49774	32.93834	29.96195	27.60866	27.50188
AFR carbon		33.04911	31.5336	31.08364	30.13333	30.14067
AFR oxygen		33.61084	29.99524	27.12913	26.21179	26.76193
AFR Lambda meter						
AFR Average		35.3859	31.48906	29.39157	27.98459	28.13483
AFR Stoich		14.60057	14.57896	14.56882	14.56399	14.55277
Phi mass		0.369656	0.442614	0.486244	0.527515	0.529155

Phi carbon		0.441784	0.462331	0.468697	0.483318	0.482828
Phi oxygen		0.434401	0.486042	0.537018	0.555627	0.543786
Phi Lambda meter		0.434401	0.486042	0.537018	0.555627	0.543786
Phi Average		0.41261	0.462985	0.49568	0.520429	0.517251
CA5 (ADTC)		-9.96234	-7.76056	-6.32743	-5.39778	-5.80461
CA10 (ADTC)		-8.56075	-6.25007	-4.94109	-4.14312	-4.4864
CA25 (ADTC)		-5.98685	-3.97738	-2.74311	-2.13622	-2.48505
CA75 (ADTC)		1.576153	1.431779	2.651755	3.035282	3.079405
CA90 (ADTC)		15.01275	7.980215	8.374413	8.213718	11.42334
CA95 (ADTC)		35.64996	26.2649	23.45325	16.0416	33.53489
CA10-90 (deg)		23.5735	14.23029	13.3155	12.35684	15.90975
CA5-90 (deg)		24.97508	15.74078	14.70184	13.6115	17.22796
dBA		67.84721	75.34189	78.89886	82.72431	85.50992
DI (mg/inj-cyl)		2.073644	2.827779	3.33296	3.240097	3.914992
PFI (mg/inj-cyl)		6.647572	5.83589	4.805302	3.588654	3.342051
eta cat (-)		0.055983	0.037477	0.055111	0.039925	0.122494
FSN (-)		0.05	0.015	0.02	0.013	0.012
Rail Press. (bar)		336.3554	401.0875	418.977	414.0094	412.5301
Main SOI (deg BTDC)		35	43.87123	43.87936	44.85173	45.87203
Opacity (%)		0.262404	0.008456	0.058934	0.046893	0.004825
PFI (ms)		3.154185	2.514329	2.434373	2.174772	1.867227
Main dur (ms)		0.553851	0.533017	0.541197	0.562057	0.578885
Pedal (%)		6.2	8.5	11	13.5	16.5
O2 int (%)		19.53933	17.86352	15.85817	15.59147	15.91002
O2 exh (%)		13.50345	11.54405	9.352281	9.349479	9.605664
Phi_charge(-)		0.298086	0.294618	0.270486	0.278521	0.291128
Pre Adv(ms)		1.445624	1.85	1.85	1.8472	1.117783
BSFC diesel equiv.		360.0151	314.3805	280.375	284.8933	298.8566

Table 7-10 Cold Start Run Conditions

Test Date:	15-Aug-13							
Run #	1	2	3	4	5	6	7	8
RPM	1499.608	1499.786	1499.841	1499.774	1499.868	1499.832	1499.735	1499.812
IMEPg (bar)	2.206	2.211	2.159	1.986	1.785	1.669	1.557	1.325
IMEPn (bar)	1.981	2.003	1.958	1.788	1.595	1.483	1.375	1.129
BMEP (bar)	1.188	1.336	1.358	1.311	1.247	1.146	1.012	0.680
FMEP (bar)	0.793	0.667	0.600	0.478	0.348	0.338	0.364	0.449
BMEP_CF (bar)	1.053	1.077	1.033	0.868	0.680	0.572	0.468	0.227
FMEP_CF (bar)	0.927	0.926	0.925	0.920	0.915	0.911	0.908	0.903
CA50 (ATDC)	-1.408	-1.274	-1.212	-1.057	-0.870	-0.820	-1.045	-0.621
COV of IMEPg	0.034	0.025	0.032	0.033	0.045	0.041	0.037	0.039
COV of PPRR	0.049	0.035	0.044	0.045	0.049	0.042	0.038	0.032
Gross Power (kW)	1.316	1.319	1.288	1.185	1.065	0.996	0.929	0.790
Net Power (kW)	1.182	1.195	1.168	1.067	0.952	0.885	0.821	0.674
Brake Power (kW)	0.709	0.797	0.810	0.782	0.744	0.684	0.604	0.406
Torque (ft-lb)	13.315	14.968	15.220	14.689	13.969	12.842	11.337	7.624
EGR %	1.575	1.338	1.022	0.781	0.408	0.000	0.000	0.000
Fuel 1	EEE	EEE	EEE	EEE	EEE	EEE	EEE	EEE
Fuel 2	ULSD	ULSD	ULSD	ULSD	ULSD	ULSD	ULSD	ULSD
Fuel1 Flow (g/s)	0.013	0.017	0.018	0.019	0.022	0.023	0.020	0.031
Fuel2 Flow (g/s)	0.081	0.081	0.081	0.077	0.073	0.068	0.062	0.052
Fuel1 Fraction	0.140	0.170	0.184	0.195	0.231	0.252	0.245	0.376
Fuel2 Fraction	0.860	0.830	0.816	0.805	0.769	0.748	0.755	0.624
Fuel Energy (J/cyc)	224.364	231.810	233.488	226.667	222.981	213.008	192.268	193.448
Fuel H/C	1.825	1.829	1.830	1.831	1.835	1.838	1.837	1.851
Fuel O/C	0.000	0.000	0.000	0.000	0.000	0.000	0.000	0.000
Fuel MW/C	13.850	13.853	13.855	13.856	13.860	13.862	13.861	13.876
Fuel mf H2O	0.000	0.000	0.000	0.000	0.000	0.000	0.000	0.000
RI (MW/m^2)	0.915	0.792	0.719	0.615	0.531	0.474	0.436	0.367
Peak HRR (J/deg)	23.865	21.950	20.661	18.605	16.943	15.647	14.421	12.845
Peak PRR (bar/deg)	3.337	3.090	2.931	2.694	2.481	2.330	2.221	2.029
PP (bar)	63.416	63.074	62.680	61.529	60.219	59.303	58.512	57.236
LPP (ATDC)	2.637	2.813	2.813	2.813	2.813	2.813	2.813	2.637
P Orifice (bar)								
P Intake (bar)	1.030	1.029	1.029	1.029	1.026	1.024	1.021	1.028
P Exhaust (bar)	1.096	1.080	1.071	1.066	1.054	1.047	1.042	1.059
T Orifice (C)								
T Intake (C)	45	45	45	45	45	45	45	45
T Exhaust Port (C)	155	155	155	155	155	155	155	155
T Exhaust Tank (C)	154	154	154	154	154	154	154	154
Gross Therm Eff	0.337625	0.32605	0.313942	0.296962	0.270909	0.263886	0.271374	0.226943
Net Therm Eff	0.303199	0.295318	0.284701	0.267376	0.242002	0.234533	0.239726	0.193499

Brake Therm Eff	0.181869	0.196949	0.197483	0.195968	0.189161	0.181168	0.176314	0.116565
Brake Therm Eff (CF)	0.16124	0.158758	0.150269	0.129839	0.103195	0.090498	0.081499	0.038828
Turbo Eff	0.062009	0.069218	0.082607	0.095962	0.068928	0.013732	-0.08615	0.094315
Vol Eff	0.914624	0.905412	0.894897	0.886805	0.877289	0.867161	0.859697	0.85472
Comb Eff	0.719367	0.716	0.711142	0.709861	0.708788	0.705422	0.701933	0.694254
Exhaust Loss	0.218527	0.208744	0.204116	0.208527	0.209598	0.216191	0.235651	0.23189
Pumping Loss	0.034426	0.030732	0.029241	0.029586	0.028907	0.029352	0.031648	0.033444
Heat Transfer Loss	0.163215	0.181205	0.193084	0.204373	0.228281	0.225345	0.194908	0.23542
ISFCg	256.916	265.7356	275.8359	291.4846	319.0794	327.3062	318.365	378.8075
ISFCn	286.0873	293.3894	304.1662	323.7382	357.1926	368.2693	360.3944	444.2803
BSFC	476.9431	439.9257	438.5016	441.7025	456.9731	476.7473	490.012	737.5108
BSFC_CF	537.9639	545.7575	576.2745	666.6719	837.6501	954.4036	1060.087	2214.085
HC (ppm)	3340.889	3474.552	3661.922	3713.758	3764.513	3899.959	4033.729	4373.361
NOx (ppm)	22.02343	15.56285	12.04541	11.66026	10.29332	8.942449	7.685684	6.476812
CO2ex (ppm)	14800	14800	14800	14800	14800	14800	14800	14800
O2in (ppm)	208198.5	208305.8	208469.3	208603.5	208798.9	209076.1	209432.2	209832.6
CO (ppm)	8350	8350	8350	8350	8350	8350	8350	8350
PM (mg/m^3)								
HC (g/kg-fuel)	125.8398	130.207	136.255	137.9129	139.5294	143.8147	148.0049	158.4541
NOx (g/kg-fuel)	1.797458	1.263398	0.970804	0.937838	0.82607	0.713888	0.610532	0.50752
CO2ex (g/kg-fuel)	1771.418	1761.968	1749.271	1745.688	1741.84	1732.689	1724.141	1700.743
O2in (g/kg-fuel)	18119.05	18031.69	17915.79	17890.6	17867.89	17797.62	17739.97	17532.68
CO (g/kg-fuel)	636.0738	632.6807	628.1214	626.8347	625.4531	622.1672	619.0978	610.6961
PM (g/kg-fuel)								
HC (g/ikW-hr)	32.33026	34.60063	37.58402	40.19948	44.52097	47.07142	47.11959	60.0236
NOx (g/ikW-hr)	0.461796	0.33573	0.267783	0.273365	0.263582	0.23366	0.194372	0.192252
CO2ex (g/ikW-hr)	455.1056	468.2176	482.5117	508.841	555.7852	567.1198	548.9062	644.254
O2in (g/ikW-hr)	4655.075	4791.66	4941.818	5214.835	5701.276	5825.27	5647.788	6641.511
CO (g/ikW-hr)	163.4176	168.1258	173.2584	182.7127	199.5692	203.6392	197.0991	231.3362
PM (g/ikW-hr)								
HC (g/bkW-hr)	60.01843	57.2814	59.74803	60.91648	63.7612	68.56324	72.52417	116.8616
NOx (g/bkW-hr)	0.857285	0.555801	0.425699	0.414245	0.377492	0.340344	0.299168	0.374301
CO2ex (g/bkW-hr)	844.8655	775.1352	767.0581	771.0747	795.974	826.0548	844.8496	1254.316
O2in (g/bkW-hr)	8641.756	7932.603	7856.103	7902.325	8165.146	8484.966	8692.8	12930.54
CO (g/bkW-hr)	303.371	278.3325	275.4322	276.8745	285.8152	296.6165	303.3653	450.3949
PM (g/bkW-hr)								
Air Flow (g/s-cyl)	6.056542	6.006237	5.956212	5.917557	5.860475	5.801857	5.736347	5.742554
AFR mass	64.4916	61.67417	60.33921	61.6694	62.07105	64.07531	69.82301	69.051
AFR carbon	78.57263	78.1435	77.56586	77.40312	77.22931	76.81343	76.42387	75.36343
AFR oxygen	69.65714	68.93276	68.41942	68.71622	69.09224	69.45467	69.98581	70.38477
AFR Lambda meter								
AFR Average	70.91	69.58	68.77	69.26	69.46	70.11	72.08	71.60
AFR Stoich	14.50	14.50	14.51	14.51	14.51	14.52	14.52	14.54
Phi mass	0.22	0.24	0.24	0.24	0.23	0.23	0.21	0.21

Phi carbon	0.18	0.19	0.19	0.19	0.19	0.19	0.19	0.19
Phi oxygen	0.21	0.21	0.21	0.21	0.21	0.21	0.21	0.21
Phi Lambda meter	0.21	0.21	0.21	0.21	0.21	0.21	0.21	0.21
Phi Average	0.20	0.21	0.21	0.21	0.21	0.21	0.20	0.20
CA5 (ADTC)	-8.88	-9.94	-10.76	-11.37	-12.20	-12.61	-12.81	-13.93
CA10 (ADTC)	-5.99	-6.49	-6.87	-7.14	-7.55	-7.69	-7.66	-8.27
CA25 (ADTC)	-3.84	-4.01	-4.14	-4.21	-4.28	-4.34	-4.48	-4.51
CA75 (ADTC)	2.51	3.13	3.42	3.93	4.58	4.60	3.89	5.28
CA90 (ADTC)	10.90	12.00	12.43	13.40	15.10	14.86	12.58	17.09
CA95 (ADTC)	22.42	24.25	25.10	27.93	31.88	33.82	31.85	43.84
CA10-90 (deg)	16.89	18.50	19.29	20.54	22.64	22.54	20.24	25.36
CA5-90 (deg)	19.78	21.94	23.19	24.77	27.29	27.47	25.39	31.02
dBA	78.76	77.37	76.23	75.00	73.71	72.81	72.06	70.75
DI (mg/inj-cyl)	6.40	6.35	6.57	6.19	5.92	5.54	5.07	4.24
PFI (mg/inj-cyl)	1.01	1.90	0.93	1.83	2.03	2.20	2.19	2.63
eta cat (-)	-0.03	0.05	0.07	0.07	0.07	0.07	0.08	0.07
FSN (-)	0.00	0.00	0.00	0.00	0.00	0.00	0.00	0.00
Rail Press. (bar)	379.90	398.49	383.51	389.62	378.99	397.34	374.59	390.78
Main SOI (deg BTDC)	32.72	34.83	37.02	37.90	38.89	39.83	40.84	40.87
Opacity (%)	0.01	0.01	0.01	0.01	0.01	0.01	0.01	0.04
PFI (ms)	0.93	0.91	0.92	0.95	1.03	1.04	1.08	1.16
Main dur (ms)	0.76	0.71	0.75	0.71	0.70	0.67	0.69	0.63
Pedal (%)	9.00	9.00	9.00	9.00	9.00	9.00	9.00	9.00
O2 int (%)	20.99	21.00	21.02	20.98	20.99	21.04	21.05	21.13
O2 exh (%)	15.54	15.73	15.78	15.78	16.04	16.12	16.49	16.80
Phi_charge(-)	0.22	0.23	0.24	0.23	0.23	0.23	0.21	0.21
total mg	7.41	8.24	7.50	8.02	7.95	7.74	7.25	6.87
total fuel	0.09	0.10	0.10	0.10	0.09	0.09	0.08	0.08

7.8 Combustion Noise Calculation

```
function [Noise]= NoiseFilters(fs,P_cyl,A)
%Copyright©: SAE2013-01-1659 As published
%Inputs:
%fs: Sampling frequency [Hz]
%P_cyl: 1 cycle of cylinder pressure [Pa]
%A: A weighting identifier 0 or 1
%Outputs:
%Noise [dB]
NFFT=length(P_cyl);      %N for N-point-FFT
f=zeros(NFFT/2+1,1);     %Initialize frequency vector
f(1:NFFT/2+1,1) = fs/2*linspace(0,1,NFFT/2+1); %Frequency vector
dB_SA=zeros(size(f));    %Initialize structural attenuation (SA)
T=zeros(size(f));        %Initialize total attenuation (T)
a=[-1.594243E+02    2.029175415E-01 -2.981767797E-04    2.494291193E-07
...
    -1.166026273E-10    2.8203001E-14   -2.747693353E-18]; %a coefficients
b=[-1.065899E+02    1.89691E-02 -7.393291E-06   1.266005E-09 ...
    -1.278282E-13   7.033316E-18    -1.621458E-22];     %b coefficients
k=find(f>2300,1);
dB_SA(1:k-1)=a(1)+a(2)*f(1:k-1)+a(3)*f(1:k-1).^2+a(4)*f(1:k-1).^3 ...
+a(5)*f(1:k-1).^4+a(6)*f(1:k-1).^5+a(7)*f(1:k-1).^6; %SA<2.3 kHz
dB_SA(k:end)=b(1)+b(2)*f(k:end)+b(3)*f(k:end).^2+b(4)*f(k:end).^3 ...
+b(5)*f(k:end).^4+b(6)*f(k:end).^5+b(7)*f(k:end).^6; %SA>2.3 kHz
f_100=find(f>=100,1);    %Find the index for f=100 Hz
f_1e4=find(f>1e4,1);     %Find the index for f=10000 Hz
dB_SA(1:f_100-1)=-500;   %SA=-500 dB for f<100 Hz
dB_SA(f_1e4:end)=-500;   %SA=-500 dB for f>10000 Hz
dB_A=zeros(size(f));     %Initialize A attenuation (A)
    if (A==1)            %The A filter can be turned off with A=0
        R=(12200.^2.*f.^4)./(f.^2+20.6.^2)./(f.^2+12200.^2)./ ...
            sqrt((f.^2+107.7.^2).*(f.^2+737.9.^2));%R
        dB_A=2+20.*log10(R);    %A filter
    end
dB=dB_SA+dB_A;           %Combine filters
T=10.^(dB./20);          %Total attenuation (T)
T(NFFT/2+1:NFFT,1)=flipud(T(2:NFFT/2+1,1)); %T from Nyquist to fs
Y=zeros(NFFT,1);         %Initialize
Y_filt=zeros(NFFT,1);    %Initialize
P_filt=zeros(NFFT,1);    %Initialize
Y(1:NFFT)= fft(P_cyl(:,:),NFFT);   % calculate FFT

Y_filt=Y.*T;             % apply filter
sp_pts=NFFT/2+1;         % # of points in one-sided spectrum
amp=(Y_filt.*conj(Y_filt))/NFFT^2; % amplitude - note you use
%NFFT points because energy is spread over that number of frequencies
delt_f= fs/2/(sp_pts-1); % Frequency differential element
amp=amp*2/delt_f;        % the 2 corrects to a two-sided spectrum
pow_fft_filt=sum(amp(1:sp_pts))*delt_f; %Sum up the one-sided spectrum
P_RMS=sqrt(pow_fft_filt);          %calculate RMS P
Noise=20*log10(P_RMS/20e-6);         %Calculate D\dB rel to 20 microPascals
```

```
end
```

7.9 Drivven RCCI Tables

Table 7-11 Drivven RCCI Intake Pressure Table

Intake Pressure [bar]												
mm3/RPM	1250	1500	1750	2000	2250	2500	2750	3000	3250	3500	3750	4000
5	1	1	1	1	1	1	1.15	1.2	1.25	1.3	1.35	1.4
8	1	1	1	1	1	1	1.19	1.235	1.285	1.335	1.383	1.43
10	1	1	1	1	1	1	1.23	1.27	1.32	1.37	1.415	1.46
13	1	1	1	1	1	1	1.278	1.315	1.365	1.424	1.466	1.513
15	1	1	1	1	1	1	1.326	1.36	1.41	1.478	1.518	1.565
18	1	1	1	1	1	1.358	1.401	1.433	1.48	1.529	1.569	1.613
20	1.05	1.05	1.1	1.215	1.26	1.43	1.46	1.495	1.535	1.58	1.62	1.66
23	1.133	1.12	1.18	1.26	1.33	1.47	1.529	1.58	1.593	1.636	1.675	1.715
25	1.165	1.17	1.23	1.3	1.41	1.545	1.598	1.655	1.67	1.693	1.73	1.77
28	1.18	1.275	1.3	1.43	1.57	1.68	1.72	1.775	1.78	1.805	1.825	1.871
30	1.2	1.34	1.4	1.61	1.685	1.796	1.825	1.885	1.89	1.91	1.935	1.985
35	1.28	1.45	1.6	1.735	1.825	1.9	1.92	2	2.02	2.05	2.09	2.115
40	1.34	1.56	1.72	1.945	2	2.06	2.1	2.115	2.174	2.188	2.211	2.228
50	1.34	1.66	1.88	2.1	2.157	2.18	2.19	2.22	2.32	2.34	2.35	2.36
60	1.34	1.75	1.97	2.13	2.21	2.265	2.285	2.32	2.33	2.34	2.35	2.36
70	1.34	1.75	2.03	2.15	2.21	2.265	2.285	2.32	2.33	2.34	2.35	2.36

Table 7-12 Drivven RCCI EGR Table

MAF [kg/h]											
mm3/RPM	750	840	1000	1250	1500	1750	2000	2250	2500	2750	3000
5	54	30	30	35	35	35	35	35	48	148.5	165.6
7.5	54	30	30	35	35	40	45	60	60	135.3	162
10	54	35	35	35	35	40	50	60	60	128.7	154.8
12.5	56.25	48	48	48	48	48	50	60	60	135.3	165.6
15	60.75	68	68	68	68	68	70	80	90	145.2	174.6
17.5	68.4	43.848	75	75	75	75	88.8	90	100	155.1	187.2
20	74.25	51.912	90	90	90	90	96	113.4	139.5	165	199.8
22.5	81.45	58.968	100	100	100	100	108	126.9	153	171.6	207

25	90	68.04	66	100	100	100	118.8	136.35	162	183.15	219.6
27.5	94.5	77.616	77.52	88.5	93.6	109.2	127.2	145.8	169.5	193.05	234
30	99	89.712	93	101.25	104.4	121.8	133.2	152.55	177	199.65	248.4
32.5	103.5	103.824	113.4	117.75	113.4	132.3	144	163.35	192	217.8	277.2
35	108	115.92	126	130.5	127.8	149.1	160.8	179.55	210	244.2	315
37.5	108	118.944	138.6	144	154.8	170.1	177.6	199.8	231	277.2	338.4
40	108	120.96	139.2	157.5	187.2	220.5	256.8	287.55	322.5	349.8	381.6
42.5	108	120.96	144	180	216	252	288	324	360	396	432

Table 7-13 Drivven RCCI Main SOI Table

Main SOI [d bTDC]											
mm3/RPM	250	500	750	1000	1250	1500	1750	2000	2250	2500	3000
5	0	38	35	35	33	33	33	38	38	38	35
7.5	0	38	35	35	38	38	38	40	40	42	40
10	0	40	35	38	40	42	43	45	45	45	45
12.5	0	40	35	40	45	47	48	48	48	45	45
15	0	40	45	45	50	52	52	48	48	48	48
17.5	0	40	45	48	52	57	57	50	48	48	48
20	0	45	45	48	60	60	60	50	48	48	48
22.5	0	45	45	48	57	57	57	50	50	48	48
25	0	45	45	48	57	59	57	55	55	48	48
27.5	0	45	45	50	57	59	57	55	55	50	48
30	0	45	45	50	57	59	57	55	55	55	7.00781
35	0	45	45	50	55	55	57	57	57	55	9
40	0	45	45	50	50	57	57	57	57	55	10.5
50	0	45	45	50	50	57	57	57	57	55	11.50781
60	0	45	45	50	50	55	57	57	57	55	12.49219
70	0	45	45	50	50	55	57	57	57	55	12.49219

Table 7-14 Drivven RCCI Rail Pressure and HPV Duty Cycle Table

Rail Pressure [bar]												
mm3/RPM	250	500	750	1000	1250	1500	1750	2000	2250	2500	2750	3000
5	300	300	300	300	350	350	350	350	350	350	605	615
8	300	300	300	300	380	375	375	375	375	375	670	670
10	300	300	300	330	400	400	400	400	400	400	750	750
13	300	300	305	360	450	450	450	450	450	450	800	800

15	300	300	325	390	475	500	500	500	500	500	880	880
18	300	300	350	420	500	500	500	525	525	525	950	950
20	300	312	375	460	525	525	525	550	550	550	1000	1000
23	300	325	400	520	550	550	575	575	575	575	1035	1040
25	300	337	425	550	600	600	600	600	600	600	1070	1085
28	300	350	445	570	600	650	650	625	650	800	1120	1140
30	300	350	450	600	700	700	970	1050	1100	1150	1170	1200
35	300	350	450	700	840	900	1000	1080	1140	1200	1240	1300
40	300	350	450	780	920	940	1040	1130	1180	1250	1350	1400
50	300	350	450	780	920	1010	1100	1180	1250	1350	1450	1500
60	300	350	450	780	920	1040	1150	1230	1350	1450	1550	1600
70	300	350	450	780	920	1040	1150	1230	1350	1450	1550	1600

HPV [%]												
mm3/RPM	250	500	750	1000	1250	1500	1750	2000	2250	2500	2750	3000
5	15	15	15	15	17	19	20	15	15	15	15	15
8	15	15	17	18	18	21	22	15	20	22	24	15
10	15	15	17	20	22	23	24	22	22	24	24	15
13	15	15	18	21	22	24	24	24	24	26	26	15
15	15	15	18	21	22	26	26	26	26	28	28	15
18	15	15	18	21	22	26	26	26	26	28	28	15
20	15	15	20	21	26	27	27	28	28	28	28	15
23	15	15	20	15	27	29	30	30	29	28	26	15
25	15	15	15	15	28	30	30	30	28	28	26	15
28	15	15	15	15	15	32	32	30	30	30	20	15
30	15	15	15	15	15	32	32	32	32	32	15	15
35	15	15	15	15	15	32	32	32	32	32	15	15
40	15	15	15	15	15	15	15	15	15	15	15	15
50	15	15	15	15	15	15	15	15	15	15	15	15
60	15	15	15	15	15	15	15	15	15	15	15	15
70	15	15	15	15	15	15	15	15	15	15	15	15

Table 7-15 Drivven RCCI PFI Fraction Table

PFI fraction [%]											
mm3/RPM	250	500	750	1000	1250	1500	1750	2000	2250	2500	3000
5	0	0	0	0	0	0	0	0	0	0	0
7.5	0	0	35	25	20	20	20	10	10	10	30
10	0	0	60	57	35	35	35	24	20	15	50
12.5	0	0	65	62	45	45	45	45	40	40	55
15	0	0	75	75	50	50	50	55	70	70	60
17.5	0	0.25781	75	75	53	53	53	72	80	80	60
20	0	0.49219	85	82	67	67	67	80	80	80	65
22.5	0	0.75	85	84	72	72	72	85	85	80	70
25	0	1.00781	85	85	86	86	85	85	85	80	80
27.5	1.00781	1.99219	85	85	86	86	86	86	88	80	80
30	1.00781	1.99219	87	87	87	87	86	88	88	80	80
35	1.00781	1.99219	0	0	0	0	0	0	0	0	80
40	1.00781	1.99219	0	0	0	0	0	0	0	0	10.5
50	1.00781	1.99219	0	0	0	0	0	0	0	0	11.50781
60	1.00781	1.99219	0	0	0	0	0	0	0	0	12.49219
70	1.00781	1.99219	0	0	0	0	0	0	0	0	12.49219

Table 7-16 Drivven RCCI ECT Correction Table

Int Press.	
delta Int P	% PFI
-0.1	-7.5
-0.08	-6
-0.06	-4.5
-0.04	-3
-0.02	-1.5
0	0
0.02	1.5
0.04	3
0.06	4.5
0.08	6
0.1	7.5

PFI corr.	
deg. C	Pfi multiply
0	0.7
10	0.72
20	0.75
30	0.8
40	0.82
50	0.85
60	0.9
70	0.95
80	1
90	1
100	1

SOI corr.	
deg. C	deg. aTDC
0	-17
10	-16
20	-14
30	-12
40	-10
50	-8
60	-4
70	-2
80	0
90	0
100	0

Table 7-17 Drivven RCCI Cylinder Balancing Table

Cyl1	
RPM	Multi
0	1
500	1
750	1
1000	0.98
1250	0.98
1500	1
1750	1
2000	1
2250	1
2500	1
2500.01	1
2500.02	1

Cyl2	
RPM	Multi
0	1
500	1
750	1
1000	1
1250	1
1500	1
1750	1
2000	1
2250	1
2500	1
2500.01	1
2500.02	1

Cyl3	
RPM	Multi
0	1
500	1
750	1
1000	1
1250	1.04
1500	1.04
1750	1.04
2000	1.03
2250	1
2500	1
2500.01	1
2500.02	1

Cyl4	
RPM	Multi
0	1
500	1
750	1
1000	1.06
1250	1.05
1500	1.05
1750	1.03
2000	1.03
2250	1
2500	1
2500.01	1
2500.02	1

Table 7-18 Drivven RCCI CA50 Table

CA50 [deg. aTDC]										
mm3/RPM	250	500	750	1000	1250	1500	1750	2000	2250	3000
5	0	0	-5	-5	-3	-3	-3	-3	-3	-3
7.5	0	0	-5	-5	-3	-2	-2	-2	-2	-2
10	0	0	-5	-5	-3	-1	-1	0	0	0
12.5	0	0	-3	-3	1	3	3	2	2	2.5
15	0	0	2.5	3	5	5	5	4	4	4
17.5	0	0	3	6	6	6	6	6	5	5
20	0	0	4	7	8.5	8.5	8.5	7	5	5
22.5	0	0	4	4	9	9	9	9	6	6
25	0	0	4	4	8	8	8	7	7	7
27.5	0	0	0	0	8	8	8	4	4	4
30	0	0	0	0	8	8	8	4	4	0
35	0	0	0	0	4	9	9	0	0	0
40	0	0	0	0	4	9	9	0	0	0
50	0	0	0	0	0	9	9	0	0	0
60	0	0	0	0	0	9	9	0	0	0
70	0	0	0	0	0	10	10	0	0	0

Table 7-19 Drivven RCCI NC CAD to PFI Adjustment Table

CAD to PFI	
delta CA50	PFI fraction multiplier
-5	0.8
-4	0.9
-3	0.9
-2	1
-1	1
0	1
1	1
2	1.1
3	1.1
4	1.1
5	1.2

7.10 Drivven CDC Tables

Table 7-20 Drivven CDC Intake Pressure Table

Int Press [bar]								
mm3/RPM	1250	1500	1750	2000	2250	2500	2750	3000
5	1	1	1	1.06	1.09	1.126	1.16	1.19
7.5	1	1	1.048	1.074	1.113	1.153	1.198	1.235
10	1	1.03	1.059	1.087	1.124	1.178	1.226	1.273
12.5	1.01	1.06	1.08	1.112	1.148	1.188	1.242	1.31
15	1.01	1.08	1.105	1.15	1.177	1.215	1.265	1.33
17.5	1.04	1.1	1.149	1.191	1.216	1.255	1.3	1.369
20	1.099	1.137	1.178	1.228	1.26	1.298	1.34	1.415
22.5	1.136	1.182	1.221	1.271	1.304	1.342	1.406	1.482
25	1.179	1.22	1.288	1.32	1.362	1.404	1.478	1.555
30	1.24	1.3	1.388	1.429	1.484	1.543	1.598	1.676
35	1.294	1.35	1.45	1.601	1.641	1.698	1.756	1.829
40	1.35	1.5	1.67	1.728	1.778	1.823	1.869	1.935
50	1.541	1.711	1.804	1.879	1.935	1.99	2.048	2.098

60	1.65	1.833	1.936	2.043	2.113	2.2	2.255	2.289
65	1.69	1.884	1.991	2.09	2.16	2.25	2.3	2.32
70	1.69	1.929	2.06	2.15	2.21	2.265	2.3	2.32

Table 7-21 Drivven CDC EGR Table

MAF [kg/hr.]											
mm3/RPM	750	840	1000	1250	1500	1750	2000	2250	2500	2750	3000
5.00	54.00	29.74	45.00	50.00	54.90	59.85	69.60	99.90	132.00	148.50	165.60
7.50	54.00	29.23	45.00	50.00	52.20	55.65	66.00	91.80	129.00	135.30	162.00
10.00	54.00	29.23	45.00	50.00	54.00	54.60	62.40	83.70	117.00	128.70	154.80
12.50	56.25	30.24	45.00	50.00	54.00	59.85	67.20	81.00	121.50	135.30	165.60
15.00	60.75	36.29	46.50	50.00	55.80	65.10	79.20	94.50	126.00	145.20	174.60
17.50	68.40	43.85	46.80	52.50	60.30	70.35	88.80	105.30	132.00	155.10	187.20
20.00	74.25	51.91	52.80	57.75	64.80	75.60	96.00	113.40	139.50	165.00	199.80
22.50	81.45	58.97	58.80	66.75	72.90	85.05	108.00	126.90	153.00	171.60	207.00
25.00	90.00	68.04	66.00	78.00	82.80	96.60	118.80	136.35	162.00	183.15	219.60
27.50	94.50	77.62	77.52	88.50	93.60	109.20	127.20	145.80	169.50	193.05	234.00
30.00	99.00	89.71	93.00	101.25	104.40	121.80	133.20	152.55	177.00	199.65	248.40
32.50	103.50	103.82	113.40	117.75	113.40	132.30	144.00	163.35	192.00	217.80	277.20
35.00	108.00	115.92	126.00	130.50	127.80	149.10	160.80	179.55	210.00	244.20	315.00
37.50	108.00	118.94	138.60	144.00	154.80	170.10	177.60	199.80	231.00	277.20	338.40
40.00	108.00	120.96	139.20	157.50	187.20	220.50	256.80	287.55	322.50	349.80	381.60
42.50	108.00	120.96	144.00	180.00	216.00	252.00	288.00	324.00	360.00	396.00	432.00

Table 7-22 Drivven CDC Main SOI Table

Main SOI [deg. bTDC]											
mm3/RPM	250	500	750	1000	1250	1500	1750	2000	2250	2500	3000
5	0	0	-3	-3	0	2	2.25	2.5	3	3.5	5.5
7.5	0	0	-3	-3	-0.5	2	0.5	1	1	1.5	3
10	0	0	-3	-3	-0.5	0	0.5	1	1	1.5	3
12.5	0	0	-3	-3	-0.5	0	0.5	1	1.5	2	3.5
15	0	0	-3	-3	0	0	1	1	1.5	2	3.5
17.5	0	0.25	0.5	0.5	0.5	0	1.5	1	2	2	3.5
20	0	0.5	1	1	1	1	1.5	1.5	2	2	4
22.5	0	0.75	1	1	1	1	2	2	2	2.5	4

25	0	1	1	1.5	1.5	1.5	2	2	2.5	3	4
27.5	1	2	2	2	2	2	2.5	2.5	3	4	5
30	1	2	2.5	2.5	2.5	2.5	3	3	3	4.5	7
35	1	2	2.75	2.75	3.5	3	3.5	3.5	3.5	6	9
40	1	2	2.75	2.75	3.5	3.5	4	4	5	7	10.5
50	1	2	2.75	2.75	3.5	3.5	4.5	4.5	6	8.5	11.5
60	1	2	2.75	2.75	3.5	3.5	5.5	5	8.5	9.5	12.5
70	1	2	2.75	2.75	3.5	3.5	5.5	6.5	8.5	9.5	12.5

Table 7-23 Drivven CDC Pilot Split Table

Fuel Split [ms]												
mm3/RPM	250	500	750	1000	1250	1500	1750	2000	2250	2500	2750	3000
5	10	10	10	10	10	10	10	10	10	10	10	10
7.5	10	10	10	10	10	10	10	10	10	10	10	10
10	10	10	10	10	10	10	10	10	10	10	10	10
12.5	8	8	8	8	8	8	8	8	8	8	8	8
15	6.66667	6.667	6.67	6.667	6.667	6.67	6.67	6.667	6.6667	6.667	6.6667	6.667
17.5	5.71429	5.714	5.71	5.714	5.71	5.71	5.71	5.714	5.7143	5.714	5.7143	5.714
20	5	5	5	5	5	5	5	5	5	5	5	5
22.5	4.44445	4.444	4.44	4.444	4.44	4.44	4.44	4.444	4.4444	4.444	4.4444	4.444
25	4	4	4	4	4	4	4	4	4	4	4	4
27.5	3.63636	3.636	3.64	3.636	3.63636	3.63636	3.6364	3.636	3.6364	3.636	3.6364	3.636
30	3.33333	3.333	3.33	3.333	3.33333	3.33333	3.3333	3.333	3.3333	3.333	3.3333	3.333
35	2.85714	2.857	2.86	2.857	2.85714	2.85714	2.8571	2.857	2.8571	2.857	2.8571	2.857
40	2.5	2.5	2.5	2.5	2.5	2.5	2.5	2.5	2.5	2.5	2.5	2.5
50	2	2	2	2	2	2	2	2	2	2	2	0
60	1.66667	1.667	1.67	1.667	1.66667	1.66667	1.6667	1.667	1.6667	1.667	0	0
70	1.42857	1.429	1.43	1.429	1.42857	1.42857	1.4286	1.429	1.4286	1.429	0	0

Table 7-24 Drivven CDC Rail Pressure and HPV Duty Cycle Table

Rail Press [bar]												
mm3/rpm	250	500	750	1000	1250	1500	1750	2000	2250	2500	2750	3000
0	300	300	300	300	300	375	400	350	400	450	500	550
5	300	300	300	300	300	400	425	375	425	475	550	600
7.5	300	300	300	350	400	425	450	400	450	500	600	650
10	300	300	300	375	425	450	500	425	500	550	650	700
12.5	300	300	305	400	450	500	550	500	575	600	700	750
15	300	300	325	450	500	525	600	525	625	675	750	800
17.5	300	300	350	550	600	600	700	550	650	700	825	850
20	300	310	375	600	650	650	750	575	725	775	800	900
22.5	300	320	400	650	700	700	825	650	775	825	900	925
25	300	330	425	700	750	750	850	750	825	850	950	1000
27.5	300	340	445	750	800	800	860	850	900	950	1000	1050
30	300	350	450	800	850	860	900	900	975	1000	1075	1100
35	300	350	450	825	875	900	950	1000	1050	1100	1175	1250
40	300	350	450	850	900	925	1000	1075	1150	1200	1275	1330
50	300	350	450	900	920	1040	1100	1225	1250	1300	1410	1500
60	300	350	450	900	920	1040	1150	1230	1350	1450	1550	1600

HPV [%]												
mm3/rpm	250	500	750	1000	1250	1500	1750	2000	2250	2500	2750	3000
5	15	15	17	17	20	21	21	20	22	20	20	20
8	15	15	17	22	22	23	23	23	22	22	20	20
10	20	20	17	24	25	25	26	26	27	27	20	20
13	25	30	20	24	27	27	28	28	30	30	20	20
15	30	30	20	28	28	29	31	31	30	30	25	25
18	35	30	20	30	30	31	32	32	31	31	30	30
20	35	35	25	30	32	33	34	34	33	33	35	35
23	35	35	35	35	34	35	36	36	35	35	35	35
25	300	40	40	40	36	37	38	37	37	37	40	40
28	300	40	40	40	38	38	38	38	38	39	40	40
30	300	40	40	40	38	38	38	38	40	40	40	40
35	300	40	40	40	40	40	40	40	40	40	40	40
40	300	40	40	40	40	40	40	40	40	40	40	40
50	300	350	40	40	40	40	40	40	40	40	40	40
60	300	350	40	40	40	40	40	40	40	40	40	40
70	300	350	450	780	920	40	40	40	40	40	40	40

Table 7-25 Drivven CDC Swirl Duty Cycle Table

Swirl [% duty cycle]												
mm3/RPM	700	750	850	1000	1250	1500	1750	2000	2250	2500	2750	3000
0	0	75	75	75	75	75	75	72.5	67.5	60	42.5	15
5	0	75	75	75	75	75	67.5	60	55	50	35	15
7.5	0	75	75	75	75	72.5	62.5	55	47.5	40	32.5	15
10	0	75	75	75	75	62	57.5	50	42.5	35	30	12.5
12.5	0	75	75	75	72.5	57	52	45	37.5	30	25	7.5
15	0	75	75	75	67.5	52	47.5	40	32.5	25	20	0
17.5	0	70	70	67.5	60	47	42.5	35	27.5	20	15	0
20	0	60	60	57.5	52.5	37	37.5	30	20	12.5	10	0
22.5	0	55	55	52.5	50	35	35	25	10	5	5	0
25	0	50	50	50	45	32	32.5	22.5	0	0	0	0
27.5	0	47.5	47.5	47.5	42.5	32	30	20	0	0	0	0
30	0	45	45	45	40	32	27.5	15	0	0	0	0
32.5	0	40	40	40	37.5	30	26	10	0	0	0	0
35	0	15	15	15	15	25	25	0	0	0	0	0
40	0	0	0	0	0	20	20	0	0	0	0	0
50	0	0	0	0	0	0	0	0	0	0	0	0

Table 7-26 Drivven CDC CA50 Table

CA50 [deg. ATDC]										
mm3/RPM	250	500	750	1000	1250	1500	1750	2000	2250	3000
5	0	0	0	16	16	16	16	16	16	0
7.5	0	0	0	16	16	16	16	16	16	16
10	0	0	0	16	16	16	16	16	16	16
12.5	0	0	0	16	16	16	16	16	16	16
15	0	0	0	16	16	16	16	16	16	16
17.5	0	0	0	16	16	16	16	16	16	16
20	0	0	0	16	16	16	16	16	16	16
22.5	0	0	0	16	16	16	16	16	16	16
25	0	0	0	0	16	16	16	0	0	0
27.5	0	0	0	0	16	16	16	0	0	0
30	0	0	0	0	16	16	16	0	0	0
35	0	0	0	0	16	16	16	0	0	0
40	0	0	0	0	16	16	16	0	0	0
50	0	0	0	0	16	16	16	0	0	0
60	0	0	0	0	16	16	16	0	0	0
70	0	0	0	0	16	16	16	0	0	0